Oriented Emitters in Plasmonic Nanoresonators

Von der Universität Bayreuth zur Erlangung des Grades eines
Doktors der Naturwissenschaften (Dr. rer. nat.)
genehmigte Abhandlung

von

Christoph Günter Schnupfhagn

geboren in Weiden i. d. Opf.

Angefertigt am Lehrstuhl für Experimentalphysik III
der Universität Bayreuth

1. Gutachter: Prof. Dr. Markus Lippitz

2. Gutachter: Prof. Dr. Jürgen Köhler

3. Gutachter: Prof. Dr. Jörg Enderlein

Tag der Einreichung: 19. Mai 2023

Tag des Kolloquiums: 20. November 2023

Abstract

Localized surface plasmon resonances in metal nanostructures allow the confinement of electromagnetic fields in exceptionally small volumes below the optical diffraction limit. In particular, the nanoparticle-on-mirror (NPoM) geometry offers precise control over all fabrication steps. Cavities on the scale of only a few nanometers are built from gold nanoparticles on a gold substrate, separated by ultrathin spacer layers. In this work, the interaction of oriented emitters with individual NPoMs is investigated in simulation and experiment. We develop sensitive optical spectroscopy methods with spatial and polarization resolution. Complementary to the experiments, we provide a universal and comprehensive theoretical framework to efficiently model the emitters, cavities, and their interaction.

First, we give a theoretical overview of light-matter interaction and quantum emitters. We introduce the Purcell enhancement of spontaneous emission in inhomogeneous environments, such as plasmonic cavities. Furthermore, we discuss the transition from weak to strong coupling, where the emitter and cavity form hybrid states.

To investigate the interaction of emitters with NPoMs, we first study both systems independently. We use dye monolayers encapsulated between two hectorite nanosheets as homogeneous incoherent emitter ensembles. The dye layers can be dropcasted onto any hydrophilic substrate, yielding uniform structures as thin as 4 nm and with lateral sizes of tens of microns. To accurately represent the dye monolayer in later simulations, we first experimentally characterize its optical properties. We determine the refractive index of the ultrathin structure by white light reflection spectroscopy with spatial resolution. The reflection spectra are fitted to transfer matrix calculations, taking into account the absorption of the dyes. The broadband fluorescence of the dye monolayer originates from two electronic transitions, which we disentangle by singular value decomposition. The orientation determination of both transition dipoles individually is essential to model the interaction with plasmonic nanoresonators. Therefore, we introduce and apply a novel and fast technique to determine the orientations of spectrally overlapping transition dipoles in dense dye layers. The presented hyperspectral imaging method generates polarization-dependent fluorescence spectra of the dye monolayers with diffraction-limited spatial resolution. We develop a statistical model for the dipole orientation distribution of incoherent ensembles to describe the measured data, revealing spatial maps of the dipole orientation on glass and gold substrates. In addition, we show how the time-averaged emission intensities of both transitions can act as a clock for picosecond molecular dynamics.

In the next part, we investigate the intrinsic resonances of NPoMs composed of a smooth gold substrate, a few-nanometer thick dielectric spacer, and a colloidal gold nanoparticle. We employ numerical simulations to decompose the optical response into quasi-normal modes (QNMs), allowing a low-level understanding of the fundamental NPoM resonances. Based on this, we quantify the influence of unavoidable variations in particle size and shape on the resonance frequencies. For comparison with the experiment, we compute the

diffraction patterns of each mode in the detector plane using a numerical far-field imaging technique. We then introduce an experimental setup for polarized scattering spectroscopy with spatial resolution to identify the fundamental modes of individual NPoMs in both the spatial and spectral domains, depending on the excitation and detection polarizations. We study the resonances of many individual NPoMs as a function of the gap size, varied between 1 nm and 4 nm by atomic layer deposition, and find a good agreement with the theoretical predictions.

Finally, we combine our results from the independent characterization of the cavity and emitters to analyze the fluorescence enhancement of the coupled system. The broadband emission of the dye monolayer allows us to determine the coupling strengths to different NPoM modes. In the simulations, we consider both excitation and emission enhancement to compute the experimentally observable fluorescence enhancement by each NPoM mode at each dipole position. In the experiment, we model the fluorescence enhancement spectra by a sum of NPoM resonances, which are determined by independent scattering spectroscopy. Thus, the coupling coefficients of the dye monolayer to the in-plane and out-of-plane NPoM modes can be directly compared between experiment and simulation. Our approach can be universally applied to describe the Purcell enhancement of emitters in cavities. We give an outlook on how strong coupling with dye monolayers might be observed in future experiments. Furthermore, we present our first results on nanostructured spacer layers to control the density and position of emitters in the future.

Zusammenfassung

Metall-Nanostrukturen besitzen lokalisierte Oberflächenplasmonen-Resonanzen. Diese ermöglichen es, elektromagnetische Felder in außergewöhnlich kleinen Volumen unterhalb der optischen Beugungsgrenze zu konzentrieren. Insbesondere Nanopartikel, die an einen Spiegel gekoppelt sind (*engl.* „nanoparticle-on-mirror“, NPoM) bieten eine präzise Kontrolle über alle Herstellungsschritte. Resonatoren mit einer Länge von wenigen Nanometern werden aus Gold-Nanopartikeln auf einem Goldsubstrat, die durch ultradünne Abstandsschichten getrennt sind, gebildet. In dieser Arbeit wird die Wechselwirkung von orientierten Emittern mit einzelnen plasmonischen Nanoresonatoren in Simulation und Experiment untersucht. Wir entwickeln sensitive optische Spektroskopiemethoden mit räumlicher und Polarisationsauflösung. Ergänzend zu den Experimenten präsentieren wir einen universellen und umfassenden theoretischen Rahmen, um Emitter, Resonatoren und deren Wechselwirkung effizient zu modellieren.

Zunächst geben wir einen theoretischen Überblick über die Licht-Materie-Wechselwirkung und Quantenemitter. Wir diskutieren den Purcell-Effekt, der die Verstärkung der spontanen Emission in inhomogenen Umgebungen wie plasmonischen Nanoresonatoren beschreibt. Darüber hinaus behandeln wir den Übergang von schwacher zu starker Kopplung, bei der Emitter und Resonator hybride Zustände bilden.

Um die Wechselwirkung von Emittern mit den Nanoresonatoren zu untersuchen, studieren wir zunächst beide Systeme unabhängig voneinander. Wir verwenden Farbstoff-Monolagen, die zwischen zwei Hectorit-Nanoschichten eingebettet sind, als homogenes, inkohärentes Emitter-Ensemble. Die Farbstoffschichten können auf ein beliebiges hydrophiles Substrat aufgebracht werden und ergeben homogene Strukturen mit einer Dicke von 4 nm und einer lateralen Größe von einigen zehn Mikrometern. Um die Farbstoff-Monolagen in späteren Simulationen präzise modellieren zu können, charakterisieren wir zunächst ihre optischen Eigenschaften experimentell. Wir bestimmen den Brechungsindex der dünnen Schichten durch Weißlicht-Reflexionsspektroskopie mit räumlicher Auflösung. Die Reflexionsspektren werden unter Berücksichtigung der Absorption der Farbstoffe an Transfermatrix-Rechnungen gefittet. Die breitbandige Fluoreszenz der Farbstoff-Monolage entsteht durch zwei elektronische Übergänge, die wir durch Singulärwertzerlegung voneinander trennen. Die Orientierungsbestimmung der beiden Übergangsdipole ist für die Modellierung der Wechselwirkung mit plasmonischen Nanoresonatoren unerlässlich. Daher zeigen und verwenden wir ein neuartiges und schnelles Verfahren zur Bestimmung der Orientierungen von spektral überlappenden Übergangsdipolen in dichten Farbstoffschichten. Die vorgestellte hyperspektrale Bildgebungsmethode erzeugt polarisationsabhängige Fluoreszenzspektren der Farbstoff-Monolagen mit beugungsbegrenzter räumlicher Auflösung. Wir entwickeln ein statistisches Modell für die Verteilung der Dipolorientierung inkohärenter Ensembles, um die experimentellen Daten zu beschreiben und schließlich räumliche Karten der Dipolorientierung auf Glas- und Goldsubstraten zu berechnen. Außerdem zeigen wir,

wie die zeitlich gemittelten Emissionsintensitäten beider Übergänge als Stoppuhr für die molekulare Dynamik im Bereich von Pikosekunden dienen können.

Im nächsten Teil untersuchen wir die Eigenresonanzen der Nanoresonatoren, die aus einem flachen Goldsubstrat, einem wenige Nanometer dicken dielektrischen Abstandshalter und einem kolloidalen Gold-Nanopartikel bestehen. Wir verwenden numerische Simulationen, um die optische Antwort in Quasi-Normalmoden (QNM) zu zerlegen, um ein tiefgehendes Verständnis der grundlegenden Resonanzen zu entwickeln. Auf dieser Grundlage quantifizieren wir den Einfluss unvermeidlicher Variationen der Partikelgröße und -form auf die Resonanzfrequenzen. Zum Vergleich mit dem Experiment berechnen wir die Beugungsmuster jeder Mode in der Detektorebene mit Hilfe einer numerischen Fernfeld-Abbildungstechnik. Anschließend stellen wir einen Versuchsaufbau für polarisierte Streuspektroskopie mit räumlicher Auflösung vor, um die fundamentalen Moden einzelner Nanoresonatoren sowohl mit räumlichen als auch mit spektralen Methoden in Abhängigkeit von Anregungs- und Detektionspolarisation zu identifizieren. Wir untersuchen die Resonanzen vieler einzelner Nanoresonatoren als Funktion der Resonatorlänge, die durch Atomlagenabscheidung zwischen 1 nm und 4 nm variiert wird, und finden eine gute Übereinstimmung mit den theoretischen Vorhersagen.

Schließlich kombinieren wir unsere Ergebnisse aus der unabhängigen Charakterisierung der Nanoresonatoren und der Emitter, um die Fluoreszenzverstärkung des gekoppelten Systems zu analysieren. Die breitbandige Emission der Farbstoff-Monolage ermöglicht es uns, die Kopplungsstärken an verschiedene Moden der Nanoresonatoren zu bestimmen. In den Simulationen berücksichtigen wir sowohl die Anregungs- als auch die Emissionsverstärkung, um die experimentell beobachtbare Fluoreszenzverstärkung durch jede einzelne Mode an jeder Dipolposition zu berechnen. Im Experiment modellieren wir die Fluoreszenz-Verstärkungsspektren durch eine Summe von Resonatormoden, die unabhängig davon durch Streuspektroskopie bestimmt werden. So können die Kopplungskoeffizienten der Farbstoff-Monolage zu den Moden des Nanoresonators, die parallel und senkrecht zum Substrat orientiert sind, direkt zwischen Experiment und Simulation verglichen werden. Unser vorgestellter Ansatz kann allgemein verwendet werden, um die Purcell-Verstärkung von Emittern in Kavitäten zu beschreiben. Wir geben einen Ausblick darauf, wie die starke Kopplung an Farbstoff-Monolagen in zukünftigen Experimenten beobachtet werden könnte. Außerdem stellen wir unsere ersten Ergebnisse zu nanostrukturierten Abstandshaltern vor, um zukünftig die Dichte und Position von Emittern kontrollieren zu können.

Publications

Publication in a scientific journal

C. Schnupfhagn, T. Schumacher, P. Markus, G. Papastavrou, O. Aftenieva, T.A.F. König, V. Dudko, M. Matejdes, J. Breu, and M. Lippitz. *Disentangling the Orientations of Spectrally Overlapping Transition Dipoles in Dense Dye Layers.* Nano Lett. 2022, 22, 18, 7499–7505

Contributions at international conferences

Talks

C. Schnupfhagn, S. Durst, T. Schumacher, and M. Lippitz. *First steps towards strong coupling between emitters and plasmonic lattices.* GRK 1640 Abschlusssymposium 2019 – Bad Honnef, Germany

C. Schnupfhagn, T. Schumacher, P. Markus, G. Papastavrou, O. Aftenieva, T.A.F. König, V. Dudko, M. Matejdes, J. Breu, and M. Lippitz. *Disentangling the Orientations of Spectrally Overlapping Transition Dipoles in Dense Dye Layers.* DPG Spring Meeting 2023 – Dresden, Germany

Posters

C. Schnupfhagn, S. Durst, T. Schumacher, and M. Lippitz. *First steps towards strong coupling between emitters and plasmonic lattices.* DPG Spring Meeting 2019 – Regensburg, Germany

C. Schnupfhagn, S. Durst, T. Schumacher, and M. Lippitz. *First steps towards long-range coherent energy transfer in plasmonic lattices.* Heraeus-Seminar “Ultrafast Quantum Phenomena in the Near Field” 2019 – Bad Honnef, Germany

C. Schnupfhagn, S. Durst, T. Schumacher, and M. Lippitz. *First steps towards strong coupling between emitters and plasmonic lattices.* 10th International Summer School “New Frontiers in Optical Technologies” 2019 – Tampere, Finland

Contributions of collaborators

J. Klier, **C. Schnupfhagn**, J. Obermeier, and M. Lippitz. *Femtosecond pulse compression for nonlinear spectroscopy.* DPG Spring Meeting 2019 – Regensburg, Germany

S. Durst, **C. Schnupfhagn**, and M. Lippitz. *Modelling Plasmon-Exciton Interaction using a Coupled-Oscillator Approach.* DPG Spring Meeting 2022 – Regensburg, Germany

S. Durst, S. Jana, **C. Schnupfhagn**, and M. Lippitz. *Phase correction and stability of a Mach-Zehnder interferometer for 2D electronic spectroscopy.* DPG Spring Meeting 2023 – Regensburg, Germany

Contents

1 Introduction

The development of the optical microscope brought about a new era for mankind to investigate the essential compartments of our environment. Antoni van Leeuwenhoek significantly contributed to the development of the microscope in the 17th century to study red blood cells and bacteria with unprecedented resolution. Knowledge about the microscopic composition of materials is essential to understand the macroscopic properties. Electronic transitions of molecules in the visible spectral region give rise to the color of materials we observe with our eyes. The invention of the laser established the field of modern optical spectroscopy, where microscopic objects can be investigated and controlled with high spatial and temporal resolution.

The optical resolution is inherently limited by diffraction. Considerable effort has been invested in the 20th century to overcome this fundamental limit. A milestone was the development of scanning near-field optical microscopy (SNOM), where scientists at IBM in 1984 could finally obtain a lateral resolution of $\lambda/20$ [1]. The Nobel Prize in Chemistry was awarded for super-resolved fluorescence microscopy techniques like photoactivated localization microscopy (PALM) [2] and stimulated emission depletion (STED) [3] in 2014. Moreover, it has been found that metal nanostructures can confine the electromagnetic energy below the optical diffraction limit by localized surface plasmon resonances (LSPR). The resonance frequencies can be tuned over a wide spectral range by the size, shape, and material of individual nanostructures and their dielectric environment [4]. Early experiments demonstrated that the roughness of metals on the nanoscale can significantly increase the efficiency of Raman scattering from adsorbed molecules [5], known today as surface-enhanced Raman scattering (SERS). The development of advanced fabrication techniques such as electron beam lithography (EBL), focused ion beam milling (FIB), and the chemical synthesis of noble metal nanoparticles meant a breakthrough for the field of nano-optics and plasmonics [6–8].

The electromagnetic field confinement of metal nanostructures enables the controlled interaction with emitters in the optical near-field. The electric field enhancement can be increased even further in hotspots between coupled plasmonic nanostructures separated by only a few nanometers [9]. In particular, the nanoparticle-on-mirror (NPoM) geometry gained growing interest in the past decade [10–13]. The simple fabrication allows the incorporation of a wide range of materials into the gap between the metal nanoparticle and the metal substrate. The nanoparticles can be metal spheres, cubes, and other shapes [14]. Ultrasmooth metal substrates are routinely fabricated by template stripping [15]. The resonances of the NPoM are very sensitive to the gap thickness and morphology, which allows for precision applications such as rulers with sub-nanometer accuracy [16]. Protrusions in the metal surface can give rise to pico-cavities where the dimensions of the field hotspot are on the order of single atoms [17, 18]. The NPoM geometry allows accessing

the ultimate level of light confinement, as the observations of nonlocality of the metal dielectric function [19] and quantum tunneling [20] demonstrate.

The photophysics of emitters significantly depends on the local environment. Incorporated into the NPoM gap, emitters experience increased radiative and non-radiative energy pathways [21]. On the one hand, losses in the metal give rise to emission quenching. It has been demonstrated that the orientation-dependent quenching above metal substrates can even facilitate the three-dimensional localization of emitters [22–24]. On the other hand, the NPoM can efficiently radiate into the far-field based on the hybridization of cavity and antenna modes [14, 25]. The balance of radiative and non-radiative decay channels, thus, impacts the observed emission enhancement. Furthermore, the electric field distribution in the gap determines the excitation enhancement of the emitter. Previous experiments have demonstrated that the radiative rates of emitters in plasmonic nanoresonators can be enhanced by several orders of magnitude while maintaining a high quantum efficiency [26, 27]. Hence, the NPoM geometry is a promising candidate for ultrafast single photon emission [28, 29] for applications in linear optical quantum computing [30]. The NPoMs support a variety of modes that allow shaping the emission spectrum [31–35]. Optimizing the interaction with emitters can lead to hybrid modes formed by gap plasmons and emitters. In the strong coupling regime, the energy coherently oscillates between the emitter and plasmon. Strong coupling at room temperature has been demonstrated for single quantum dots [36, 37], single molecules [38], molecule aggregates [39–43], and two-dimensional materials [44].

This work aims to investigate the coupling of oriented emitters with plasmonic nanoparticle-on-mirror resonators, which requires sophisticated experimental and theoretical methods. Two main aspects set this work apart from previously published works. First, the transition dipoles of emitters need to be aligned with the nanoresonator modes for efficient coupling. Therefore, we present a novel all-optical method to determine the transition dipole orientations in dense dye layers. Our hyperspectral imaging approach allows us to disentangle the orientations of multiple transition dipoles. Second, we use the broadband fluorescence of the dye monolayers to investigate the coupling to the in-plane and out-of-plane modes provided by the NPoM. Complementary numerical simulations enable us to determine the coupling strengths of the fundamental NPoM modes with the dye monolayer for an intuitive comparison with the experiments. We generalize the quasi-normal mode excitation coefficients of Kongsuwan et al. [45] to model the incoherent ensemble of broadband emitters with polarization resolution.

Chapter 2 reviews fundamental theoretical concepts of light-matter interaction and quantum emitters. We start with the macroscopic description of dielectrics and metals and then introduce the field of plasmonics. Furthermore, we discuss the spontaneous emission of dipoles in homogeneous and inhomogeneous environments. Specifically, we focus on the Purcell enhancement of dipoles at conductive interfaces and inside cavities. We then continue with the general photophysics of molecules and line broadening mechanisms. Finally, we describe the transition from weak to strong coupling in the framework of cavity quantum electrodynamics.

In Chapter 3, we characterize the dye monolayer, which will be coupled to plasmonic resonators in Chapter 5. The dye monolayer is encapsulated between hectorite nanosheets. Therefore, we first introduce numerical methods for radiating dipoles in layered media.

Numerical simulations require the refractive index and thickness of the encapsulated dye monolayer as input parameters. Hence, we demonstrate a general method to determine the dielectric function of multilayer systems with spatial resolution. We apply this technique to the hectorite nanosheets and the dye monolayers. Moreover, the transition dipole orientations of the dye monolayer are essential for efficient interaction with nanoresonators. Therefore, we present a novel method to disentangle the orientations of multiple spectrally overlapping transition dipoles to characterize the orientational order of the dye monolayer on different substrates. Finally, we discuss the fluorescence quenching depending on the orientation and distance of the dipoles to the gold substrate.

Chapter 4 presents the fabrication, experimental characterization, and numerical modeling of individual gold nanoparticles on a gold substrate with defined gap thickness. We aim for a fundamental understanding of the basic modes supported by the NPoM. Therefore, we introduce and calculate the quasi-normal modes of NPoMs and investigate the influence of geometric and dielectric variations on the resonance frequencies. We compute the far-field radiation associated with the individual modes to obtain the polarization-dependent diffraction patterns in the detector plane for comparison with experiments. Our hyperspectral imaging setup allows us to investigate the scattering of many individual NPoMs in the spectral and spatial domains. We model the polarization-dependent spectra by in-plane and out-of-plane NPoM resonances.

Chapter 5 combines the ingredients of Chapters 3 and 4 by studying the coupling of the dye monolayer to individual NPoMs. We first employ a theoretical model for the interaction of the dye monolayer with the NPoM modes. Specifically, we calculate the excitation coefficients of the quasi-normal modes, considering the inhomogeneous excitation of the dipoles in the gap. Each dipole incoherently emits into the far-field via the NPoM modes in the weak coupling regime. The results are compared with experimental results for many individual NPoMs. We combine scattering and fluorescence spectroscopy of many individual NPoMs to compare the experimental findings with the numerical simulations. Furthermore, we study the photobleaching of the dye monolayer inside the NPoM gap. Finally, we give an outlook toward strong coupling and future experiments with nanostructured emitter layers. We end with a general conclusion in Chapter 6.

Theory of emitters in structured environments

2

In this thesis, we investigate the coupling of dye monolayers with plasmonic nanoresonators. Hence, we briefly review some fundamental concepts of light-matter interaction and quantum emitters. In particular, we discuss the spontaneous emission in homogeneous and inhomogeneous environments. Finally, we describe the transition from weak to strong coupling of emitters in cavities.

2.1 Light-matter interaction

As long as the involved structures are significantly larger than the atomic scale, Maxwell's classical theory provides an accurate description of electrodynamics. In free space, the fundamental solutions to Maxwell's equations are transverse electromagnetic waves [46]. The vectorial electric field $\boldsymbol{E}$ and magnetic field $\boldsymbol{B}$ of a plane wave depend on the position $\boldsymbol{r}$ and time t and are represented as

$$\boldsymbol{E}(\boldsymbol{r},t) = \boldsymbol{E}_0 \left[e^{\mathrm{i}(\boldsymbol{k}\cdot\boldsymbol{r}-\omega t)} + \text{c.c.} \right] \quad , \tag{2.1}$$

$$\boldsymbol{B}(\boldsymbol{r},t) = \boldsymbol{B}_0 \left[e^{\mathrm{i}(\boldsymbol{k}\cdot\boldsymbol{r}-\omega t)} + \text{c.c.} \right] \quad . \tag{2.2}$$

Unless otherwise noted, we use the negative sign convention $e^{-\mathrm{i}\omega t}$ for electromagnetic waves, consistent with physics literature. The wave vector $\boldsymbol{k} = \boldsymbol{k}_0$ in vacuum determines the wave propagation direction and the wavelength $\lambda = 2\pi/|\boldsymbol{k_0}|$. Electromagnetic waves in free space are transverse, i.e., $\boldsymbol{k}$, $\boldsymbol{E}$, and $\boldsymbol{B}$ are perpendicular to each other. The wave propagation speed is the ratio between frequency ω and the magnitude of the wave vector. In vacuum, the speed of light $c_0 = \omega/k_0 = (\varepsilon_0\mu_0)^{-1/2}$ is determined by the vacuum permittivity ε_0 and the vacuum permeability μ_0.

Inside matter, the electric field displaces the negatively charged bound electrons from the positively charged atomic nuclei. The charge separation induces a small dipole moment $\boldsymbol{p}$ in each atom. The sum over all dipoles $\boldsymbol{p}_i$ in a unit volume, hence, gives rise to a macroscopic polarization $\boldsymbol{P}(\boldsymbol{r}) = \sum_i \boldsymbol{p}_i$. The polarization, in turn, generates an electric field which in isotropic media points in the opposite direction of the incoming wave. In the context of the presented work, it is sufficient to assume a linear relation $\boldsymbol{P} = \varepsilon_0\chi\boldsymbol{E}$ with susceptibility χ. The susceptibility is generally a tensor but reduces to a scalar value for isotropic media.

To describe the reaction of matter to an incoming electromagnetic wave, we introduce the dielectric displacement $\boldsymbol{D}$ in the macroscopic description of Maxwell's equations

$$\boldsymbol{D} = \varepsilon_0\boldsymbol{E} + \boldsymbol{P} = \varepsilon\varepsilon_0\boldsymbol{E} \quad , \tag{2.3}$$

with relative permittivity $\varepsilon = 1 + \chi$. A similar relation $\boldsymbol{B} = \mu_0 \mu \boldsymbol{H}$ exists between the magnetic flux density $\boldsymbol{B}$ and magnetic field strength $\boldsymbol{H}$. Since only nonmagnetic media are considered in this work, we set the relative permeability $\mu = 1$ in the following.

Resonances of the material, such as electronic transitions, lead to a frequency-dependent response to incoming waves. Hence, the dielectric function $\varepsilon(\omega) = \varepsilon'(\omega) + \mathrm{i}\varepsilon''(\omega)$ is generally complex-valued and varies with frequency. Similarly, the refractive index $\tilde{n}(\omega) = \sqrt{\varepsilon(\omega)} = n(\omega) + \mathrm{i}\kappa(\omega)$ can be separated into real and imaginary parts. Inside media, the wave vector depends on the refractive index as $\boldsymbol{k}(\omega) = \tilde{n}(\omega)\boldsymbol{k}_0$. The plane wave in Equation 2.1 then reads

$$\boldsymbol{E}(r,t) = \boldsymbol{E}_0 \left[e^{\mathrm{i}(n(\omega)\boldsymbol{k}_0 \cdot \boldsymbol{r} - \omega t)} + \text{c.c.} \right] e^{-\kappa(\omega)\boldsymbol{k}_0 \cdot \boldsymbol{r}} \quad . \tag{2.4}$$

Hence, the real part of the refractive index determines the wave propagation speed, known as phase velocity, given by the dispersion relation

$$c(\omega) = \frac{\omega}{n(\omega)|\boldsymbol{k}_0|} \quad . \tag{2.5}$$

The imaginary part of the refractive index gives rise to an exponential decay of the electric field magnitude with the propagation distance. Hence, $\kappa(\omega)$ describes the absorption in dissipative media.

2.1.1 Lorentz oscillator model

As outlined in the previous section, the material response depends on the frequency of the incident electromagnetic wave. In a simple model, the electrons are bound to the nuclei by a mechanical spring. Due to their much smaller mass m_e, the electrons oscillate against the stationary nucleus when driven by an external electric field $\boldsymbol{E}(t) = \boldsymbol{E}_0 e^{-\mathrm{i}\omega t}$. The equation of motion for the displacement $\boldsymbol{x}(t)$ of a damped driven harmonic oscillator reads [47]

$$\ddot{\boldsymbol{x}}(t) + \gamma \dot{\boldsymbol{x}}(t) + \omega_0^2 \boldsymbol{x}(t) = -\frac{e}{m_e} \boldsymbol{E}(t) \quad , \tag{2.6}$$

with elementary charge e, damping constant γ and resonance frequency ω_0. The solution of the differential equation has the form

$$\boldsymbol{x}(t) = \frac{e}{m_e} \frac{1}{\omega_0^2 - \omega^2 - \mathrm{i}\gamma\omega} \boldsymbol{E}_0 e^{-\mathrm{i}\omega t} \quad . \tag{2.7}$$

The displacement has a maximum at the frequency $\omega = \sqrt{\omega_0^2 - \gamma^2/2}$. Furthermore, finite damping causes a phase shift between the driving electric field and the charge oscillation. The charge separation generates a dipole moment $\boldsymbol{p}(t) = -e\boldsymbol{x}(t)$. The macroscopic polarization $\boldsymbol{P} = n_e \boldsymbol{p} = \varepsilon_0 \chi \boldsymbol{E}$ in a medium with electron density n_e is expressed by the susceptibility

$$\chi_L(\omega) = \frac{n_e e^2}{\varepsilon_0 m_e} \frac{1}{\omega_0^2 - \omega^2 - \mathrm{i}\gamma\omega} \quad . \tag{2.8}$$

If multiple resonances exist, the susceptibilities of all resonances with index i add up due to the linear relation of polarization and electric field. Using the definition of the plasma frequency $\omega_p = \sqrt{\frac{n_e e^2}{\varepsilon_0 m_e}}$, the dielectric function reads [48]

$$\varepsilon_L(\omega) = \varepsilon_\infty + \sum_i \frac{\omega_{p,i}^2}{\omega_{0,i}^2 - \omega^2 - \mathrm{i}\gamma_i\omega} \quad . \tag{2.9}$$

An offset ε_∞ is introduced to account for unknown high-energy resonances, which takes the value $\varepsilon_\infty = 1$ otherwise. The dielectric function is split into real and imaginary parts

$$\begin{aligned}\varepsilon_L(\omega) &= \varepsilon_L'(\omega) + \mathrm{i}\varepsilon_L''(\omega) \\ &= \varepsilon_\infty + \sum_i \omega_{p,i}^2 \frac{\omega_{0,i}^2 - \omega^2}{(\omega_{0,i}^2 - \omega^2)^2 + \gamma_i^2\omega^2} + \mathrm{i}\sum_i \omega_{p,i}^2 \frac{\gamma_i\omega}{(\omega_{0,i}^2 - \omega^2)^2 + \gamma_i^2\omega^2} \quad .\end{aligned} \tag{2.10}$$

2.1.2 Dielectric function of metals

In the discussion about the Lorentz-oscillator model, we argued that the electrons experience a restoring force due to their interaction with the positively charged nuclei. In metals, however, electrons can move freely against the fixed lattice of positively charged atom cores [49]. Collisions with ions damp the movement of the electrons. In the Drude model, the equation of motion for a free electron driven by an electric field reads [47, 50]

$$\ddot{\boldsymbol{x}}(t) + \gamma\dot{\boldsymbol{x}}(t) = -\frac{e}{m_e}\boldsymbol{E}(t) \quad . \tag{2.11}$$

The solution can be derived from the Lorentz oscillator model in the limit of vanishing eigenfrequency $\omega_0 \to 0$. The dielectric function at an electron density n_e has the form

$$\begin{aligned}\varepsilon_D(\omega) &= \varepsilon_\infty - \frac{\omega_p^2}{\omega^2 + \mathrm{i}\gamma\omega} \\ &= \varepsilon_\infty - \frac{\omega_p^2}{\omega^2 + \gamma^2} + \mathrm{i}\frac{\omega_p^2\gamma}{\omega(\omega^2 + \gamma^2)} \quad ,\end{aligned} \tag{2.12}$$

where again the the offset ε_∞ is introduced. For comparison, the measured dielectric function of various bulk metals can be found in the literature. Here, we will focus on the optical properties of gold, the material investigated in this work. Johnson and Christy measured the dielectric function of gold in the ultraviolet and visible range [51]. Figure 2.1 compares the measured values with the Drude model using $\hbar\omega_p = 8.95\,\mathrm{eV}$, $\hbar\gamma = 65.8\,\mathrm{meV}$, and $\varepsilon_\infty = 6$ [47]. The Drude model reproduces the shape of real and imaginary parts in the measured data well in the visible to near-infrared range. However, the validity of the Drude model breaks down at higher energies where the transition between the d-band and the sp-conduction band occurs [47]. The influence of the interband transition can be seen very clearly in the imaginary part of the dielectric function, which increases at energies above 2 eV.

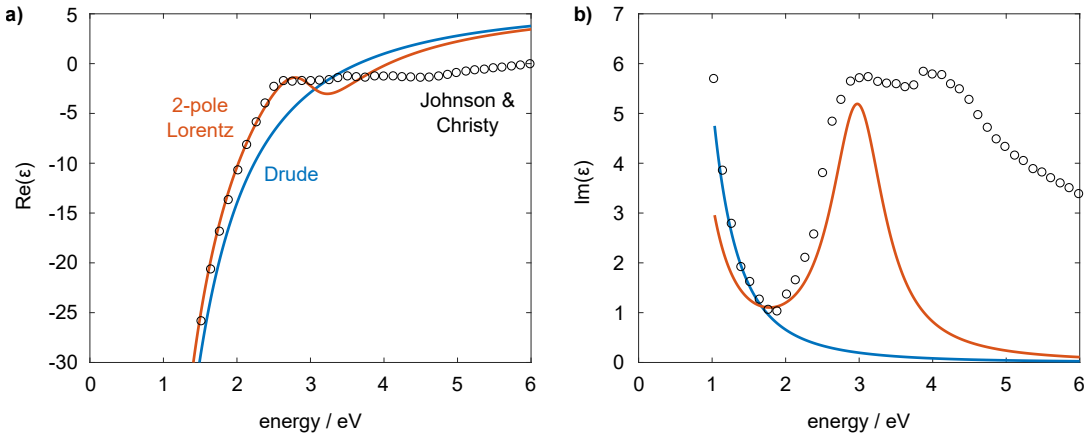

Fig. 2.1.: Dielectric function of gold. Comparison of the measurement by Johnson and Christy (black), the Drude model (blue), and a two-pole Lorentzian model (orange) using the parameters in the main text.

As already introduced in Equation 2.9, a sum of Lorentzian oscillator terms can model a material with multiple resonances. As all terms fulfill the Kramers-Kronig relation individually, causality is also ensured for the sum of the contributions. For the numerical simulations in this work, we use a two-pole Lorentzian function

$$\varepsilon_{2PL}(\omega) = \varepsilon_\infty \left(1 + \frac{\omega_{p,1}^2}{\omega_{0,1}^2 - \omega^2 - \mathrm{i}\gamma_1\omega} + \frac{\omega_{p,2}^2}{\omega_{0,2}^2 - \omega^2 - \mathrm{i}\gamma_2\omega} \right) \quad , \tag{2.13}$$

using the parameters from Ref. [45]

$$\begin{aligned} \varepsilon_\infty = 6, \quad & \omega_{p,1} = 5.37 \cdot 10^{15}\,\mathrm{rad/s}, \quad && \omega_{p,2} = 2.2636 \cdot 10^{15}\,\mathrm{rad/s}, \\ & \omega_{0,1} = 0, && \omega_{0,2} = 4.572 \cdot 10^{15}\,\mathrm{rad/s}, \\ & \gamma_1 = 6.216 \cdot 10^{13}\,\mathrm{rad/s}, && \gamma_2 = 1.332 \cdot 10^{15}\,\mathrm{rad/s}. \end{aligned}$$

The resulting dielectric function is shown as the orange line in Figure 2.1 and describes the measured data well in the visible range investigated in this work. This demonstrates that gold can be well approximated by a Drude term (index 1) for a free electron gas and a Lorentz term (index 2) for the interband transition. Other resonances at higher frequencies contribute to the offset ε_∞.

2.1.3 Plasmonics

Noble metals possess extraordinary optical properties. The high reflectivity at visible wavelengths originates from the negative real part of the dielectric function [47, 50]. In the bulk material, the electron gas can be freely displaced against the fixed atom lattice by an external electric field, as already discussed in the Drude model. On the surface, however, a displacement of the electrons perpendicular to the interface generates an electric field pointing in the opposite direction. This electric field provides a restoring force for the electrons. The characteristic frequency associated with this restoring force is the plasma

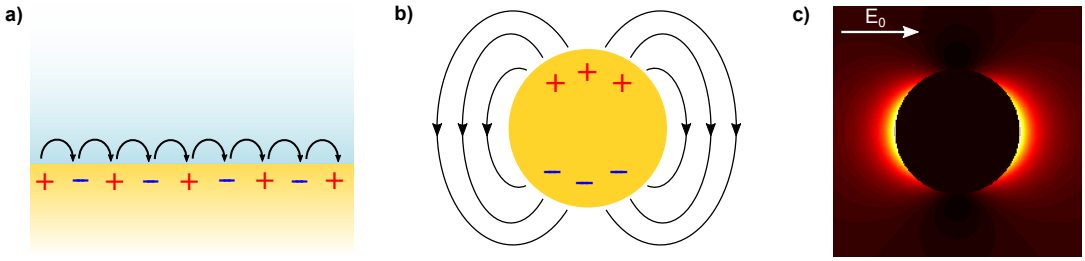

Fig. 2.2.: Charge distribution of (a) surface plasmons at the interface between metal and dielectric and (b) localized surface plasmons at metal nanoparticles. (c) Calculated electric field distribution around a 10 nm gold nanoparticle in the quasi-static approximation.

frequency ω_p. Hence, the electrons can sustain collective charge-density oscillations. The quanta of these oscillations are called (volume) plasmons. Consequently, the inelastic scattering of electrons at metal surfaces peaks at multiples of the energy $\hbar\omega_p$ [47].

To describe the interaction of electromagnetic waves with metallic structures, we need to consider the boundary conditions between different materials imposed by Maxwell's equations. Interfaces can support waves propagating along the interface while the electromagnetic field is exponentially damped perpendicular to the boundary. It can be shown that interface modes only exist if the dielectric functions of the materials fulfill [47]

$$\varepsilon_1(\omega)\cdot\varepsilon_2(\omega) < 0 \quad \text{and} \quad \varepsilon_1(\omega)+\varepsilon_2(\omega) < 0 \quad .$$

We assume that one material has a real-valued dielectric function $\epsilon_2(\omega)$. Consequently, the dielectric function of the other material $\epsilon_1(\omega)$ needs to have a negative real part with a larger absolute value. It is apparent from Figure 2.1 that gold has a significant negative real part and therefore supports localized modes at interfaces to dielectrics. These surface charge density oscillations are called surface plasmon polaritons (SPP, see Figure 2.2a). A non-vanishing imaginary part of the dielectric function leads to damping of the waves propagating along the surface. Typical plasmon propagation lengths on gold surfaces are on the order of 10 µm in the visible range. At the same time, the penetration depth is a few tens of nanometers into the metal and a few hundreds of nanometers into the dielectric [47]. The controlled propagation of these localized waves in plasmonic waveguides has, for instance, applications in optical circuitry with quantum emitters [52–54].

The excitation of SPPs requires both energy and momentum conservation. However, it can be shown that the dispersion of the SPP does not intersect with the light line $\omega = ck$, prohibiting an excitation from the far-field. Alternatively, SPPs can be excited by evanescent waves from total internal reflection or near-field interaction with nanoscopic scatterers. Evanescent waves provide the necessary wavevector to match the SPP dispersion. Furthermore, grating structures and other discontinuities can facilitate coupling into the interface mode from free space by providing additional momentum [47].

In contrast to propagating plasmons at the interface between metals and dielectrics, small metal particles feature non-propagating localized modes, as sketched in Figure 2.2b. Due to the curved surface of the particles, these modes couple to free-space radiation very efficiently. The localized surface plasmon resonances (LSPR) heavily depend on the particle size and the materials involved. The presence of a resonance condition can easily be derived

by solving Maxwell's equations in the quasi-static limit, assuming a spherical metal particle with a diameter d much smaller than the wavelength [47]. In this approximation, the electric field distribution of a 10 nm gold nanoparticle is presented in Figure 2.2c. It can be shown that the electric field outside of the sphere matches that of a dipole placed in the sphere center. The quasi-static approximation breaks down if the particle size becomes comparable to the wavelength. Notably, the electric field distribution around an arbitrary spherical particle in a homogeneous environment can be solved analytically within the framework developed by Gustav Mie [55]. The nanoparticles behave like nanoscopic resonators, where the resonance frequency strongly depends on the particle size, shape, and its dielectric environment. Furthermore, the electric field around the metal nanoparticle is confined to length scales below the optical diffraction limit (compare Figure 2.2c). Hence, plasmonic nanoparticles provide a sensing platform for a wide range of fluorescent and non-fluorescent molecules down to the single molecule limit with sub-diffraction position accuracy [56, 57]. Importantly, the radiation from quantum emitters is very sensitive to the local environment. Therefore, the following section will give an overview of the emission in homogeneous and inhomogeneous environments.

2.2 Quantum emitters

2.2.1 Emission from a classical dipole

In a classical model, a quantum emitter can be considered an electric dipole source emitting electromagnetic waves. The dipole momentum $\boldsymbol{p}(\boldsymbol{r},t)=\boldsymbol{p}(\boldsymbol{r})e^{-\mathrm{i}\omega t}$ generates an electromagnetic field [46]

$$\boldsymbol{E}(\boldsymbol{r},t)=\frac{1}{4\pi\varepsilon_0\varepsilon}\left[k^2(\hat{\boldsymbol{r}}\times\boldsymbol{p})\times\hat{\boldsymbol{r}}\frac{e^{\mathrm{i}kr}}{r}+(3\hat{\boldsymbol{r}}(\hat{\boldsymbol{r}}\cdot\boldsymbol{p})-\boldsymbol{p})\left(\frac{1}{r^3}-\frac{\mathrm{i}k}{r^2}\right)e^{\mathrm{i}kr}\right] \quad , \tag{2.14}$$

$$\boldsymbol{H}(\boldsymbol{r},t)=\frac{ck^2}{4\pi}(\hat{\boldsymbol{r}}\times\boldsymbol{p})\frac{e^{\mathrm{i}kr}}{r}\left(1-\frac{1}{\mathrm{i}kr}\right) \quad , \tag{2.15}$$

with unit vector $\hat{\boldsymbol{r}}=\frac{\boldsymbol{r}}{r}$ and distance from the dipole $r=|\boldsymbol{r}|$. The components of $\boldsymbol{E}$ and $\boldsymbol{H}$ decay with different powers of r. The field components $\propto r^{-2}$ and r^{-3} decay quickly with distance and are called electromagnetic near-field. These components dominate when dipoles in close distance interact to exchange energy or excite surface plasmons. Only the r^{-1} term, called electromagnetic far-field, survives at larger distances. The time-averaged Poynting vector

$$\langle\boldsymbol{S}\rangle=\frac{1}{2}\mathrm{Re}(\boldsymbol{E}\times\boldsymbol{H}^*) \tag{2.16}$$

quantifies the energy flux density and has the dimension energy per area and time. The radiated power $\mathrm{d}P$ per solid angle $d\Omega$ is

$$\frac{\mathrm{d}P}{\mathrm{d}\Omega}=r^2\langle\boldsymbol{S}\rangle\cdot\hat{\boldsymbol{r}}=\frac{|\boldsymbol{p}|^2\omega^4}{32\pi^2\varepsilon_0\varepsilon c^3}\sin^2\theta \quad . \tag{2.17}$$

The radiation pattern of a dipole has the well-known $\sin^2\theta$ shape, where most power is emitted perpendicular to the dipole axis. Integrating the Poynting vector over a closed sphere in the far-field yields the total radiated power [47]

$$P = \int \frac{\mathrm{d}P}{\mathrm{d}\Omega}\mathrm{d}\Omega = \int_{\partial V} \langle \boldsymbol{S} \rangle \cdot \hat{\boldsymbol{r}}\,\mathrm{d}A = \frac{|\boldsymbol{p}|^2}{4\pi\varepsilon_0\varepsilon}\frac{\omega^4}{3c^3} \quad . \tag{2.18}$$

An important finding is that P scales with the fourth power of the frequency. Knowing that electromagnetic waves are radiated as photons with energy $\hbar\omega$, we can calculate the number of emitted photons per second

$$\Gamma_D = \frac{P}{\hbar\omega} = \frac{|\boldsymbol{p}|^2}{4\pi\hbar\varepsilon_0\varepsilon}\frac{\omega^3}{3c^3} \quad . \tag{2.19}$$

2.2.2 Fermi's golden rule and the density of states

Up to now, we have modeled an atom as a point dipole that absorbs and emits light by harmonic oscillations of the charge distribution. However, we did not consider that the electrons in the atom have discrete energy levels. Transitions between the energy levels describe the absorption and emission of photons with matching energy. If the atom is in the ground state, no further emission can occur without prior excitation. Hence, the classical dipole model for an atom has restrictions that only a quantum mechanical treatment can overcome.

A first step towards this is describing the absorption in a semi-classical approach [58, 59]. Here, an atom with discrete energy levels E_n and corresponding wave functions $|\psi_n\rangle$ interacts with a classical electric field $\boldsymbol{E}(t)$. The wavefunction is a superposition of these states

$$|\psi(t)\rangle = \sum_n c_n(t)\,|\psi_n\rangle \quad , \tag{2.20}$$

with time-dependent expansion coefficients $c_n(t)$. The Hamiltonian $\tilde{H}_0$ defines the stationary system of the electron residing in its eigenstates. Hence, the $|\psi_n\rangle$ are the eigenfunctions of the time-independent Schrödinger equation $\tilde{H}_0\,|\psi_n\rangle = E_n\,|\psi_n\rangle$. The interaction with electromagnetic waves is described as a first-order perturbation $\tilde{H}'(t) = -\boldsymbol{E}(t)\cdot\tilde{\boldsymbol{\mu}}$, corresponding to the classical energy of a dipole in an electric field. Here, $\tilde{\boldsymbol{\mu}} = e\boldsymbol{r}$ is the dipole operator. The Hamiltonian then reads

$$\tilde{H}(t) = \tilde{H}_0 + \tilde{H}'(t) \quad . \tag{2.21}$$

The transition rate from initial state $|\psi_i\rangle$ to final state $|\psi_f\rangle$ with corresponding energies E_i and E_f can then be deduced from the time evolution of the coefficients. We need to consider the density of states $\rho(\omega)$, where $\rho(\omega)\mathrm{d}\omega$ gives the number of final states in a frequency interval between ω and $\omega + \mathrm{d}\omega$. The final states can be photon and electron states. In a two-level system, the initial and final states are discrete, so $\rho(\omega_{fi})$ is the

density of photon states at the resonance frequency $\hbar\omega_{fi} = E_f - E_i$ [58]. First-order perturbation theory yields the famous Fermi's golden rule of the transition rate [58]

$$\Gamma_{A,fi} = \frac{2\pi}{\hbar^2}|\boldsymbol{E}_0 \cdot \langle\psi_f|\tilde{\boldsymbol{\mu}}|\psi_i\rangle|^2\rho(\omega_{fi}) \quad . \tag{2.22}$$

The transition rate scales with the squared absolute value of the transition matrix element, which is the scalar product of the transition dipole moment $\boldsymbol{\mu}_{fi} = \langle\psi_f|\tilde{\boldsymbol{\mu}}|\psi_i\rangle$ and the electric field amplitude. Furthermore, the transition rate is proportional to the density of final states.

2.2.3 Spontaneous emission in homogeneous environments

Stimulated emission can be seen as a reverse absorption process where the energy of the final state is smaller than the initial state; hence, $\omega_{fi} = E_i - E_f > 0$. In contrast, spontaneous emission can only be described in a fully quantum treatment where the atom interacts with the vacuum field. It can be shown that the spontaneous emission rate is given by [58, 60]

$$\Gamma_{fi} = \frac{\pi\omega_{fi}}{3\hbar\varepsilon_0\varepsilon}|\boldsymbol{\mu}_{fi}|^2\rho(\omega_{fi}) \quad . \tag{2.23}$$

The density of states in free space

$$\rho(\omega) = \frac{\omega^2}{\pi^2 c^3} \tag{2.24}$$

can be derived by counting the allowed modes in a box with dimensions $L \times L \times L$ and taking the limit $L \to \infty$. Remarkably, the spontaneous emission rate obtained from quantum mechanics agrees with the classical emission rate up to a factor of 4, which is discussed in the literature [60].

2.2.4 Purcell enhancement in inhomogeneous environments

The spontaneous emission rate is partly a property of the quantum emitter itself, influenced by the transition frequency ω_{fi} and the absolute value of the transition dipole moment $\boldsymbol{\mu}_{fi}$. Nevertheless, Γ also scales with the density of states the atom can emit into. The availability of modes heavily depends on the surrounding of the emitter. If an emitter is placed at a node of the electric field in a cavity, there is no available mode to emit into, and the spontaneous emission rate would be zero. For example, guitar strings cannot be excited at the points where they are attached to the body due to the boundary conditions. Similarly, the in-plane electric field at the interface of a dielectric and a conductor must be zero. If an in-plane electric field were present, the electrons inside the conductor would move to compensate for the electric field.

Karl Drexhage has conducted pioneering experiments on the variations of the spontaneous emission rate of rare earth ions Eu^{3+} close to a silver mirror [61]. He found that the spontaneous emission lifetime $\tau = 1/\Gamma$ oscillates with the distance between the ion and

the mirror. Our experiments in this thesis are closely related to this work. On the one hand, the polarized emission of dipole emitter layers on glass and gold substrates will be investigated in Chapter 3. On the other hand, the nanoparticle-on-mirror systems are equivalent to a scattering dipole on a metal substrate (see Chapter 4). To motivate the fundamental principle, we analytically derive the density of states of a quantum emitter near a perfect conductor, following the tutorial by Barnes et al. [60].

A cube with lengths $L \times L \times L$ supports the wave vectors

$$\boldsymbol{k}(n_x, n_y, n_z) = \frac{2\pi}{L}\left(n_x\hat{\boldsymbol{e}}_x + n_y\hat{\boldsymbol{e}}_y + n_z\hat{\boldsymbol{e}}_z\right) \quad , \tag{2.25}$$

with integer numbers $n_{x,y,z}$ and cartesian unit vectors $\hat{\boldsymbol{e}}_{x,y,z}$. The corresponding discrete frequencies are

$$\omega(n_x, n_y, n_z) = \frac{2\pi c_0}{Ln}\sqrt{n_x^2 + n_y^2 + n_z^2} \quad , \tag{2.26}$$

where n is the refractive index. The polarization of the waves needs to be perpendicular to the wave propagation direction given by wave vector $\boldsymbol{k}$. We choose one polarization direction $\hat{\boldsymbol{e}}_1$ in the xy-plane and a second polarization direction $\hat{\boldsymbol{e}}_2$ perpendicular to it

$$\hat{\boldsymbol{e}}_1(n_x, n_y, n_z) = \frac{n_x\hat{\boldsymbol{e}}_y - n_y\hat{\boldsymbol{e}}_x}{\sqrt{n_x^2 + n_y^2}} \quad , \tag{2.27}$$

$$\hat{\boldsymbol{e}}_2(n_x, n_y, n_z) = \frac{1}{\sqrt{n_x^2 + n_y^2 + n_z^2}}\left(\sqrt{n_x^2 + n_y^2}\hat{\boldsymbol{e}}_z - n_z\frac{n_x\hat{\boldsymbol{e}}_x + n_y\hat{\boldsymbol{e}}_y}{\sqrt{n_x^2 + n_y^2}}\right) \quad , \tag{2.28}$$

such that $\boldsymbol{k}$, $\hat{\boldsymbol{e}}_1$ and $\hat{\boldsymbol{e}}_2$ are orthogonal at every choice of $n_{x,y,z}$. In a homogeneous environment, modes with every wavevector defined above are allowed. However, the electric field at the interface to the perfect conductor must fulfill the boundary conditions. Charges can move freely inside the conductor at the interface to the dielectric. Hence, any in-plane electric field component must be zero at the boundary. The following superpositions of upward and downward traveling plane waves ensure vanishing x and y field components at the metal-dielectric interface at $z = 0$:

$$\boldsymbol{E}^{(1)}_{n_x,n_y,n_z}(\boldsymbol{r}) = \frac{1}{\sqrt{L^3}}\left[\hat{\boldsymbol{e}}_1(n_x, n_y, n_z)e^{\mathrm{i}\boldsymbol{k}(n_x,n_y,n_z)\cdot\boldsymbol{r}} - \hat{\boldsymbol{e}}_1(n_x, n_y, -n_z)e^{\mathrm{i}\boldsymbol{k}(n_x,n_y,-n_z)\cdot\boldsymbol{r}}\right] \quad , \tag{2.29}$$

$$\boldsymbol{E}^{(2)}_{n_x,n_y,n_z}(\boldsymbol{r}) = \frac{N(n_z)}{\sqrt{L^3}}\left[\hat{\boldsymbol{e}}_2(n_x, n_y, n_z)e^{\mathrm{i}\boldsymbol{k}(n_x,n_y,n_z)\cdot\boldsymbol{r}} + \hat{\boldsymbol{e}}_2(n_x, n_y, -n_z)e^{\mathrm{i}\boldsymbol{k}(n_x,n_y,-n_z)\cdot\boldsymbol{r}}\right] \quad , \tag{2.30}$$

with normalization constants $N(n_z > 0) = 1$ and $N(n_z = 0) = 1/\sqrt{2}$. We only consider positive values for n_z, as negative values correspond to the same mode and would be counted twice otherwise. Since the electric fields are normalized in the unit volume, the partial (or projected) local density of states (PLDOS) follows from counting the modes at a certain frequency ω for a certain dipole position $\boldsymbol{r}_0$ and dipole orientation $\hat{\boldsymbol{e}}_d$

$$\rho_p(\hat{\boldsymbol{e}}_d, \boldsymbol{r}_0, \omega) = \sum_{n_x,n_y,n_z \leq 0}\sum_{\zeta=1,2}|\hat{\boldsymbol{e}}_d \cdot \boldsymbol{E}^{(\zeta)}_{n_x,n_y,n_z}(\boldsymbol{r}_0)|^2\delta(\omega - \omega(n_x, n_y, n_z)) \quad , \tag{2.31}$$

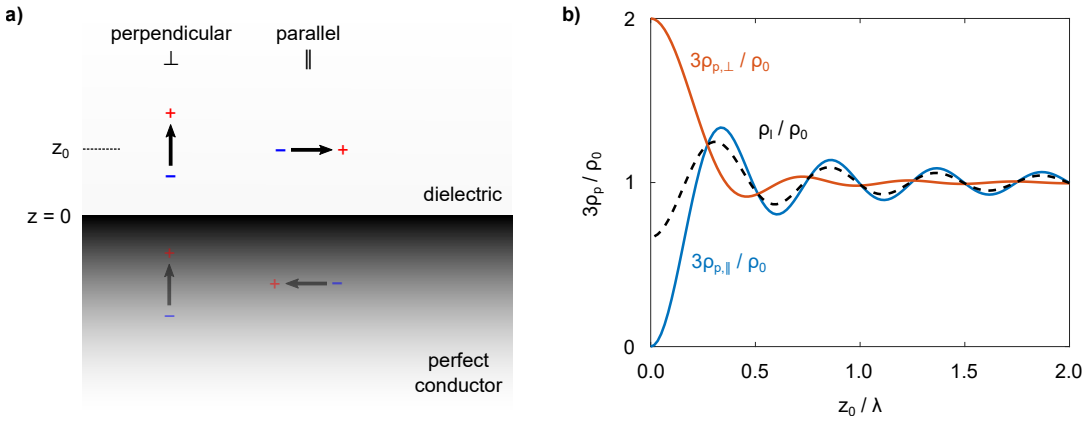

Fig. 2.3.: Spontaneous emission of a single dipole at a distance z_0 to a perfect conductor. (a) Sketch of the perpendicular (left) and parallel (right) dipole and its image dipole in the conductor. (b) Calculated PLDOS for both dipole orientations and the LDOS as a function of the distance to the conductor interface. Inspired by Ref. [60].

with Kronecker delta δ. In the limit $L \to \infty$, the sum turns into an integral that can be evaluated numerically. It is instructive to look at two separate cases, a dipole oriented parallel ($\rho_{p,\parallel}$) to the interface $\hat{\boldsymbol{e}}_d = \hat{\boldsymbol{e}}_x$ and a dipole oriented perpendicular ($\rho_{p,\perp}$) to the interface $\hat{\boldsymbol{e}}_d = \hat{\boldsymbol{e}}_z$.

At small distances $z_0 \to 0$, the radiation from a horizontal dipole is canceled by the image dipole in the conductor pointing in the opposite direction. Hence, the PLDOS for parallel dipole orientation $\rho_{p,\parallel}$ vanishes. In contrast, at small distances, $\rho_{p,\perp}$ is twice the DOS in free space since the dipole and its image dipole add up to radiate even more efficiently (see Figure 2.3). At large distances $z_0 \to \infty$, the influence of the mirror on the radiative properties becomes negligible. Hence, the PLDOS $\rho_{p,\parallel} = \rho_{p,\perp} = \frac{\rho_0}{3}$ approaches that of free space up to a factor of three, as further discussed below. The oscillations of the PLDOS with distance and the dependency on dipole orientation show that the local environment of a dipole significantly influences its emission properties. Therefore, nanostructures must be carefully designed for efficient coupling to free-space radiation.

The analytic derivation provided the partial local density of states (PLDOS). This is the density of states that an emitter at a certain position $\boldsymbol{r}_0$ and with a certain orientation $\hat{\boldsymbol{e}}_d$ experiences. For unknown orientations, the PLDOS becomes the local density of states (LDOS) which emitters with arbitrary orientations see on average. The LDOS is the sum over all three dipole orientations

$$\rho_l(\boldsymbol{r}_0, \omega) = 2\rho_{p,\parallel}(\boldsymbol{r}_0, \omega) + \rho_{p,\perp}(\boldsymbol{r}_0, \omega) \quad , \tag{2.32}$$

where x- and y-directions are equal. At small distances, the local density of states still differs from the density of states (DOS) introduced in the discussion of homogeneous environments. LDOS and DOS only become equivalent at large distances, where the

influence of the mirror is negligible (see Figure 2.3b). In general, the DOS is a volume average of the LDOS for all possible dipole positions

$$\rho(\omega) = \frac{\int_V \rho_l(\boldsymbol{r}, \omega)\, \mathrm{d}^3\boldsymbol{r}}{\int_V \mathrm{d}^3\boldsymbol{r}} \quad . \tag{2.33}$$

For a dipole in an inhomogeneous environment, the DOS needs to be replaced by the PLDOS in the spontaneous emission rate

$$\Gamma_{fi} = \frac{\pi\omega_{fi}}{3\hbar\varepsilon_0\varepsilon}|\boldsymbol{\mu}_{fi}|^2\rho_p(\hat{\boldsymbol{e}}_d, \boldsymbol{r}_0, \omega_{fi}) \quad . \tag{2.34}$$

In this work, we investigate dye layers embedded in a nanoresonator. The cavity can be assigned a certain volume V. In its fundamental meaning, the DOS is the number of possible states with index n divided by the volume

$$\rho(\omega) = \frac{1}{V}\sum_n \delta(\omega - \omega_n) \quad . \tag{2.35}$$

The cavity has a certain resonance frequency ω_c. Due to inevitable losses, the resonance is not infinitely sharp, requiring a spectral width $\Delta\omega_c$. The resonance typically has a Lorentzian shape; hence, we can define the DOS on resonance ($\omega_0 = \omega_c$) as

$$\rho(\omega_0) = \frac{2}{\pi\Delta\omega_c V} \quad . \tag{2.36}$$

We introduce the quality factor $Q = \omega/\Delta\omega$ and multiply a factor of 3, assuming that the dipole orientation matches the electric field direction of the cavity mode. This yields

$$\rho(\omega_0) = \frac{6Q}{\pi\omega_0 V} \quad . \tag{2.37}$$

We define the Purcell factor F_p as the enhancement of the spontaneous emission rate in the resonator with respect to free space [60]

$$F_p = \frac{\Gamma_{\text{in cavity}}}{\Gamma_{\text{no cavity}}} = \frac{\rho(\omega_c)}{\rho_0(\omega_c)} = \frac{6\pi c^3}{\omega_c^3}\frac{Q}{V} = \frac{3}{4\pi^2}\frac{Q}{V}\left(\frac{\lambda}{n}\right)^3 \quad . \tag{2.38}$$

The Purcell factor thus scales with the ratio of the quality factor and the mode volume. Large quality factors around 20,000 have been achieved for photonic crystal nanocavities at room temperature, while the mode volume is on the order of the optical wavelength [62]. In contrast, plasmonic nanocavities have much smaller quality factors $Q < 100$, while the mode volume can be well below the diffraction limit [63]. In leaky optical cavities like the plasmonic nanoresonators investigated in this work, an effective mode volume needs to be introduced [64, 65]. Furthermore, we assumed in our discussion that there is only one cavity resonance, while real cavities can feature multiple spectrally overlapping resonances [66].

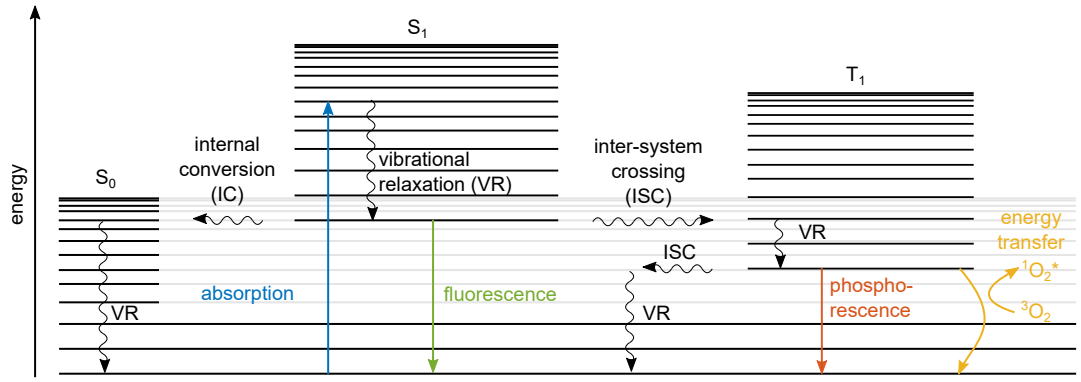

Fig. 2.4.: Radiative and non-radiative decay pathways for organic molecules upon excitation (blue arrow), known as the Jablonski diagram. The molecule has a singlet ground state S_0 and excited state S_1, as well as a triplet excited state T_1.

2.2.5 Radiative and non-radiative processes in molecules

The considerations about spontaneous emission and its enhancement in cavities apply to any quantum emitter. In the presented work, we specifically use organic molecules. The photophysics of this emitter class is briefly reviewed in this section, as an understanding of radiative and non-radiative rates is essential to model the interaction with plasmonic nanostructures.

In organic molecules, the photon emission is typically red-shifted to the absorption frequency. This process is known as Stokes shift and originates from rearrangements in the molecule's environment upon excitation. Furthermore, the atoms of the molecule can oscillate relative to each other at infrared frequencies. These quantized vibrations give rise to a fine structure of electronic energy levels. Based on the much smaller mass of the electrons, the motion of electrons and atom cores can be separated, known as the Born-Oppenheimer approximation. Hence, the molecule wave function can be written as a product of the electronic and the vibrational wave functions. Transitions between the discrete energy levels require a non-vanishing electronic transition dipole moment. The transition rate scales with the Franck-Condon factor, quantifying the spatial overlap of the vibrational wavefunctions of initial and final states. Furthermore, the spin must be conserved in the transition [59].

Our previous discussion about spontaneous emission focused on the radiative decay from an excited state, called fluorescence. However, various non-radiative decay pathways exist where the energy is dissipated as heat, transferred to long-lived states, or transferred to other molecules [67]. The singlet ground state S_0 and the first excited singlet state S_1 are schematically shown in the Jablonski diagram in Figure 2.4. The excitation from the ground state typically originates from the lowest vibrational level at ambient conditions, as shown by the vertical blue arrow. The final state might be a higher vibrational level. On a picosecond timescale, the molecule relaxes to the lowest vibrational level in the excited electronic state in a process called vibrational relaxation (VR). From here, the molecule can radiate a fluorescence photon, shown by the vertical green arrow. Alternatively, the excitation in the molecule can decay to the ground state non-radiatively by internal con-

version (IC) and subsequent vibrational relaxation. These non-radiative processes are summarized in the Figure as wavy black vertical arrows. The reduction of fluorescence intensity by non-radiative processes is called quenching. Due to spin-orbit coupling in aromatic molecules, a nonzero probability exists for a spin-flip, where the excitation decays from a singlet (S1) to a triplet (T1) state or vice-versa. The wavy black horizontal arrow depicts this intersystem crossing (ISC) process. Compared to the excited state, the triplet state is long-lived as a second spin flip is required for decay to the singlet ground state. The decay can be radiative by phosphorescence (red arrow) or non-radiative by ISC and subsequent VR. The population of the molecule triplet state is the dominant photodegradation pathway for many organic chromophores, as the energy can be exchanged with molecular oxygen. Oxygen has a triplet ground state $^3O_2$ and a singlet excited state $^1O_2^*$. Therefore, oxygen can quench the population of the molecule triplet state. Excited state oxygen is very reactive and can destroy chromophores irreversibly. Thus, fluorescence experiments are often carried out in oxygen-free environments.

The rates of radiative decay γ_r and non-radiative decay γ_{nr} add up, so the total rate constant is

$$\gamma_{tot} = \gamma_r + \gamma_{nr} \quad . \tag{2.39}$$

The inverse time constant $\tau = 1/\gamma_{tot}$ is called fluorescence lifetime, typically on the order of nanoseconds. The percentage of energy radiated as photons defines the quantum efficiency

$$\eta = \frac{\gamma_r}{\gamma_r + \gamma_{nr}} \quad . \tag{2.40}$$

2.2.6 Line broadening mechanisms

Heisenberg's uncertainty principle requires that the fluorescence lifetime τ and the full width at half maximum (FWHM) of the peak in the emission spectrum $\delta\omega$ have an inverse relation [68]

$$\delta\omega = \frac{\delta E}{\hbar} \gtrapprox \frac{1}{\tau} \quad . \tag{2.41}$$

The spectral lineshape is Lorentzian, consistent with the results from the Lorentz oscillator model in Chapter 2.1.1. As the uncertainty relation defines a lower limit, the linewidth is called natural linewidth.

The observed linewidth typically differs from this lower limit. At ambient conditions, the environment of the emitter fluctuates statistically. The fluctuations act back on the molecule's transition energy. An example is the scattering with phonons in a solid environment, which can be eliminated at cryogenic temperatures. If every molecule exhibits the same fluctuations, the linewidth is homogeneously broadened, and the lineshape remains Lorentzian.

In contrast, the line is inhomogeneously broadened if the probability for absorption or emission at a particular frequency is not equal for all molecules. For instance, irregularities in the molecule environment inhomogeneously shift the transition energies. In this case, the lineshape changes from Lorentzian to a Voigt profile, which is the convolution of a Lorentzian and a Gaussian distribution.

2.2.7 From weak to strong coupling

Incorporating emitters into nanostructured environments can amplify the spontaneous emission by the Purcell effect. If the coupling strength between the emitter and the local environment – in this work, the plasmonic nanoresonator – is strong enough, hybrid light-matter states (polaritons) are formed. Energy is then coherently exchanged between the plasmonic system and the emitter, known as Rabi oscillations. Cavity quantum electrodynamics (cavity QED) provides a general mathematical framework. We approximate the emitter as a two-level system with transition frequency ω_{em} and the cavity as a single-mode plasmonic resonator with frequency ω_{pl}. Neglecting decoherence and damping, we then write the Jaynes-Cummings Hamiltonian [69, 70]

$$\hat{H} = \hbar\omega_{\mathrm{pl}}\hat{a}^{\dagger}\hat{a} + \hbar\omega_{\mathrm{em}}\hat{\sigma}^{\dagger}\hat{\sigma} + \hbar\frac{g}{2}\left(\hat{a}^{\dagger}\hat{\sigma} + \hat{\sigma}^{\dagger}\hat{a}\right) \quad , \tag{2.42}$$

where $\hat{a}^{\dagger}$, $\hat{a}$ are the bosonic raising and lowering operators for the plasmon, and $\hat{\sigma}^{\dagger}$, $\hat{\sigma}$ are the Pauli raising and lowering operators for the two-level system. The coupling constant

$$g = \frac{2\boldsymbol{\mu}_{\mathrm{em}} \cdot \boldsymbol{E}_0}{\hbar} \tag{2.43}$$

quantifies the interaction of the emitter transition dipole $\boldsymbol{\mu}_{\mathrm{em}}$ with the electric field $\boldsymbol{E}_0$ at the emitter position. In a cavity with mode volume V where the emitter is at the position of maximum electric field and aligned with the field direction, the coupling strength is estimated as [47, 69, 70]

$$g = \frac{|\boldsymbol{\mu}_{\mathrm{em}}|}{\hbar}\sqrt{\frac{\hbar\omega_{\mathrm{pl}}}{2\varepsilon_0\varepsilon V}} \quad . \tag{2.44}$$

Diagonalization of the Jaynes-Cummings Hamiltonian yields two hybrid mode frequencies

$$\omega_{\pm} = \frac{1}{2}(\omega_{\mathrm{pl}} + \omega_{\mathrm{em}}) \pm \Omega_R \quad . \tag{2.45}$$

The vacuum Rabi frequency

$$\Omega_R = \frac{1}{2}\sqrt{g^2 + (\omega_{\mathrm{pl}} - \omega_{\mathrm{em}})^2} \quad . \tag{2.46}$$

quantifies the inverse time period of the energy oscillation between the plasmon and emitter. Damping can be considered using the general master equation in Lindblad form [71]. However, an accurate solution requires significant computational effort. In many cases, the electric field generated by the plasmon can be approximated in a classical description. Furthermore, to compute the linear scattering of the coupled system, we assume that the coherences between ground and excited states are small and the population of the ground state dominates. In addition, we make the approximation that the energy decays much slower than the dephasing of the emitter at room temperature. It can be shown that the

quantum mechanical equations then reduce to two coupled classical harmonic oscillators for the plasmon μ_{pl} and the emitter μ_{em} [69, 72]

$$\ddot{\mu}_{\mathrm{pl}} + \gamma_{\mathrm{pl}}\dot{\mu}_{\mathrm{pl}} + \omega_{\mathrm{pl}}^2\mu_{\mathrm{pl}} = g\frac{\omega_{\mathrm{pl}}d_{\mathrm{pl}}}{d_{\mathrm{em}}}\mu_{\mathrm{em}} + F_0(t) \quad , \tag{2.47}$$

$$\ddot{\mu}_{\mathrm{em}} + \gamma_{\mathrm{em}}\dot{\mu}_{\mathrm{em}} + \omega_{\mathrm{em}}^2\mu_{\mathrm{em}} = g\frac{\omega_{\mathrm{em}}d_{\mathrm{em}}}{d_{\mathrm{pl}}}\mu_{\mathrm{pl}} \quad . \tag{2.48}$$

This simple coupled oscillator description is used frequently in the literature as it provides an intuitive access to the relevant properties of the coupled system, including damping [73, 74]. Here, both plasmon and emitter are described by individual dipole moments. As the plasmon dipole is typically much stronger than the emitter transition dipole moment, $d_{\mathrm{pl}} \gg d_{\mathrm{em}}$, only the plasmon is driven by the term $F_0(t) = 4\omega_{\mathrm{pl}}d_{\mathrm{pl}}^2E(t)$ originating from the external electric field $E(t)$. In absence of the driving field and in the limit g, γ_{em}, γ_{pl}, $|\omega_{\mathrm{em}} - \omega_{\mathrm{pl}}| \ll \omega_{\mathrm{pl}}$, the normal mode frequencies read

$$\omega_{\pm} = \frac{1}{2}(\omega_{\mathrm{pl}} + \omega_{\mathrm{em}}) - \frac{1}{4}\mathrm{i}(\gamma_{\mathrm{pl}} + \gamma_{\mathrm{em}}) \pm \Omega_R \quad , \tag{2.49}$$

with normal mode splitting

$$\Omega_R = \frac{1}{2}\sqrt{g^2 + \left(\omega_{\mathrm{pl}} - \omega_{\mathrm{em}}\right)^2 - \frac{1}{4}\left(\gamma_{\mathrm{pl}} - \gamma_{\mathrm{em}}\right)^2} \quad . \tag{2.50}$$

Similar to coupled mechanical oscillators, we obtain two normal modes. The low-energy mode corresponds to both systems oscillating in phase (symmetric), whereas the systems oscillate with opposite phase (antisymmetric) in the high-energy mode. The hybrid modes inherit the linewidths from the uncoupled systems. It is therefore required to define a threshold for strong coupling where the coupling exceeds the losses. Although definitions vary in the literature [69, 74, 75], a common threshold is that the system needs to conduct at least one Rabi oscillation before damping, corresponding to

$$g > \frac{1}{4}\left(\gamma_{\mathrm{pl}} + \gamma_{\mathrm{em}}\right) \quad . \tag{2.51}$$

A peak splitting is, however, only observable in the spectra if the energy splitting exceeds the average linewidths of the uncoupled resonances, i.e., $g > \frac{1}{2}\left(\gamma_{\mathrm{pl}} + \gamma_{\mathrm{em}}\right)$. In contrast, the system is in the weak coupling regime for smaller coupling strengths, where the Purcell effect enhances the spontaneous emission.

In the presence of a harmonic external driving field with frequency ω, the solution for the coupled oscillator model is given by

$$\mu_{\mathrm{pl}}(\omega) = \frac{F_0\left(\omega_{\mathrm{em}}^2 - \omega^2 - \mathrm{i}\omega\gamma_{\mathrm{em}}\right)}{\left(\omega_{\mathrm{em}}^2 - \omega^2 - \mathrm{i}\omega\gamma_{\mathrm{em}}\right)\left(\omega_{\mathrm{pl}} - \omega^2 - \mathrm{i}\omega\gamma_{\mathrm{pl}}\right) - \omega_{\mathrm{em}}\omega_{\mathrm{pl}}g^2} \quad , \tag{2.52}$$

$$\mu_{\mathrm{em}}(\omega) = \frac{F_0\omega_{\mathrm{em}}\frac{d_{\mathrm{em}}}{d_{\mathrm{pl}}}}{\left(\omega_{\mathrm{em}}^2 - \omega^2 - \mathrm{i}\omega\gamma_{\mathrm{em}}\right)\left(\omega_{\mathrm{pl}} - \omega^2 - \mathrm{i}\omega\gamma_{\mathrm{pl}}\right) - \omega_{\mathrm{em}}\omega_{\mathrm{pl}}g^2} \quad . \tag{2.53}$$

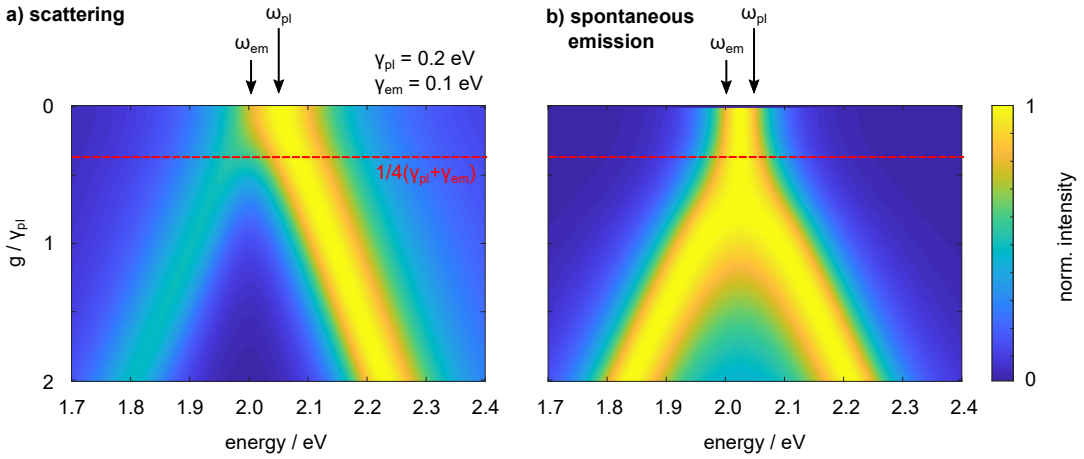

Fig. 2.5.: Calculated (a) scattering cross section $\sigma_{\mathrm{scat}}(\omega)$ from the classical coupled oscillator model and (b) spontaneous emission spectra $I_{\mathrm{pl}}(\omega)$ from the full quantum model as a function of the coupling strength g. The parameters used in the calculations are $\omega_{\mathrm{em}} = 2\,\mathrm{eV}$, $\omega_{\mathrm{pl}} = 2.05\,\mathrm{eV}$, $\gamma_{\mathrm{pl}} = 0.2\,\mathrm{eV}$, and $\gamma_{\mathrm{em}} = 0.1\,\mathrm{eV}$. The spectra are normalized to the respective maxima at each g value.

The plasmon dominates the scattering, as $d_{\mathrm{pl}} \gg d_{\mathrm{em}}$. Therefore, the scattering cross section is proportional to the squared dipole moment of the plasmon [72]

$$\sigma_{\mathrm{scat}}(\omega) \propto \omega^4 |\mu_{\mathrm{pl}}(\omega)|^2 \quad . \tag{2.54}$$

Besides scattering, the simple coupled oscillator model also allows calculating the absorption of plasmon and emitter using $\sigma_{\mathrm{abs}} \propto \omega \cdot \mathrm{Im}[\mu(\omega)]$. Due to the quantum nature of spontaneous emission, the fluorescence emission is not equivalent to an inverse absorption process. Therefore, a full quantum treatment is required to determine the spontaneous emission of the coupled system. The intensity of a single emitter radiated via the plasmon is [69, 76]

$$I_{\mathrm{pl}}(\omega) = \frac{\gamma_{\mathrm{pl}}}{\pi} \left| \frac{-\mathrm{i}g/2}{\left[(\gamma_{\mathrm{pl}} + \gamma_{\mathrm{em}})/2 + \mathrm{i}(\omega_{\mathrm{em}} - \omega_{\mathrm{pl}})/2 - \mathrm{i}(\omega - \omega_{\mathrm{pl}})\right]^2 + \Omega_R^2} \right|^2 \quad . \tag{2.55}$$

Figure 2.5 compares the scattering and emission spectra of the coupled system as a function of the coupling strength using exemplary parameters. In both scattering and emission spectra, the lines broaden and then split into two modes when increasing the coupling strength. Notably, the peak splitting into upper and lower polariton in the scattering spectra emerges even for coupling parameters below the strong coupling threshold. The apparent dip in the scattering cross section is caused by destructive interference of the broad plasmon and the more narrow emitter resonance, known as a Fano lineshape [36, 72]. To distinguish this intermediate coupling regime from strong coupling, it is a consensus in the literature that the line broadening and peak splitting must be visible also in the emission spectra.

In this work, we investigate the coupling between dye monolayers and nanoresonators. In this case, many emitters with individual coupling constants g_i are present in the cavity.

Assume an ensemble of N independent emitters with identical damping constants. If each emitter interacts with a single mode of the plasmonic structure, the strong coupling condition can be generalized to [69, 73]

$$\sqrt{N} g_{\mathrm{rms}} > \frac{1}{4} \left(\gamma_{\mathrm{pl}} + \gamma_{\mathrm{em}} \right) \quad , \tag{2.56}$$

with $g_{\mathrm{rms}} = \sum_{i=1}^{N} g_i / N$. The observable coupling constant, therefore, scales with the square root of the number of emitters in a first approximation. The interaction of a molecule ensemble with plasmonic modes will be investigated in Chapter 5.

Oriented dye monolayers in hectorite nanosheets

3

The coupling efficiency of emitters with plasmonic nanoresonators depends not only on the photophysics of the dye itself but also on the position and orientation of the emitter. Precise control over these parameters on the nanoscale requires considerable effort [77–79]. The sample fabrication becomes much more reliable and robust using spatially extended emitter structures such as two-dimensional materials. For instance, tungsten diselenide (WSe_2) can facilitate strong coupling with plasmonic nanoresonators [37, 44, 80, 81]. These materials can be routinely exfoliated onto different substrates or chemically grown to cover large areas [82]. The optical properties can be altered by introducing defects and fabricating heterostructures [83, 84].

Yet, the growth of self-assembled monolayers (SAM) on plasmonic substrates provides an even more versatile framework. A precise design of the molecules allows control over the height on a sub-nanometer scale [85–87]. The position-dependent surface-enhanced Raman scattering even allows sensing the inhomogeneous electric field distribution inside the nanocavities [88]. Furthermore, substantial fluorescence enhancement has been observed for ultrathin dye-loaded spacer layers incorporated into particle-on-mirror plasmonic nanoresonators [89]. A wide variety of molecule monolayers can be attached to the substrates using click-chemistry with the SAMs [90].

In this work, we use dye monolayers sandwiched between two ultrathin hectorite nanosheets, a synthetic clay material [91]. This renders the fabrication of the dye monolayer independent of the substrate, as the layers are already formed in solution. The resulting quasi-two-dimensional sandwich structure can be dropcasted on any hydrophilic substrate. The synthetic procedure is summarized as follows[1]: Sodium hectorite is obtained by melt synthesis following a published procedure [91–95]. After partial ion exchange with a cationic fluorophore, strictly alternating interlayers of the dye and the hydrated sodium are obtained. The transparent hectorite nanosheets provide the separation of the layers. This state is called “ordered interstratified” and is shown in Figure 3.1. Note that the local charge balance facilitates the symmetry breaking in the stacking direction. We use cationic pyrene-derivative dye (C16Py), which has a spectrally broad emission between 500 and 700 nm. The broadband emission will allow us to determine the coupling strength with plasmonic nanoresonators in a wide spectral range in Chapter 5.

The clay platelets spontaneously delaminate after osmotic swelling in water. The resulting hectorite double stacks provide an encapsulated dye monolayer and can be dropcasted onto any hydrophilic substrate on demand. Previous works have shown that this synthesis

[1] Volodymyr Dudko from Prof. Breu’s group (Inorganic Chemistry I, University of Bayreuth) synthesized the encapsulated dye monolayer and characterized the structure by powder x-ray diffraction (PXRD) and CHN analysis.

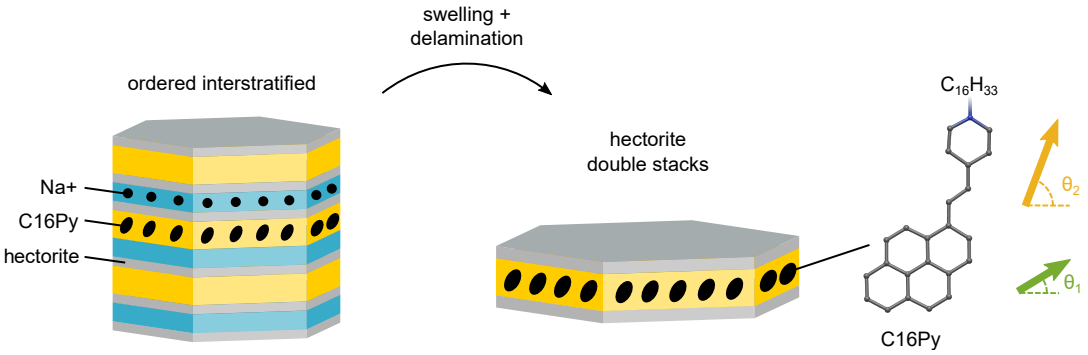

Fig. 3.1.: The sodium ions in the hectorite crystal are partially exchanged with the dye (C16Py), organized as strictly alternating interlayers. The left state is called "ordered interstratified". Individual hectorite double stacks are obtained after swelling and delamination [91]. The chemical structure of the C16Py dye and the orientations of the two transition dipoles (green and orange) are shown on the right.

procedure provides exceptionally high aspect ratios and consistent thickness [92]. Furthermore, the dye is expected to be densely packed with a significant out-of-plane orientation of the transition dipole [96]. Hence, these structures are promising candidates for efficient coupling with plasmonic nanoresonators. In principle, the dye can be substituted by a wide variety of other cationic dyes tailored for specific applications [93]. Furthermore, the dye density could be adjusted by mixing with other non-fluorescing cationic molecules. Thus, the hectorite nanosheets provide a versatile framework for controlled light-matter interaction on the nanoscale.

In this chapter, we investigate the optical properties of the encapsulated C16Py dye monolayers. We first introduce the transfer matrix formalism to calculate the polarization-dependent absorption and emission of dipoles in arbitrary multilayered environments. We cover radiative and non-radiative decay pathways to model the radiation even in dissipative environments like gold. We then introduce an intuitive and generally applicable experimental method based on white light reflection spectroscopy to determine the refractive index of the hectorite double stacks with diffraction-limited spatial resolution. This will enable us to model the encapsulated dye monolayers in later numerical simulations precisely.

Knowledge of the orientation of the dye molecules and their spatial homogeneity is crucial for efficient coupling with plasmonic nanostructures. Therefore, we present a novel, universal, and fast method to disentangle the orientations of spectrally overlapping transition dipoles in dense dye layers [97]. We demonstrate that the dye monolayer has two dominating transitions contributing to the fluorescence spectrum, as sketched by the two transition dipole moments in Figure 3.1. A comprehensive theoretical model allows an individual orientation determination of both transition dipoles. Furthermore, we investigate the orientational order on different substrates. Precise knowledge about the dipole orientations will be required in Chapter 5 to model the interaction of the dyes with plasmonic nanostructures.

Parts of this chapter are published in Nano Letters 2022, 22, 7499–7505 [97]. Figure adaptations with permission.

3.1 Numerical methods for the optics of layered media

3.1.1 Reflection and transmission at interfaces

The simplest example of a multilayered structure is two media separated by a planar interface. Therefore, we start with the reflection and transmission of electromagnetic waves at boundaries between two different materials [47, 98]. The wave vectors of incoming, reflected, and transmitted waves lie in one plane. Thus, it is sufficient to consider only this plane of incidence in our analysis. We choose the xz-plane, as shown in Figure 3.2a. The electric field of a plane wave then reads

$$\boldsymbol{E}e^{\mathrm{i}(\boldsymbol{k}\cdot\boldsymbol{r}-\omega t)} = \boldsymbol{E}e^{\mathrm{i}k_x x}e^{\mathrm{i}k_z z}e^{-\mathrm{i}\omega t} \quad . \tag{3.1}$$

Using the wave vector $k_0 = 2\pi/\lambda$ in vacuum, we get

$$k_x^2 + k_z^2 = n^2 k_0^2 \quad . \tag{3.2}$$

The electric fields can be decomposed into s- and p-polarization, where s denotes the polarization perpendicular and p denotes the polarization parallel to the plane of incidence. This defines the respective unit vectors

$$\hat{\boldsymbol{E}}^{(s)} = \begin{pmatrix} 0 \\ 1 \\ 0 \end{pmatrix} \quad \text{and} \quad \hat{\boldsymbol{E}}^{(p)} = \frac{1}{nk_0}\begin{pmatrix} \pm k_z \\ 0 \\ k_x \end{pmatrix} \tag{3.3}$$

with $|\hat{\boldsymbol{E}}^{(s)}|^2 = |\hat{\boldsymbol{E}}^{(p)}|^2 = 1$. The $\pm$ sign in the x-component denotes the direction of travel, as incoming and reflected electric field point into opposite x-directions (see Figure 3.2a). Maxwell's equations for nonmagnetic media impose boundary conditions on the electric field. Hence, we define reflection and transmission coefficients r_{12} and t_{12} for the electric fields propagating from medium 1 to medium 2 [47, 98]

$$r_{12}^{(s)} = \frac{k_{z,1} - k_{z,2}}{k_{z,1} + k_{z,2}} = -r_{21}^{(s)} \quad , \tag{3.4}$$

$$t_{12}^{(s)} = \frac{2k_{z,1}}{k_{z,1} + k_{z,2}} = \frac{k_{z,1}}{k_{z,2}} t_{21}^{(s)} \quad , \tag{3.5}$$

$$r_{12}^{(p)} = \frac{\varepsilon_2 k_{z,1} - \varepsilon_1 k_{z,2}}{\varepsilon_2 k_{z,1} + \varepsilon_1 k_{z,2}} = -r_{21}^{(p)} \quad , \tag{3.6}$$

$$t_{12}^{(p)} = \frac{2\sqrt{\varepsilon_1\varepsilon_2}k_{z,1}}{\varepsilon_2 k_{z,1} + \varepsilon_1 k_{z,2}} = \frac{k_{z,1}}{k_{z,2}} t_{21}^{(p)} \quad . \tag{3.7}$$

Similarly, the reflection and transmission coefficients of an incoming wave traveling in the opposite direction are denoted r_{21} and t_{21}. Due to our definition of the electric field vectors in Figure 3.2, the signs of $r_{12}^{(s)}$ and $r_{12}^{(p)}$ differ at perpendicular incidence. The x-component of the wavevector is conserved upon reflection and transmission and is thus

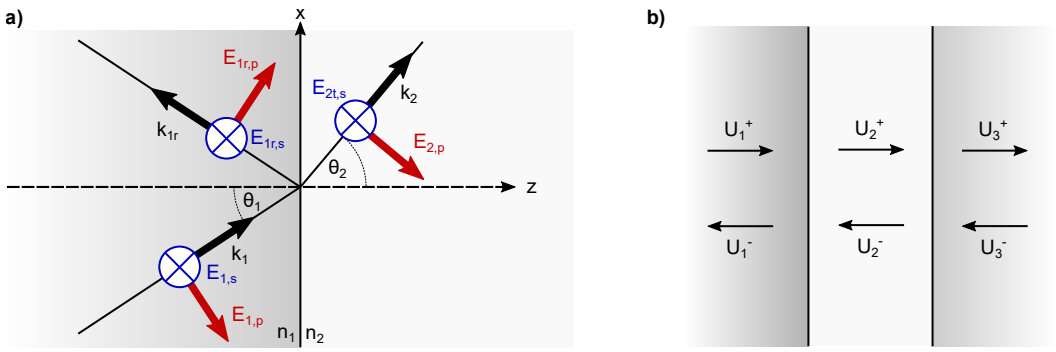

Fig. 3.2.: (a) Electric field and wave vector direction of incoming, reflected and transmitted plane waves at a planar interface between two media. The p-polarized field vector is shown in red, the s-polarized in blue. (b) We discriminate right and left traveling waves with amplitudes $U^{\pm}$ in a multilayer structure.

determined by the incident wave only. The propagation direction defines an angle θ with respect to the z-axis

$$\theta = \arcsin\frac{k_x}{nk_0} = \arcsin\sqrt{1-\frac{k_z}{nk_0}} \quad . \tag{3.8}$$

We define the power reflection coefficient $R_{12} = |r_{12}|^2$, which quantifies the percentage of the incident power reflected at the interface. In transmission, we must consider that the propagation direction changes as a result of refraction. Therefore, the power transmission coefficient is $T_{12} = \frac{n_2\cos\theta_2}{n_1\cos\theta_1}|t_{12}|^2 = \frac{k_{z,2}}{k_{z,1}}|t_{12}|^2$. This ensures energy conservation $T_{12} + R_{12} = 1$.

3.1.2 Transfer matrix formalism

In the general case of a multilayer system, the electric field in a layer with index i can be decomposed into waves traveling in left and right directions with amplitudes U_i^- and U_i^+ (see Figure 3.2b). We follow the formalism in Refs. [98, 99] and write

$$\boldsymbol{E}_i^{(s,p)} = \hat{\boldsymbol{E}}^{(s,p)}\left(U_{i,(s,p)}^- e^{-\mathrm{i}k_z z} + U_{i,(s,p)}^+ e^{\mathrm{i}k_z z}\right)e^{\mathrm{i}(k_x x-\omega t)} \quad . \tag{3.9}$$

Since both polarizations can be treated separately, we drop the indices s and p from now on. The amplitudes in the neighboring media with indices 1 and 2 have a linear relation

$$\begin{pmatrix} U_2^+ \\ U_2^- \end{pmatrix} = \begin{pmatrix} A & B \\ C & D \end{pmatrix}\cdot\begin{pmatrix} U_1^+ \\ U_1^- \end{pmatrix} = \boldsymbol{M}\begin{pmatrix} U_1^+ \\ U_1^- \end{pmatrix} \tag{3.10}$$

with transfer matrix $\boldsymbol{M}$. In general, the propagation through a multilayer system is described by the product of the individual matrices $\boldsymbol{M}_i$ according to

$$\boldsymbol{M}_{\text{total}} = \boldsymbol{M}_n\cdot\boldsymbol{M}_{n-1}\cdots\boldsymbol{M}_1 \quad . \tag{3.11}$$

Consider the case of an incident wave traveling to the right with amplitude U_1^+. The reflected amplitude U_1^- enters on the right side of Equation 3.10 but is unknown in the first place. Therefore, we define the scattering matrix $\boldsymbol{S}$, relating the wave amplitudes propagating toward the interface with those traveling away from it. The entries of the scattering matrix are the transmission and reflection coefficients we defined earlier

$$\begin{pmatrix} U_2^+ \\ U_1^- \end{pmatrix} = \begin{pmatrix} t_{12} & r_{21} \\ r_{12} & t_{21} \end{pmatrix} \cdot \begin{pmatrix} U_1^+ \\ U_2^- \end{pmatrix} = \boldsymbol{S} \begin{pmatrix} U_1^+ \\ U_2^- \end{pmatrix} \quad . \tag{3.12}$$

The following relations between the entries of $\boldsymbol{M}$ and $\boldsymbol{S}$ allow us to switch between the two representations if $D \neq 0$ and $t_{21} \neq 0$ [99]:

$$\boldsymbol{M} = \begin{pmatrix} A & B \\ C & D \end{pmatrix} = \frac{1}{t_{12}} \begin{pmatrix} t_{12}t_{21} - r_{12}r_{21} & r_{21} \\ -r_{12} & 1 \end{pmatrix} \quad , \tag{3.13}$$

$$\boldsymbol{S} = \begin{pmatrix} t_{12} & r_{21} \\ r_{12} & t_{21} \end{pmatrix} = \frac{1}{D} \begin{pmatrix} AD - BC & B \\ -C & 1 \end{pmatrix} \quad . \tag{3.14}$$

Using our definitions of reflection and transmission coefficients from Chapter 3.1.1, the transfer matrix of an interface reads for both polarizations

$$\boldsymbol{M}_{12} = \frac{1}{t_{21}} \begin{pmatrix} 1 & r_{21} \\ r_{21} & 1 \end{pmatrix} = \frac{1}{2\eta} \begin{pmatrix} 1+\kappa & 1-\kappa \\ 1-\kappa & 1+\kappa \end{pmatrix} \tag{3.15}$$

with $\eta^{(s)} = 1$, $\eta^{(p)} = \sqrt{\varepsilon_2/\varepsilon_1}$ and $\kappa = \eta^2 k_{z,1}/k_{z,2}$. The wave propagation over a distance d imposes a phase of the electric field, corresponding to a complex transmission coefficient $t = t_{12} = t_{21} = e^{\mathrm{i}k_z d}$. As the propagation direction has already been included in our definition of the electric field in Equation 3.9, the exponent has a positive sign in both t_{12} and t_{21}. The reflection coefficient for propagation inside media is $r = r_{12} = r_{21} = 0$. Therefore, the transfer matrix of propagation in a homogeneous medium reads

$$\boldsymbol{M} = \begin{pmatrix} e^{\mathrm{i}k_z d} & 0 \\ 0 & e^{-\mathrm{i}k_z d} \end{pmatrix} \quad . \tag{3.16}$$

We can determine the overall reflectivity R and transmissivity T of a multilayer structure by calculating the entries of the scattering matrix.

3.1.3 Dipoles in multilayer environments

Consider an incoming plane wave under a certain angle from the right side of the multilayer system. The transfer matrix formalism allows us to calculate the electric field at every position in the multilayer structure. Consequently, we can obtain the excitation strength of an arbitrary dipole with a known position and orientation inside this system. Since the propagation of light beams can be reversed, the excitation of the dipole by a plane wave is equivalent to a dipole radiating into the far-field under the same angle. Hence, the transfer matrix method enables us to determine the emission pattern of a dipole in a multilayered environment following Ref. [98]. This derivation will be used in Chapter 3.3

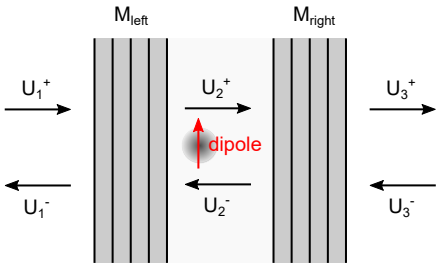

Fig. 3.3.: The multilayer structure can be reduced to an effective three layer system to compute the radiation from a single dipole (red).

to model the polarization-dependent emission from the encapsulated dye monolayer on arbitrary substrates. The comparison between the experiment and simulation will allow us to determine the transition dipole orientations in the dye monolayer.

The electric field at the position of a dipole is obtained by reducing an arbitrary multilayer environment to an effective three-layer system, as sketched in Figure 3.3. The layers on the left and right sides of the dipole are combined in the transfer matrices $\boldsymbol{M}_{\text{left}}$ and $\boldsymbol{M}_{\text{right}}$, including the propagation to and from the dipole. Therefore, the complex field amplitudes of the left and right propagating waves at the dipole position are given by U_2^+ and U_2^-. The system is described by

$$\begin{pmatrix} U_3^+ \\ U_3^- \end{pmatrix} = \boldsymbol{M}_{\text{right}} \begin{pmatrix} U_2^+ \\ U_2^- \end{pmatrix} \quad \text{and} \quad \begin{pmatrix} U_2^+ \\ U_2^- \end{pmatrix} = \boldsymbol{M}_{\text{left}} \begin{pmatrix} U_1^+ \\ U_1^- \end{pmatrix} \quad . \tag{3.17}$$

Imagine a plane wave entering the system from the right (medium 3). Medium 1 will only have an outgoing wave to the left, i.e., $U_1^+ = 0$. Furthermore, we choose $U_1^- = 1$. This gives the relations

$$\begin{pmatrix} U_2^+ \\ U_2^- \end{pmatrix} = \boldsymbol{M}_{\text{left}} \begin{pmatrix} 0 \\ 1 \end{pmatrix} = \frac{1}{t_{21}} \begin{pmatrix} t_{12}t_{21} - r_{12}r_{21} & r_{21} \\ -r_{12} & 1 \end{pmatrix} \cdot \begin{pmatrix} 0 \\ 1 \end{pmatrix} \tag{3.18}$$

$$= \frac{1}{t_{21}} \begin{pmatrix} r_{21} \\ 1 \end{pmatrix} \quad , \tag{3.19}$$

$$\begin{pmatrix} U_3^+ \\ U_3^- \end{pmatrix} = \boldsymbol{M}_{\text{right}} \begin{pmatrix} U_2^+ \\ U_2^- \end{pmatrix} = \frac{1}{t_{32}} \begin{pmatrix} t_{23}t_{32} - r_{23}r_{32} & r_{32} \\ -r_{23} & 1 \end{pmatrix} \cdot \frac{1}{t_{21}} \begin{pmatrix} r_{21} \\ 1 \end{pmatrix} \tag{3.20}$$

$$= \frac{1}{t_{21}t_{32}} \begin{pmatrix} (t_{23}t_{32} - r_{23}r_{32})r_{21} + r_{32} \\ -r_{23}r_{21} + 1 \end{pmatrix} \quad . \tag{3.21}$$

After normalization to the amplitude of the incident plane wave U_3^-, the electric fields at the dipole position are

$$E_2^+ = \frac{U_2^+}{U_3^-} = \frac{r_{21}}{t_{21}} \cdot \frac{t_{21}t_{32}}{1 - r_{23}r_{21}} = \frac{r_{21}t_{32}}{1 - r_{23}r_{21}} \quad , \tag{3.22}$$

$$E_2^- = \frac{U_2^-}{U_3^-} = \frac{1}{t_{21}} \cdot \frac{t_{21}t_{32}}{1 - r_{23}r_{21}} = \frac{t_{32}}{1 - r_{23}r_{21}} \quad . \tag{3.23}$$

The electric field for illumination from the left can easily be obtained by swapping the indices 1 and 3 and the propagation direction

$$E_2^- = \frac{U_2^+}{U_3^-} = \frac{r_{23}t_{12}}{1-r_{21}r_{23}} \quad , \tag{3.24}$$

$$E_2^+ = \frac{U_2^-}{U_3^-} = \frac{t_{12}}{1-r_{21}r_{23}} \quad . \tag{3.25}$$

We define a Finesse parameter

$$F^{(s,p)} = \frac{1}{1-r_{23}^{(s,p)}r_{21}^{(s,p)}} \quad . \tag{3.26}$$

For incident waves from the right (←) and left (→), we determine the electric field at the dipole position as a superposition of left and right traveling waves $E_2^{\pm}$ according to

$$\boldsymbol{E}_{\leftarrow} = \begin{pmatrix} -F^{(p)}t_{32}^{(p)}\left(1-r_{21}^{(p)}\right)\frac{k_{z,1}}{k_2} \\ F^{(s)}t_{32}^{(s)}\left(1+r_{21}^{(s)}\right) \\ F^{(p)}t_{32}^{(p)}\left(1+r_{21}^{(p)}\right)\frac{k_x}{k_2} \end{pmatrix} \quad \text{and} \quad \boldsymbol{E}_{\rightarrow} = \begin{pmatrix} F^{(p)}t_{12}^{(p)}\left(1-r_{23}^{(p)}\right)\frac{k_{z,1}}{k_2} \\ F^{(s)}t_{12}^{(s)}\left(1+r_{23}^{(s)}\right) \\ F^{(p)}t_{12}^{(p)}\left(1+r_{23}^{(p)}\right)\frac{k_x}{k_2} \end{pmatrix} \quad . \tag{3.27}$$

The difference of left and right propagating waves, not the sum, enters in the x-components, as the x-component of the p-polarized wave flips sign following our definition in Figure 3.2a. The global minus in the x-component of $\boldsymbol{E}_{\leftarrow}$ originates from the propagation to the left.

3.1.4 Polarization-dependent emission patterns of dipoles

In the last section, we determined the electric field $\mathbf{E} = (E_x', E_y', E_z')$ at the position of a dipole upon plane-wave excitation of the multilayer system at an angle θ. The calculated field was normalized by the amplitude of the incident wave. In the following, we choose the position of the dipole as the origin $(x, y, z) = (0, 0, 0)$. As the beam path can be reversed, the calculated field strength, projected onto the dipole direction, quantifies its emission into the far-field under the angle θ. In this section, we develop an analytical framework to obtain the polarization-resolved emission pattern of the dipole. Calculating the radiation pattern is essential for comparison with the experiment, as the finite numerical aperture of the microscope objective only captures a particular angle interval of the radiation. Our model considers a linear polarizer in the collimated beam after the microscope objective.

To describe the refraction at the microscope objective, we switch from cartesian to spherical coordinates (see Figure 3.4a) with angular unit vectors

$$\hat{\boldsymbol{e}}_\theta = \begin{pmatrix} \cos\theta\cos\phi \\ \cos\theta\sin\phi \\ -\sin\theta \end{pmatrix} \quad \text{and} \quad \hat{\boldsymbol{e}}_\phi = \begin{pmatrix} -\sin\phi \\ \cos\phi \\ 0 \end{pmatrix} \quad . \tag{3.28}$$

We combine the p-polarized field components E_x and E_z in a field E_θ pointing along the elevation unit vector $\mathbf{e}_\theta$. Initially, we only consider rays in the xz-plane, corresponding to

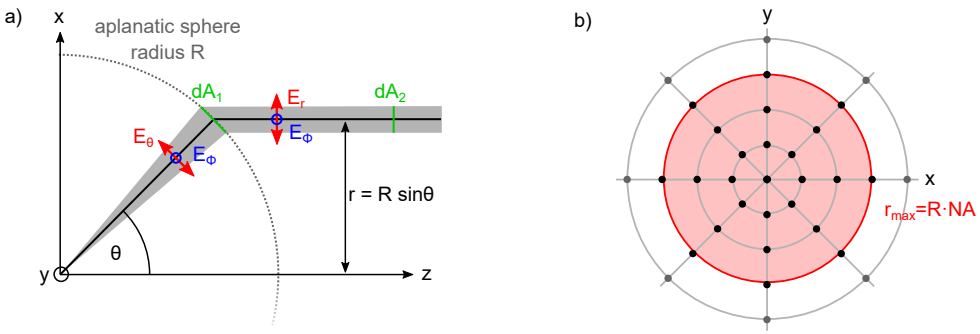

Fig. 3.4.: (a) Sketch of the dipole emission refracted by an aplanatic objective. The radius R of the aplanatic sphere equals the focal length. (b) In the numerical calculations, the electric field in the collimated beam path is calculated at discrete points. The points are equidistantly spaced in radial and angular directions. The numerical aperture of the objective defines an upper limit $r_{\max}$ of the radial coordinate marked in red.

an azimuth angle $\phi = 0$. Hence, the s-polarized field E_y equals the azimuthal field E_ϕ pointing along $\mathbf{e}_\phi$. We find

$$\begin{pmatrix} E_\theta \\ E_\phi \end{pmatrix} = \begin{pmatrix} E'_x \hat{\boldsymbol{e}}_x \cdot \hat{\boldsymbol{e}}_\theta + E'_z \hat{\boldsymbol{e}}_z \cdot \hat{\boldsymbol{e}}_\theta \\ E'_y \hat{\boldsymbol{e}}_y \cdot \hat{\boldsymbol{e}}_\phi \end{pmatrix} = \begin{pmatrix} E'_x \cos\theta - E'_z \sin\theta \\ E'_y \end{pmatrix} = \begin{pmatrix} E_x - E_z \\ E_y \end{pmatrix} \quad . \tag{3.29}$$

Following the previous definition of the normalized electric fields (see Equation 3.3), we write $E'_x \cos\theta = E_x$ and $E'_z \sin\theta = E_z$. We now consider a single dipole $\boldsymbol{\mu} = (\mu_x, \mu_y, \mu_z)$. To generalize our calculations to three dimensions, we need to rotate the plane of incidence at an angle ϕ around the z-axis. This is equivalent to rotating the dipole moment in the opposite direction $-\phi$. Applying the corresponding rotation matrix yields

$$\boldsymbol{\mu}' = \begin{pmatrix} \cos(-\phi) & -\sin(-\phi) & 0 \\ \sin(-\phi) & \cos(-\phi) & 0 \\ 0 & 0 & 1 \end{pmatrix} \cdot \begin{pmatrix} \mu_x \\ \mu_y \\ \mu_z \end{pmatrix} = \begin{pmatrix} \mu_x \cos\phi + \mu_y \sin\phi \\ -(\mu_x \sin\phi - \mu_y \cos\phi) \\ \mu_z \end{pmatrix} \quad . \tag{3.30}$$

Like the dipole absorption, the emission we are about to calculate scales with the projection $\boldsymbol{\mu}' \cdot \boldsymbol{E}$ of its dipole moment onto the local electric field. To obtain the dipole radiation pattern, the electric field (E_x, E_y, E_z) calculated in the transfer matrix framework is substituted by the projection $(E_x \mu'_x, E_y \mu'_y, E_z \mu'_z)$. Thus, the electric field radiated by the dipole is

$$\begin{pmatrix} E_{\theta,\mathrm{dip}} \\ E_{\phi,\mathrm{dip}} \end{pmatrix} = \begin{pmatrix} (\mu_x \cos\phi + \mu_y \sin\phi) E_x - \mu_z E_z \\ -(\mu_x \sin\phi - \mu_y \cos\phi) E_y \end{pmatrix} \quad . \tag{3.31}$$

The time-averaged Poynting vector [47]

$$\langle \mathbf{S} \rangle = \frac{1}{2} \mathrm{Re}(\mathbf{E} \times \mathbf{H}^*) = \frac{1}{2} \sqrt{\frac{\varepsilon_0 \varepsilon_r}{\mu_0 \mu_r}} |\mathbf{E}|^2 \mathbf{n}_r = \frac{1}{2} n c_0 |\mathbf{E}|^2 \mathbf{n}_r \tag{3.32}$$

with radial unit vector $\mathbf{n}_r$ determines the radiated power in the solid angle $\mathrm{d}\Omega$

$$p(\Omega)\mathrm{d}\Omega = r^2 \langle \mathbf{S} \rangle \cdot \mathbf{n}_r \quad . \tag{3.33}$$

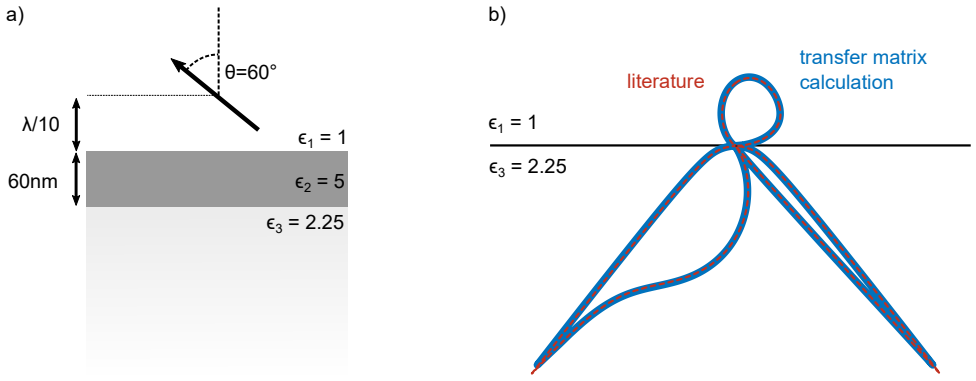

Fig. 3.5.: Validation of the dipole radiation pattern computation by comparison with the literature (Figure 10.7 in Ref. [47]). (a) Sketch of the simulation geometry with a single dipole above a planar waveguide. (b) The dipole radiation pattern $p(\theta)$ at $\lambda = 488\,\text{nm}$ obtained with the transfer matrix method (blue) agrees very well with the pattern retrieved from the literature (red).

For example, Figure 3.5b shows the radiation pattern $p(\theta)$ of a dipole above a planar dielectric waveguide at a wavelength $\lambda = 10\,\text{nm}$. The dipole is embedded in air at a distance of $\lambda/10$ to the waveguide, as sketched in Figure 3.5a. The 60° inclination to the surface normal gives rise to the asymmetry of the radiation pattern. Most of the power is radiated into the lower hemisphere with a higher refractive index. For comparison, the red dashed line shows the radiation pattern from the literature [47]. The perfect agreement proves the validity and accuracy of the presented calculations.

To calculate the polarization-resolved emission pattern of the collimated beam, we need to consider the refraction by the microscope objective. We model the objective as an aplanatic lens that follows geometrical optics [47]. In this approximation, a beam radiated from the dipole at an angle θ is redirected parallel to the z-axis as it intersects the aplanatic sphere (see Figure 3.4a). The radius R of the aplanatic sphere is the focal length of the lens. The refraction is equivalent to switching from spherical to cylindrical coordinates. Upon refraction, the p-polarized component of the electric field $E_{\theta,\text{dip}}$ pointing along the elevation unit vector $\hat{\boldsymbol{e}}_\theta$ is redirected in the radial direction $\hat{\boldsymbol{e}}_r$. The orientation of the s-polarized component $E_{\phi,\text{dip}}$ is not affected by refraction. Furthermore, in air, energy conservation adds an amplitude scaling factor $1/\sqrt{\cos\theta}$ to the refracted beam. This factor originates from the different areas of the infinitesimal surface elements $\mathrm{d}A_1$ before and $\mathrm{d}A_2$ after refraction, as depicted in the Figure. In total,

$$\mathbf{E} = (E_{\theta,\text{dip}}\hat{\boldsymbol{e}}_r + E_{\phi,\text{dip}}\hat{\boldsymbol{e}}_\phi)\frac{1}{\sqrt{\cos\theta}} \quad \text{with} \quad \hat{\boldsymbol{e}}_r = \begin{pmatrix}\cos\phi\\ \sin\phi\end{pmatrix} \quad \text{and} \quad \hat{\boldsymbol{e}}_\phi = \begin{pmatrix}-\sin\phi\\ \cos\phi\end{pmatrix} . \tag{3.34}$$

Projecting the refracted fields onto the cartesian coordinate system yields

$$\begin{pmatrix}E_{x,\text{dip}}\\ E_{y,\text{dip}}\end{pmatrix} = \begin{pmatrix}E_{\theta,\text{dip}}\cos\phi - E_{\phi,\text{dip}}\sin\phi\\ E_{\theta,\text{dip}}\sin\phi + E_{\phi,\text{dip}}\cos\phi\end{pmatrix}\frac{1}{\sqrt{\cos\theta}} . \tag{3.35}$$

To model a linear polarizer in the detection pathway along the x- and y-direction, we can set the perpendicular components of the electric field to zero, respectively.

The power emitted from the dipole is essential for comparison with experimental data. Integration over the power per solid angle $\int p\mathrm{d}\Omega$ yields the total power P_{tot} of the dipole radiated into the far-field. Only a fraction of this power is collected by the microscope objective. In the experiment, we use an objective with a numerical aperture (NA) of 0.9 in air. Therefore, the radiation collected by the objective is calculated by integration over the air hemisphere (called the upper hemisphere in the following) within the objective NA.

In the numerical implementation, the computation grid points are equidistantly spaced along the normalized in-plane wavenumber $q = n\sin\theta$ in the radial direction and along the azimuthal direction. This corresponds to a grid with equidistant radial and azimuthal spacing in real space, as shown in Figure 3.4b. The maximum radius $r_{\mathrm{max}} = R{\cdot}\mathrm{NA}/n$ is determined by the numerical aperture and the radius R of the aplanatic sphere. In this polar coordinate system, we can write

$$P = \int p\mathrm{d}\Omega = \iint p(r,\phi) r\mathrm{d}r\mathrm{d}\phi = \iint p(q,\phi)(R/n)^2 q\mathrm{d}q\mathrm{d}\phi \quad , \tag{3.36}$$

because $q = n\sin\theta$ yields $r = R\sin\theta = R\cdot q/n$ and $\mathrm{d}r/\mathrm{d}q = R/n$. We define P_{tot} as the integral of the Poynting vector in the upper and lower hemisphere and P_{NA} as the integral over the Poynting vector in the upper hemisphere within the objective NA. This result enables us to calculate the total polarization-resolved intensity of a dipole for comparison with measurements.

3.1.5 Radiative and non-radiative rates

Using the reciprocity of dipole absorption and emission, we could characterize the coupling of the dipole to far-field radiation. However, the dipole can also emit evanescent waves with normalized wavenumbers $q > n$, which do not propagate into the far-field. The spontaneous decay rate is the sum of radiative and non-radiative rates $\gamma = \gamma_{\mathrm{r}} + \gamma_{\mathrm{nr}}$. Although we only detect the radiative contributions in far-field experiments, calculating non-radiative contributions is, nevertheless, important. The coupling of dipoles to evanescent waves depends on their orientation and position. Hence, we need to scale the radiative contribution accordingly to compare the radiated power of dipoles at different angles and distances from a substrate. Our calculations assume an intrinsic quantum efficiency of 1 for the emitter.

Consider a dipole in medium 1 at a distance z_0 to medium 2 (see Figure 3.6a). A general expression for the dissipated power of the dipole is [47]

$$P = \frac{\omega}{2}\mathrm{Im}[\boldsymbol{\mu}^* \cdot \boldsymbol{E}(\boldsymbol{r}_0)] \quad , \tag{3.37}$$

where $\boldsymbol{E}$ is the electric field at the dipole position $\boldsymbol{r}_0$. The electromagnetic waves radiated from the dipole are partly reflected at the interface between the two materials. Hence, the electric field at the dipole position has contributions from the primary field $\boldsymbol{E}_0$ and the secondary field $\boldsymbol{E}_s$

$$\boldsymbol{E}(\boldsymbol{r}_0) = \boldsymbol{E}_0(\boldsymbol{r}_0) + \boldsymbol{E}_s(\boldsymbol{r}_0) \quad . \tag{3.38}$$

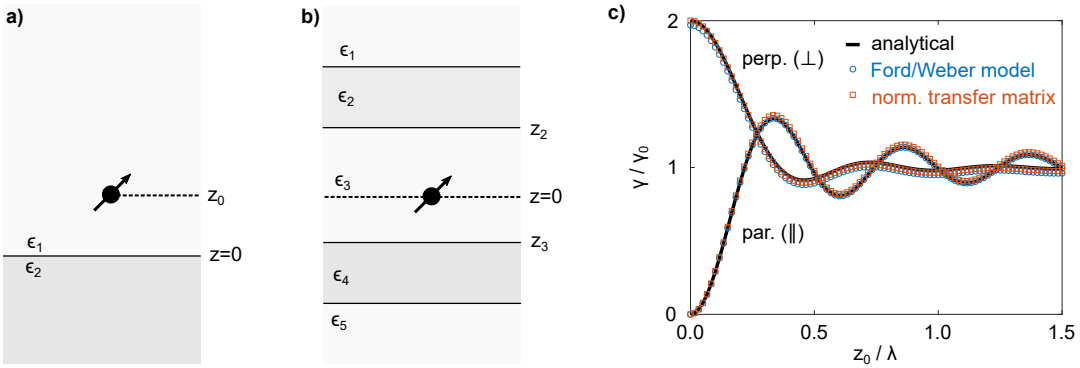

Fig. 3.6.: (a) Sketch of a dipole at distance z_0 from an interface between two materials. (b) Dipole in a 5-layer system. (c) Emission rate of a dipole at a distance z_0 to a perfect conductor in parallel and perpendicular orientation. The results from the model based on Ford and Weber (blue) and the transfer matrix (orange) agree very well with the analytical calculations.

The power radiated from a dipole in a homogeneous environment is given by Equation 2.18

$$P_0 = \frac{\omega|\boldsymbol{\mu}|^2}{12\pi\varepsilon_0\varepsilon}k^3 \quad . \tag{3.39}$$

Hence, the radiated power in the inhomogeneous environment can be written as [47]

$$\frac{P}{P_0} = 1 + \frac{6\pi\varepsilon_0\varepsilon}{|\boldsymbol{\mu}|^2}\frac{1}{k^3}\mathrm{Im}[\boldsymbol{\mu}^* \cdot \boldsymbol{E}_s(\boldsymbol{r}_0)] \quad . \tag{3.40}$$

We split the dipole moment $\boldsymbol{\mu}$ into a component parallel to the substrate $\mu_\parallel = \sqrt{\mu_x^2 + \mu_y^2}$ and a component perpendicular to the substrate $\mu_\perp = \mu_z$. The secondary field at the position of the dipole originates from the reflection of its own radiation at the interface. We define $k_\parallel = \sqrt{k_x^2 + k_y^2}$, $s = k_\parallel/k_1$, and $s_z = \sqrt{1-s^2}$. The reflected wave, therefore, collects a phase $2ik_1z_0s_z$ for propagation to the interface and back which we include in the reflection coefficients $r_{12}^{(s,p)}$.

As we assumed an intrinsic quantum efficiency of 1, the radiated power is proportional to the emission rate $P/P_0 = \gamma/\gamma_0$. Using the angular spectrum decomposition of the Green's function, the power radiated from the dipole is [47, 98]

$$\begin{aligned}\frac{P}{P_0} =& 1 + \frac{3}{4}\frac{|\mu_\parallel|^2}{|\boldsymbol{\mu}|^2}\mathrm{Re}\int_0^\infty \frac{s}{s_z}\left[r_{12}^{(s)} - s_z^2 r_{12}^{(p)}\right]\mathrm{d}s \\ &+ \frac{3}{2}\frac{|\mu_\perp|^2}{|\boldsymbol{\mu}|^2}\mathrm{Re}\int_0^\infty \frac{s^3}{s_z}r_{12}^{(p)}\mathrm{d}s \quad .\end{aligned} \tag{3.41}$$

Note that $s > 1$ describes an evanescent wave with in-plane wavenumber $k_\parallel > k_1$. For a general treatment of a dipole in a multilayer system, we summarize the theory developed by Ford and Weber [100]. In this framework, the multilayer system is reduced to five effective layers, as sketched in Figure 3.6b. Layers 1 and 5 need to be non-absorbing materials with real-valued dielectric functions. Layers 2 and 4 can be absorbing materials

with a given thickness. The dipole is located between these layers in material 3 at a certain distance from the interface with layers 2 and 4, respectively. This structure generally acts as a planar waveguide for the dipole radiation. Therefore, the scattered field at the dipole position is an infinite sum of reflections.

Let $a = r^{(p)}_{d345} = r^{(p)}_{345} e^{-2ik_1 z_3 s_z}$ be the total amplitude change of a p-polarized wave propagating from the dipole to the interface (345) and back. Similarly, let $b = r^{(p)}_{d321} = r^{(p)}_{321} e^{2ik_1 z_2 s_z}$ be the total amplitude change for the interface (321). Downward radiation from the dipole will therefore generate a total amplitude of the form

$$a + ab + aba + abab + \dots \tag{3.42}$$

at the position of the dipole. Analogously, upward radiation will generate an amplitude

$$b + ba + bab + baba + \dots \tag{3.43}$$

at the position of the dipole. The sum of these geometric series is

$$A^{(p)}_{\perp} = \frac{(1+a)(1+b)}{1-ab} - 1 \quad . \tag{3.44}$$

The result is the same for the parallel component of an s-polarized wave. For the $\perp$ component of the s-polarized wave, however, we need to account for the sign change at each reflection. This gives the same result but with opposite signs of a and b, respectively. The final result is [100]

$$\begin{aligned}\frac{P}{P_0} =& \frac{3}{4}\frac{|\mu_{\parallel}|^2}{|\boldsymbol{\mu}|^2}\mathrm{Re}\int_0^{\infty} \frac{s}{s_z}\frac{(1+r^{(s)}_{d345})(1+r^{(s)}_{d321})}{1-r^{(s)}_{d321}r^{(s)}_{d345}}\mathrm{d}s \\ &+ \frac{3}{4}\frac{|\mu_{\parallel}|^2}{|\boldsymbol{\mu}|^2}\mathrm{Re}\int_0^{\infty} s\,s_z\frac{(1-r^{(p)}_{d345})(1-r^{(p)}_{d321})}{1-r^{(p)}_{d321}r^{(p)}_{d345}}\mathrm{d}s \\ &+ \frac{3}{2}\frac{|\mu_{\perp}|^2}{|\boldsymbol{\mu}|^2}\mathrm{Re}\int_0^{\infty} \frac{s^3}{s_z}\frac{(1+r^{(p)}_{d345})(1+r^{(p)}_{d321})}{1-r^{(p)}_{d321}r^{(p)}_{d345}}\mathrm{d}s \quad .\end{aligned} \tag{3.45}$$

The integrals run from $s = 0 \dots \infty$, capturing the total radiated and dissipated power. To validate this model, we compare the spontaneous emission rate of a dipole in air ($\varepsilon_1 = 1$) at a distance z_0 from an ideal conductor ($\varepsilon_2 \to \infty$) with the analytical results in Chapter 2.2.4 (see Figure 3.6c). As the dipole only radiates propagating waves in this geometry, we also calculated the normalized integrated intensity with the transfer matrix calculation from the last section. The results from both models are in perfect agreement with the analytical solution.

Integrating Equation 3.45 over the interval $s = 0 \dots 1$ yields the far-field emission rate $\frac{\gamma_r}{\gamma_0}$ of the dipole. The fraction of the total power radiated as photons into the far-field, i.e., the quantum efficiency, is then given by $\eta_r = \frac{\gamma_r}{\gamma}$. This result can be used to correct the

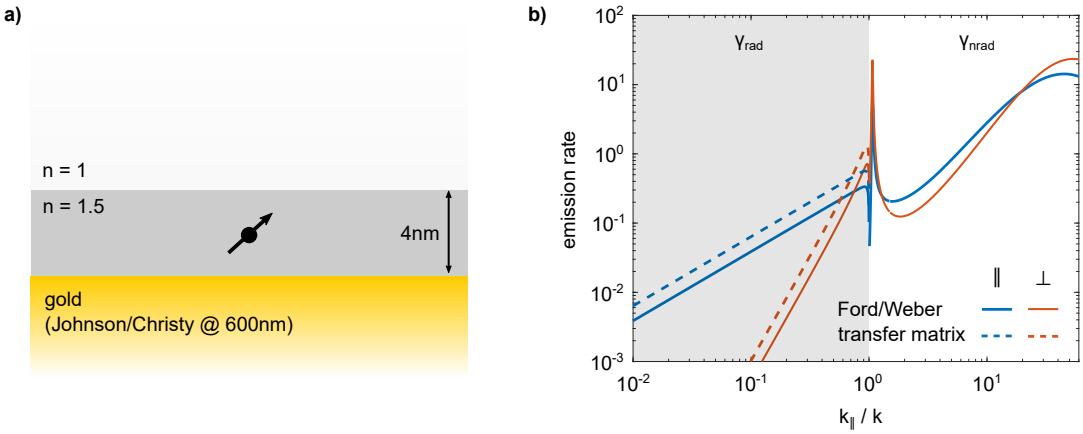

Fig. 3.7.: Radiative and non-radiative rates of a dipole in a 4 nm thin dielectric above a gold substrate at $\lambda = 600\,\text{nm}$. (a) Sketch of the geometry. (b) Comparison of the computed emission rates from the Ford/Weber model (solid lines) and the transfer matrix method (dotted lines) for a dipole oriented parallel (blue) and perpendicular (orange) to the interface. A large part of the power is dissipated non-radiatively.

calculations from the transfer matrix method. Therefore, the far-field intensity we detect in the experiment is the transfer matrix result P_{NA} scaled by η_{r}

$$P_{\text{detected}} = P_{\text{NA}} \frac{\gamma_{\text{r}}}{\gamma} \quad . \tag{3.46}$$

Figure 3.7 illustrates the radiative and non-radiative contributions of a dipole in the center of a 4 nm thin layer with a refractive index 1.5 above a gold substrate. This geometry corresponds to a single dipole embedded in the hectorite double stacks. The refractive index of gold at $\lambda = 600\,\text{nm}$ is interpolated from the literature [51]. Figure 3.7b shows the power density as a function of the normalized in-plane wavevector, which is the integrand of Equation 3.45. Compared are dipole orientations parallel and perpendicular to the substrate shown as blue and orange solid lines. Hence, much of the total power is radiated as evanescent waves with $s = k_{\parallel}/k_{\text{air}} > 1$. The associated power is either dissipated in the metal or can propagate along the interface between gold and dielectric as surface plasmons. Importantly, the radiative and non-radiative contributions vary with the dipole orientation. We ensured that our results were consistent with a previous implementation in the literature [101]. As a comparison, the dotted lines in Figure 3.7b represent the power density per wave vector calculated with the transfer matrix framework. As it relies on far-field radiation, this method only covers the interval $s = 0 \ldots 1$. In this interval, the functional shape of both models agrees very well up to a scaling factor of about 2.

3.2 Determination of dielectric functions in multilayer systems with spatial resolution

The structure investigated in this work is a dye monolayer sandwiched between hectorite nanosheets. As outlined in Chapter 2.2, the dielectric environment of emitters has a crucial

influence on their radiation properties. Therefore, the refractive index of the hectorite double stacks is an essential parameter in our numerical simulations. The refractive index of hectorite as a bulk material is given in the literature [102]. Still, we must ensure it also holds within the quasi-two dimensional structure investigated in this work. Furthermore, the presence of the dye alters the refractive index because of its absorption.

Ellipsometry is an established technique for the experimental determination of layer heights and refractive indices based on a model of the sample [103]. For this, the reflectivity of the sample at different angles and polarizations is measured. Fitting a model function to the experimental data allows the determination of all relevant parameters of the sample simultaneously. However, the size of the excitation spot is typically on the order of tens to hundreds of microns, averaging over smaller spatial features. Furthermore, the illumination area becomes more and more elliptic as the illumination angle is decreased. Therefore, conventional ellipsometry is typically applied to large-area homogeneous materials. In contrast, the typical lateral size of hectorite double stacks is on the order of 20 µm. An accurate determination of the refractive index and its spatial homogeneity requires a more sophisticated technique.

3.2.1 White light reflection spectroscopy

In this section, we present a general method to determine the refractive indices of planar materials. The spatial resolution is determined by the optics and is, therefore, only limited by diffraction. Our technique measures the interference of the reflected light from the interfaces to air and the underlying substrate. This allows us to determine the length of the optical beam path of the planar structure, which is the product of refractive index n and thickness d. As in ellipsometry, illumination at different angles allows independent determination of n and d. However, we decide for a separate thickness measurement by atomic force microscopy (AFM, Dimension 3100, Bruker) with a silicon probe (AC160TS) in tapping mode. The lateral resolution provided by the AFM topography measurements is well below the optical diffraction limit and, therefore, allows to characterize the homogeneity of the sample on the nanoscale. In the second step, we use the thickness obtained by AFM to determine the refractive index from white light reflection spectra using only a single illumination angle.

Only a fraction of the sample surface is covered with the hectorite nanosheets. We compare the reflection spectra on the hectorite $R(\lambda)$ and the bare substrate next to it $R_0(\lambda)$ to calculate the reflection contrast $[R(\lambda)-R_0(\lambda)]/R_0(\lambda) = R(\lambda)/R_0(\lambda)-1$. The reflection contrast is generally small for weakly absorbing and very thin materials $d \ll \lambda$ like the hectorite double stacks. For instance, transfer matrix calculations demonstrate that a layer with thickness $d = 4\,\mathrm{nm}$ on a silicon wafer yields a reflection contrast of only $\sim 0.4\,\%$ ($n = 1.4$) and $\sim 0.5\,\%$ ($n = 1.5$) at $\lambda = 400\,\mathrm{nm}$. This low contrast hinders an accurate determination of the refractive index. However, the contrast is greatly enhanced by adding a 300 nm SiO_2 layer on the Si wafer. For example, this principle has been exploited in the literature to determine the number of atomically thin graphene layers [104]. In our example, the Si/SiO_2 substrate features multiple reflections, which amplify the reflection

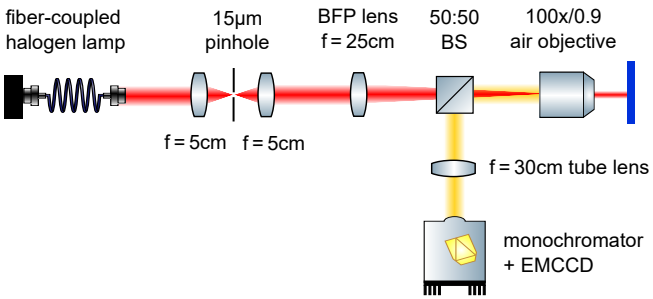

Fig. 3.8.: Experimental setup for white light reflection spectroscopy to determine the refractive index of thin layers with spatial resolution.

contrast to $\sim 10\,\%$ ($n = 1.4$) and $\sim 12\,\%$ ($n = 1.5$). This high sensitivity makes our approach very suitable for precise refractive index determination.

The sample is illuminated with white light from a fiber-coupled halogen lamp (DH-2000, Ocean Optics) at perpendicular incidence, as shown in Figure 3.8. We use a 100x/0.9NA microscope objective (MPlanFL N BD P, Olympus) for high spatial resolution. Plane-wave illumination of the sample is achieved by spatially filtering the white light with a pinhole and focusing on the center of the back focal plane of the objective. The reflection spectrum is measured with a sensitive camera (ProEM 1024BX3, Princeton Instruments) attached to a monochromator (IsoPlane 160, Princeton Instruments, with 150 lines/mm grating blazed at 500 nm). A magnified image of the sample is projected onto the entrance slit of the monochromator. The spatial resolution in the horizontal direction is therefore given by the entrance slit width. The resolution in the vertical direction is limited by the detector pixel size relative to the magnification of the optics. In our experiment, we define a region of interest for the camera readout and average over an area of about $1.6 \times 1.6\,\mu m^2$ per measurement on the sample.

Similar to our technique, other ellipsometry imaging approaches use a camera to measure monochromatic reflection images of the sample with high spatial resolution [103, 105]. However, our method determines the reflection contrast with both spatial and spectral resolution using unpolarized white light. As outlined in the following, the additional spectral resolution allows us to determine the refractive index with very high precision.

3.2.2 Hectorite monolayers and bilayers

We first investigate hectorite monolayers and bilayers without the intercalated dye monolayer. The diluted aqueous solution is dropcasted on a silicon wafer with a 300 nm oxide layer purchased from MicroChemicals. The AFM topography in Figure 3.9a shows that monolayers and bilayers are present on the sample. The corresponding histogram of height values in Figure 3.9b has three prominent peaks for substrate, monolayers, and bilayers. Fitting the distribution with a sum of three Gaussian functions yields monolayer and bilayer heights of 1.53 nm and 3.06 nm, respectively. This is slightly larger than the monolayer thickness of 1 nm reported in the literature, which we attribute to water layers at ambient conditions [93]. In the following, the retrieved values are used as input parameters for the refractive index determination.

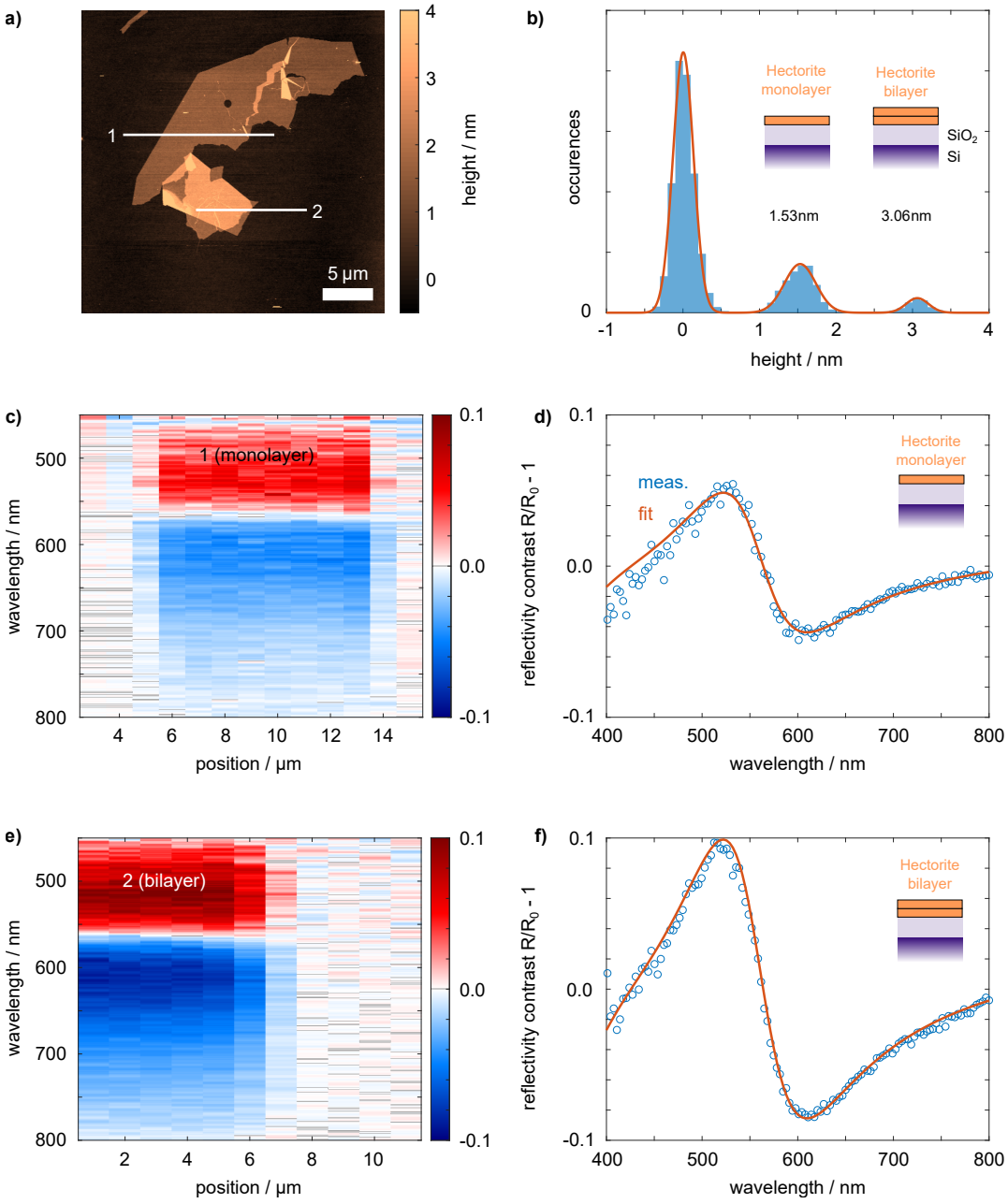

Fig. 3.9.: Thickness and refractive index determination of hectorite monolayers and bilayers on a Si/SiO_2 substrate. The AFM topography (a) has a discrete distribution of heights (b). The reflection contrast spectra (c) of a line scan (number 1 in (a)) across the hectorite monolayer are very homogeneous. The averaged contrast spectrum (d, blue dots) is fitted to the transfer matrix calculation (orange line) to obtain the refractive index. The same procedure is applied to a line scan (number 2 in (a)) across the hectorite bilayer (e-f).

The white light reflection spectra were measured at the same position as the AFM topography. Figure 3.9c shows the reflection contrast spectra of a line scan across substrate and hectorite monolayer along the first white line marked in the AFM topography image. The averaged reflection spectra next to the monolayer, i.e., on the substrate, are used for normalization ($R_0(\lambda)$). We observe a significant reflection contrast on the hectorite monolayer despite the layer height of only 1.5 nm. The reflection contrast oscillates as a function of wavelength with a maximum value of $\sim 6\,\%$. The oscillation period is defined primarily by the SiO_2 layer thickness. The reflection contrast spectra are very homogeneous across the monolayer, as expected from the extremely smooth surface characterized by the AFM topography measurement. Due to the spatial homogeneity, we take the average of the reflection contrast spectra on the monolayer, as shown in Figure 3.9d. Similar results are obtained for the line scan across the hectorite bilayer, as depicted in Figure 3.9e-f. The second white line in Figure 3.9a marks the position of the line scan. On the bilayer, the maximum reflection contrast increases to $\sim 10\,\%$.

We use dielectric functions from the literature for Si and SiO_2 [106, 107]. The hectorite monolayer and bilayer are modeled as non-absorbing dielectrics with thickness determined from the AFM topography. The transfer matrix formalism introduced in Chapter 3.1.2 allows us to calculate the reflectivity of this particular geometry. The fit to the experimental data has two free parameters, the SiO_2 layer thickness d_{SiO_2} and the hectorite refractive index n. The contrast values are weighted by the inverse local standard deviation. We obtain the following results:

	n	d_{SiO_2} / nm
Hectorite monolayer	1.519 ± 0.005	288.8 ± 0.4
Hectorite bilayer	1.518 ± 0.003	287.9 ± 0.2

As expected, both measurements yield identical refractive indices of the hectorite monolayer and bilayer. Note that the uncertainty of n is only 0.003 in the case of the bilayer, proving the high sensitivity of the described method. The fitted height of the SiO_2 slightly differs from the specification of 300 nm. We attribute this to uncertainties in the fabrication or slight deviations from the perpendicular plane-wave illumination we assumed in the calculations. The optical properties of the hectorite nanosheets are very similar to the literature values of the bulk material, having refractive indices $n_a = 1.49$, $n_b = 1.50$, and $n_c = 1.52$ of the three principal axes [102]. Polarized excitation would allow us to detect the slight birefringence reported in the literature. However, the minor variations in the refractive index are negligible for our applications. In the scope of this work, we treat the material as isotropic.

3.2.3 Hectorite double stacks modeled as an effective medium

After determining the refractive index of the hectorite nanosheets, we are now able to investigate the more complex system of the hectorite double stacks. These structures consist of a dye monolayer sandwiched between two individual hectorite layers. We expect similar refractive index values as our results in the last section. However, the absorbance of the dye at blue wavelengths enters into the refractive index of the heterostructure.

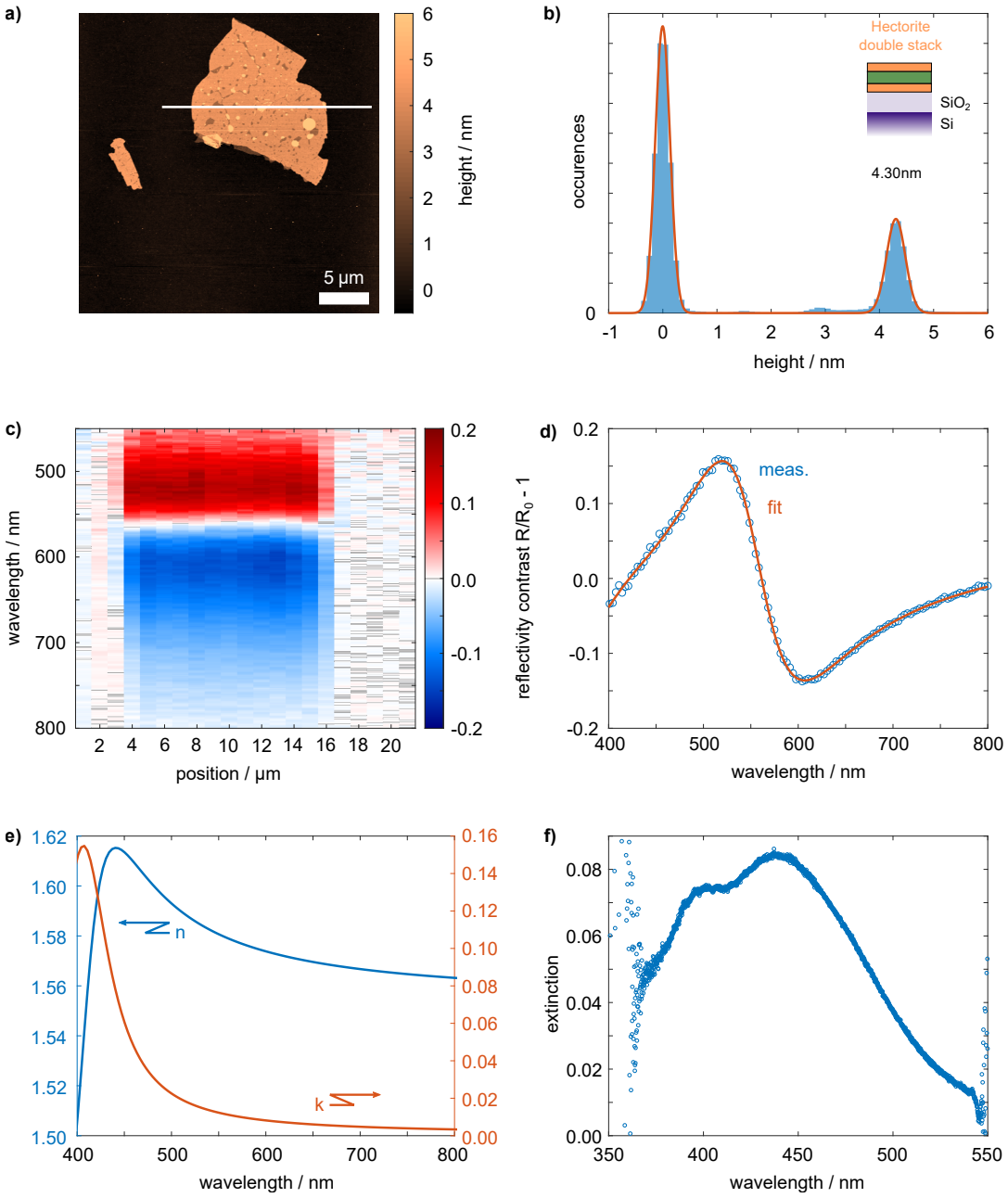

Fig. 3.10.: Thickness and refractive index determination of hectorite double stacks on a Si/SiO_2 substrate. The AFM topography (a) has a sharp peak in the histogram (b) at 4.3 nm. The reflection contrast spectra of the line scan (marked by white line in (a)) average over the sub-diffraction features in the topography. The reflection contrast spectrum averaged over the double stack (d, blue dots) agrees very well with our effective medium model with a single Lorentz oscillator (orange line). (e) Real and imaginary parts of the dielectric function are retrieved from the fitted dielectric function. (f) Normalized extinction of hectorite double stacks on a glass substrate, measured with an independent spectrometer. The results qualitatively match the imaginary part of the refractive index $k(\lambda)$ from (e).

Figure 3.10a-b shows the measured AFM topography of a representative hectorite double stack on a Si/SiO_2 substrate and the distribution of height values. Fitting the histogram with two Gaussian functions yields a double stack height of 4.3 nm, averaging over small patches with lower and higher topography. These inhomogeneities will be discussed in more detail in Chapter 3.3. The patches can not be resolved optically due to their small size. However, we expect them to have a minor influence on the computed refractive index. Due to the optical averaging, the line scan of reflection contrast spectra in Figure 3.10c shows only little variations within the double stack. Figure 3.10d shows the reflection contrast spectrum averaged over the double stack, exhibiting a maximum of $\sim 15\,\%$.

We model the hectorite double stack as an effective medium with a thickness of 4.3 nm obtained from the AFM measurements. To take the energy-dependent absorption of the dye into account, we use a single Lorentz oscillator term for the dielectric function

$$\varepsilon(E) = \varepsilon_\infty + \frac{A}{E_0^2 - E^2 - i\gamma E} \quad . \tag{3.47}$$

This dielectric function is assigned to the effective medium in the transfer matrix calculation. To obtain the best fit to the experimental data, we optimize the free parameters amplitude A, resonance energy E_0, damping γ, offset ε_∞, and SiO_2 thickness d_{SiO_2}. We obtain the fit values

$$\begin{aligned} A &= (0.7 \pm 0.3)\,\mathrm{eV}^2 \quad , \\ E_0 &= (3.05 \pm 0.11)\,\mathrm{eV} \quad , \\ \gamma &= (0.47 \pm 0.08)\,\mathrm{eV} \quad , \\ \varepsilon_\infty &= 2.35 \pm 0.05 \quad , \\ d_{SiO_2} &= (286.5 \pm 0.2)\,\mathrm{nm} \quad . \end{aligned}$$

The fitted reflection contrast spectrum agrees very well with the experimental data (see Figure 3.10d). As expected, the refractive index $n_\infty = \sqrt{\varepsilon_\infty} = 1.53$ far from the resonance is very close to the values obtained for the hectorite monolayer and bilayer. The resonance of the Lorentz oscillator peaks at approximately 400 nm, corresponding to the dye absorption in the blue spectral range. The uncertainties of the Lorentz oscillator parameters are relatively large since our measured reflection contrast spectra do not cover wavelengths below 400 nm. The retrieved dielectric function is converted to real and imaginary parts of the refractive index $\tilde{n} = n + ik$ (see Figure 3.10e). The resonance of the Lorentz oscillator translates to a peak of the absorption coefficient k at 400 nm. The real part of the refractive index n has a dispersive lineshape with values decreasing from about 1.62 to 1.56 above 450 nm in the measured interval.

For comparison, we measured the transmission spectra of the hectorite double stacks on a glass substrate $T(\lambda)$ with a commercial spectrometer (Lambda 19, Perkin Elmer). Here, the large-area illumination spatially averages over the sample. The transmission is normalized to the bare glass substrate $T_0(\lambda)$ to obtain the normalized extinction spectra $T(\lambda)/T_0(\lambda) - 1$ (see Figure 3.10f). We observe a broad absorption of the encapsulated dye between 350 and 480 nm. The absorption parameter $k(\lambda)$ obtained from the fit to the reflection contrast spectra qualitatively agrees with this independent measurement.

However, the single Lorentzian oscillator in our model can not reproduce all contributions to the absorption spectrum.

An important finding of our analysis is that the refractive index of the hectorite monolayer matches the literature values for bulk hectorite [102]. Furthermore, the refractive index of the hectorite double stacks with encapsulated dye monolayer is spectrally very flat above wavelengths of 550 nm. This is the relevant spectral range for the fluorescence emission of the dye and its coupling with plasmonic nanostructures. Based on these results, we use a spectrally constant refractive index $n = 1.5$ in theoretical calculations throughout this work, consistent with the literature.

The refractive index characterizes the macroscopic dielectric properties of the encapsulated dye monolayer. In the next section, we focus on the microscopic properties of the dye monolayer to accurately model its absorption and emission properties.

3.3 Disentangling the orientations of spectrally overlapping transition dipoles in dense dye layers

The transition dipole orientation of emitters greatly influences their interaction with the environment and the emission properties. An important example is fluorescence resonance energy transfer (FRET), where both the distance between the molecules and the relative transition dipole orientations enter [108]. Moreover, Chapter 3.1 already showed that the spontaneous emission rate of a dipole at a metal interface strongly depends on the distance and its orientation [61]. At small distances, the emission of a dipole oriented parallel to an ideal conductor completely vanishes due to destructive interference with the image dipole. This has, for instance, been exploited by the Enderlein group to localize single fluorescent molecules in three dimensions [23, 24, 109]. Furthermore, the emitter orientation is crucial for efficient interaction with plasmonic nanoresonators, which will be discussed in detail in Chapter 5 [44, 110, 111]. The Baumberg group claims that single-molecule strong coupling can be switched on and off when changing the emitter orientation [38]. It has also been shown that changing the orientation of molecule crystals in plasmonic cavities allows tuning from weak to the onset of strong coupling [112].

Controlling the orientation of molecules on substrates remains challenging [113]. Many parameters, such as steric and electrostatic effects, influence the orientation and packing of molecules. Therefore, the actual orientation needs to be determined experimentally to optimize the efficiency of novel devices. Several orientation determination techniques are routinely applied to individual fluorescent molecules with a single transition. The most important methods are defocused imaging [114–119] and back focal plane imaging [120].

The emitters in the hectorite double stacks are very densely packed and have multiple transitions. At the same time, the lateral size is tens of microns, requiring a fast orientation determination technique for large-area screening. Similar heterostructures can be found in novel optoelectronic devices such as light-emitting diodes and thin-film transistors. Also in these applications, the device efficiency substantially depends on the molecule orientations

[121–125]. In principle, the single-molecule orientation determination techniques mentioned above can be applied to emitter ensembles in dye films. However, time-consuming 2D scanning of the sample and spatial filtering is required for orientation determination with spatial resolution [126–128]. Instead, we analyze the polarization-dependent fluorescence emission of the dye monolayer, which only requires a single intensity value per polarizer angle for orientation determination [129–131]. Polarized widefield fluorescence allows direct imaging of spatial variations with a resolution only limited by the optics and the camera for detection. In this section, we extend the spatial resolution by spectral resolution provided by a powerful hyperspectral imaging setup. This allows disentangling the transition dipole orientations of multiple chromophores with diffraction-limited spatial resolution. Unlike other dye-specific methods such as Ref. [132], our fast and simple orientation screening method works, in principle, for any dye layer down to the single-molecule level.

In the following, we present the experimental setup, the data analysis, and the validation of our technique with an isotropic incoherent dye ensemble. We then apply our method to the dye monolayer in the hectorite double stacks on a glass substrate for simultaneous orientation determination of both transition dipoles with spatial resolution.

3.3.1 Hyperspectral imaging setup

Figure 3.11a outlines the experimental setup for hyperspectral imaging. We use picosecond laser pulses from a fiber-coupled supercontinuum laser (SuperK Extreme EXR-15, NKT Photonics). A tunable filter (SuperK Varia, NKT Photonics) cuts out the 470-480 nm interval from the white light spectrum. After collimation (RC04APC-P01, Thorlabs) and bandpass filtering (470/22 BrightLine HC BP, AHF Analysentechnik), two cylindrical lenses with 75 mm and 10 mm focal lengths compress the beam horizontally. A wire grid polarizer (WP25M-VIS, Thorlabs) on a motorized rotation mount (PRM1/MZ8 with TDC001 controller, Thorlabs) defines the linear excitation polarization angle α from the horizontal direction. A third cylindric lens with 300 mm focal length focuses the vertical dimension of the beam into the back focal plane of the microscope objective (MPlanFLN 100x/0.9 NA, Olympus) for plane wave illumination at perpendicular incidence. On the sample, the resulting elliptical excitation spot has an FWHM width of $\sim 1.8\,\mu$m and a height of $10\,\mu$m. The sample can be moved by a 3-axis piezo positioner (TRITOR 100SG with NV40/3 CLE controller, Piezosystem Jena).

Assume a single absorbing dipole moment $\boldsymbol{\mu}_a$ with in-plane angle ϕ_a to the horizontal direction and out-of-plane angle θ_a to the sample plane, as sketched in Figure 3.11b. The absorption scales with the projection of the linearly polarized incident electric field $\boldsymbol{E}_{\mathrm{exc}}$ onto the dipole moment as $\eta(\alpha) \propto |\boldsymbol{\mu} \cdot \boldsymbol{E}_{\mathrm{exc}}|^2 \propto \cos^2\theta_a \cos^2(\alpha - \phi_a)$. The fluorescence emitted from the dipole is reflected by a 50:50 cube beamsplitter (BS016, Thorlabs). A spatial filter built from two achromatic 100 mm lenses (AC254-100A, Thorlabs) with an iris limits the field of view on the sample to $\sim 25\,\mu$m. A Wollaston prism (PWQ 60.15 ARES350-900, B. Halle) separates horizontal (h) and vertical (v) polarizations by 1° in the vertical direction. After passing a 488 nm longpass filter (488 LP Edge Basic, AHF Analysentechnik), a 300 mm achromatic lens (AC508-300A, Thorlabs) images the fluorescence onto the

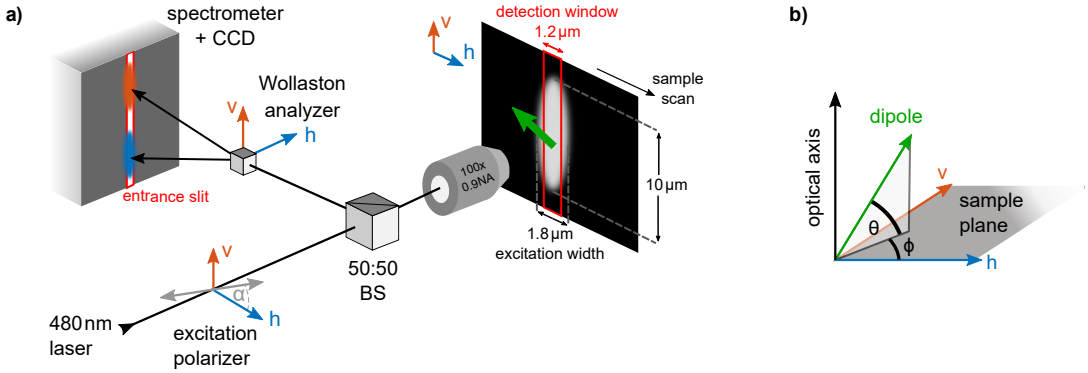

Fig. 3.11.: (a) Hyperspectral imaging setup for dipole orientation determination. The green dipole is excited by an elliptical spot profile for widefield imaging in the vertical direction. (b) Sketch of the dipole with out-of-plane angle θ and in-plane angle ϕ with respect to the substrate.

entrance slit of the spectrometer (IsoPlane 160 with 150 lines/mm grating blazed at 500 nm, Princeton Instruments). The width of the entrance slit projected onto the sample defines the width of the detection window and, thus, the horizontal spatial resolution. The 1.2 µm wide detection window matches the width of the elliptical excitation spot. The detector is an EMCCD camera with 1024×1024 pixels (ProEM 1024BX3, Princeton Instruments) with a pixel size corresponding to 75 nm on the sample. The sub-diffraction sampling allows us to estimate measurement uncertainties. All measured intensities are corrected by the polarization-dependent excitation power.

Due to the spatial separation of the detection polarizations (h,v) by the Wollaston prism, we can measure fluorescence spectra with both polarizations simultaneously in one camera image. Technically, the fluorescence is radiated by a dipole with angles ϕ_e and θ_e. Therefore, the v- and h-polarized intensity on the detector is

$$\begin{pmatrix} I_h(\alpha) \\ I_v(\alpha) \end{pmatrix} \propto \eta(\alpha) \cos^2\theta_e \begin{pmatrix} \cos^2\phi_e \\ \sin^2\phi_e \end{pmatrix} \quad , \tag{3.48}$$

assuming that the dipole is embedded in a homogeneous medium and using a low-NA objective. Transfer matrix calculations enable us to generalize for dipoles in layered media using high-NA objectives [133]. Based on the optical properties of the investigated dyes in this work, we assume that at least a fraction of the detected fluorescence originates from the absorbing dipole, i.e., $\phi_a = \phi_e$ and $\theta_a = \theta_e$. This general assumption will be discussed in more detail later in the text.

The elliptical excitation area minimizes the exposure of dyes outside the detection area to reduce photobleaching. At the same time, the 10 µm FWHM of the excitation spot in the vertical direction allows widefield fluorescence spectroscopy. Combined with the 75 nm projected pixel size, our setup yields fluorescence intensities of 133 points on the sample simultaneously in one camera image for h- and v-polarized detection. We measure spectra at multiple polarizer angles α to determine the dipole orientations. Horizontal scanning of the sample in steps of the half slit width provides a two-dimensional image of the sample. Hence, our technique generates a five-dimensional data set covering the spectrally resolved

fluorescence at discrete polarizer and analyzer directions at each two-dimensional position on the sample.

The presented method provides a significant speed-up with respect to conventional techniques based on two-dimensional confocal scanning:

- **Defocused imaging:** This technique uses the diffraction pattern of single molecules for orientation determination [114–119]. If an ensemble of dipoles below the optical diffraction limit emits incoherently, as in the dye layers discussed here, an additional polarization resolution is required for orientation determination. One would then need to scan an excitation spot in two dimensions. In contrast, our method only requires scanning in the horizontal direction due to its intrinsic spatial resolution in the vertical direction.
- **Back focal plane (BFP) spectroscopy:** Here, the dipole orientation is reconstructed from angle-resolved emission patterns [120, 126–128]. The monochromator slit needs to be closed to provide spectral resolution. Consequently, the majority of emitted photons are discarded. Obtaining a similar signal-to-noise ratio requires an approximately ten times longer exposure time. As in defocused imaging, the BFP spectra only yield an averaged dipole orientation over one sample position per measurement. Considering both the factor of 10 in integration time and the 133 simultaneously detected points, we estimate a speed-up of about 1330 using our hyperspectral imaging approach.

We did not consider the time to rotate the polarizer between the measurements since electro-optic modulators [134] and liquid-crystal waveplates [135] could rotate polarizations in fractions of a second. Furthermore, a larger excitation area and a camera with more pixels could increase this significant speed-up even further.

3.3.2 Raw data processing

The wavelength axis of the spectra is calibrated with a Neon-Argon lamp (IntelliCal, Princeton Instruments) for each camera pixel row. This calibration procedure accounts for the imaging distortions of the spectrometer to be able to compare spectra at different positions on the camera sensor.

The Wollaston prism spatially separates the h- and v-polarized fluorescence on the camera. However, the deflection angle is wavelength-dependent, producing curved spectra on the camera, as sketched in the left part of Figure 3.12. To correct this deformation in the post-processing, we probe the curvature of the spectrum of a point-like scatterer at various positions within the field of view (FOV). We spin-coat individual polystyrene beads with 200 nm diameter (FluoSpheres, Thermo Fischer Scientific) onto a glass cover slip. We center an isolated bead in the entrance slit and move the sample step-wise vertically across the field of view while measuring the white light scattering spectra. At each position, the scattering spectrum appears as a curved line on the camera image, sketched as black lines in Figure 3.12. To quantify the deviation from a horizontal line, we fit a 4th-order polynomial to the scattering intensity maxima in each frame for both h- and v-polarizations. Repeating this fit at every scan position and interpolating the

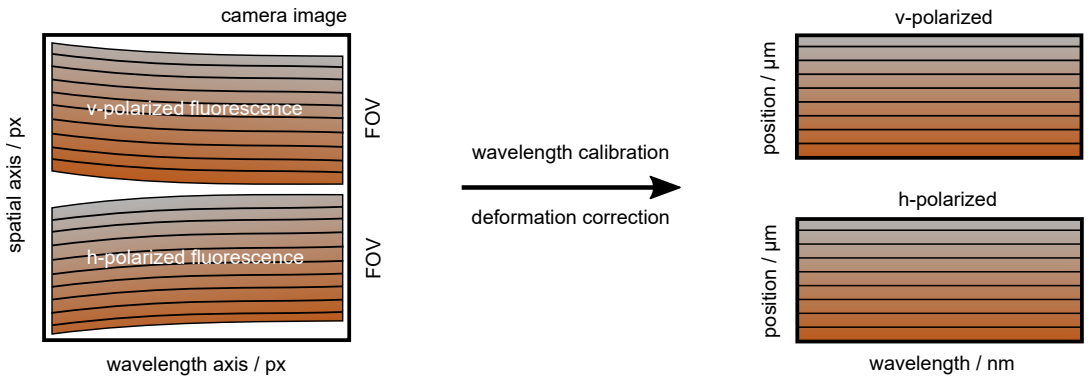

Fig. 3.12.: Post-processing of the camera frames acquired with the hyperspectral imaging setup. Each frame (left) contains v- and h-polarized spectra which are deformed by the wavelength-dependent deflection of the Wollaston prism. After applying the deformation correction described in the text, the h- and v-polarized spectra cover the identical spatial area (right) in the entire field of view (FOV).

points in between allows us to determine a deformation matrix for the entire field of view. Furthermore, we can spatially overlay the spectra of both detection polarizations. The inverse of this deformation matrix is applied to any measured image along with the wavelength calibration. As shown in Figure 3.12, the procedure separates both detection polarizations for individual analysis. Our implementation ensures energy conservation by scaling the intensity values appropriately.

3.3.3 Validation with an isotropic and incoherent molecule ensemble

We validate our setup with an ensemble of fluorophores embedded in a polymer matrix. As there is no preferential direction, the dyes are randomly oriented. We use the Atto-532 dyes (ATTO-TEC, Germany), which absorb well at our laser wavelength and have an emission maximum at 552 nm, as shown in Figure 3.13a. The dye powder is dissolved in a 1:1 mixture of ethanol and poly-methyl-methacrylate (PMMA) resist (ARP671.015, Allresist) and then diluted to the desired concentration. This homogeneous solution is spin-coated onto a cleaned glass substrate at 4,000 rotations per minute. The calculated average molecule distance is 5.5 nm. Hence, energy transfer between the molecules is negligible (see discussion later in this section), and the sample can be modeled as an isotropic and incoherent emitter ensemble [136]. Using the transfer matrix formalism, we determine the emission of a single dipole with orientation (θ, ϕ) in the center of a 20 nm thick dielectric layer above a glass substrate. We use a refractive index of $n = 1.5$ for the PMMA layer and substrate and calculate the polarization-dependent emission intensity $P_{\theta,\phi}$ collected by the objective with a numerical aperture of 0.9 in air. The excitation efficiency of the dipole $\eta_{\mathrm{exc}} \propto |\boldsymbol{\mu} \cdot \boldsymbol{E}|^2$ scales with the projection of the dipole orientation $\boldsymbol{\mu}$ onto the incident electric field direction $\boldsymbol{E}$. Due to the plane-wave illumination at perpendicular incidence, the incident electric field is always polarized in the sample plane. The power detected in the experiment is the product of excitation probability and emission from the dipole. The simulation is repeated for various dipole orientations (θ, ϕ) to sample the isotropic dipole distribution in the experiment numerically. We sum up the emission intensities at

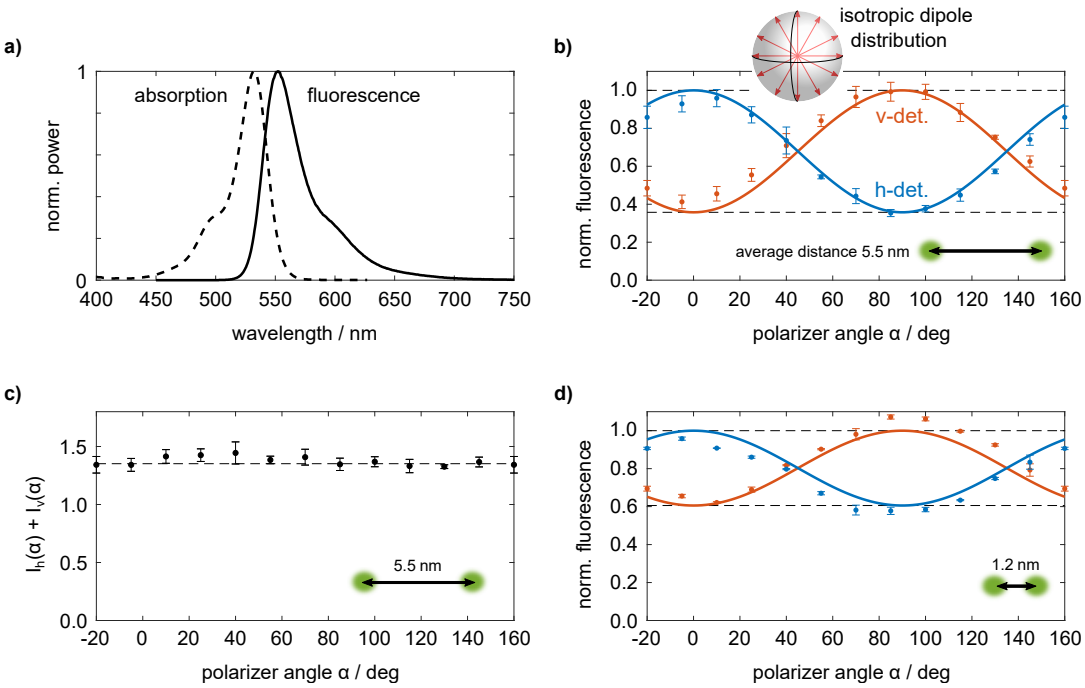

Fig. 3.13.: (a) Absorption and emission of Atto 532 dyes in solution, retrieved from the manufacturer website [137]. (b) Verification of the experimental setup by the polarization-dependent fluorescence of Atto 532 dyes embedded in a polymer thin film at an average molecule distance of 5.5 nm. Orange and blue colors depict the v- and h-polarized detection, respectively. The measured data (dots) are fitted to the theory (solid lines). (c) The sum of h- and v-polarized fluorescence intensity demonstrates that the absorption dipoles have no preferential direction. (d) The measurement at a much smaller molecule distance of 1.2 nm shows the effect of depolarization on the polarization-dependent fluorescence. The measurements are fitted to $\cos^2$ and $\sin^2$ model functions (solid lines).

all dipole orientations to obtain the theoretical expectation for the polarization-dependent emission of the incoherent dipole ensemble.

Figure 3.13b shows the polarization-resolved spectrally integrated fluorescence measurement of the Atto dyes in the PMMA thin film. The measurement was repeated at five positions to quantify the uncertainties. The excitation polarization angle α is increased step-wise from $\alpha = -20°$ to $\alpha = 160°$. The intensity modulation of linear polarizers is 180° periodic; hence, the first and last data points must have the same intensity. These two data points are used for a linear intensity correction to account for the inevitable photobleaching. The measured data points show a $\cos^2$ and $\sin^2$ modulation for h- and v-polarized detection, respectively. A single dipole absorbs most efficiently if in-plane dipole orientation ϕ and excitation polarizer angle α are collinear. In contrast, the absorption is zero if α and ϕ are perpendicular to each other. The emitted fluorescence has a maximum if also the Wollaston analyzer axes (h, v) coincide with α and ϕ. Consequently, $I_v(\alpha)$ and $I_h(\alpha)$ oscillate with opposite phases. Since all dipole orientations are present on the sample and we measure the average over the isotropic emitter ensemble, we detect a non-zero fluorescence intensity at any excitation polarization angle. The numerical simulations

predict a minimum value of 0.36, as shown by the dashed line in Figure 3.13b. The solid lines in the Figure represent the results from the transfer matrix calculations. The overall scaling factor between measurement and simulation is determined by least-squares fitting. The numerical simulations agree very well with the measurements, proving the validity of our experimental setup. Furthermore, the $\cos^2$ shape of the measured intensity proves that our first-order photobleaching correction is justified.

In our calculations, we required absorption and emission dipoles to be collinear, i.e., $\phi_e = \phi_a$ and $\theta_e = \theta_a$. The in-plane orientation of the absorption dipole is encoded in the excitation efficiency $\eta(\alpha)$. We assume that every dye excitation produces a detected fluorescence photon with a fixed probability. Summing up the fluorescence intensities of both detection polarizations $I_h(\alpha) + I_v(\alpha)$ then renders the fluorescence measurements independent of the in-plane emission dipole direction. Figure 3.13c shows that the result is independent of the excitation polarization. This finding demonstrates that the absorption dipole has no preferential direction, proving our assumption of isotropic molecule orientations.

Generally, the assumption of collinear absorption and emission dipoles breaks down if energy transfer happens between the randomly oriented dyes. As a consequence, the intensity modulation in polarization-dependent fluorescence would decrease. This depolarization effect can be observed in a second Atto dye sample with 100 times higher dye concentration, corresponding to an average molecule distance of only 1.2 nm. The measured fluorescence intensities are shown in Figure 3.13d. The $\cos^2$ fit to the experimental data illustrates that the offset of the intensity modulation has increased significantly. In the limiting case where the absorbed energy is always transferred to another molecule, the modulation as a function of α would disappear completely. In contrast, the measured data from the more diluted sample discussed above agree very well with the theory. This proves our assumption for the previous experiment to neglect energy transfer.

After validating the measurement principle with an unoriented dye ensemble, we now focus on the pyrene derivative dye monolayer embedded in ultrathin hectorite nanosheets. Although we concentrate on this specific system, the general principle for orientation determination is universally applicable to any dye layer with multiple transitions.

3.3.4 Fluorescence imaging of encapsulated dye monolayers

Determining the transition dipole orientations in the dye monolayer is essential to model the interaction with the plasmonic nanoresonators (see Chapter 5). We prepare samples with hectorite double stacks on a glass substrate to characterize the dye monolayer. The aqueous hectorite double stack solution is centrifuged at 3,000 rpm for 2 minutes. Only the central part of this solution is used for the sample, as it mainly contains individual hectorite double stacks with large aspect ratios. The solution is diluted with deionized water to the desired concentration. Glass cover slides are thoroughly cleaned and heated to 400 °C for about one minute to make the surface hydrophilic. About 100 µl of the hectorite solution is then dropcasted onto the glass substrate and dried at room temperature. Finally, the samples are baked at 100 °C for 12 hours to remove residual water.

Figure 3.14a shows a fluorescence intensity map of the hectorite double stacks on a glass substrate at an excitation power of 1 μW. As a result of the widefield excitation and detection, each vertical slice originates from a single measurement. The spectrally integrated fluorescence intensities are corrected for the non-uniform excitation. To obtain the two-dimensional image, the sample is scanned horizontally in steps of the half projected entrance slit width. The intensity histogram reveals that the fluorescence is emitted at discrete intensities where the lowest intensity corresponds to dye monolayers (1L). The dye monolayers have lateral sizes on the order of 10 μm. The discrete intensities allow us to reliably distinguish monolayers from multilayers (2L, 3L, ...).

As a complementary method to the optical experiment, we investigate the sample by atomic force microscopy in peak force mode[2] (Dimension Icon, Bruker). Figure 3.14b shows the AFM topography of an exemplary hectorite double stack on a glass substrate. A second double stack partially covers the layer. The histogram indicates that an individual double stack on a glass substrate is 4.3 nm thick. Small islands have discrete topography levels around 1.2 nm above and below the average value, matching the height of single hectorite nanosheets [93]. The optical measurements average over these islands spatially. However, we expect that small intensity variations within the double stack correlate with topography changes.

We characterize the optical resolution of our setup by the decay of the fluorescence intensity at monolayer edges. Figure 3.14c-d shows the intensity decay across an approximately vertical and horizontal monolayer edge. Assuming a Gaussian shape of the point spread function, we use a Gaussian error function to fit the data [138]. The optical resolution in the vertical direction is around 600 nm (FWHM). The resolution in the horizontal direction is determined by the spectrometer entrance slit width projected onto the sample, which is 1.2 μm. Consequently, the 1 μm (FWHM) optical resolution obtained from the Gaussian error function fit must be considered an estimate.

Up to now, we have only analyzed the spectrally integrated fluorescence intensities of dye ensembles as a function of position and polarization. On the one hand, the observed discrete intensities allowed us to identify dye monolayers and their spatial extent. On the other hand, we used the polarization-dependent fluorescence of the isotropic Atto dye layer to validate the experimental setup. The fluorescence of the Atto molecule is emitted by a single electronic transition. In general, molecules can have multiple chromophores contributing to the fluorescence. These transitions can, for example, originate from different parts of the molecule after energy transfer or a mixture of different dye species. The chromophores typically have different transition dipole orientations. The additional spectral information provided by our hyperspectral imaging setup allows us to disentangle these contributions and calculate the dipole orientations of all transitions individually.

The pyrene derivative dyes incorporated into the hectorite nanosheets are known to have two transitions, as discussed in the literature [139, 140]. Each molecule is described as a three-level system where absorption happens from the ground to the excited state. Fluorescence is emitted from this excited state or from an energetically lower state after molecule planarization. Based on this model, we assume that the orientations of absorption

[2] Paul Markus from Prof. Papastavrou's group (Physical Chemistry II, University of Bayreuth) took all AFM measurements in peak force mode.

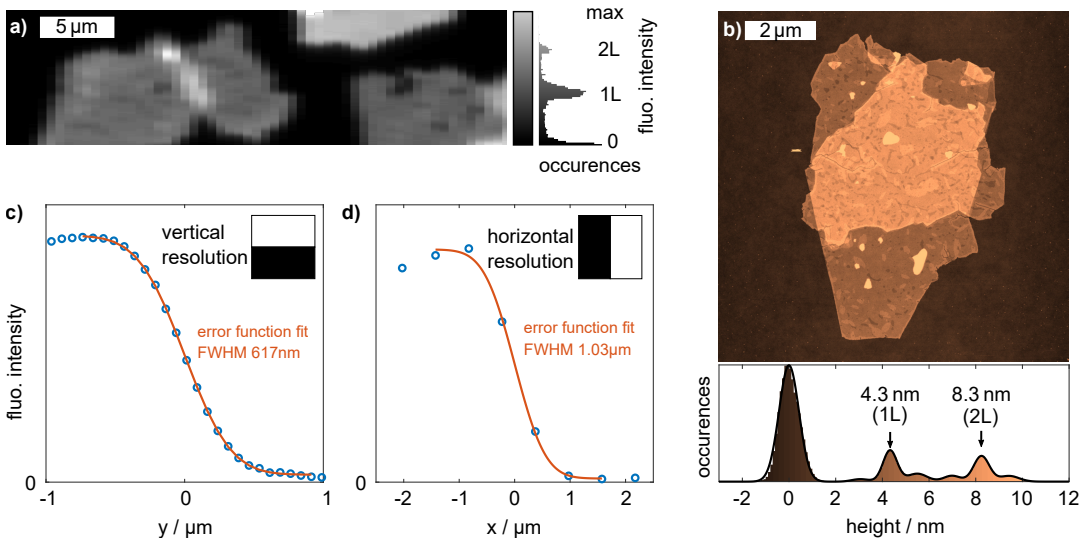

Fig. 3.14.: (a) The spectrally integrated fluorescence map of hectorite double stacks on a glass substrate has discrete intensity levels originating from different number of layers. (b) AFM topography measurement of a hectorite double stack. The 4.3 nm thickness of the monolayer is obtained from the histogram. (c-d) The optical resolution of the hyperspectral imaging setup is determined from the decay of the fluorescence intensity across approximately vertical and horizontal monolayer edges. The measured data are fitted with a Gaussian error function.

and emission dipoles are identical for the high-energy transition. Note that rotational diffusion between absorption and emission can be excluded in our solid-state sample. Our technique is not sensitive to the out-of-plane orientation of the absorption dipole, as the plane-wave illumination perpendicular to the substrate only probes its projection onto the sample plane. Consequently, our polarization-dependent method measures the out-of-plane orientation of the emission dipole. In particular, we assume that the in-plane orientations of absorption and emission dipoles coincide. This assumption could only be relaxed if microscopic information about the relative orientations of absorption and emission dipoles for the molecule is known, e.g., from density functional calculations.

3.3.5 Disentangling spectrally overlapping transitions by singular value decomposition (SVD)

Using our hyperspectral imaging technique, we measured the polarization-dependent fluorescence spectra at every point in the two-dimensional map in Figure 3.14a. The black curve in Figure 3.15a shows an exemplary fluorescence spectrum of the dye monolayer. The fluorescence covers a broad spectral range from 500 to 700 nm. This broadband emission will allow us to investigate the coupling with different modes of the plasmonic nanoresonators in Chapter 5. We observe that the shape of the fluorescence spectrum varies at different positions and polarizations. To analyze these variations, we decompose the spectra into their fundamental contributions using singular value decomposition (SVD). This method finds the dominating contributions in our large measurement dataset. Using

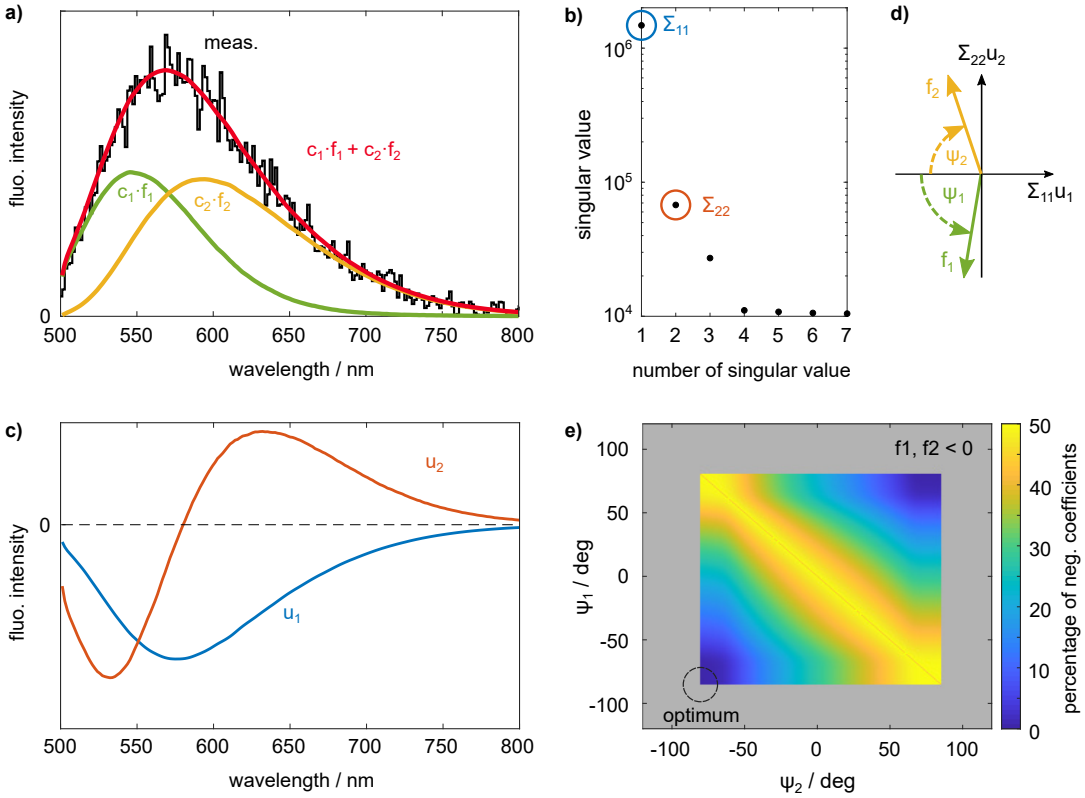

Fig. 3.15.: (a) Measured fluorescence spectrum of a dye monolayer on glass at an exemplary position. Using SVD of the entire dataset, the spectrum is decomposed into the two dominating components $c_1 \cdot f_1$ (green) and $c_2 \cdot f_2$ (orange). The sum of both contributions (red) agrees very well with the measured spectrum. (b) As the singular values Σ_{ii} drop off very fast, the first two contributions are sufficient to describe the dataset. (c) The basis functions $\boldsymbol{u}_{1,2}$ contain negative values due to their orthonormality. (d) To obtain physically meaningful basis function f_i, the SVD functions $\boldsymbol{u}_i \Sigma_{ii}$ are rotated by angles ψ_i. (e) The optimum rotation angles ψ_i are determined by minimizing the percentage of negative expansion coefficients c_{ij}. The angle interval with negative basis functions f_i is marked grey.

SVD, the lineshapes of the individual contributions are a result and not an input parameter. This is a particular advantage of SVD over least-squares fitting of all spectra, which would require assuming certain lineshapes for each spectral contribution.

SVD is a matrix factorization method used for principal component analysis (PCA). PCA is an established multivariate analysis technique, e.g., in Raman spectroscopy, where each spectrum comprises individual spectral features originating from different molecules. In this framework, PCA is used to reduce the dimensionality of the dataset and to decompose the spectra into their uncorrelated contributions [141, 142]. Similarly, we use SVD to determine the dominant spectral contributions in our large data set. The result is an optimal low-rank approximation of the measured spectra. We can then describe each spectrum by a small number of expansion coefficients instead of the intensity values of all m camera pixels. We fill the columns of the measurement matrix $\boldsymbol{M}$ with the fluorescence spectra $\boldsymbol{x}_j$, $j = 1 \ldots n$, of all positions in the two-dimensional scan area with non-vanishing

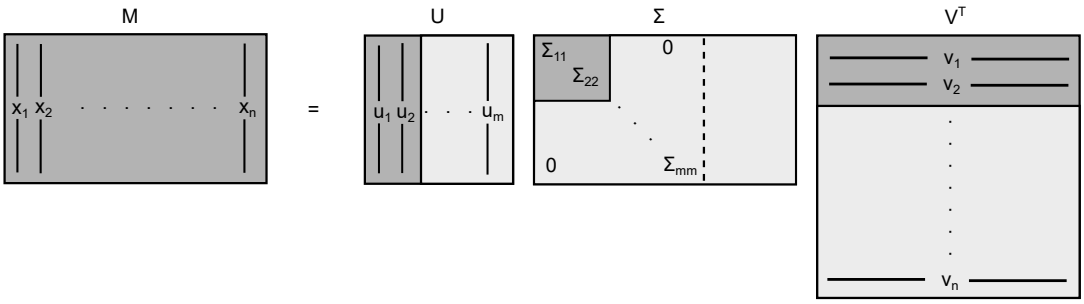

Fig. 3.16.: Visualization of the matrix factorization by SVD. Each column in the matrix $\boldsymbol{M}$ contains a measured spectrum x_j. Matrix $\boldsymbol{U}$ contains the basis functions $u_{1\ldots m}$, $\boldsymbol{\Sigma}$ has the singular values on the main diagonal, and $\boldsymbol{V}^T$ contains the expansion coefficients. We approximate the measurement matrix $\boldsymbol{M}$ using only the first two basis functions, as shown by the dark grey area in the matrices.

fluorescence intensity. We include each individual polarizer angle α and both analyzer directions; thus, $n \gg m$. The SVD of our real-valued measurement matrix $\boldsymbol{M} \in \mathbb{R}^{m\times n}$ reads [143]

$$\boldsymbol{M} = \boldsymbol{U}\boldsymbol{\Sigma}\boldsymbol{V}^T \tag{3.49}$$

with $\boldsymbol{U} \in \mathbb{R}^{m\times m}$, $\boldsymbol{\Sigma} \in \mathbb{R}^{m\times n}$, and $\boldsymbol{V} \in \mathbb{R}^{n\times n}$, as visualized in Figure 3.16. The SVD can be understood as a generalization of eigendecomposition for non-square matrices $m \neq n$. $\boldsymbol{\Sigma}$ has non-zero values with descending magnitude only on the main diagonal, called the singular values. The columns of $\boldsymbol{U}$ provide orthonormal basis functions $\boldsymbol{u}_1 \ldots \boldsymbol{u}_m$ of our measured spectra. The very fast drop-off of the singular values (see Figure 3.15b) demonstrates that the first two contributions $\boldsymbol{u}_{1,2}$ dominate our data set, matching the two transitions of the investigated dyes. This allows us to approximate $\boldsymbol{M}$ by the truncated SVD

$$\boldsymbol{M} \approx \tilde{\boldsymbol{U}}\tilde{\boldsymbol{\Sigma}}\tilde{\boldsymbol{V}}^T \tag{3.50}$$

with $\tilde{\boldsymbol{U}} \in \mathbb{R}^{m\times 2}$, $\tilde{\boldsymbol{\Sigma}} \in \mathbb{R}^{2\times 2}$, and $\tilde{\boldsymbol{V}} \in \mathbb{R}^{n\times 2}$. Due to the orthonormality of the basis functions per definition, at least one of the two basis functions inevitably contains negative values (see Figure 3.15c). This contradicts the requirement of optical spectra to have non-negative intensities. To lift the orthonormality claim, we rotate the product of the basis function and the singular value $\boldsymbol{u}_1\Sigma_{11}$ and $\boldsymbol{u}_2\Sigma_{22}$ by the angles ψ_1 and ψ_2 in the two-dimensional plane, as sketched in Figure 3.15d. The corresponding rotation matrix

$$\boldsymbol{R} = \begin{pmatrix} -\cos\psi_1 & -\cos\psi_2 \\ \sin\psi_1 & -\sin\psi_2 \end{pmatrix} \tag{3.51}$$

fulfills the identity $\boldsymbol{R}\boldsymbol{R}^{-1} = 1$. Thus, we can write

$$\boldsymbol{M} \approx \left(\tilde{\boldsymbol{U}}\tilde{\boldsymbol{\Sigma}}\boldsymbol{R}\right)\left(\boldsymbol{R}^{-1}\tilde{\boldsymbol{V}}^T\right) \quad . \tag{3.52}$$

Each measured spectrum $\boldsymbol{x}_j$ can then be approximated as

$$\boldsymbol{x}_j = \sum_{i=1}^{2} c_{ij}\boldsymbol{f}_i \quad . \tag{3.53}$$

The rotated basis functions $\boldsymbol{f}_i$ are the columns in in $\tilde{\boldsymbol{U}}\tilde{\boldsymbol{\Sigma}}\boldsymbol{R}$. The expansion coefficients c_{ij} are the entries of $\boldsymbol{R}^{-1}\tilde{\boldsymbol{V}}^T$. The non-negativity requirement for spectra imposes two constraints on the choice of ψ_1 and ψ_2. First, the basis functions f_i must be non-negative. Second, the expansion coefficients c_{ij} of all input spectra must be positive since the spectral contributions can not cancel each other. Due to inevitable noise, the second requirement can not be fulfilled for all data points. Figure 3.15e demonstrates that there is an optimum at $\psi_1 = -85°$ and $\psi_2 = -80°$ where our requirements are met by the vast majority of 99.97% of all data points. Note that the two basis functions have maximum spectral separation at this optimum [144].

In principle, our method can be generalized to more than two transitions. In contrast to conventional least-squares fitting, we did not need to assume a certain spectral lineshape. Our universal approach can be applied to any spectrally overlapping resonances with complex lineshapes.

3.3.6 Transition-dependent orientation anisotropy imaging

According to Equation 3.53, each spectrum can be written as a weighted sum of the basis functions $\boldsymbol{f}_{1,2}$. Thus, each individual spectrum measured at a specific position, polarizer angle α, and analyzer direction (h,v) is fully described by its expansion coefficients c_1 and c_2. The exemplary measured spectrum in Figure 3.15a is decomposed into the contributions $c_1 \cdot \boldsymbol{f}_1$ (green) and $c_2 \cdot \boldsymbol{f}_2$ (orange). The sum of both (red) is an optimal approximation of the measured spectrum.

In the following, we analyze the polarization dependence of the coefficients $c_{1,2}$ to determine the dipole orientations for each transition individually. Note that we can not determine the orientations of individual molecules within densely packed monolayers due to the enormous number of degrees of freedom. Instead, we develop a statistical model for the orientation distribution of the dipole ensemble in our particular sample. Fitting this model to our data then allows us to obtain statistical information about the dipole orientations within a diffraction-limited area. Furthermore, we characterize spatial variations of the dipole orientations across the sample.

During synthesis, the sodium ions in the hectorite are exchanged with the cationic dye. A chemical composition analysis proves that after the ion exchange, almost 100% of the former sodium positions inside the double stack are occupied by individual dye molecules [97]. We conclude from the hectorite crystal structure that the available area per dye is about $1\,\mathrm{nm}^2$ [145, 146]. As the area of the chromophoric part of the dye (about $1.5\,\mathrm{nm}^2$) is larger than the available area, the dyes are very densely packed in the hectorite double stack. Previous experiments have shown that the electrostatic interaction and the steric pressure produce a uniform inclination of $[\mathrm{Ru(bpy)_3}]^{2+}$ complexes incorporated into the hectorite [96]. As the surface of the hectorite double stacks is very flat (see Figure 3.14b), we expect a uniform inclination of the dye molecules with a particular out-of-plane angle θ and an initially unknown in-plane angle ϕ. Initially, we assume a statistical distribution of in-plane angles. This is equivalent to a homogeneous distribution of dipoles on the surface of a cone with an opening angle θ. In the literature, cone-shaped dipole orientation distributions are frequently encountered in modeling biological membranes [147–149].

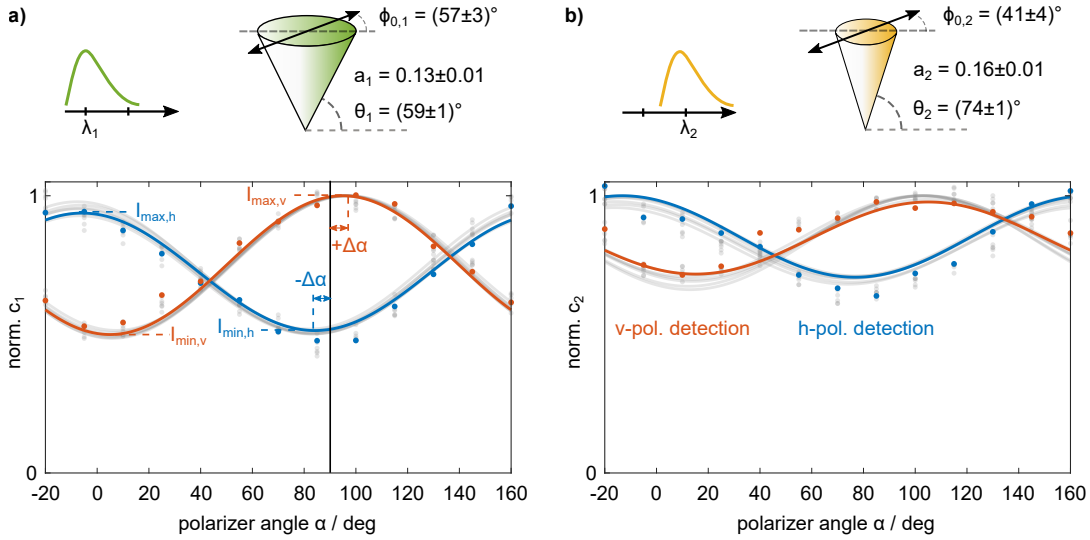

Fig. 3.17.: Polarization-dependent fluorescence of (a) high-energy and (b) low-energy transitions at an exemplary monolayer position. The normalized coefficients c_1 and c_2 are obtained from singular value decomposition. The measured data (dots) are fitted with the cone-shaped dipole orientation model with preferential direction (solid lines). The fit results for θ, ϕ_0, and a are illustrated in the cone above. The grey points and lines in the plot show the results from neighboring pixels for uncertainty estimation.

Figure 3.17 shows the measured polarization-dependent fluorescence at an exemplary position on a dye monolayer for the (a) high-energy and (b) low-energy transition. The colored dots correspond to the respective SVD expansion coefficients c_1 and c_2. The modulation depth $M = (I_{\max} - I_{\min})/I_{\max}$ of the low-energy transition is significantly smaller than the high-energy transition. M is inherently linked to the out-of-plane angle of a cone-shaped dipole distribution. If the dipoles lie flat on the substrate, i.e., $\theta = 0°$, the linearly polarized incident light excites only a fraction of the dipoles proportional to the geometric projection. This subset of dipoles then emits polarized fluorescence corresponding to a modulation $M > 0$. In contrast, a strictly out-of-plane oriented dipole ensemble ($\theta = 90°$) yields zero modulation, as the polarization directions are indistinguishable. Quantitative calculations show that the modulation depth monotonically decreases from $M(\theta = 0°) = 2/3$ to $M(\theta = 90°) = 0$. We can, therefore, conclude that the out-of-plane angle of the high-energy transition dipole is smaller than that of the low-energy transition dipole. We point out that the interval of possible values for $M(\theta)$ significantly differs from that of an isotropic dipole ensemble, where we found $M_{\text{iso}} = 0.64$ for the Atto thin film.

A symmetric distribution of dipoles requires the v- and h-polarized fluorescence to oscillate with opposite phases since the detection polarizations are perpendicular to each other. However, the measured data does not meet this requirement as there is a phase shift $2\Delta\alpha$ between both analyzer directions (see Figure 3.17). In addition, the minimum intensities $I_{\min}^{(v,h)}$ and maximum intensities $I_{\max}^{(v,h)}$ of both detection polarizations do not coincide. Based on this asymmetry, we conclude that the in-plane distribution of dipoles has a preferential direction, while the out-of-plane orientation of the dipoles is constant. This concept is further supported by a microscopic understanding of the molecule layer, as $\pi - \pi$ stacking allows the molecules to be packed more tightly [67]. For instance, a

dipole ensemble that is preferentially oriented in h-direction has a stronger absorption and emission at h-polarization; thus, $I_{\max}^{(h)} > I_{\max}^{(v)}$. Suppose the preferential orientation does not coincide with h- and v-polarization. In that case, an additional phase shift $\Delta\alpha$ is introduced, as absorption and emission scale with the projection onto the respective polarization direction. This consideration demonstrates that the intensity levels and the phase shift encode information about the out-of-plane orientation as well as the direction and strength of the in-plane preferential orientation.

Let $f(\phi)\mathrm{d}\phi$ be the probability of a dipole to have an in-plane orientation between ϕ and $\phi + \mathrm{d}\phi$, such that $\int_0^{2\pi} f(\phi)\mathrm{d}\phi = 1$. We can generally decompose the real-valued probability density $f(\phi)$ in a Fourier series

$$f(\phi) = \sum_{k=0}^{\infty} A_k \cos(k\theta) + B_k \sin(k\theta) \tag{3.54}$$

with coefficients A_k and B_k. As shown in Appendix A, only two angle-dependent components can be detected with a linear polarizer while the others average out [150]. Therefore, we define the angular distribution

$$f(\phi) = \frac{1}{2\pi}\left(1 + a\cos\left(2(\phi - \phi_0)\right)\right) \quad , \tag{3.55}$$

where the anisotropy parameter $a \in [0, 1]$ quantifies the deviation from a homogeneous distribution with constant value $f(\phi) = 1/(2\pi)$. The angle ϕ_0 represents the in-plane preferential direction, where linear polarizers can not distinguish ϕ_0 from $\phi_0 + \pi$. This ambiguity could be resolved with an angle-resolved fluorescence detection setup such as the dual-view design in Ref. [151]. Nevertheless, we expect the molecules in hectorite to have a single preferred orientation ϕ_0 rather than zigzag orientation with molecules also pointing in the opposite direction $\phi_0 + \pi$.

Using the transfer matrix method, we calculate the polarization-dependent absorption and emission of individual dipoles following the angular distribution function in Equation 3.55. The incoherent dipole ensemble is simulated by summing up the intensities emitted from all dipoles. In the simulations, the dipoles are embedded into the center of the 4 nm thick hectorite double stacks with $n = 1.5$ on the glass substrate with the same refractive index. We use a wavelength of $\lambda = 600\,\mathrm{nm}$. The solid lines in Figure 3.17 show the least-squares fit of the model function to the measured data for both transitions individually. The data from both detection polarizations are fitted simultaneously using the four free parameters a, θ, ϕ_0, and an overall intensity scaling factor. The fit agrees very well with the measured data. The sub-diffraction sampling of the experimental setup allows us to quantify the measurement uncertainties. Specifically, we use the standard deviation of the neighboring three pixels above and below the evaluated point (shown in grey in Figure 3.17) to quantify the uncertainty of the fit parameters. At the particular position in the Figure, the out-of-plane angle of the high-energy transition $\theta_1 = 59 \pm 1^\circ$ is significantly smaller than the low-energy transition $\theta_2 = 74 \pm 1^\circ$. The in-plane preferential directions $\phi_{0,1} = 57 \pm 3^\circ$ and $\phi_{0,2} = 41 \pm 4^\circ$ and the anisotropy values $a_1 = 0.13 \pm 0.01$ and $a_2 = 0.16 \pm 0.01$ of both transitions are very similar. In particular, the non-vanishing anisotropy proves the existence of a well-defined preferential orientation.

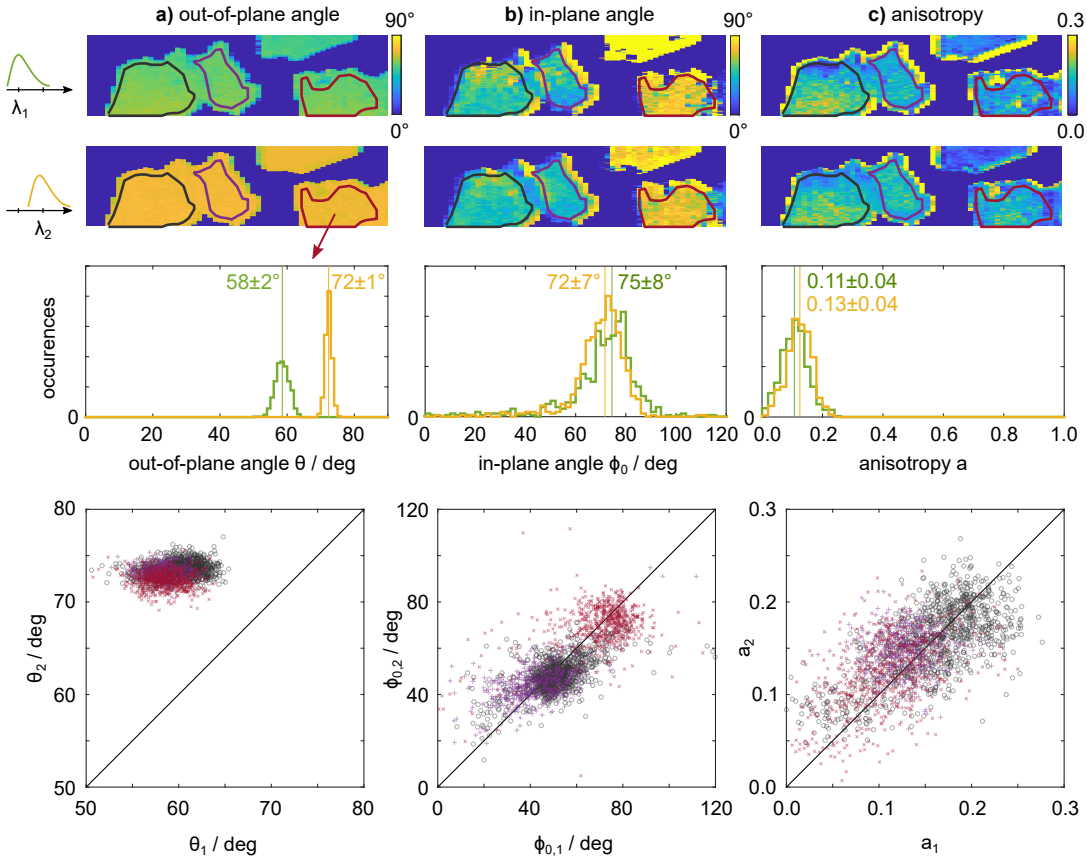

Fig. 3.18.: Two-dimensional map of fit results for (a) out-of-plane angle θ, (b) in-plane preferential direction ϕ_0, and (c) anisotropy a for both transitions individually. The monolayer boundaries are depicted as solid lines. The histograms show the color-coded distribution of fit parameters of the right monolayer. The scatter plots below visualize correlations in the fit results of both transitions, where the colors match the monolayer boundaries.

To model the interaction with plasmonic nanoresonators, we need to characterize the spatial homogeneity of the orientational order within the monolayers. Repeating the fit at every position in the fluorescence map in Figure 3.14a enables us to image the orientations of the two transition dipoles with high spatial resolution on large areas. Figure 3.18 shows two-dimensional maps of (a) out-of-plane angle, (b) in-plane preferential direction, and (c) anisotropy for both transitions individually. For a separate investigation of each monolayer, we threshold the discrete fluorescence intensity and cluster the connected areas. The color-coded contours in the Figure denote the monolayer boundaries obtained from shrinking the connected regions by the optical resolution of our experimental setup (see Chapter 3.3.4). Below the orientation images in the Figure, histograms depict the distribution of fit parameters of the right monolayer. An analysis of the fit residues proves that our model describes the measured data very well at any monolayer position.

The out-of-plane angle θ is very homogeneous within each monolayer and among all monolayers. As expected, the high packing density and confinement of the dye within the hectorite double stacks cause a uniform inclination of the molecules. The well-defined

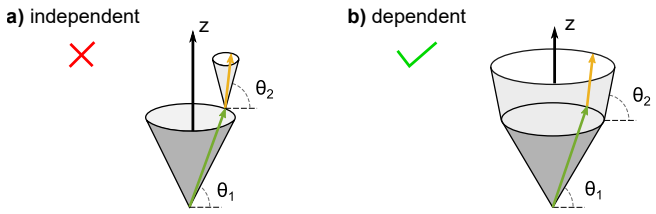

Fig. 3.19.: Comparison of (a) independent and (b) dependent orientations of both transition dipoles.

peaks in the histogram indicate that the peak width is an estimate of the overall uncertainty of our orientation determination method. The mean fit values $\theta_1 = 58 \pm 2°$ and $\theta_2 = 72 \pm 1°$ reveal that the out-of-plane orientations of both transitions differ by 14°. This result is consistent among all color-coded monolayers, as shown by the correlation plots of θ_1 and θ_2 at the bottom of Figure 3.18. The in-plane preferential directions $\phi_{0,1} = 72 \pm 7°$ and $\phi_{0,2} = 75 \pm 8°$ of both transitions are equal within the error, supported by the strong correlation found in the scatter plot for all monolayers. The in-plane orientation is uniform within each monolayer but significantly varies across different monolayers. We conclude that each monolayer has an intrinsic preferential direction imposed during chemical synthesis. Due to our random deposition method, each monolayer orientation on the substrate is equally probable. Hence, the point clouds for all monolayers are well separated in the correlation plot. Finally, the anisotropy values $a_1 = 0.11 \pm 0.04$ and $a_2 = 0.13 \pm 0.04$ are uniform among all monolayers and both transitions. All monolayers display a strong correlation between a_1 and a_2.

Our analysis demonstrates that our cone-shaped dipole distribution model with preferential direction can explain the measured data well. However, we did not make an assumption about how the cones of both transitions are related. Figure 3.19 compares two possible scenarios. In sketch (a), the two cones sit on top of each other, meaning that the in-plane orientations of both transition dipoles are independent. However, this is not consistent with our fit results, which demonstrate that the in-plane orientations and anisotropy values of both transitions are identical within the error. This strong correlation indicates that the direction of one transition dipole determines the orientation of the other, as visualized by the two interconnected cone surfaces in sketch (b). We conclude that both transition dipoles lie in the plane defined by the aromatic system of each molecule (compare the structural formula in Figure 3.1). Knowing the orientation of a single transition dipole is not enough to specify the three-dimensional orientation of the emitting molecule, as the molecule can rotate around the dipole direction. However, the independent orientation determination of two transition dipoles can provide this third degree of freedom. Hence, our method for independent orientation determination of multiple transition dipoles paves the way to determine the three-dimensional orientations of entire molecules and not only their transition dipole orientations. This requires additional information about the relative orientation of the transition dipoles with respect to the molecule backbone, which could be obtained, e.g., by density functional calculations [152].

The constant in-plane preferential direction across the $\sim 10\,\mu$m large monolayers reveals a long-range orientational order of the dye. We expect this orientation to form spontaneously during synthesis in solution. However, the intermediate values of the anisotropy $a \approx 0.1$

show that not all molecules are oriented in the same direction. We expect the aliphatic C_{16} chain attached to the dye (see Figure 3.1) to prevent a macroscopic ordering of the molecules. Instead, we believe that the molecules cluster in strictly ordered domains which almost average out within our optical resolution. The domains interact with each other by steric and electrostatic effects and therefore maintain a single preferential direction over long distances. The broad fluorescence spectra suggest that the molecules do not form J- or H-aggregates [67].

At some small areas inside the monolayers, the in-plane angles and anisotropy values slightly differ from the uniform distribution discussed up to now. A comparison with the fluorescence map in Figure 3.14a shows that the areas correlate with brighter or darker fluorescence intensities. The AFM topography of an exemplary monolayer and bilayer on the sample (see Figure 3.14b) also reveals patches with lower and higher topography matching the height of single hectorite nanosheets. Our optical measurements mainly average over these small areas due to the diffraction limit. We expect that these topography features correlate with the observed variations in fluorescence intensity and dipole orientation, suggesting slight variations in dye packing density at these positions. Note that the strong electrostatic bonding of the dye molecules to the clay surface does not allow the dye to detach. Furthermore, powder x-ray diffraction (PXRD) measurements as an independent method prove that the height of the dye layer is uniform on the scale of the PXRD focus volume with about 50 nm edge length.

In conclusion, we presented a powerful technique to disentangle the transition dipole orientations with diffraction-limited spatial resolution. Despite the simplicity of the experimental setup, a thorough analysis of the polarization-resolved fluorescence spectra allowed us to gain detailed information about the local structure. Based on a fundamental microscopic understanding, we developed a comprehensible dipole orientation model for the molecules embedded in the hectorite nanosheets. Our method revealed previously unattainable insights about the long-range orientational order and the strong correlation between both transition dipole orientations. The presented method can, in principle, be universally applied to all emitters down to the single-molecule limit.

3.4 Increased orientation anisotropy of the dye monolayer on gold substrates

Up to now, we have presented the orientation anisotropy of the dye monolayer on a dielectric substrate. For coupling with plasmonic nanoresonators in Chapter 5, the dye monolayer is dropcasted onto a gold substrate. Precise knowledge of the dipole orientations is crucial to understand the interaction with the nanostructures. As electrostatic interactions can alter the molecule orientation, we apply the orientation imaging technique to the dye monolayer on gold substrates. We use the template-stripping method to prepare smooth gold substrates [15]. A silicon wafer with a 300 nm oxide layer purchased from MicroChemicals is thoroughly cleaned by sonication in acetone and isopropanol. Then, a 50 nm thick gold film is thermally evaporated onto the wafer at a slow rate of 0.12 nm/s. Afterwards, glass slides are glued onto the gold film with UV-curable adhesive (NOA 81,

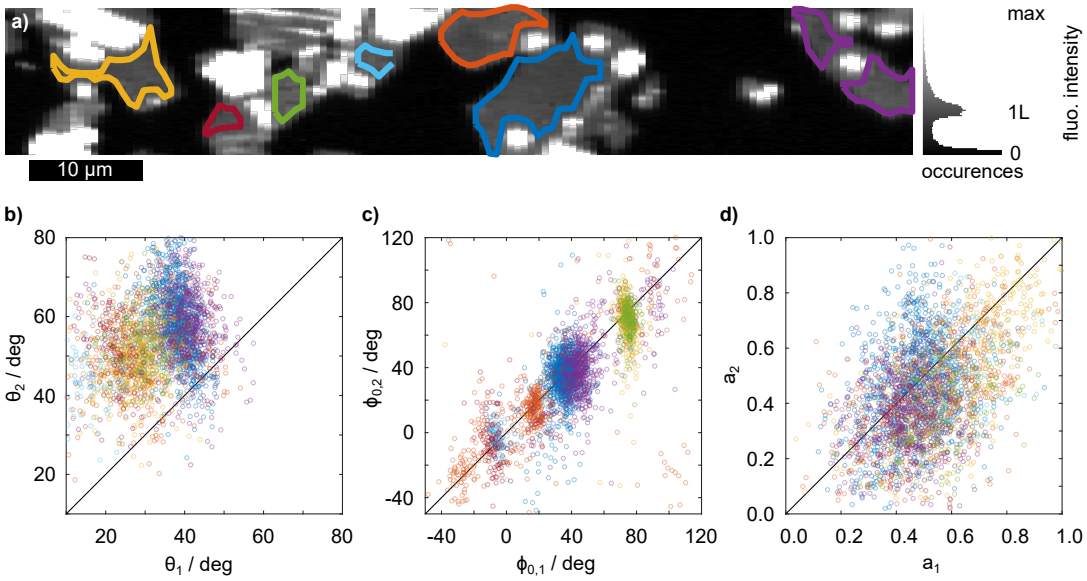

Fig. 3.20.: (a) The spectrally integrated fluorescence map of hectorite double stacks on a gold substrate reveals a discrete monolayer emission intensity. The correlation of the (b) out-of-plane orientation, (c) in-plane preferential direction, and (d) anisotropy of both transitions are shown in the scatter plot. Every data point represents a single position in the color-coded monolayer in (a).

Norland). The slides are peeled off on demand and made hydrophilic using low-pressure oxygen plasma (Zepto Q Spezial, Diener electronic) at 0.7 mbar using 50 W power for 1 minute. With the same procedure as for the glass substrate, the hectorite double stacks are then dropcasted onto the gold substrate, dried at room temperature, and baked at 100 °C for 12 hours to remove residual water. More information about gold substrate fabrication can be found in Chapter 4.1.2.

For the optical experiments, we use an excitation power of about 1 µW and an integration time of 8 s per camera frame. The singular value decomposition of the entire dataset again yields two dominant spectral contributions. Compared to the results on the glass substrate, the low-energy transition is slightly blue-shifted. We attribute this to the quenching on gold, which competes with the planarization of the dye upon excitation. This competition will be discussed in more detail in Chapter 3.5. Figure 3.20a shows the spectrally integrated fluorescence intensity map. The intensity histogram confirms that the monolayer fluorescence intensity is again very discrete and allows precise localization of the monolayers. The colored lines visualize their boundaries. The brighter areas indicate multiple stacked dye layers which are not further investigated.

The molecule orientation of the dye monolayer is primarily defined by the hectorite nanosheets during synthesis. Therefore, we apply the same cone-shaped orientation model with preferential direction as on the glass substrate. In the transfer matrix calculations, we embed the dipoles in the center of a 4 nm thick hectorite layer with $n = 1.5$ on a gold substrate using the dielectric function from Johnson and Christy [51] at $\lambda = 600$ nm. The transfer matrix calculations are fitted to the measured data at every point on the sample to obtain the orientation parameters for both transitions individually. In the following,

we exclude points within the monolayers where the least-squares fitting encounters a singular matrix. Figure 3.20b-d shows the respective correlations of the out-of-plane angle θ, in-plane angle ϕ_0, and anisotropy a of both transition dipoles.

Similar to our previous results on the glass substrate, the anisotropy values and in-plane angles strongly correlate. Each monolayer has an individual in-plane orientation given by the random deposition on the substrate. Hence, the preferential directions of each monolayer are localized as individual point clouds along the identity $\phi_{0,1} = \phi_{0,2}$ in the scatter plot. In contrast to the previous findings, however, the out-of-plane angle varies among the investigated monolayers while θ_1 and θ_2 are still correlated. Generally, the out-of-plane angles $\theta_1 \sim 40°$ and $\theta_2 \sim 60°$ are significantly smaller than on the glass substrate, suggesting that the dye layer is squeezed on the gold substrate. At the same time, the mean anisotropy is about 0.5, much larger than $a \approx 0.1$ on the glass substrate. For comparison, imagine a bunch of flowers that is squeezed from the top. In this example, the out-of-plane angle of the flowers would decrease, but the anisotropy would be conserved. This suggests that besides squeezing, the molecules in the hectorite perform additional rearrangements after being deposited on the substrate. Nevertheless, the area density of the dye molecules is determined by the hectorite during synthesis and is independent of the substrate. Hence, we conclude that the densely packed molecules in the dye monolayer can only be compressed further if the molecules get more aligned with each other.

Figure 3.21 compares the fit parameters of the glass and gold substrate for both transitions in a histogram. The results from all individual monolayers are added up for better visibility. To compare the in-plane preferential directions, we subtracted the median in-plane angles of the respective monolayers from each fit value ϕ_0. Generally, the fit parameter distributions of a and θ are broader on gold than on glass. We attribute this to the lower signal-to-noise ratio of the measurements on gold due to the significant fluorescence quenching. Furthermore, the compression of the dye monolayer might introduce more variations within each monolayer as local inhomogeneities are amplified. In contrast, the in-plane angle distribution $\phi_{0,1}$ is narrower than on glass, as the larger anisotropy allows a more precise determination of the preferential orientation.

Our hypothesis that the dye layer is squeezed on the gold substrate can be verified by AFM topography measurements in peak-force mode. Figure 3.22 shows the topography of hectorite double stacks on different substrates and baking conditions. Specifically, we compare glass, gold, and indium tin oxide (ITO) coated glass cover slips (VisionTek, $70 - 100\,\Omega$/sq with a nominal thickness of 30 nm). Gold and ITO substrates were plasma-treated before the hectorite deposition. AFM measurements at different positions on the glass and gold substrates prove the repeatability of the measurements and the homogeneity of the samples. Furthermore, all AFM measurements were conducted at the same ambient conditions to rule out temperature- and humidity-dependent swelling and water layer formations.

As shown by the AFM topography scans and corresponding histograms in Figure 3.22, the thickness of the hectorite double stacks at a baking temperature of 100 °C on the gold substrate (3.3 nm) is significantly smaller than on the glass substrate (4.3 nm). To obtain the height of the dye monolayer, we need to subtract the 2×1 nm height of the two hectorite nanosheets and the ~ 0.2 nm height of the water monolayer [153] on top of the hectorite double stacks at ambient conditions (see sketches in Figure 3.21). We find that the height

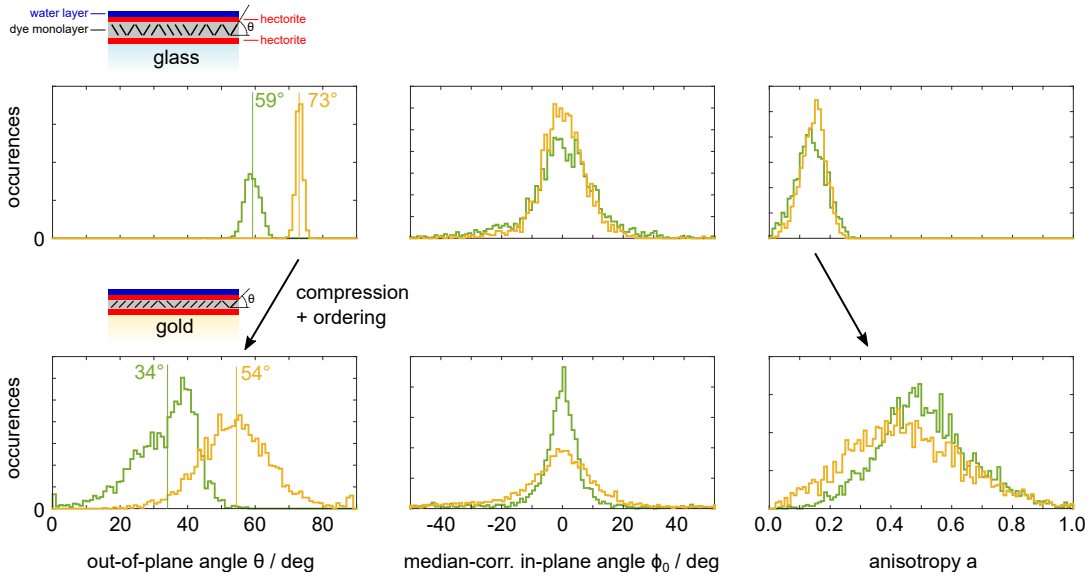

Fig. 3.21.: Fit result histograms of all investigated hectorite monolayers on glass (top) and gold substrates (bottom), comparing out-of-plane angle (left), in-plane angle (center), and anisotropy (right) of both color-coded transitions. We subtracted the median in-plane angle of the respective monolayer from each individual in-plane angle. We conclude that the dye layer on gold is more compressed, as shown by the sketch in the insets and the black arrows, leading to a decrease in θ and an increase in a.

of the dye monolayer shrinks by a factor of 2, from $(4.3-2.2)\,\mathrm{nm} = 2.1\,\mathrm{nm}$ on glass to $(3.3-2.2)\,\mathrm{nm} = 1.1\,\mathrm{nm}$ on gold. At the same time, the optical measurements reveal that the average out-of-plane angle of the first transition decreases from 59° on glass to 34° on gold. Assuming rigid rod-shaped molecules, the height of the dye monolayer is determined by the projection $\sin\theta$ onto the vertical axis. The height ratio on both substrates is, thus, $\sin(58°)/\sin(35°) \approx 1.5$. Hence, the optical measurements suggest that the height of the dye monolayer shrinks by a factor of 1.5 between glass and gold substrates, while the AFM measurements predict a factor of $2.1/1.1 = 1.9$. However, we must consider that the alkyl chain attached to the chromophore is flexible and not rigid as we assumed in the simple comparison. Hence, the AFM and optical measurements yield very similar results, supporting our claim of substrate-dependent molecule rearrangements.

As already discussed, the dye layer is densely packed within the hectorite nanosheets. Nevertheless, the aliphatic chain attached to the chromophoric part of the dye might allow further compression after reorientation and ordering of the molecules. The image charges provided by the gold substrate might provide a sufficient electrostatic force to rearrange the molecules. Comparative measurements on an ITO substrate suggest an even smaller thickness of the hectorite double stack on this substrate, around 3 nm (see Figure 3.22d). Since the ITO layer is conductive, this finding might prove that electrostatic interactions contribute to molecule rearrangements.

As a second comparative measurement, we lowered the baking temperature on the gold substrate to 60°C (see Figure 3.22b). To reduce the surface roughness of the gold film, we evaporated a 100 nm thick gold film on a silicon wafer. Then, we used a different

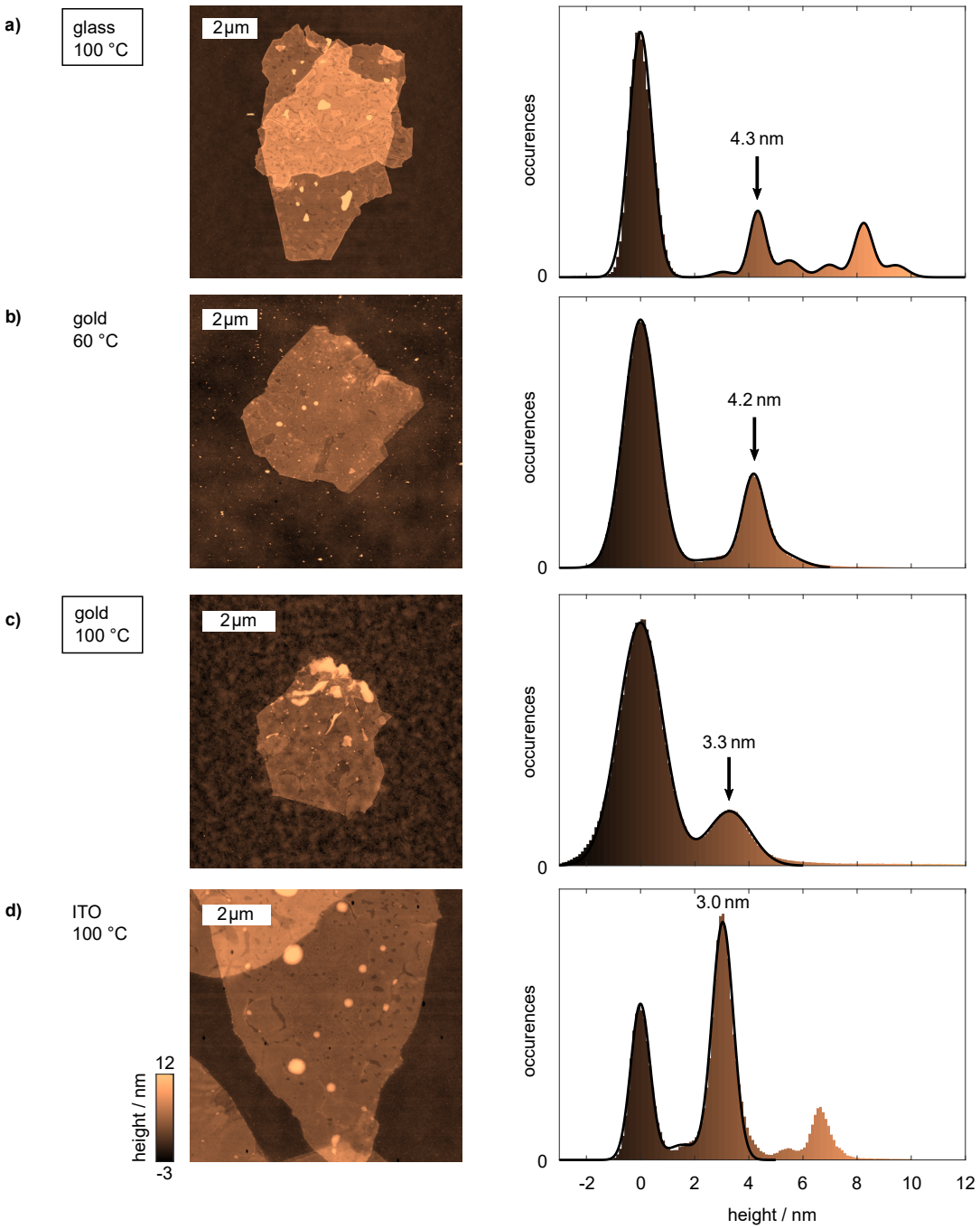

Fig. 3.22.: AFM topography scans of hectorite double stacks on a glass substrate, template-stripped gold substrates, and an ITO substrate after different baking temperatures. The histograms prove that the height of the structures is impacted by both temperature and substrate type. The arrows indicate the respective monolayer heights retrieved from Gaussian fits. Samples (a) and (c) were investigated by the optical orientation determination method.

UV-curable glue (Norland NOA63 instead of NOA81) for the template stripping and air plasma instead of oxygen plasma in the sample preparation. Consequently, the peaks in the histograms are more narrow, while the general properties of the gold substrate remain unchanged. At the lower baking temperature, the hectorite double stack thickness of 4.2 nm matches our results on glass. We conclude that the molecule reorientation might require a specific activation energy which can be overcome by the thermal energy provided by the baking step. In addition, our results indicate that the conductivity of the substrate facilitates the molecule rearrangement. This claim is further supported by PXRD measurements showing that solely a temperature change in the interval 60 . . . 220°C on a dielectric substrate does not impact the double stack height. To gain a deeper understanding, we propose future AFM measurements on an individual hectorite double stack while increasing the baking temperature step-wise. We expect a decrease in the double stack thickness after exceeding a certain transition temperature. It has also been demonstrated in the literature that electric fields can induce phase transitions in molecule monolayers [154]. Furthermore, molecular dynamics simulations could complement the experimental findings [155].

3.5 Orientation- and distance-dependent fluorescence quenching of dye layers on gold

The photophysics of emitters significantly changes as a function of the dipole orientation and its distance to a conductive interface. In contrast to a perfect mirror, the gold substrate features non-radiative decay pathways, such as the generation of surface plasmons propagating along the interface and dissipation as heat. Consequently, the spontaneous emission rate can be orders of magnitude larger than in free space. The fluorescence lifetime of typical dyes in free space is some nanoseconds and decreases to a few picoseconds at metal interfaces [24]. The excited state planarization of the pyrene derivative dye used in this work also happens on the picosecond timescale, as reported for the dye in different solvents [140]. Hence, we expect to observe a competition between spontaneous emission and molecule rearrangements in the experiment.

The investigated dye layers feature two transitions, where the high-energy fluorescence is emitted from the excited state. The low-energy fluorescence is only emitted after molecule planarization. Hence, the fluorescence intensity ratios of both transitions serve as a probe for the spontaneous emission rate with respect to the planarization rate. The intensity ratios are obtained from the ratio of SVD expansion coefficients c_1/c_2. We multiply the coefficients by the integral over their resonance spectra $\boldsymbol{f}_1$ and $\boldsymbol{f}_2$ to compare the total power radiated from both transitions. Figure 3.23b shows the spatial variations of the ratio in the investigated area on the gold substrate. A comparison with the fluorescence intensity map in (a) demonstrates that the intensity ratio is significantly larger on monolayers ($c_1/c_2 \approx 2.5$) than on multilayers ($c_1/c_2 \approx 1$). Monolayers and multilayers have distinct peaks in the histogram.

Furthermore, Figure 3.24a shows a scatter plot of c_1/c_2 as a function of the out-of-plane angle θ_1, color-coded for all investigated monolayers. The variations within each monolayer

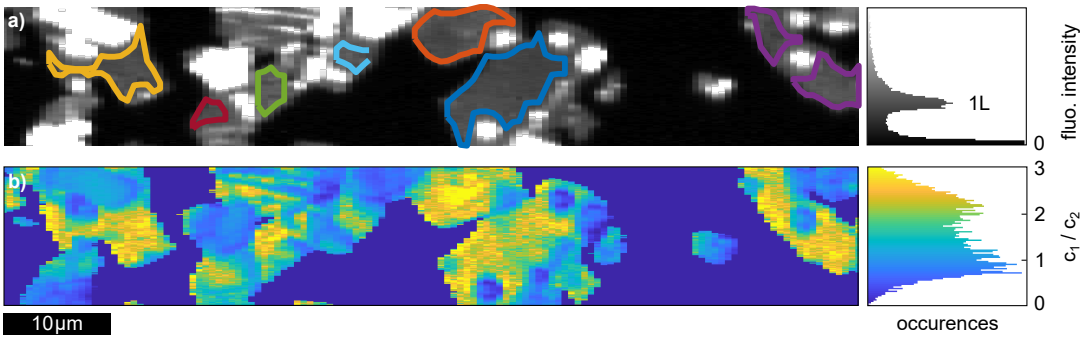

Fig. 3.23.: The fluorescence intensity map in (a) strongly correlates with the map of the c_1/c_2 ratio in (b). Monolayers have significantly larger c_1/c_2 ratios than multilayers. Non-fluorescent areas are colored dark blue on the map and are excluded from the histogram on the right.

are relatively large. Nevertheless, the mean values of each monolayer indicate that the intensity ratio increases with the out-of-plane orientation of the molecules. To compare these findings with the theory, we calculated the spontaneous emission rate of a single dipole in the center of a 4nm thick dielectric ($n = 1.5$) above a gold substrate in the transfer matrix formalism (see Chapter 3.1.5). Figure 3.24b plots the computed γ/γ_0 against the out-of-plane angle θ of the dipole. The spontaneous emission rate enhancement increases from about 1,200 to 2,000, comparing in-plane and out-of-plane dipoles. The in-plane dipole radiates less efficiently as it couples with the antiparallel image dipole in the gold substrate.

The larger the spontaneous emission rate, the smaller the timescale between absorption and emission. Consequently, there is less time for the molecule to planarize before emitting a fluorescence photon. Most of the emission will then originate from the high-energy transition, corresponding to a larger ratio c_1/c_2. This theoretical consideration qualitatively explains our experimental finding that the intensity ratio c_1/c_2 increases with the out-of-plane angle θ_1. A quantitative comparison would require detailed information about the excited state dynamics in the confined environment. Femtosecond transient absorption spectroscopy measurements of the pyrene-derivative dye in solution have demonstrated that the timescale of the molecule excited state planarization combined with the solvation is a few picoseconds, depending on the polarity of the solvent [140]. These results in solution are not directly applicable to the dyes encapsulated in the hectorite nanosheets, as the confinement might suppress conformational changes. Nevertheless, our results indicate that the molecule planarization competes with the enhanced spontaneous emission rate of the dyes on the gold substrate.

Our argumentation is supported by the drastically reduced c_1/c_2 ratio of multiple stacked dye layers, as shown in Figure 3.23 and the associated histogram. Transfer matrix calculations suggest that the spontaneous emission rate of a dipole in the center of the second layer has a more than 20 times lower spontaneous emission rate than in the monolayer (see Figure 3.24b). Note that this curve has been amplified by a factor of 20 for easier comparison with the monolayer. At the same time, the quantum efficiency of a dipole in the second layer is more than 20 times higher than in the first layer due to the larger distance from the dissipative gold substrate. Hence, most of the measured fluorescence

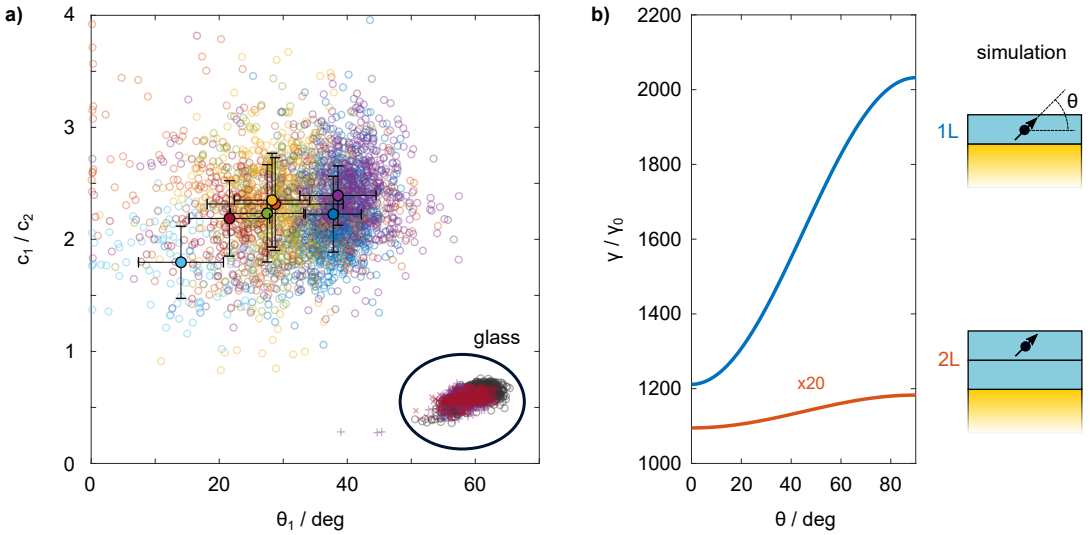

Fig. 3.24.: (a) Correlation between the ratio c_1/c_2 and the out-of-plane angle θ_1 for every measured point in the monolayer on the gold substrate. The colors match the monolayer outlines in Figure 3.20a. As shown by the mean values and their standard deviation, the ratio increases with θ_1 and generally has larger values than the monolayers on glass. (b) The computed spontaneous emission rate of a single dipole above a gold substrate increases with the out-of-plane angle. As sketched on the right, we compare a dipole in a monolayer (1L) and in a double layer (2L, amplified by a factor of 20).

from a double-layer structure (2L) comes from the top layer. The reduced spontaneous emission rate and the higher quantum efficiency of multilayers explain the smaller ratio $c_1/c_2 \approx 1$ in the measurements. In comparison, the spontaneous emission enhancement of dyes on a glass substrate is close to unity. Consequently, the ratio $c_1/c_2 \approx 0.5$ is even smaller, as shown in Figure 3.24a.

In conclusion, we qualitatively demonstrated that the fluorescence intensity ratio of both transitions c_1/c_2 acts as a clock for the spontaneous emission rate relative to the molecule planarization dynamics. Numerical simulations on the excited state dynamics of the confined dye monolayer are required for quantitative comparisons. In principle, the knowledge of the planarization time constant allows probing the spontaneous emission rate on the picosecond scale by measuring time-averaged intensity ratios only.

Plasmonic nanoresonators: Nanoparticles on mirror

4

The previous chapter discussed the orientation- and position-dependent radiation from emitter layers in planar environments. We found that the dielectric environment significantly impacts the photophysics of emitters. Hence, clever engineering of the local environment of emitters introduces many setscrews to tune the radiation in the spatial, spectral, and temporal domains.

The localized surface plasmon resonances in metallic nanostructures provide large electric field enhancements on a sub-wavelength scale. Therefore, the field of plasmonics has gained a lot of interest in the past decades [10, 11, 156]. The commercialization of electron-beam lithography (EBL) and focused ion-beam milling (FIB) paved the way for the accurate fabrication of plasmonic nanostructures with high resolution on large areas. The size and shape of individual disks, rods, triangles, etc., offer tunability of the plasmon resonance over a wide spectral range [4]. In particular, dimers and multimers formed from multiple interacting nanostructures introduce many degrees of freedom to control the resonance energy and the coupling to far-field radiation. Modes of the individual particles hybridize to create bonding and anti-bonding modes [157, 158]. Furthermore, it was found that the interference of spectrally broad and narrow modes gives rise to Fano resonances which provide, for example, spectrally very narrow transmission features for sensing applications [159, 160].

Most interestingly, nanosphere dimers and bowtie nanoantennas possess superior confinement of the electromagnetic energy with enhancements of the near-field intensity of more than 10^3 [9]. The gap size is, however, limited by the resolution of the fabrication method, which is between 10 and 20 nm for EBL or gallium ion beam milling and about 5 nm for helium ion beam milling [6, 7]. Fabrication methods based on the self-assembly of gold nanoparticles facilitate sub-nanometer gap widths but typically lack control over the exact gap size and the incorporation of emitters into the cavity [85]. As an alternative to these complex and limited approaches, the nanoparticle-on-mirror (NPoM) geometry has been extensively studied in recent years [10–13]. Here, colloidal metal nanoparticles are placed on top of an ultrasmooth metal substrate. In contrast to lithographically fabricated nanostructures, the crystallinity and size of chemically grown metallic nanoparticles can be accurately controlled [8]. Furthermore, metallic substrates with low surface roughness can be fabricated by template stripping [15]. The bottom-up approach enables a simple and step-wise fabrication of the NPoM samples. The gap size between particle and film can be precisely determined by the deposition of ultrathin materials onto the metal film [16, 161]. For example, sub-nanometer gaps provided by single graphene layers allow entering the quantum tunneling regime [20]. Ultimately, the nonlocality of the metal dielectric function limits the field enhancement [19]. Furthermore, individual atomic features can form tiny cavities with picometer separation [17, 18].

In this chapter, we study the optical properties of nanoparticle-on-mirror systems. The resonances of the NPoMs strongly depend on the morphology, size, and dielectric properties of the nano-sized gap. Thus, accurate theoretical modeling is required to understand the resonances in the experiment and their variations. We decompose the optical response of NPoMs into their fundamental modes using finite element numerical simulations. We classify the modes based on the symmetry of their electric near-field. Using the inherent relation between optical near-field and far-field, we calculate the radiation patterns and the corresponding polarization-dependent point-spread functions of each mode. The computed resonances and point spread functions are compared with a large number NPoMs in the experiment as a function of the gap size. A fundamental understanding of the optical response will be required in Chapter 5 to characterize the coupling of a dye monolayer with the NPoM.

4.1 Sample fabrication

The reproducible fabrication of high-quality nanoparticle-on-mirror structures with dielectric spacers requires a high level of control over all fabrication steps. In this section, we characterize the colloidal gold nanoparticles. Furthermore, we discuss the fabrication of ultrasmooth gold substrates and the subsequent deposition of thin dielectric spacers. Finally, we introduce the polarization-dependent scattering of the prepared NPoM structures.

4.1.1 Characterization of the colloidal gold nanoparticles

Colloidal gold nanoparticles with 80 nm diameter are purchased from two manufacturers (Accurate Spherical Gold Nanoparticles, Nanopartz, and gold colloids, BBI Solutions). The nanoparticles are surrounded by capping agents to increase the stability of the solution. Due to the absorption in the visible range, the concentrated aqueous solution has a dark red color in transmission. The morphology of the nanoparticles is determined by scanning electron microscopy (Leo 1530, Zeiss) located in the KeyLab Electron and Optical Microscopy at the BPI Bayreuth. The nanoparticle solutions are dropcasted onto a cleaned glass cover slip and dried at room temperature for SEM analysis. Due to the high concentration, the nanoparticles form aggregates, allowing imaging of many nanoparticles in a single scan. The sample is sputtered with a thin conductive platinum layer. SEM images were acquired with an acceleration voltage of 3 kV using the SE2 detector.

Figure 4.1 compares the morphology of the 80 nm nanoparticles obtained from (a) BBI Solutions and (b) Nanopartz. Most noble metals, including gold, have a face-centered cubic crystalline lattice. Growth of the nanoparticles from single-crystal seeds yields faceted crystals with different macroscopic shapes. Typically shapes are cuboctahedrons, rhombicuboctahedrons, and pentagonal bipyramids [162]. Truncation during growth may produce different nanoparticle shapes [163]. Different crystal facets can be observed in the SEM image of the BBI nanoparticles, indicating a high degree of crystallinity. In comparison, the nanoparticles obtained from Nanopartz are very monodisperse and have a

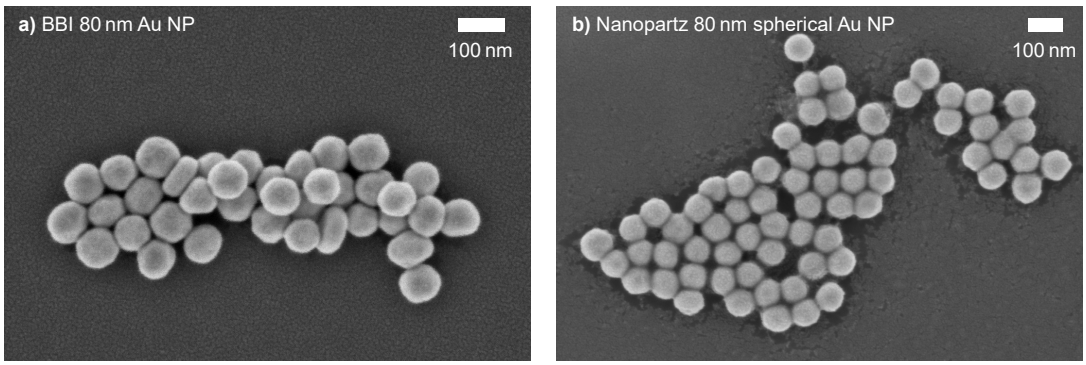

Fig. 4.1.: Scanning electron microscope (SEM) image of 80 nm gold nanoparticle aggregates obtained from (a) BBI Solutions and (b) Nanopartz on glass cover slips. The crystal faces are clearly observable.

more spherical shape. Nevertheless, crystal facets are still apparent from the nanoparticle contour.

X-ray scattering methods could provide quantitative information about the crystallinity of the gold nanoparticles [164]. Furthermore, transmission electron microscopy would allow determining the shape and size of the gold nanoparticles with high resolution. In the context of this work, however, it is sufficient to know that the morphology of the nanoparticles varies. As we show later by numerical calculations, variations in the nanoparticle shape give rise to spectral shifts of the NPoM resonances. The literature indicates that more spherical nanoparticles reduce these spectral variations between different NPoMs [165]. Therefore, we use the gold nanoparticles from Nanopartz with more rounded facet edges in the following to fabricate NPoM systems.

4.1.2 Ultrasmooth gold substrates obtained from template stripping

The surface roughness of the underlying gold substrate also impacts the performance of NPoM resonators. First, surface roughness generates unwanted scattering from the substrate, which increases the background signal and might even interfere with the optical response of the investigated NPoM [166]. Second, the surface roughness alters the morphology of the gap in a non-deterministic way, making the optical response of the NPoM less reproducible. Specifically, the spectral positions of the resonances can shift significantly [167].

Thermally evaporated gold films have a rough surface with typical 5-10 nm peak-to-valley variations on a lateral scale of only tens of nanometers. These variations are large compared with the desired distances of only few nanometers between the gold substrate and gold nanoparticle. Ultrasmooth gold substrates can be routinely prepared by template stripping [15]. Here, the gold film is thermally evaporated[1] at a low rate of 0.12 nm/s onto an atomically flat template (silicon wafer with 300 nm oxide layer, MicroChemicals

[1]Thermal evaporation by Jonas Mayer and Adrian Hochgesang from Prof. Thelakkat's group (Macromolecular Chemistry I, University of Bayreuth).

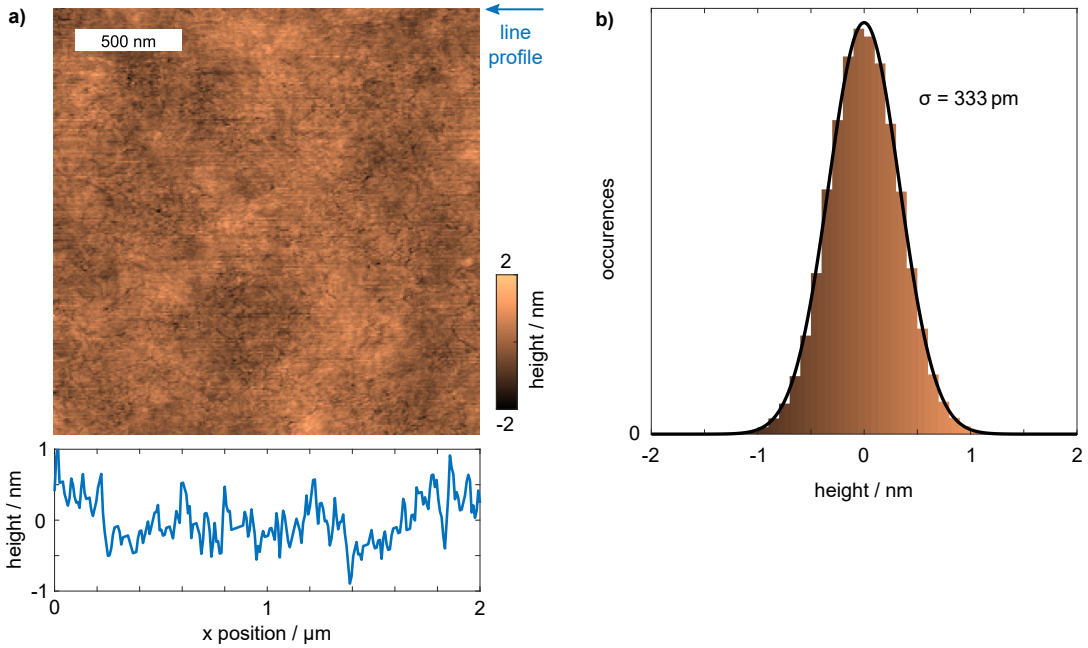

Fig. 4.2.: AFM characterization of the fabricated template-stripped gold film at an exemplary position. (a) $2 \times 2\,\mu$m AFM topography scan. The line profile at the position indicated by the blue arrow reveals height variations on the order of only 1 nm. (b) The height distribution is fitted by a Gaussian distribution (black line), revealing an RMS surface roughness of $\sigma = 333$ pm.

GmbH) which has been thoroughly cleaned with water and isopropanol in the ultrasonic bath. As a result, the bottom of the evaporated gold film is very smooth. A transparent substrate is glued onto the gold film in the second step. We use UV-curable glue (NOA 81, Norland) and a cleaned 1 mm thick glass slide that is transparent for ultraviolet light. After curing, the adhesion of the gold film to the silicon template is much smaller than to the glued glass substrate. Therefore, mechanical cleaving of the substrate with a scalpel exposes an ultrasmooth gold film which we use as a substrate for the NPoMs.

Figure 4.2a shows a $2 \times 2\,\mu$m AFM topography scan of the gold surface obtained by template stripping at an exemplary position. The raw data were flattened line-by-line with a linear function. The surface is exceptionally smooth on a lateral scale of micrometers. As shown by the line profile, the height variations are on the order of 1 nm peak-to-valley. The fit of the height histogram to a Gaussian function reveals a root-mean-square (RMS) roughness of only $\sigma = 333$ pm (see Figure 4.2b). The measurement at two other positions on the sample yields RMS values of 351 pm and 436 pm. These results are comparable to the 200 pm roughness reported in the literature, which was determined in a much smaller area of only 500×500 nm [15]. For comparison, gold has a face-centered cubic crystal lattice with lattice constant $a = 4.08$ Å [49]. Notably, our measured surface roughness is similar to the atom separation of $a/\sqrt{2} = 289$ pm in the gold crystal.

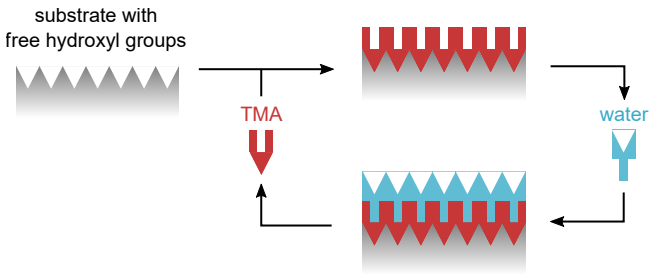

Fig. 4.3.: Simplified sketch of Al_2O_3 thin film formation by atomic layer deposition from the precursors TMA and water. In each cycle, the two chemicals are introduced into the reaction chamber one after another. The surface reaction is self-terminating.

4.1.3 Controlled growth of ultrathin dielectric layers by atomic layer deposition (ALD)

Atomic layer deposition (ALD) is an established technique to deposit a wide range of materials with sub-nanometer thickness control. The process is based on chemical reactions between precursor chemicals, thus enabling a complete surface coverage of the desired sample [168]. We use ALD to deposit thin alumina layers (Al_2O_3) onto the template-stripped gold substrates. The oxide layer then acts as a dielectric spacer to tune the gap thickness of the NPoM with high precision. The precursor materials for alumina are trimethylaluminium (TMA) and water. We use a commercial device for ALD (Savannah, Ultratech/Cambridge NanoTech) at the KeyLab Device Engineering at the University of Bayreuth.

The process is conducted in a reaction chamber at 80 °C and a base pressure of 0.5 Torr. At first, TMA is introduced into the chamber in a short 15 ms pulse and reacts with hydroxyl groups on the surface of the substrate (see Figure 4.3). The reaction terminates when all reaction sites on the surface are occupied. After purging the reaction chamber with gaseous argon for 10 s, the second precursor, water, is introduced. The water molecules react with the TMA, leaving free hydroxyl groups on the surface. Therefore, ALD is a cyclic process where the thickness of the deposited surface linearly scales with the number of cycles. The calibrated thickness of deposited alumina per cycle is 0.75 Å.

4.1.4 Polarization-dependent scattering from NPoMs

After depositing oxide layers onto the template-stripped gold substrate, we dropcast the aqueous gold nanoparticle solution onto the sample. The nanoparticles which are close to the substrate will adhere to the surface. After some minutes, the residual droplet is blown off the substrate with nitrogen. The time between dropcast and blow-off determines the average spatial separation between the nanoparticles. Good surface coverage is achieved when the separation between neighboring nanoparticles is a few micrometers, well above the diffraction limit.

As an introduction to the optical properties of NPoMs, we briefly discuss their polarization-dependent scattering on a phenomenological level. The optical setup will be presented

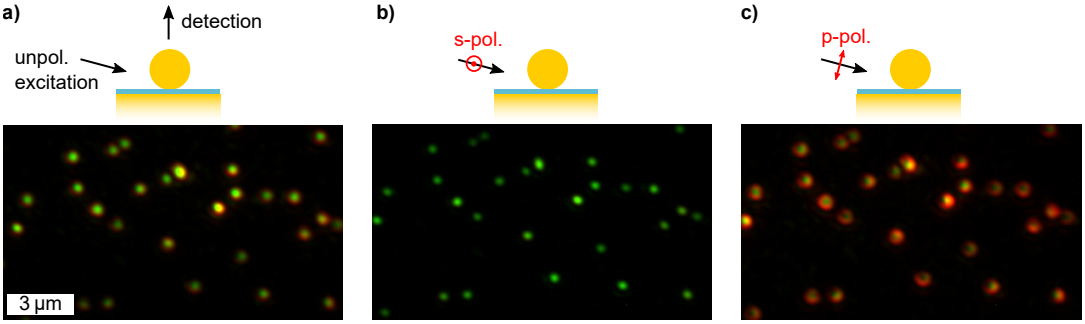

Fig. 4.4.: Scattering images of NPoMs with 2 nm dielectric spacer, obtained by white light illumination at almost grazing incidence and detection with a microscope objective and a color camera. Compared are (a) unpolarized, (b) s-polarized, and (c) p-polarized excitation.

in more detail in Chapter 4.4.1. For now, we illuminate the sample at an almost grazing incidence with white light, as sketched in the insets of Figure 4.4. We collect the scattered light from the top using a microscope objective with a high numerical aperture, while the excitation light misses the objective aperture. The light is imaged with a color CMOS camera. The colored spots in the images show individual 70 nm gold nanoparticles (Nanopartz) on a gold substrate with a 2 nm alumina spacer. The images demonstrate that the excitation polarization allows switching between green and red scattering, where the red scattering is only observed at p-polarized excitation. Furthermore, the point-spread function of the red mode does not resemble the familiar Airy pattern. We conclude that the NPoM features a set of modes with different dipole orientations. To understand the emergence of these modes, their near- and far-field properties, and the dependence on the gap morphology, we introduce numerical simulations of NPoMs in the following section. This will allow comparing the theoretical expectations with experimental data in Chapter 4.4.

4.2 Numerical methods

Analytical solutions to Maxwell's equations can often be obtained in simple geometries. For example, the transfer matrix formalism presented in Chapter 3.1 is an analytic treatment of multilayered structures. Furthermore, the scattering theory developed by Gustav Mie provides an analytical solution to Maxwell's equations for spherical particles in homogeneous environments [55]. More complex geometries often require numerical solutions of Maxwell's equations. Common solvers operate in the time domain (e.g., finite-difference time domain, FDTD) or frequency domain (e.g., finite-element method, FEM) to calculate the optical response to incident electromagnetic waves [169]. These computations are very time-consuming since multiple calculations must be combined at different pulse lengths, frequencies, and polarization directions to obtain meaningful connections with experimental data like scattering spectra. Furthermore, the calculated spectra and electromagnetic field distributions might be challenging to interpret due to the interference of multiple fundamental modes of the investigated structure [66, 170]. Finally, simulations can never

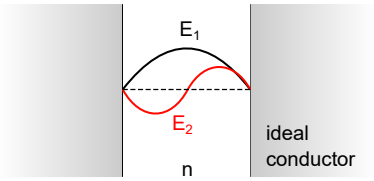

Fig. 4.5: Normal modes E_1 and E_2 of a cavity bounded by ideal conductors.

match the measured data quantitatively due to uncertainties in sample fabrication. Instead, numerical simulations often aim to develop a deep physical understanding of the investigated structure and for parameter optimization.

A low-level physical picture of any structure can be obtained by decomposing the material response into its natural modes with indices m. Each electromagnetic mode of the investigated plasmonic nanoresonators has an eigenfrequency $\tilde{\omega}_m = \Omega_m - \mathrm{i}\Gamma_m/2$ and features a certain electric field distribution $\boldsymbol{E}_m(\boldsymbol{r})$. Note that the eigenfrequencies are complex-valued in dissipative systems. The modes are calculated without an external electric field and are, therefore, independent of the experimental details. The modes form a complete orthonormal basis set for the specific geometry. After the computation, the optical response to a particular external impulse can be written as a sum over all modes with individual excitation coefficients $A_m(t)$ [170]. Using the $e^{-\mathrm{i}\omega t}$ convention, the measurable electric field in time and space reads

$$\boldsymbol{E}(\boldsymbol{r},t) = \mathrm{Re}\left[\sum_m A_m(t)\tilde{\boldsymbol{E}}_m(\boldsymbol{r})e^{-\mathrm{i}\Omega_m t}e^{-\Gamma_m t/2}\right] \tag{4.1}$$

with the spatial mode profile $\tilde{\boldsymbol{E}}_m(\boldsymbol{r})$. The mode-specific damping constant Γ_m enforces an exponential temporal decay of the electric field.

4.2.1 Quasi-normal modes (QNM) of open cavities

The decomposition into normal modes has widespread applications in physics. The most prominent example is the motion of coupled oscillators. The coupling of two harmonic oscillators gives rise to a symmetric and an antisymmetric mode with oscillators moving in the same and opposite directions, respectively. In optics, normal modes are frequently encountered in resonators like laser cavities, Fabry-Pérot etalons, dielectric microresonators, and plasmonic nanoresonators. The simplest example is a planar cavity with refractive index n and length L bounded by ideal conductors (see Figure 4.5). The boundary conditions imposed by Maxwell's equations require zero electric field strength at the cavity walls, corresponding to unity reflection coefficients. The normal modes are superpositions of waves traveling to the left and right. The resulting standing waves have equidistant real-valued frequencies

$$\omega_m = \frac{2\pi m c_0}{nL} \tag{4.2}$$

with $m = 1, 2, \ldots \infty$. The electric fields of the two lowest-energy modes are sketched in Figure 4.5.

In real-world systems, the refractive index inside and outside the cavity is finite, lowering the reflection coefficient r of the electric field at the cavity walls. The amplitude of the waves decreases at every reflection as part of the wave is absorbed or transmitted to the outside. The presence of a stationary state requires that the amplitude A of a traveling wave inside the cavity is recovered in each round trip [170]

$$A \stackrel{!}{=} Ar^2 e^{2iknL} \quad \Leftrightarrow \quad 1 - r^2(\tilde{\omega}_n) e^{2i\frac{\tilde{\omega}_m}{c} n(\tilde{\omega}_m) L} = 0 \quad . \tag{4.3}$$

If the cavity is leaky, i.e., $|r|^2 < 1$, and/or the cavity medium absorbs energy, i.e., $\mathrm{Im}[n(\tilde{\omega}_m)] > 0$, the steady state requirement can only be fulfilled with complex frequencies

$$\tilde{\omega}_m = \Omega_m - i\Gamma_m/2 \quad . \tag{4.4}$$

Hence, the imaginary part of the complex eigenfrequency amplifies the waves in the cavity to counteract the damping [170]. Notably, the electric field of a spherical wave radiated from a cavity mode has the form $e^{i(kr-\tilde{\omega}_m t)} \cdot r^{-1} = e^{i\tilde{\omega}_m(r/c-t)} \cdot r^{-1}$ and therefore diverges in space as $e^{\Gamma_m r/2c} \cdot r^{-1}$. This divergence has implications for the normalization of the QNMs discussed later in the text.

4.2.2 Auxiliary-field eigenvalue approach for QNM computation

The source-free Maxwell's equations for non-magnetic media in the frequency domain take the form of an eigenvalue problem [66]

$$\begin{pmatrix} 0 & -i\mu_0^{-1}\nabla\times \\ i\varepsilon^{-1}(\boldsymbol{r},\tilde{\omega}_m))\nabla\times & 0 \end{pmatrix} \begin{pmatrix} \tilde{\boldsymbol{H}}_m(\boldsymbol{r}) \\ \tilde{\boldsymbol{E}}_m(\boldsymbol{r}) \end{pmatrix} = \tilde{\omega}_m \begin{pmatrix} \tilde{\boldsymbol{H}}_m(\boldsymbol{r}) \\ \tilde{\boldsymbol{E}}_m(\boldsymbol{r}) \end{pmatrix} \tag{4.5}$$

with dielectric function $\varepsilon = \varepsilon_0\varepsilon_r$, eigenvalues $\tilde{\omega}_m$, and eigenvectors $\left(\tilde{\boldsymbol{H}}_m(\boldsymbol{r}), \tilde{\boldsymbol{E}}_m(\boldsymbol{r})\right)$. In the case of non-dispersive media, the permeability and permittivity are independent of the frequency, and the eigenvalue problem is linear. Robust and efficient solvers are implemented, for example, in the commercial software Comsol Multiphysics.

However, the NPoMs consist of gold nanostructures with a frequency-dependent dielectric function, introducing nonlinearities into the eigenvalue problem. A linearization is possible when decomposing the dielectric function into multiple Lorentzian poles. For demonstration, we limit ourselves to the single-pole Lorentzian function introduced in Chapter 2.1.1 and abbreviate $\varepsilon_\infty\varepsilon_0$ as ε_∞ to obtain

$$\varepsilon(\omega) = \varepsilon_\infty \left(1 + \frac{\omega_p^2}{\omega_0^2 - \omega^2 - i\gamma\omega}\right) \quad . \tag{4.6}$$

For linearization, we define two auxiliary fields, the polarization

$$\boldsymbol{P} = \varepsilon_\infty \frac{\omega_p^2}{\omega_0^2 - \omega^2 - i\gamma\omega} \boldsymbol{E} \quad , \tag{4.7}$$

and the current density

$$\boldsymbol{J} = -\mathrm{i}\omega\boldsymbol{P} \quad . \tag{4.8}$$

These definitions allow us to reformulate Equation 4.5 as the linear eigenvalue problem [66]

$$\begin{pmatrix} 0 & -\mathrm{i}\mu_0^{-1}\nabla\times & 0 & 0 \\ \mathrm{i}\varepsilon_\infty^{-1}\nabla\times & 0 & 0 & -\mathrm{i}\varepsilon_\infty^{-1} \\ 0 & 0 & 0 & \mathrm{i} \\ 0 & \mathrm{i}\omega_p^2\varepsilon_\infty & -i\omega_0^2 & -i\gamma \end{pmatrix} \begin{pmatrix} \tilde{\boldsymbol{H}}_m(\boldsymbol{r}) \\ \tilde{\boldsymbol{E}}_m(\boldsymbol{r}) \\ \tilde{\boldsymbol{P}}_m(\boldsymbol{r}) \\ \tilde{\boldsymbol{J}}_m(\boldsymbol{r}) \end{pmatrix} = \tilde{\omega}_m \begin{pmatrix} \tilde{\boldsymbol{H}}_m(\boldsymbol{r}) \\ \tilde{\boldsymbol{E}}_m(\boldsymbol{r}) \\ \tilde{\boldsymbol{P}}_m(\boldsymbol{r}) \\ \tilde{\boldsymbol{J}}_m(\boldsymbol{r}) \end{pmatrix} \quad . \tag{4.9}$$

This formulation can be generalized to n-pole Lorentzian dielectric functions by introducing n polarization $\boldsymbol{P}_n$ and current density vectors $\boldsymbol{J}_n$ and expanding the matrices accordingly. Consistent with the literature [45], we use the two-pole Lorentzian function with the parameters shown in Chapter 2.1.2 to model gold.

4.2.3 QNM computation in Comsol

We use the software package Comsol Multiphysics to solve Maxwell's equations with predefined boundary conditions. The software implements the finite element method (FEM), suitable for general time-harmonic systems with linear media described by partial differential equations. In our case, the spatial distribution of the electric and magnetic fields $\tilde{\boldsymbol{E}}_m(\boldsymbol{r})$ and $\tilde{\boldsymbol{H}}_m(\boldsymbol{r})$ are computed as solutions to the general source-free Maxwell's equations 4.5. The computation of the QNMs furthermore requires the determination of the complex-valued eigenfrequencies $\tilde{\omega}_m$.

In FEM simulations, the three-dimensional geometry is segmented into a mesh of small volume elements such as tetrahedra. The tetrahedras' size, shape, and orientation are optimized to represent curved objects and narrow structures precisely. The size of each element must always be much smaller than the wavelength. Each element represents the solution as a superposition of differentiable base functions that fulfill the boundary conditions. The solver optimizes the coefficients of these base functions in all volume elements to minimize the residues of Maxwell's equations [169].

As indicated above, the QNM fields diverge in space, preventing the normalization of the modes by conventional energy considerations [66, 170]. Nevertheless, a consistent normalization is essential for the computation of mode excitation coefficients for near-field coupling with emitters in Chapter 5. Fortunately, introducing perfectly matched layers (PMLs) around the finite simulation domain facilitates exponential damping of the QNM fields, rendering the modes square-integrable. Per definition, the boundary between simulation and PMLs does not reflect outgoing waves from the investigated nanostructures. The orthonormality condition of the QNMs can then be written as a volume integral over the entire model, including the finite simulation domain and the PMLs [66]

$$\iiint_\Omega \left[\varepsilon_\infty \tilde{\boldsymbol{E}}_i \cdot \tilde{\boldsymbol{E}}_j - \mu_0 \tilde{\boldsymbol{H}}_i \cdot \tilde{\boldsymbol{H}}_j + \frac{\omega_0^2}{\varepsilon_\infty \omega_p^2} \tilde{\boldsymbol{P}}_i \cdot \tilde{\boldsymbol{P}}_j - \frac{1}{\varepsilon_\infty \omega_p^2} \tilde{\boldsymbol{J}}_i \tilde{\boldsymbol{J}}_j \right] \mathrm{d}^3\boldsymbol{r} = \delta_{ij} \quad . \tag{4.10}$$

Consequently, determining electric and magnetic fields in the entire domain, including the PMLs, is required for QNM normalization. The introduction of PMLs generates a subset of quasi-normal modes, which are typically denoted as PML modes. These modes can represent standing waves within the PML or actual QNMs, which are not sufficiently damped in the PML. The PML modes are relevant for the completeness of the QNM basis set and can be identified by the spatial field profile and the mode dispersions [66].

Equation 4.10 requires an integration over the entire simulation geometry Ω. In the numerical simulations, the integral of an arbitrary function $f(\boldsymbol{r})$ is translated into a sum over the function values $f(\boldsymbol{r}_n)$ at all mesh element positions. The infinitesimal volume element in the integral is replaced by the product of the mesh element volume $V(\boldsymbol{r}_n)$ and the associated Jacobian determinant $\det(\boldsymbol{J}(\boldsymbol{r}_n))$. The Jacobian differs from 1 in the perfectly matched layer environment due to the complex coordinate stretching [171]. Hence, the numerical integration over the simulation domain is approximated as

$$\iiint_{\Omega} f(\boldsymbol{r}) d^3\boldsymbol{r} \approx \sum_{n=1}^{N} f(\boldsymbol{r}_n) V(\boldsymbol{r}_n) \det(\boldsymbol{J}(\boldsymbol{r}_n)) \quad . \tag{4.11}$$

The quasi-normal mode theory had its roots in the derivation of scattering cross sections of nuclear reactions more than 80 years ago [172]. The progress in the past years has made the QNM expansion an established method in electrodynamics to simulate cavities. In this work, we use the freeware "QNMEig" developed by the Lalanne group to compute the QNMs using Comsol Multiphysics [173]. The corresponding publication by Yan et al. summarizes the implementation details of the auxiliary fields in the weak formulation [66].

Besides the QNM framework, other numerical expansions exist, which all have particular advantages and disadvantages. The generalized normal mode expansion (GENOME) was developed to decompose the Green's tensor in the cavity eigenmodes [174]. Similar to the QNM approach, GENOME solves an eigenvalue problem. The complex eigenvalues are, however, the permittivities of the nanostructure $\tilde{\varepsilon}_m$ and not the eigenfrequencies $\tilde{\omega}_m$. Therefore, the GENOME solutions do not diverge in space and allow a more intuitive normalization. In contrast to the QNM framework, GENOME enables an expansion in a small number of modes also outside the resonator. Furthermore, GENOME can provide an advantage in computational speed for the simulation of nanoparticle clusters [175]. A different approach introduced by Lin et al. can determine and tailor the lineshape of arbitrary coupled nanostructures from the computation of the individual structures only [176]. This method could help optimize the lineshapes of nanoparticle dimers on metallic mirrors [63]. Nevertheless, we use the more established quasi-normal mode decomposition in this work to simulate the optical response of individual NPoMs [45, 177]. Determining resonance frequencies provides a very intuitive connection to the experimental spectra.

4.2.4 Modes of gold nanoparticles in homogeneous environments

We start with the QNM computation of a spherical gold nanoparticle in a homogeneous dielectric environment. This problem has an analytical solution that enables us to demonstrate the validity of the numerical calculations by direct comparison. We use a cylindrical

simulation geometry in Comsol based on the "cube on mirror" model retrieved from Ref. [173]. This will allow adding a substrate below the nanoparticle for NPoM simulations in Chapter 4.3. We exploit the symmetry of this structure by computing the solution only in a quarter of the cylinder, as sketched in Figure 4.6a. We assign perfect magnetic conductor (PMC) boundary conditions to the cut sides of the cylinder, enforcing zero electric field components perpendicular to the boundary planes (xz- and xy-plane, respectively). Besides significantly reducing computation time, symmetry considerations also improve numerical accuracy. Nevertheless, more care must be taken to evaluate the simulation results correctly. For example, a spherical particle has three energetically degenerate transverse electric dipolar modes with orthogonal orientations. The computation with PMC boundary conditions only allows a single dipolar mode oriented along the z-direction. The electric field distributions in the other three parts of the cylindrical geometry and the field distributions of the other two degenerate modes can be reconstructed using symmetry operations. The 300 nm radius of the dielectric environment is chosen significantly larger than the radius of the gold sphere, which is varied in the interval $r_{\text{sphere}} = 20 \ldots 120\,\text{nm}$. The dielectric is surrounded by a PML shell with 150 nm thickness and perfect electric conductor (PEC) boundary conditions on the outside. We assign a refractive index of $n_{\text{med}} = 1.33$ to the effective medium surrounding the nanoparticle. This matches the refractive index of water, a common solvent in commercially available nanoparticle solutions.

Figure 4.6b shows the real part of the first two quasi-normal mode frequencies $\tilde{\omega}_m$ as a function of the nanoparticle radius. Here, $m = 1$ denotes the dipolar and $m = 2$ the quadrupolar mode, as shown by the exemplary distribution of the electric field norm $|\boldsymbol{E}_m|$ for the $r_{\text{sphere}} = 80\,\text{nm}$ sphere in the insets. Generally, $\text{Re}(\tilde{\omega}_m)$ red-shifts with increasing radius, as the size of the plasmonic resonator determines the eigenfrequencies. Furthermore, the marker diameters in the plot are proportional to the imaginary part of $\tilde{\omega}_m$, quantifying radiation and absorption losses. Intuitively, the losses increase with particle radius. Furthermore, the losses of the quadrupolar mode are smaller than the dipolar modes due to their weak coupling to free space radiation.

Fortunately, the optical response of spherical scatterers with radius a in a homogeneous environment has an analytical solution originally published by Gustav Mie [55]. A direct comparison with our simulation results allows us to validate our implementation of the quasi-normal mode decomposition. Important results of the analytical solution are the scattering cross section σ_{sca}, the extinction cross section σ_{ext}, and the absorption cross section σ_{abs} of the spherical particle. These three quantities are the ratio of the power scattered, extinct, and absorbed by the nanoparticle to the incident energy flux density. Note that $\sigma_{\text{ext}} = \sigma_{\text{sca}} + \sigma_{\text{abs}}$. The analytical result is an infinite series [178]

$$\sigma_{\text{sca}} = \frac{2\pi}{k^2} \sum_{m=1}^{\infty} (2m+1) \left[|a_m|^2 + |b_m|^2 \right] \quad , \tag{4.12}$$

$$\sigma_{\text{ext}} = \frac{2\pi}{k^2} \sum_{m=1}^{\infty} \text{Re}\left[a_m + b_m \right] \quad , \tag{4.13}$$

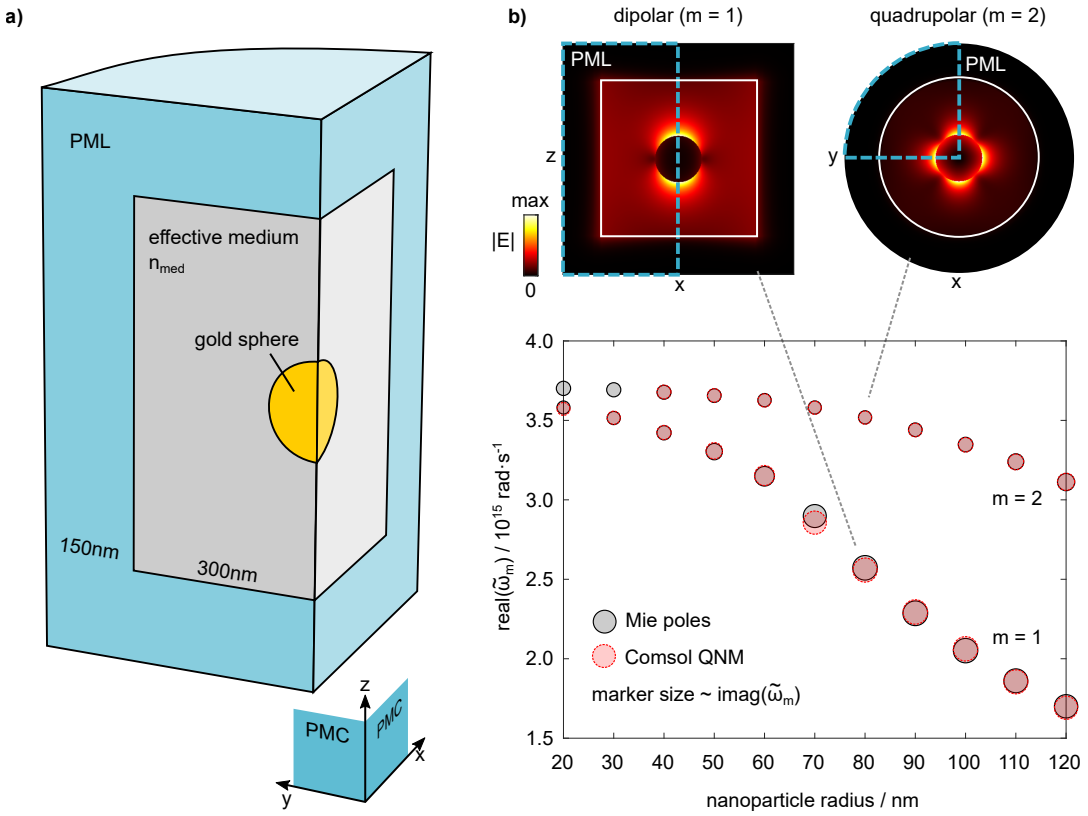

Fig. 4.6.: QNM calculations of a gold sphere in a dielectric environment with $n_{\mathrm{med}} = 1.33$. (a) The simulation domain in Comsol is a quarter cylinder, using the symmetry of the problem. The outer shell is a perfectly matched layer (PML). The cut faces of the cylinder are assigned perfect magnetic conductor (PMC) boundary conditions. (b) Dispersion of the real QNM frequencies of the first two modes as a function of the nanoparticle radius. The marker diameter is proportional to the imaginary part of the frequency. The results of numerical (Comsol QNM) and analytical calculations (Mie poles) agree very well. The quadrupolar QNMs for the two smallest particle radii are not shown, as they could not be stably computed with the chosen mesh size. The insets show the calculated electric field distributions $|\boldsymbol{E}_m|$ for the 80 nm particle radius. The blue dashed segment is simulated in Comsol, and the rest has been calculated by applying symmetry considerations.

where $k = 2\pi n_{\text{med}}/\lambda$ is the wavenumber of the incident wave in the homogeneous medium with refractive index n_{med}. The help functions a_m and b_m can be expressed as [178]

$$a_m = \frac{n_r \psi_m(n_r x)\psi'_m(x) - \psi_m(x)\psi'_m(n_r x)}{n_r \psi_m(n_r x)\zeta'_m(x) - \zeta_m(x)\psi'_m(n_r x)} \quad , \tag{4.14}$$

$$b_m = \frac{\psi_m(n_r x)\psi'_m(x) - n_r \psi_m(x)\psi'_m(n_r x)}{\psi_m(n_r x)\zeta'_m(x) - n_r \zeta_m(x)\psi'_m(n_r x)} \quad , \tag{4.15}$$

in non-magnetic media ($\mu_r = 1$), where $n_r = n_{\text{particle}}/n_{\text{med}}$ is the refractive index ratio between the particle and surrounding medium, and $x = kr_{\text{sphere}}$ is the dimensionless sphere size. ψ_m and ζ_m are the Riccati-Bessel functions of m-th kind. The index m determines the order in the multipole expansion with $m = 1$ describing the dipolar and $m = 2$ the quadrupolar mode. We restrict ourselves to the electric multipoles described by the coefficients a_m [178]. The Padé approximation of the coefficients a_m allows us to investigate the resonance behavior using a power series expansion for both the numerator and denominator. A third-order expansion of the first coefficient is given by [179]

$$a_1^P = -\mathrm{i}\frac{2}{3} \cdot \frac{n_r^2 - 1}{n_r^2 + 2} \frac{x}{1 - \frac{3}{5}\frac{n_r^2-2}{n_r^2+2}x^2 - \mathrm{i}\frac{2}{3}\frac{n_r^2-1}{n_r^2+2}x^3} \quad . \tag{4.16}$$

The three resonant parts represent static polarizability, dynamic depolarization, and radiative damping. The coefficient has a pole for values of x where the denominator is zero. Generally, this resonance condition is met for discrete complex frequencies which enter into the dimensionless parameter x. The resonance frequencies of the coefficients a_m are the complex-valued quasi-normal mode frequencies $\tilde{\omega}_m$ of the sphere, also called natural frequencies in the literature [180].

For comparison with the numerical solutions, we search for poles of the exact Mie scattering coefficients a_1 and a_2 in the complex frequency plane in a 20% frequency interval around the Comsol results [66]. The obtained complex frequencies are plotted as grey markers in Figure 4.6b. Real and imaginary parts agree very well with the numerical results, proving the validity of our simulations.

4.2.5 Polarized far-field imaging computation

Up to now, we have discussed the fundamental properties of the QNMs in terms of their complex frequencies and near-field distributions. The electromagnetic near-field distributions are essential to model the interaction of plasmonic nanostructures with emitters (see Chapter 5). However, in the present chapter, we will investigate the far-field response of individual plasmonic nanoresonators by scattering spectroscopy. Therefore, we present a framework to calculate the far-field radiation of the QNMs imaged into the detector plane by a two-lens system. This method will enable a direct comparison with the experimental results in Chapter 4.4.

The far-field radiation can be obtained by decomposing the electric and magnetic field in a single plane, e.g., the object plane, into propagating plane waves [47, 181]. However, this

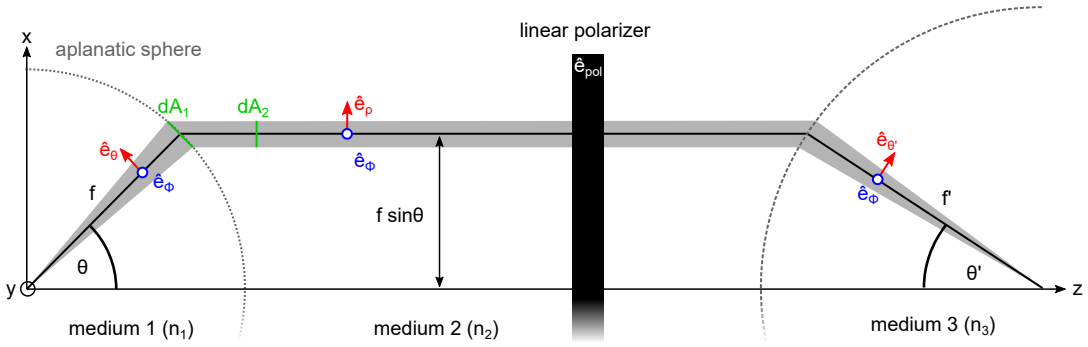

Fig. 4.7.: Far-field imaging with two aplanatic lenses with focal lengths f and f'. A beam radiated at an angle θ with respect to the optical axis is refracted at the aplanatic sphere. A linear polarizer projects the electric field onto the direction $\hat{\boldsymbol{e}}_{\mathrm{pol}}$. Upon refraction at the second aplanatic sphere, the beam is redirected to the focus at an angle θ'.

approach requires knowledge of the fields in an infinitely extended plane. This requirement is incompatible with the limited computing power and storage in numerical simulations. Fortunately, applying the Lorentz reciprocity theorem enables far-field computations from the knowledge of electromagnetic near-fields on a rectangular box surrounding the inhomogeneities [182]. This approach is generally applicable to inhomogeneities like scatterers or emitting dipoles in planar stratified media. Technically, the far-field radiation into a particular direction is calculated from an overlap integral of the electromagnetic near-field on the box with a plane traveling in the opposite direction. This near-to-far-field transformation has been implemented by Yang et al. in the open-source software package RETOP [183]. Hence, we post-process the computed near-fields with RETOP using the Comsol-Matlab Livelink. In the following, we analytically derive the polarization-dependent imaging of the electric far-field into the detector plane by a two-lens system, as sketched in Figure 4.7. The first lens represents the infinity-corrected microscope objective, and the second lens provides the imaging into the detector plane.

Let $\boldsymbol{E}_\infty = (E_{\infty,x}, E_{\infty,y}, E_{\infty,z})$ be the electric far-field evaluated in a sphere with radius $R \geq \lambda$. Due to its transverse nature, the electric field has components in the directions of the elevation $\hat{\boldsymbol{e}}_\theta$ and azimuth $\hat{\boldsymbol{e}}_\phi$. The unit vectors in spherical coordinates are related to their cartesian counterparts $\hat{\boldsymbol{e}}_x$, $\hat{\boldsymbol{e}}_y$, and $\hat{\boldsymbol{e}}_z$ as

$$\hat{\boldsymbol{e}}_\phi = -\sin\phi\hat{\boldsymbol{e}}_x + \cos\phi\hat{\boldsymbol{e}}_y \quad , \tag{4.17}$$

$$\hat{\boldsymbol{e}}_\theta = \cos\theta\cos\phi\hat{\boldsymbol{e}}_x + \cos\theta\sin\phi\hat{\boldsymbol{e}}_y - \sin\theta\hat{\boldsymbol{e}}_z \quad . \tag{4.18}$$

Upon refraction at the aplanatic sphere, the optical ray propagates in z-direction, i.e., parallel to the optical axis. Therefore, the electric field component in direction $\hat{\boldsymbol{e}}_\theta$ now points along the cylindrical unit vector $\hat{\boldsymbol{e}}_\rho$ defined as

$$\hat{\boldsymbol{e}}_\rho = \cos\phi\hat{\boldsymbol{e}}_x + \sin\phi\hat{\boldsymbol{e}}_y \quad . \tag{4.19}$$

Furthermore, energy conservation requires a scaling factor $\sqrt{n_1/n_2}(\cos\theta)^{-1/2}$ in the electric field caused by the distortion of the infinitesimal cross sections $\mathrm{d}A_1$ and $\mathrm{d}A_2$ upon refraction, as sketched in Figure 4.7 [47]. At this point, the electric far-field reads

$$\boldsymbol{E}_{\infty,\mathrm{cyl}} = \left[\left(\boldsymbol{E}_{\infty}\cdot\hat{\boldsymbol{e}}_{\phi}\right)\hat{\boldsymbol{e}}_{\phi} + \left(\boldsymbol{E}_{\infty}\cdot\hat{\boldsymbol{e}}_{\theta}\right)\hat{\boldsymbol{e}}_{\rho}\right]\sqrt{\frac{n_1}{n_2\cos\theta}} \quad . \tag{4.20}$$

For comparison with the polarization-dependent experiments in the following sections, we account for a linear polarizer oriented along the unit vector $\hat{\boldsymbol{e}}_{\mathrm{pol}}$. The transmitted electric field is the projection onto the polarizer direction

$$\boldsymbol{E}_{\infty,\mathrm{pol}} = \left(\boldsymbol{E}_{\infty,\mathrm{cyl}}\cdot\hat{\boldsymbol{e}}_{\mathrm{pol}}\right)\hat{\boldsymbol{e}}_{\mathrm{pol}} \quad . \tag{4.21}$$

Upon refraction at the aplanatic tube lens, the beam propagates towards the optical axis at an angle θ' which is determined by the ratio of focal lengths f and f' of the first and second lens

$$\frac{\sin\theta}{\sin\theta'} = \frac{f'}{f} \quad . \tag{4.22}$$

Energy conservation again requires a scaling factor. Hence the electric field in spherical coordinates reads

$$\boldsymbol{E}_{\infty,\mathrm{tube}} = \left[\left(\boldsymbol{E}_{\infty,\mathrm{pol}}\cdot\hat{\boldsymbol{e}}_{\phi}\right)\hat{\boldsymbol{e}}_{\phi} + \left(\boldsymbol{E}_{\infty,\mathrm{pol}}\cdot\hat{\boldsymbol{e}}_{\rho}\right)\hat{\boldsymbol{e}}_{\theta'}\right]\sqrt{\frac{n_2\cos\theta'}{n_3}} \quad . \tag{4.23}$$

We express the electric field in the cartesian spatial frequencies given by

$$k_x = k\sin\theta'\cos\phi \quad , \tag{4.24}$$

$$k_y = k\sin\theta'\sin\phi \quad , \tag{4.25}$$

$$k_z = k\cos\theta' \quad , \tag{4.26}$$

omitting the primes in the following for better readability. It can be shown that the electric field in the focal plane at the detector is given by [47, 181]

$$\boldsymbol{E}_{\mathrm{detector}}(x,y) = -\frac{\mathrm{i}f'e^{-ikf'}}{2\pi}\iint_{k_x^2+k_y^2\le k_{max}^2}\boldsymbol{E}_{\infty,\mathrm{tube}}\left(\frac{k_x}{k},\frac{k_y}{k}\right)e^{\mathrm{i}(k_x x+k_y y)}\frac{1}{k_z}\mathrm{d}k_x\mathrm{d}k_y \quad . \tag{4.27}$$

The integral runs over all spatial frequencies covered by the numerical aperture $\mathrm{NA} = n\sin\theta_{\max}$ of the objective. The objective used in the experiments has a numerical aperture of 0.9 corresponding to an acceptance angle of $\theta_{\max} \approx 64°$ in air. Note that the lens naturally performs a Fourier transform in the paraxial limit $k_z \approx k$. This property is used in the field of Fourier optics, e.g., for optical image processing [47, 99].

To demonstrate the far-field imaging computation routine, we return to the example of a spherical gold nanoparticle with 80 nm radius embedded in an effective medium. We use the near-field distributions obtained from Comsol QNM computations to analyze the far-field radiation of electric dipole modes with two orthogonal orientations. Specifically, we compare the in-plane dipolar mode oriented in x-direction and the out-of-plane dipolar mode in z-direction. The near-field distributions of both modes are identical upon rotation of the coordinate system. The near-to-far-field transform employed by the RETOP software requires the electric and magnetic field distribution on a rectangular box surrounding the nanoparticle. We choose a cube with 250 nm edge length centered on the nanoparticle.

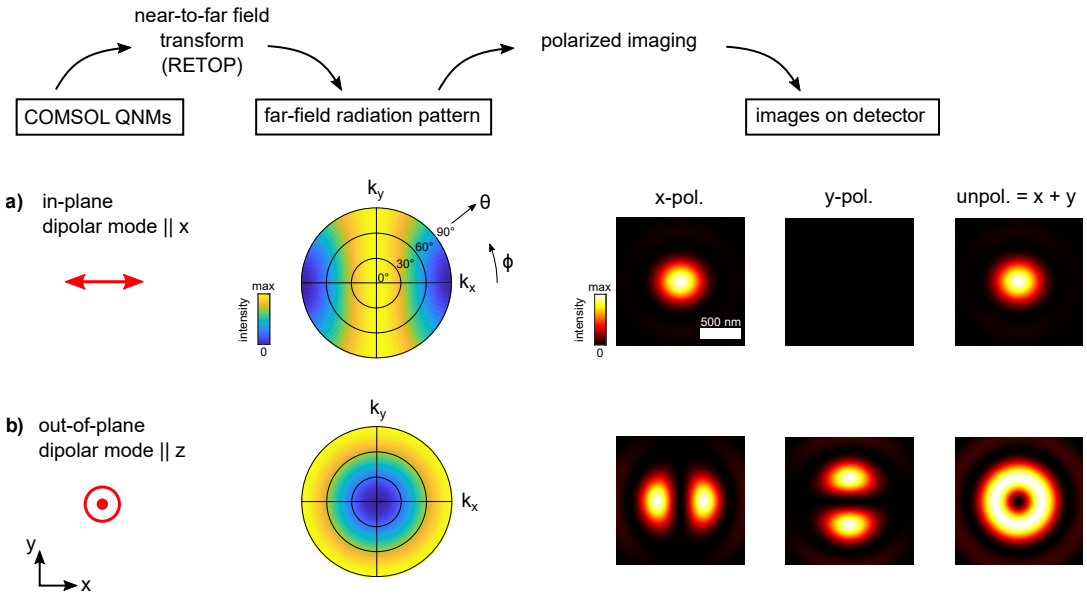

Fig. 4.8.: Polarized far-field imaging computation of the QNMs of gold nanoparticles ($r_{\text{sphere}} = 80\,\text{nm}$) embedded an effective medium ($n_{\text{eff}} = 1.33$). Compared are the in-plane (upper row) and out-of-plane (lower row) dipolar modes. The RETOP software is used for near-to-far-field-transformation of the QNMs. The imaging computation reveals the shape of the diffraction spots for x-polarized, y-polarized and unpolarized detection. The out-of-plane mode gives rise to a donut-shaped pattern on the detector.

This box is already introduced as a dedicated surface in the QNM computation for the highest numerical accuracy. The far-field computation provides the radiation pattern into the $+z$-hemisphere shown in Figure 4.8. The radiation pattern visualizes the power emitted into the far-field along the direction (k_x, k_y). No radiation is emitted along $(k_x, k_y) = (k, 0)$ for the x-dipole and along $(0, 0)$ for the z-dipole. The maximum radiation is observed perpendicular to the dipole axis, i.e., at $k_x = 0$ for the x-dipole and along $k_x^2 + k_y^2 = k^2$ for the z-dipole, consistent with the expectations for a point dipole.

Using the polarized imaging computation method described above, we determine the point-spread functions (PSF) $I_{\text{detector}} = |\boldsymbol{E}_{\text{detector}}|^2$ of the dipolar modes in the detector plane. The right column of Figure 4.8 compares the PSFs of both modes for x- and y-polarized detection. The intensity sum of both polarizations yields the unpolarized PSF. As expected for an in-plane dipole oriented in the x-direction, an emission is only observable with a linear polarizer pointing along x. The shape of the PSF matches the Airy diffraction pattern. Importantly, the out-of-plane dipolar mode generates a donut-shaped PSF with zero intensity in the center. Linear polarization along x and y yields dumbbell-shaped PSFs oriented in the respective polarization directions. The sum of the x- and y-polarized images is a PSF with radial symmetry due to the symmetry imposed by the z-dipole. The comparison shows that the polarization-resolved PSF in real space carries information about the dipole orientation of the modes excited in the sample plane. This information will be used in the experiment to separate different modes of the NPoMs based on their PSF shape.

4.2.6 FEM simulations of scattered fields and near-field distributions

The quasi-normal mode decomposition yields a fundamental understanding of the resonance frequencies, line widths, electromagnetic field distributions, and far-field radiation of nanostructures. In particular, the near-field coupling of emitters can be written very intuitively as an expansion in QNMs, which will be discussed in Chapter 5. In scattering experiments, however, the excitation amplitude and phase of each mode are determined by external parameters of the excitation field, such as wavelength and polarization [184]. The accurate representation of the scattering spectra over a broad spectral range requires computing a large number of contributing modes. Therefore, we introduce a complementary approach for the simulation of scattering spectra which does not depend on a mode decomposition. Instead, the electric field around the plasmonic nanostructure is calculated at monochromatic plane-wave illumination from a fixed angle. The total electric field at frequency ω is separated into a background field $\boldsymbol{E}_{\text{back}}$ and a scattered field $\boldsymbol{E}_{\text{sca}}$

$$\boldsymbol{E}(\boldsymbol{r},\omega) = \boldsymbol{E}_{\text{back}}(\boldsymbol{r},\omega) + \boldsymbol{E}_{\text{sca}}(\boldsymbol{r},\omega) \quad . \tag{4.28}$$

The background field represents the electric field in the simulation domain without the scatterer and can often be determined analytically. The scatterer acts as a small perturbation to this background field, so we calculate only E_{sca} by the numerical simulation. The dome-like simulation domain consists of planar layers denoting the substrate, a thin dielectric spacer layer, and air, as sketched in Figure 4.9. The background field is obtained analytically for s- and p-polarized incident waves at an angle θ, using the transfer matrix method for planar multilayer systems (see Chapter 3.1). Each layer is assigned a downward and upward propagating wave satisfying the boundary conditions imposed by the interfaces. The downward propagating excitation wave in air is normalized to $|\boldsymbol{E}| = 1$. The scattered field is computed by numerical Comsol simulations. Considering the symmetry of this structure and the asymmetry imposed by the excitation wave, it is sufficient to simulate only half of the dome, as sketched in the Figure. The xz-plane is assigned PEC boundary conditions for s-polarized excitation and PMC boundary conditions for p-polarized excitation. We use the dielectric function from Johnson and Christy for gold [51].

Up to now, we have used a spherical gold nanoparticle to calculate the optical response in a homogeneous environment. However, the NPoM geometry breaks the symmetry of the previous effective medium description in z-direction, as the nanoparticle is coupled to a gold substrate. As we will discuss in Chapter 4.3, the optical response of the NPoM significantly depends on the morphology of the gap region. After deposition onto the gold substrate, the gold nanoparticles lie flat on their facets. We model the gold nanoparticle as a truncated sphere with a circular facet pointing to the gold substrate. Consistent with the literature [45, 162], we use a facet diameter $w = 20\,\text{nm}$ (see Figure 4.9b).

The scattered electric field $\boldsymbol{E}_{\text{sca}}$ in the simulation domain is obtained from numerical Comsol simulations at a particular frequency ω. The simulation is repeated for multiple frequencies of the incident plane wave to obtain the wavelength-dependent optical response. The scattering spectra can be calculated by integrating the Poynting vector of the scattered field over the solid angle covered by the numerical aperture of the microscope objective. The integration area needs to be outside of the optical near-field and, thus, requires increasing the simulation domain size. Instead, we again use the RETOP software for near-to-far-field

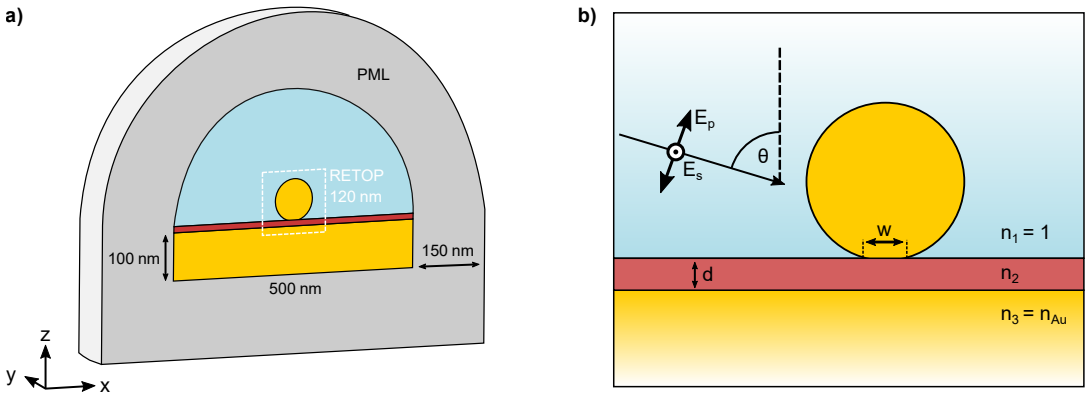

Fig. 4.9.: (a) The dome-like simulation domain for scattered field calculations has three layers and is enclosed by perfectly matched layers (PML). The symmetry allows computing only the half dome, applying PEC boundary conditions to the cut plane for s-polarized and PMC boundary conditions for p-polarized excitation. The cube surface for the far-field transform via RETOP is depicted by the dotted white line. (b) Sketch of the truncated nanosphere in the three-layer system and the incident plane wave.

transformation. RETOP evaluates the electric and magnetic field on the cube's surface sketched by the dotted white line in Figure 4.9a. This procedure allows us to compute the wavelength-dependent scattering intensity and point-spread function for comparison with experiments.

4.3 Near- and far-field response of NPoMs

Spherical plasmonic nanoparticles feature dipolar, quadrupolar, and higher-order modes with resonance frequencies and linewidths depending on the particle size. In comparison, the mode structure of coupled nanostructures is much more diverse. An intuitive plasmon hybridization model describes the optical response by plasmons interacting between the individual nanoparticles, in analogy to the molecular orbital theory in molecular physics [157]. The energy level diagram of two coupled identical spherical nanoparticle dimers is shown in Figure 4.10a. The dipolar modes of the individual particles hybridize, forming transverse and longitudinal resonances. The charge distributions determine the energetic order of the four coupled modes [185]. Two modes are "dark" as the dipoles cancel each other. The other two modes (highlighted in the sketch) couple to the far-field, yielding a high-energy transverse and a low-energy longitudinal mode. The excitation of the modes depends on the excitation polarization, as the dipole orientations of the two bright modes are orthogonal to each other.

An NPoM can be seen as a nanoparticle dimer with an infinite radius of one of the nanoparticles. In contrast to the spherical nanoparticle, the infinitely extended nanoparticle does not have a localized plasmon resonance, as the plasmon resonance shifts to zero energy. Here, the hybrid plasmon emerges from the coupling of the dipolar nanoparticle resonance with its image dipole in the metal in the quasistatic limit [10, 186]. Again, the symmetry of the NPoM features two distinct modes sketched in Figure 4.4b-c. First, the

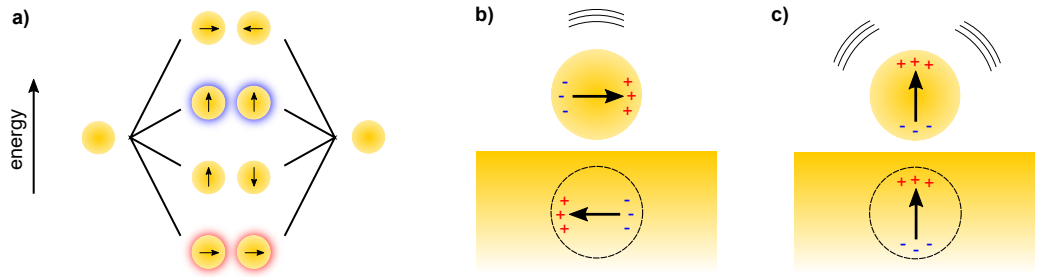

Fig. 4.10.: (a) The energy level diagram shows the hybridization of dipolar modes supported by two identical nanoparticles, similar to Ref. [185]. Only two of the modes are radiative, highlighted by the blue and red outlines. In the NPoM, the (b) horizontal and (c) vertical dipole in the nanoparticle couples with the image dipole in the metal substrate.

excitation of a horizontal dipole in the nanoparticle generates an image dipole in the metal substrate pointing in the opposite direction. Since the dipoles partly cancel each other, the coupling to the optical far-field is small. Therefore, this mode is often denoted as "dark". Second, a vertical dipole excited in the nanoparticle adds up constructively with its image dipole and efficiently couples to the far-field [187]. The dipole orientations suggest that the optical response of the NPoM is strongly polarization-dependent, which has already been shown by darkfield images in Figure 4.4. Our qualitative model can, however, not describe the spectral positions of the respective modes. Furthermore, higher-order modes beyond the dipole approximation might interfere in the far-field. Therefore, we employ numerical simulations in the following to characterize NPoM systems in terms of the near- and far-field properties of their quasi-normal modes.

4.3.1 QNM characterization based on spherical harmonics

Figure 4.11a shows a sketch of the cylindric simulation geometry. We extended the simulation model for the QNM calculations of a gold sphere in a homogeneous environment by a 100 nm optically thick gold film and a dielectric Al_2O_3 spacer with $d = 1$ nm thickness. We use the tabulated refractive index $n(Al_2O_3) = 1.6764$ of amorphous alumina at a wavelength of 650 nm [188]. The gold nanoparticle is modeled as a truncated sphere with facet diameter $w = 20$ nm, qualitatively matching the SEM images in Figure 4.1. The symmetry of the problem allows us to simulate only a quarter of the cylinder, as shown in Figure 4.11a, applying appropriate boundary conditions at the two cut faces.

We obtain modes with different symmetries depending on the boundary conditions of the cut faces. The perfect electric conductor (PEC) boundary condition prohibits electric field components parallel to the interface. The electric field distributions on both sides of the boundary are symmetric to each other in terms of their absolute value. However, the sign of the electric field can flip depending on the relative orientation to the boundary. As sketched in Figure 4.11c, the electric field parallel to the boundary has a zero-crossing at the boundary and swaps signs. In contrast, electric field components perpendicular to the boundary maintain their sign. The magnetic field vectors behave opposite to the electric field. Furthermore, the signs of the electric and magnetic field vectors at perfect magnetic

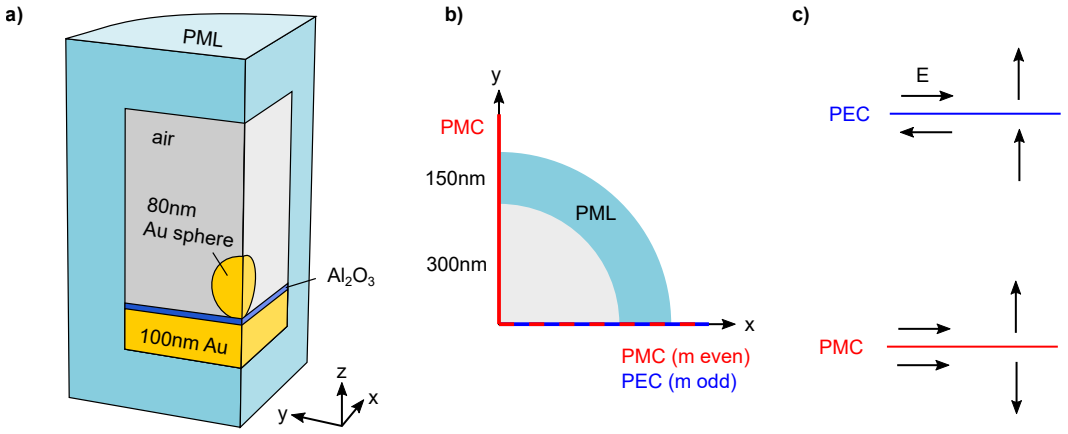

Fig. 4.11.: (a) Simulation domain for QNM calculations of NPoMs in Comsol. The nanoparticle is modeled as a truncated sphere with an 80 nm diameter on an alumina layer. (b) Sketch of the PEC and PMC boundary conditions for xz- and yz-plane viewed along the z-axis. (c) Symmetry of the electric field components parallel and perpendicular to PEC (top) and PMC (bottom) boundaries.

conductor (PMC) boundaries behave opposite to the PEC boundary. Based on symmetry considerations, these sign rules allow us to reconstruct electric and magnetic fields in the entire cylindrical domain. To obtain the complete set of all QNMs, the computations need to be repeated for the four combinations of boundary conditions for the two cut sides. Some QNMs are energetically degenerate with equivalent electromagnetic field profiles upon discrete rotation in the xy-plane. We, therefore, restrict ourselves to two combinations of boundary conditions, as sketched in Figure 4.11b, namely PMC/PMC and PMC/PEC.

Figure 4.12 shows the near-and far-field distributions of the five energetically lowest quasi-normal modes of the NPoM. In the near-field distributions, we only show the vertical component of the electric field E_z, as it dominates over the in-plane components. The real part of E_z is largest in the gap region between the facet and the gold substrate. The electric field distributions in the xy-plane are evaluated in the center of the dielectric gap. Following the spherical harmonic nomenclature introduced by Kongsuwan et al. [45], we assign each QNM a label (l,m) with $l = 1,2,3,\ldots$ and $-l \leq m \leq l$. The label indices are determined by the symmetry of the respective mode. The integer l quantifies the number of radial nodes and antinodes of E_z in the gap. Similarly, the integer m denotes the number of antinode pairs in the angular direction $\phi = \arctan y/x$. As we restrict ourselves to the QNMs for two of the four possible boundary conditions, we discuss only QNMs with $m \geq 0$. The energetically degenerate equivalents with index $-m$ are obtained by rotating the electric field distribution around the z-axis by angles $\pi/(2m)$.

The energetically lowest QNM has a radially symmetric E_z distribution and is, thus, labeled as $(l,m) = (1,0)$. This mode originates from the longitudinal dipole coupling of the nanoparticle plasmon with its image dipole. The vertical orientation of the resulting dipole moment gives rise to a radially symmetric far-field emission pattern, where most radiation is emitted at large angles from the substrate normal. In contrast to a vertical dipole in free space, the maximum emission is not observed at $\theta = 90°$ but at an optimum angle

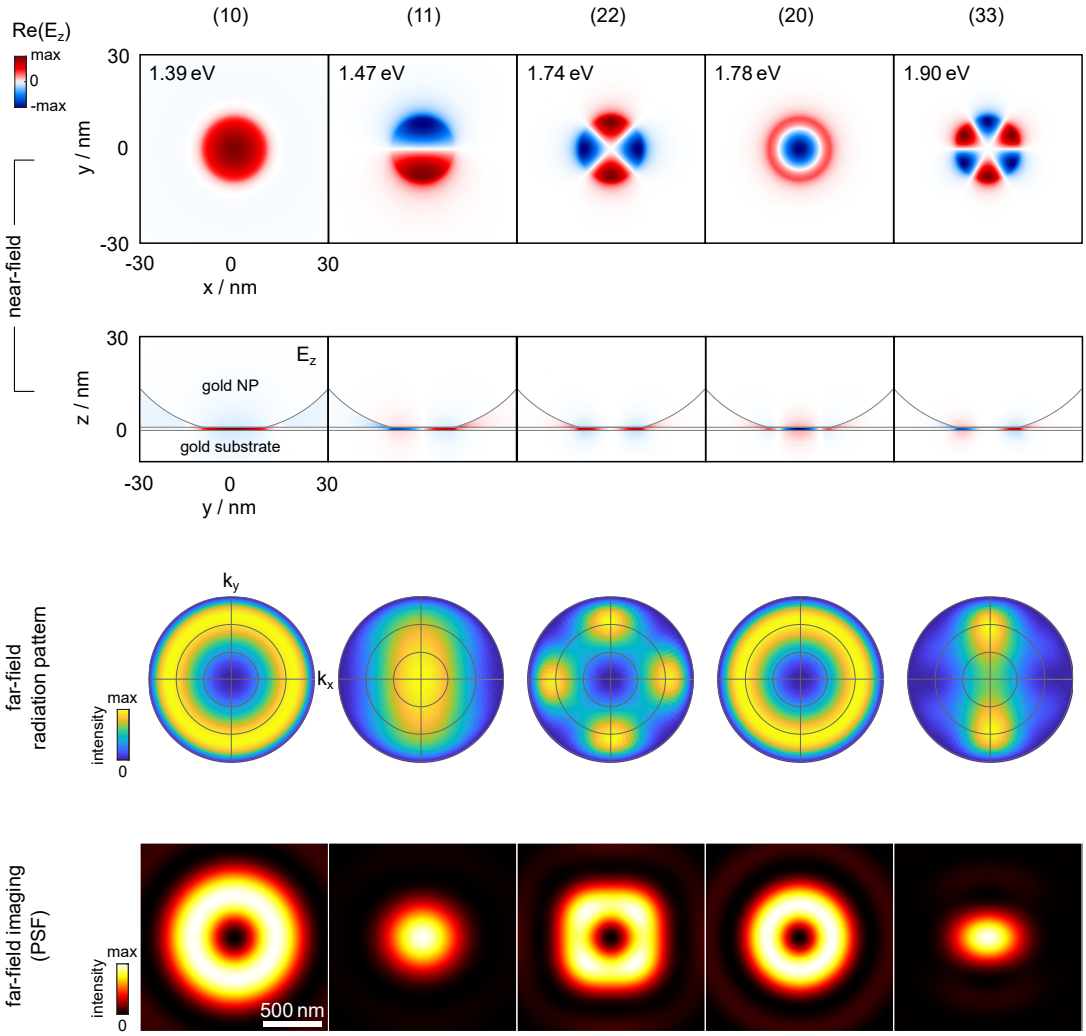

Fig. 4.12.: Comparison of the five energetically lowest QNMs of an NPoM with $w = 20\,\text{nm}$ facet diameter and 1 nm alumina spacer. The modes are identified by the spherical harmonics (l, m) and the resonance energy in eV in ascending order from left to right. The top images show the computed near-field distributions of $\text{Re}(E_z)$ in the xy-plane (evaluated in the center of the gap) and in the yz-plane. Furthermore, we show the far-field radiation patterns (center) and the point-spread functions (bottom) in the detector plane.

of about 60°. To collect the far-field emission with high efficiency, we use a microscope objective with 0.9 NA corresponding to an acceptance angle of 64° in air. After imaging the far-field radiation in the detector plane, the diffraction spot has a donut shape with zero intensity in the center. This result finally explains the low-energy (red-colored) donut in the color scattering image, which can only be observed at p-polarized excitation (see Figure 4.4) [12, 45, 187].

The index of the mode with the second lowest energy is $(l, m) = (1, 1)$. Corresponding to the odd value of m, the E_z distribution in the $y = 0$ plane is antisymmetric. This mode resembles the transverse dipole coupling of the dipolar nanoparticle mode with the image dipole. Due to the in-plane dipole orientation, the far-field radiation is most intense for directions perpendicular to the substrate. Moreover, the far-field radiation pattern is slightly elliptical as the dipole is oriented in y-direction. The real-space diffraction pattern in the detector plane is point-shaped, which renders the (10) and (11) modes easily discernible in far-field images. Based on the PSF shape and the observed polarization dependence, we assign the green Airy diffraction spots in the color scattering image in Figure 4.4 to the (11) mode [12, 45, 187].

The modes with $l \geq 2$ denote quadrupolar and higher-order plasmonic modes of the nanoparticle coupled with its image multipoles. Higher-order modes radiate less efficiently into the far-field. Furthermore, the higher-order modes typically have a large spectral overlap, making their separate observation difficult [45]. Nevertheless, nanostructures such as emitters in the gap can couple to all available modes depending on their local density of states. Therefore, higher-order modes must also be considered in mode expansions [45, 64, 66, 184]. The calculated point-spread functions suggest that modes with even m generate donut-shaped patterns and can be excited with out-of-plane polarization from the far-field. In contrast, odd modes generate point-shaped patterns and can be excited with in-plane polarization.

Our analysis mainly focuses on the two energetically lowest QNMs that emerge from the dipolar coupling. Figure 4.13 shows a more detailed comparison of their electric field distribution. In the gap region, the in-plane components E_x and E_y of the real electric field are more than one order of magnitude smaller than the out-of-plane component E_z. Furthermore, the in-plane components only have significant contributions at the facet edge and outside the facet region. Generally, the absolute value of the electric field $|E|$ is strongly localized in the gap, as shown in the side-view field plots.

4.3.2 Mode dispersion of truncated nanoparticles and waveguide modes

The SEM images in Figure 4.1 revealed that the facet size varies among the investigated gold nanoparticles. Up to now, we assumed a facet width of $w = 20\,\text{nm}$. Variations in the gap morphology can lead to significant spectral shifts of the QNM [162, 165, 167, 189–191]. In this section, we study the dependence of the QNM properties on geometric parameters, which will allow us to compare the numerical simulations with experimental data in Chapter 4.4. Our discussion is based on Ref. [45].

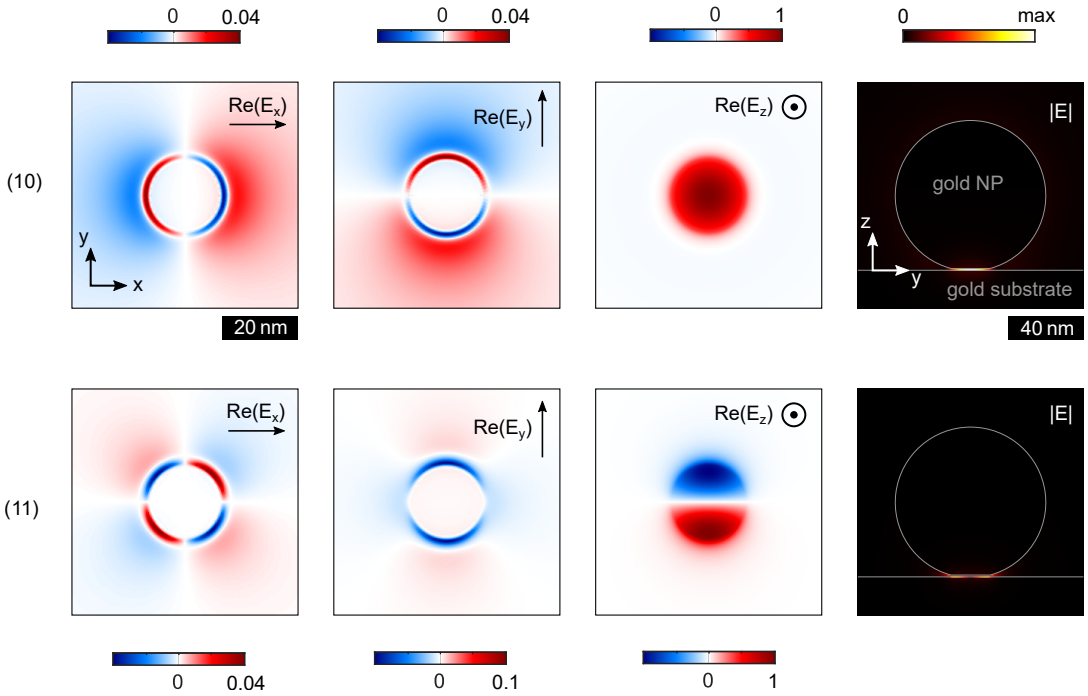

Fig. 4.13.: Near-field distributions of the energetically lowest modes (10, upper row) and (11, lower row) of an NPoM with an 80 nm gold nanosphere, $w = 20$ nm facet diameter, and a 1 nm alumina spacer. Shown are the real electric field components of E_x, E_y and E_z evaluated in the xy-plane in the center of the gap. The right image shows the respective $|\boldsymbol{E}|$ distributions in the yz-plane. Notably, the electric field is only confined in the gap area. Each field plot has its own color map limits for better comparison.

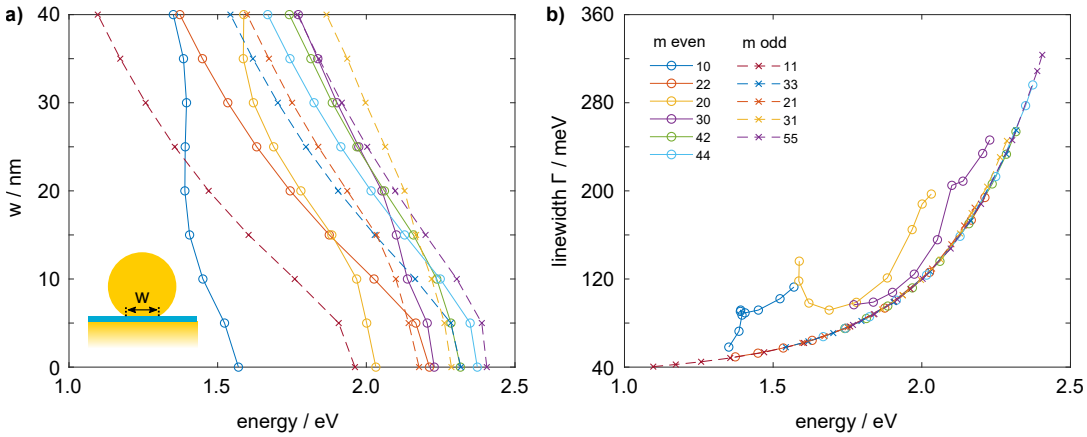

Fig. 4.14.: (a) Simulated QNM energy dispersion of the modes (l, m) as a function of the facet width w for an NPoM with 80 nm gold nanoparticle and 1 nm thick Al_2O_3 gap. (b) Correlation of QNM energy and linewidth as a function of the facet width (connected lines). Each QNM is assigned an individual color with solid lines representing modes with even m and dashed lines odd m.

Figure 4.14a shows the variation of the QNM energies as a function of the facet width between 0 and 40 nm. Most of the modes continuously red-shift with increasing w. This behavior can be qualitatively understood by viewing the truncated sphere-on-mirror as a finite metal-insulator-metal (MIM) resonator. It can be shown that the dispersion of MIM modes in the limit of gap thickness $d \to 0$ reads [18, 25, 192]

$$\left(\frac{k}{k_0}\right)^2 = \varepsilon_d + \frac{\zeta}{2}\left(1 + \sqrt{1 + \frac{4(\varepsilon_d - \varepsilon_m)}{\zeta}}\right) \tag{4.29}$$

with vacuum wave number $k_0 = 2\pi/\lambda$, wave number k in the MIM, ε_d and ε_m the permittivities of dielectric and metal, and a constant $\zeta = [2\varepsilon_d/(k_0 d\varepsilon_m)]^2$. From this equation, the effective refractive index can be deduced as $n_{\text{eff}} = \text{Re}(k)/k_0$. The calculation is based on an infinitely extended planar MIM cavity. The NPoM structure made from a planar mirror and dielectric is capped with a truncated nanosphere, introducing a discrete one-dimensional standing-wave resonance condition with integer m [192]

$$\frac{2\pi}{\lambda} w n_{\text{eff}} = m\pi + \phi \quad . \tag{4.30}$$

Here, ϕ denotes a mode-specific reflection phase. Note that a Bessel function enters into the resonance condition in circular resonators [25, 193], which is beyond the scope of this work. Generally, the resonance condition shows that the truncated MIM resonance wavelength linearly increases with the facet width w for a given mode m. This proportionality explains the asymptotic behavior of the QNM energies for increasing facet widths.

The interaction between the transverse MIM modes and the nanoparticle antenna modes gives rise to the apparent mode dispersion in Figure 4.14a. As only modes with matching symmetry can interact, the dispersions of the (10) and (11) modes cross unperturbed. Generally, the dispersion of the (10) mode is not linear with the facet width, originating from avoided crossings with radially symmetric waveguide modes [25]. The unique

behavior of the (l0) modes also becomes apparent in Figure 4.14b. Here, all modes except the (l0) lie on a convex curve relating the energy and FWHM linewidth $\Gamma = 2\mathrm{Im}(\tilde{\omega}_m)$ of the respective QNM. Again, this curve can be modeled in the limiting case of MIM theory [45]. The dispersion of the (l0) modes always lies above the other modes corresponding to a larger damping than expected from the MIM theory. The larger damping is connected to the radiative nature of these modes, allowing an efficient coupling to the far-field.

Generally, this discussion has demonstrated that variations in the gap morphology significantly influence the QNM energy and damping. This has to be taken into account when comparing simulated and experimental spectra. Irregularities in the shape of the nanoparticles and their impact on the NPoM properties have been investigated in both simulation and experiment [162, 165, 190, 191, 194]. Notably, it has been demonstrated that the resonance of the nanoresonator can even be tuned by intense illumination with blue light [189]. The authors concluded that gold surface atoms continuously move into the cavity, increasing the facet width. Despite the strong dependency of QNM energies and spatial field distributions on the exact geometry, it has been shown that the nomenclature based on spherical harmonics (l,m) is universally applicable [195].

Besides the NPoMs discussed in this work, film-coupled nanocubes, termed nanocube-on-mirror systems (NCoM), have attracted interest in the nano-optics community. For example, NCoMs have been demonstrated to facilitate ultrafast single photon emission from individual quantum dots [28]. In the NCoM, the electric field hot spots are located at the edges of the nanocube. As the cube faces lie flat on the substrate, NCoMs feature waveguide modes that interact with radiative antenna modes, similar to the faceted NPoMs [196]. The larger Q-factor of the NCoM resonances comes along with larger mode volumes. As a comparison of silver nanocubes and nanoparticles on gold substrates shows, the NPoM geometry allows for considerably larger Purcell enhancements at small gap sizes [14]. Therefore, we decided on the NPoM geometry in this work for efficient coupling with the dye monolayer.

4.3.3 Dependency on gap size and refractive index

Apart from the morphology of the gold nanoparticle, also the gap thickness influences the QNM frequencies and spatial field distributions. We will experimentally study the shift of the NPoM resonances as a function of the spacer thickness in Chapter 4.4. For later comparison with experiments, Figure 4.15a shows the numerically calculated evolution of QNM energy and linewidth $\Gamma = 2\mathrm{Im}(\tilde{\omega}_m)$ when increasing the thickness d of the dielectric alumina spacer from 1 to 10 nm. We concentrate on the (10) and (11) modes, which are representative of all other QNMs. Both real and imaginary parts of the QNM frequencies increase monotonically with d. The strong sensitivity of the resonance position at small particle-to-film separations has, for instance, been used to demonstrate a plasmonic ruler with sub-nanometer resolution [16]. The susceptibility of the QNM energy to gap thickness variations decreases for larger gaps. In general, the blue-shift of the modes is bounded by the interband transition of gold [47], which explains the accumulation of modes at around 530 nm. In the limiting case of infinite gap separation, the influence of the gold mirror is negligible, and the optical response of an isolated nanoparticle is recovered.

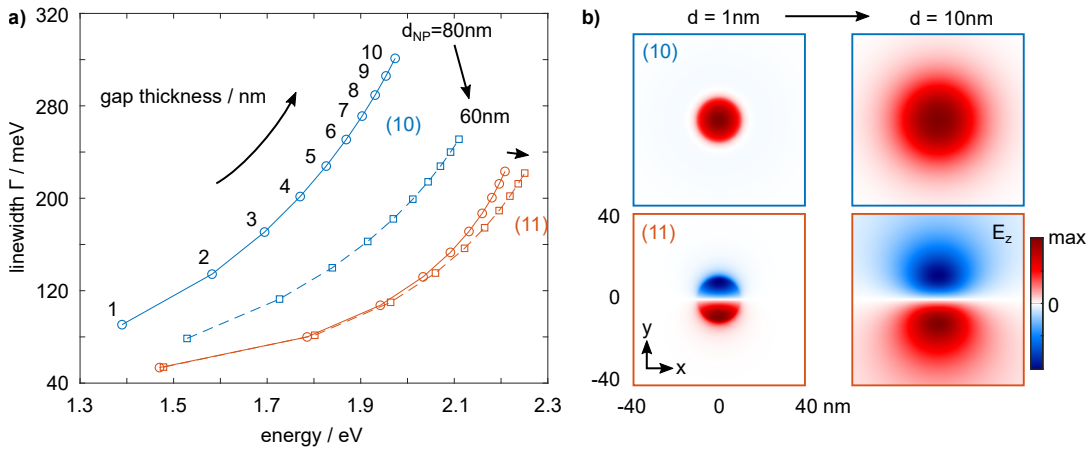

Fig. 4.15.: (a) Energy and linewidth of the (10) and (11) QNMs and their dependency on the gap thickness varied between $1 \ldots 10$ nm. The NPoM gap material is Al_2O_3. Compared are the results for an NPoM with an 80 nm (solid line) and 60 nm gold nanoparticle (dashed line) and a facet width $w = 20$ nm. (b) Spatial distribution of $\mathrm{Re}(E_z)$ in the xy-plane evaluated in the gap center, comparing $d = 1$ nm and $d = 10$ nm for an 80 nm nanoparticle.

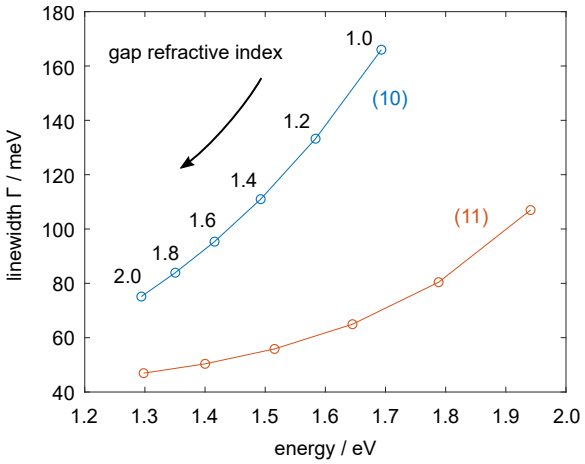

Fig. 4.16.: Energy and linewidth of the (10) and (11) QNMs and their dependency on the refractive index of the gap at a constant gap thickness of $d = 1$ nm. The nanoparticle diameter of the NPoM is 80 nm and the facet width is 20 nm.

As the gap thickness increases, the electric field distribution becomes less confined in the gap. This is illustrated by the near-field plots evaluated in the gap center (see Figure 4.15b). The weaker confinement increases the energy loss, consistent with our observed increase of the QNM damping parameter. The near-field interaction with emitters in the gap generally gets weaker as the electric field confinement decreases. To observe strong coupling with emitters, the ratio of gap thickness and oscillator strength of the emitter should be as small as possible [36, 38, 44].

Similar behavior is observed for the evolution of the QNM frequencies with the refractive index of the spacer material n_{gap} at a constant gap thickness $d = 1\,\mathrm{nm}$. The (10) and (11) modes red-shift with increasing n_{gap}, as shown in Figure 4.16. In a first-order approximation, the optical response is determined by the optical path length $n_{\mathrm{gap}} \cdot d$. Hence, the spectral shift when increasing n_{gap} is opposite to the shift when increasing d.

We only investigate NPoMs with a nominal 80 nm nanoparticle diameter in the experiments. Nevertheless, the actual diameter varies slightly between the nanoparticles, as the SEM images in Figure 4.1 illustrate. Figure 4.15a compares the simulation results for NPoMs with 80 nm and 60 nm nanoparticle diameter at a constant 20 nm facet width. The (10) mode is susceptible to the nanoparticle size in resonance energy and width. The smaller particle can radiate less efficiently into the far-field and, thus, experiences less radiative damping. The waveguide-like (11) mode is much less sensitive to the nanoparticle diameter as the resonance mainly depends on the facet width, gap size, and refractive index [25].

4.4 Polarization-resolved scattering spectroscopy of NPoMs

In the last sections, we motivated the fundamental modes of NPoMs and their dependency on geometrical parameters in numerical simulations. This general understanding will allow us to investigate the scattering spectra of individual NPoMs in the experiment. In the following, we present a method for widefield polarization-resolved scattering spectroscopy of the NPoMs. We model the experimental spectra with multiple Lorentz-shaped functions and investigate the properties for different gap sizes. The polarization resolution lets us separate the modes emerging from in-plane and out-of-plane dipole coupling between the nanoparticle and the mirror.

4.4.1 Experimental setup

Figure 4.17 shows a sketch of the experimental setup for polarized scattering spectroscopy. The setup shares the core components with the hyperspectral imaging setup presented in Chapter 3.3.1. The incoherent broadband light from a 100 W halogen lamp (U-LH100L-3, Olympus, IR filter removed) is focused into a multimode fiber with a 50 µm core diameter (M42L02, Thorlabs) using a 25 mm plan-convex lens. After propagation in the fiber, the unpolarized white light is collimated by a 30 mm achromatic lens and linearly polarized. The wire-grid polarizer is attached to a motorized rotation mount for automated

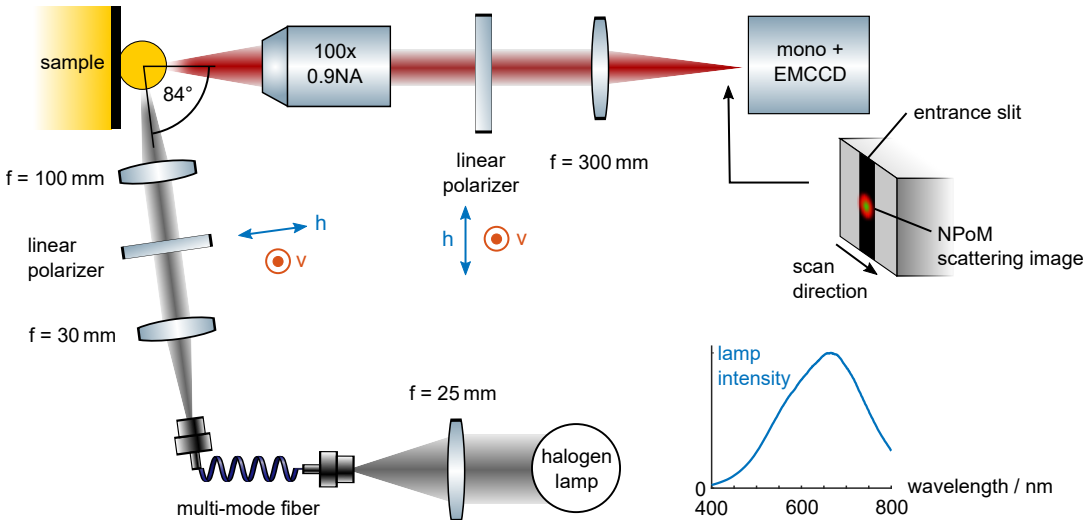

Fig. 4.17.: Experimental setup for polarized scattering spectroscopy. The sample is illuminated with white light at almost grazing incidence (84° angle of incidence). The scattered light is imaged onto a spectrometer with an entrance slit width matching the size of the donut-shaped NPoM point-spread function (see sketch on the right). The spectrum shows the scattering of the lamp from a diffusely scattering sample.

measurements to switch between horizontal (h) and vertical (v) excitation polarizations. The white light is loosely focused onto the sample at an almost grazing angle of incidence (84°) with a 100 mm achromatic lens. This provides an elliptical illumination area on the sample with approximate dimensions of $170 \times 1,700\,\mu m$. The total white light excitation power is $50\,\mu W$. The scattered light from the sample is collected by a 100x/0.9NA microscope objective. The high numerical aperture and relatively small 1 mm working distance of the microscope objective impose strict geometrical boundaries on the white light illumination. These considerations explain our specific choice of angle of incidence and numerical aperture for the white light illumination.

As for the excitation polarizer, the linear polarizer in the detection pathway is motorized for automated experiments. The scattered light is focused onto the spectrometer entrance slit. The slit width matches the size of the donut-shaped diffraction pattern, as sketched in the Figure. As in the previous chapter on transition dipole orientation imaging, the experimental setup provides spectral and spatial resolution in a single camera frame. At each position, the scattering spectra are measured at all four combinations of excitation (h,v) and detection polarization (h,v). The sample is scanned horizontally in 600 nm steps, matching the half slit width projected onto the sample. Our technique, thus, provides polarization-dependent scattering spectra in a two-dimensional region of interest.

The halogen lamp covers the spectral range between 500 and 800 nm to observe all NPoM modes in the experiment. We measured the white light scattering from a certified diffuse reflectance standard (USRS-99-010, Labsphere), as shown in the inset of Figure 4.17. The lamp spectrum includes the spectral transmission of all optical components in the

experimental setup. Therefore, we use it as the reference spectrum I_{lamp} to normalize the measured scattering spectra of the nanoparticle samples according to

$$I_{\mathrm{sca}}(\lambda) = \frac{I_{\mathrm{particle}}(\lambda) - I_{\mathrm{bg}}(\lambda)}{I_{\mathrm{lamp}}(\lambda) - I_{\mathrm{dark}}(\lambda)} \quad . \tag{4.31}$$

Here, the measured lamp spectrum $I_{\mathrm{lamp}}(\lambda)$ is corrected by the counts in the dark frame $I_{\mathrm{dark}}(\lambda)$ acquired with the halogen lamp switched off. In the numerator, the scattering of the nanoparticle $I_{\mathrm{particle}}(\lambda)$ is corrected by the background intensity $I_{\mathrm{bg}}(\lambda)$ next to the particle.

4.4.2 In-plane and out-of-plane resonances of gold nanoparticles on glass substrates

To validate the experimental setup, we investigate the polarization-dependent scattering spectra of individual gold nanoparticles on a glass cover slip with spatial resolution. The sample is fabricated by dropcasting colloidal gold nanoparticles with 80 nm nominal diameter onto an activated glass substrate. A representative individual nanoparticle is moved to the center of the spectrometer entrance slit. Camera images of the nanoparticle scattering with spectral and spatial resolution are acquired for all four excitation and detection polarization combinations. The measurements are shown in Figure 4.18, with each quadrant representing a particular polarization combination (see pictograms). At each polarization, the measurement (top part of each quadrant) is compared with simulations (bottom part). In the following, we abbreviate the polarization combinations as (excitation)/(detection), i.e., v/h stands for vertically (v) polarized excitation and horizontally (h) polarized detection.

We begin our analysis with images of the nanoparticle scattering recorded in the zeroth diffraction order of the spectrometer (quadratic images in the Figure). Each image is normalized to the respective maximum value. The shape of the diffraction spot changes significantly with polarization. Vertically polarized excitation induces an in-plane dipole moment in the nanoparticle. The scattered light from the in-plane dipole maintains this polarization direction. Consequently, scattering is only observed at v-polarized and none at h-polarized detection up to background noise. As the results of the v/v measurement demonstrate, the in-plane dipole orientation generates an Airy-shaped diffraction pattern.

In contrast, due to the grazing incidence, the horizontally polarized excitation induces a superposition of in-plane and out-of-plane dipoles. V-polarized detection only selects the out-of-plane mode, which explains the prominent dumbbell-shaped diffraction pattern in the vertical direction. This becomes even more apparent looking at the profile of the horizontally integrated image, approaching almost zero in the center. H-polarized detection supports both in-plane and out-of-plane dipole orientations, generating the superposition of a dumbbell shape in the horizontal direction and an Airy-shaped diffraction pattern. In general, the high magnification of the experimental setup enables us to observe the dipole orientation and structural asymmetries based on the diffraction pattern.

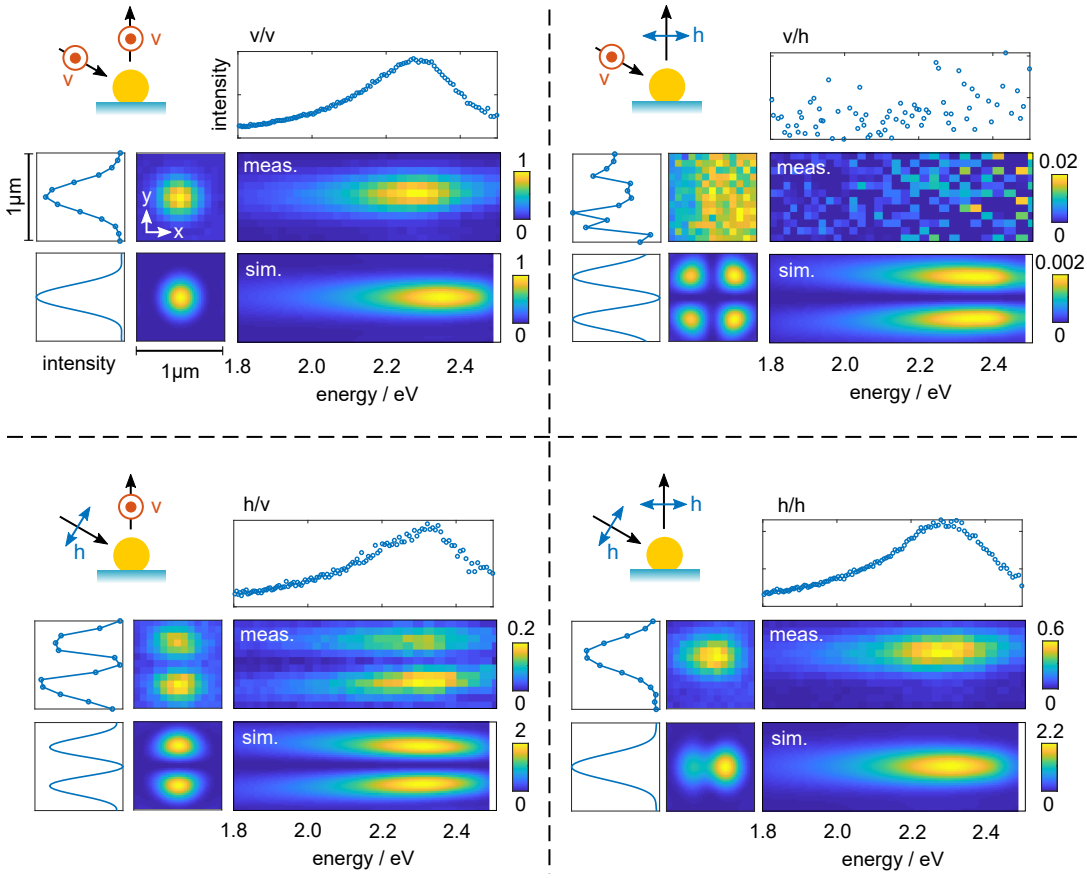

Fig. 4.18.: Comparison of measured and simulated polarization-dependent scattering from a single 80 nm gold nanoparticle on a glass substrate, assuming a facet width $w = 20$ nm in the simulations. As shown in the pictograms, the four quadrants stand for the excitation and detection polarization combinations. In each quadrant, from left to right: real-space profile and real-space image of the diffraction spot, scattering spectrum with spatial resolution normalized to the maximum in the v/v measurement. On top, the spatially integrated measured scattering spectrum is depicted.

Figure 4.18 compares the experimentally obtained diffraction patterns with scattered field FEM simulations. We model the sample as an 80 nm spherical nanoparticle with a 20 nm facet size lying on a dielectric with a refractive index $n = 1.5$. The far-field imaging calculation is repeated for wavelengths at 500...700 nm. The real-space images of all computed wavelengths are summed up for comparison with the experiment. The normalized simulated images are shown in Figure 4.18 below the measurements at the respective polarization combination. The simulated diffraction patterns at v/v and h/v agree very well with the experiment. In the h/v experiment, the lower part of the dumbbell pattern is slightly brighter than the upper part. We attribute this asymmetry in the diffraction pattern to structural asymmetries in the gold nanoparticle, tilting the dipole orientation somewhat to the positive y-direction. Due to the grazing incidence, the simulated diffraction pattern at h/h polarization has an asymmetric horizontally oriented dumbbell shape. Similarly, the center of mass in the measurement is slightly shifted to the right. At v/h polarization, the simulation predicts a four-spot diffraction pattern. This results from a coupling between horizontal and vertical polarization directions in an imaging system with a high numerical aperture. However, the integrated power of the computed diffraction spot is more than 100 times lower than at v/v polarization. Observing this pattern in the experiment would require significantly longer integration times.

In the previous analysis, we focused on the far-field scattering images of the nanoparticle. In the first diffraction order of the monochromator grating, our experimental setup provides combined information about the spatial and spectral characteristics of the scattered light. Figure 4.18 shows the measured scattering spectra of the individual nanoparticle with spatial resolution in the y-direction. As the optical diffraction limit scales with the wavelength, the diffraction pattern becomes larger at smaller energies. Besides this, the diffraction pattern does not significantly change shape across the spectrum. This suggests that the dipolar modes of the gold nanoparticle dominate the scattering spectra. For comparison with the experiment, the simulated spectra with spatial resolution are obtained by stitching the simulated far-field images together at their respective wavelengths. Again, simulation and measurement show an excellent qualitative agreement. As mentioned above, the measured signal at v/h polarization is too low for comparison with the simulation. The spatially resolved spectra in measurement and simulation are normalized to the respective maximum values at v/v polarization. The measured intensities at h-polarized excitation are generally smaller than the simulations. Quantitatively, the peak values in the spectra differ by a factor of about 10 (h/v) and about 4 (h/h). First, this might be caused by asymmetries of the nanoparticle in the experiment compared with a perfectly symmetric nanoparticle in the simulation. Second, Fresnel's equations determine the local intensity of the excitation field at the nanoparticle position. This local intensity determines the excitation strength of the charge oscillations inside the nanoparticle. In the simulation, the intensity of the background field at the nanoparticle position is much higher at h-polarized than at v-polarized excitation due to the grazing incidence. In the experiment, however, small irregularities in the glass substrate might alter the local electric field.

Finally, Figure 4.18 shows the spatially integrated scattering spectra of the measured nanoparticle. The peak position and width do not significantly change with polarization. This finding indicates that the particle is approximately spherical, which qualitatively matches the results from the SEM image in Figure 4.1b. The measured peak is slightly

red-shifted to the simulation, which we attribute to differences in the dielectric function of gold between the experiment and simulation. Furthermore, the investigated nanoparticle might be slightly larger than assumed in the simulation.

4.4.3 Experimental observation and modeling of NPoM resonances

After introducing and validating the measurement principle, we can now investigate the scattering of NPoMs in the experiment. As a representative example, we focus on an 80 nm gold nanoparticle separated from the gold substrate by a 2 nm dielectric alumina spacer. Capping agents enclose the colloidal nanoparticles in the experiment, increasing the effective spacer thickness. Specifically, the nanoparticles from BBI have citrate, while those from Nanopartz used in the experiments have an unspecified carboxylic acid with similar molecular weight as capping agents. To account for this, we generally add 1 nm to the spacer thickness in the simulations. Figure 4.19 compares the measured and simulated scattering from an individual NPoM at the four combinations of excitation and detection polarization (see pictograms). All spectra are normalized to the maximum intensity in the h/h measurement and simulation to compare relative intensities easily. Qualitative analysis of the measured spectra reveals two dominating modes, as expected from our previous theoretical considerations.

At v-polarized excitation, we only excite the in-plane $(l, m) = (1, 1)$ mode at around 2.05 eV. This attribution is supported by the spatially resolved spectra exhibiting an Airy-shaped profile in the y-direction. As the dipole orientation is pre-determined by the excitation polarization direction, we only observe a strong signal at v-polarized detection. This behavior matches the simulation results where the (11) mode peaks at around 1.95 eV. The intensity contrast between v/v and v/h is more than 100 in the simulation. This value is more than a factor of 10 smaller in the experiment. We attribute this to the asymmetry of the nanoparticle, which is not considered in the simulation [194]. Briefly, we expect the facet of the gold nanoparticle to be elliptical, where the semi-axes are not necessarily aligned with the experimental polarization directions due to the random deposition of the nanoparticles on the substrate. We will discuss the ellipticity in more detail in Chapter 4.4.4. Both measurement and simulation show a spectrally broad and intense scattering at energies above 2.2 eV. This property results from higher-order modes that accumulate towards the interband transition energy of gold (compare Figure 4.14a). Although the higher-order modes are less radiative, the combined scattering of all modes can generate significant scattering intensity. Our following analysis demonstrates that we can assign the intense scattering peaks below 2.2 eV to the energetically lowest modes $(1, 0)$ and $(1, \pm 1)$.

At h-polarized excitation, the dominating scattering originates from the out-of-plane mode $(l, m) = (1, 0)$, peaking at around 1.9 eV in the experiment. Consistent with the out-of-plane orientation of the dipole, the scattering intensity at v- and h-polarized detection is almost identical. The resonance peak width is broader than the in-plane mode due to larger radiation losses. The out-of-plane orientation is eminent from the spatially resolved h/v spectrum exhibiting two peaks in y-direction corresponding to a dumbbell shape. These findings qualitatively agree very well with the simulation results. The simulation

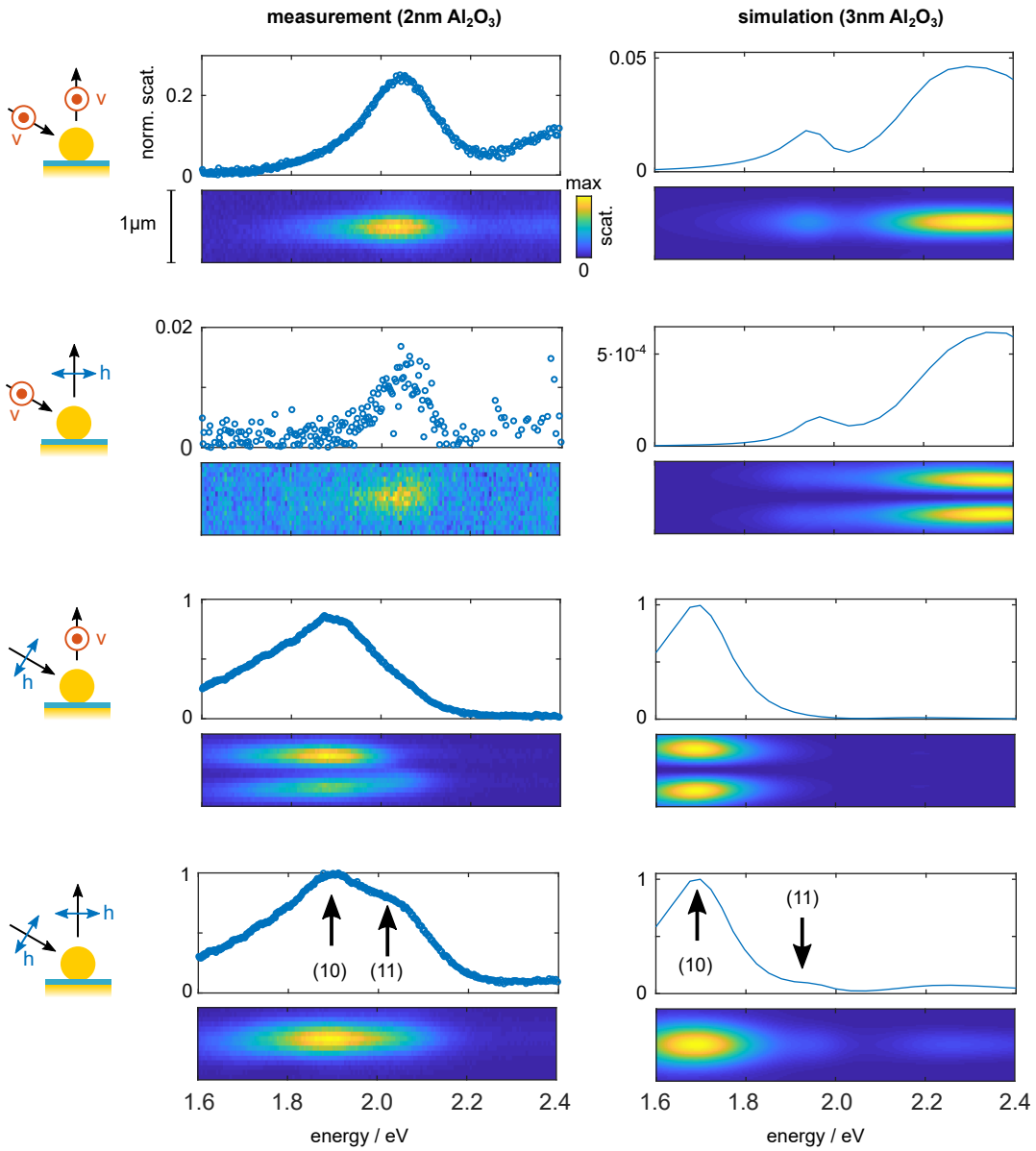

Fig. 4.19.: Comparison of the measured (left) and simulated (right) scattering from an 80 nm gold nanoparticle on a gold substrate with an Al_2O_3 spacer layer. Due to ligands in the experiment, we compare a 2 nm spacer in the measurement with a 3 nm spacer in the simulation ($w = 20$ nm). The scattering spectra are shown above the spatially resolved scattering spectra for each excitation and detection polarization combination sketched on the left. The spectra are normalized to the maximum intensities in the h/h measurement and simulation.

predicts a peak energy of around 1.7 eV, significantly red-shifted to the experiment. We attribute the spectral shift to differences in the dielectric function of gold in the experiment and simulation. Furthermore, modeling the gold nanoparticle as a truncated sphere in the simulations is only an approximation of the actual geometry.

Due to the grazing incidence, the h-polarized illumination has a non-vanishing projection in the sample plane and, therefore, also excites an in-plane mode. This mode is oriented perpendicular to the (11) mode discussed above and is, thus, labeled as $(l, m) = (1, -1)$. Due to the dipole orientation matching the h-polarization in detection, this mode is efficiently detected in the h/h measurement. The in-plane modes $(1, \pm 1)$ are energetically degenerate for radially symmetric NPoMs. First, we attribute the small shoulder of the (10) peak at the (11) frequency to the perpendicular in-plane mode. Second, the spatially resolved spectra reveal an altered diffraction profile at the (11) frequency, similar to the superposition of a dumbbell-shaped (10) and a single-peaked (11) spot profile. Hence, the combined analysis of spatial and spectral emission properties of the NPoMs allows the assignment of the fundamental modes to the measured spectra. As mentioned above, an asymmetry of the nanoparticle allows observing the in-plane mode also in the h/v measurement.

Finally, the simulations predict an intensity ratio of (10) and (11) modes on the order of 10. In the measurements, however, the contrast ratio is much smaller. This discrepancy is evident in comparing the relative intensities of (10) and (11) modes in the h/h configuration and the relative intensity of the (11) mode in the v/v measurement. The in-plane modes are less often considered in publications because the symmetry of the near-field distribution suppresses efficient radiation into the far-field [25]. We believe that asymmetries in the nanoparticle shape, especially in the gap region, significantly enhance the radiation of the (11) mode. Furthermore, rounded nanoparticle edges and the asymmetric white-light illumination at almost grazing incidence contribute to our intense observation of the in-plane modes in the experiment [194]. The characterization of in-plane and out-of-plane modes is crucial to understand the coupling of broadband emitters with plasmonic nanoresonators in Chapter 5. In this context, the in-plane modes will play an essential role.

4.4.4 Influence of nanoparticle asymmetries on the NPoM scattering

Modeling the gold nanoparticles as truncated spheres provides valuable information about the near- and far-field properties of the NPoMs. Our simulations demonstrate that the morphology of the gap significantly influences the NPoM resonance frequencies. For example, doubling the facet width from 10 to 20 nm gives rise to a red-shift of more than 300 meV for the (11) mode (see Figure 4.14a).

The nanoparticles inevitably have small asymmetries in the experiment, which we could consider in the numerical simulations. However, every nanoparticle has a slightly different shape, and the reproduction of a real particle in the simulation would never be exact. Instead, we use a simple yet realistic approach to model the facet as elliptical instead of circular. Consequently, the energetical degeneracy of the orthogonal in-plane modes $(l, m) = (1, 1)$ and $(1, -1)$ is lifted [194]. The degree of energy splitting is a measure

of facet ellipticity. In general, the semi-axes of the ellipse do not necessarily coincide with the experimental coordinate system given by the (h) and (v) directions. The gold nanoparticles are randomly deposited on the substrate, so every rotation angle is equally probable. The excitation and detection efficiency of the respective modes then scales with the projection of the semi-axes onto the experimental coordinate system. The in-plane modes of elliptical NPoMs can, thus, be imagined as nanoscale linear polarizers.

Figure 4.20a shows the variations of the scattering spectra with the detection polarizer angle after vertically (left) and horizontally (right) polarized excitation. The scattering maxima at v-polarized excitation continuously shift with the rotation of the detection polarizer on a scale of around 100 meV. This shift proves the existence of two superimposed in-plane modes where the relative amplitudes vary with the detection polarizer angle. At h-polarized excitation, the total amplitude of the in-plane modes oscillates with the detection polarization. In contrast, the out-of-plane mode centered at around 1.9 eV is barely sensitive to the detection polarization.

Based on our simple model of elliptical facets, we describe all experimental scattering spectra as a superposition of three Lorentzian contributions of $(1,0)$, $(1,1)$ and $(1,-1)$ modes

$$I_{\mathrm{sca}}(E) = \sum_{(l,m)=\{(1,0),(1,1),(1,-1)\}} \frac{A^{(l,m)}}{2\pi} \cdot \frac{\gamma^{(l,m)}}{\left(E - E_0^{(l,m)}\right)^2 + \left(\gamma^{(l,m)}/2\right)^2} \quad . \tag{4.32}$$

The contribution from each mode is normalized to its energy content based on the amplitude $A^{(l,m)}$, the resonance energy $E_0^{(l,m)}$, and the damping $\gamma^{(l,m)}$. By definition, the damping parameter γ is identical to the peak FWHM. Figure 4.20b shows the results of a single fit to the spectra at all polarizations simultaneously. For increased accuracy, we set the amplitude of the (10) Lorentzian mode to zero at v-polarized excitation. The fit function describes the measured spectra very well. The computation reveals two in-plane resonances at 2.01 and 2.07 eV with similar damping parameters 160 and 150 meV, consistent with our expectations. For a better visibility, the maxima of the fit functions are marked as red crosses in the two-dimensional plot. The out-of-plane resonance of the NPoM is centered at 1.87 eV according to the fit. Consistent with the simulations, the damping parameter is significantly larger (280 meV) than the in-plane resonances.

4.4.5 Statistical analysis and gap size dependence

Our analysis in the last sections demonstrated that the gap morphology ultimately impacts the NPoM scattering spectra. Therefore, the statistical investigation of many NPoMs is required to determine the average mode energies and damping parameters and quantify particle variations. To accomplish this, we scan the sample in steps of the half projected monochromator slit width in the horizontal direction, similar to the transition dipole orientation determination procedure in Chapter 3.3. The spatially resolved scattering spectra are measured at all four combinations of excitation and detection polarization successively at every position on the sample. The entire measurement over a scan area of around $30 \times 30\,\mu\mathrm{m}^2$ is automated in Labview. By spectral integration over all frames, we

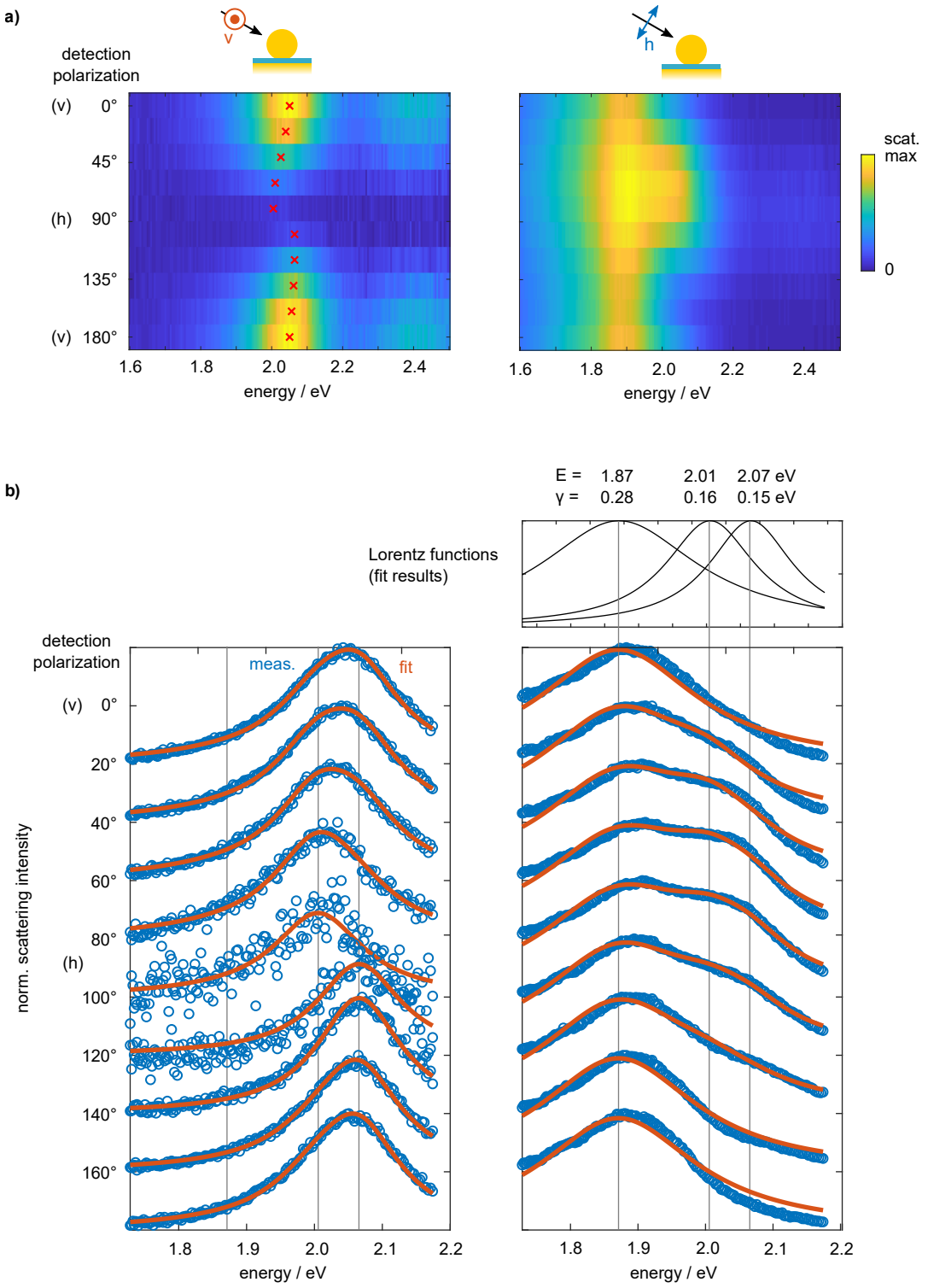

Fig. 4.20.: (a) Variations of the NPoM scattering spectra (80 nm gold nanoparticle, $d_{gap} = 2\,nm$) after vertically (left) and horizontally (right) polarized excitation as a function of the detection polarization. At v-polarized excitation, the peak position shifts significantly with the detection polarization, as marked by the red crosses. At h-polarized excitation, the out-of-plane mode is always visible, while the appearance of the in-plane mode depends on the detection polarization. (b) All measured spectra are globally fitted with three Lorentzian functions, considering the ellipticity of the nanoparticles.

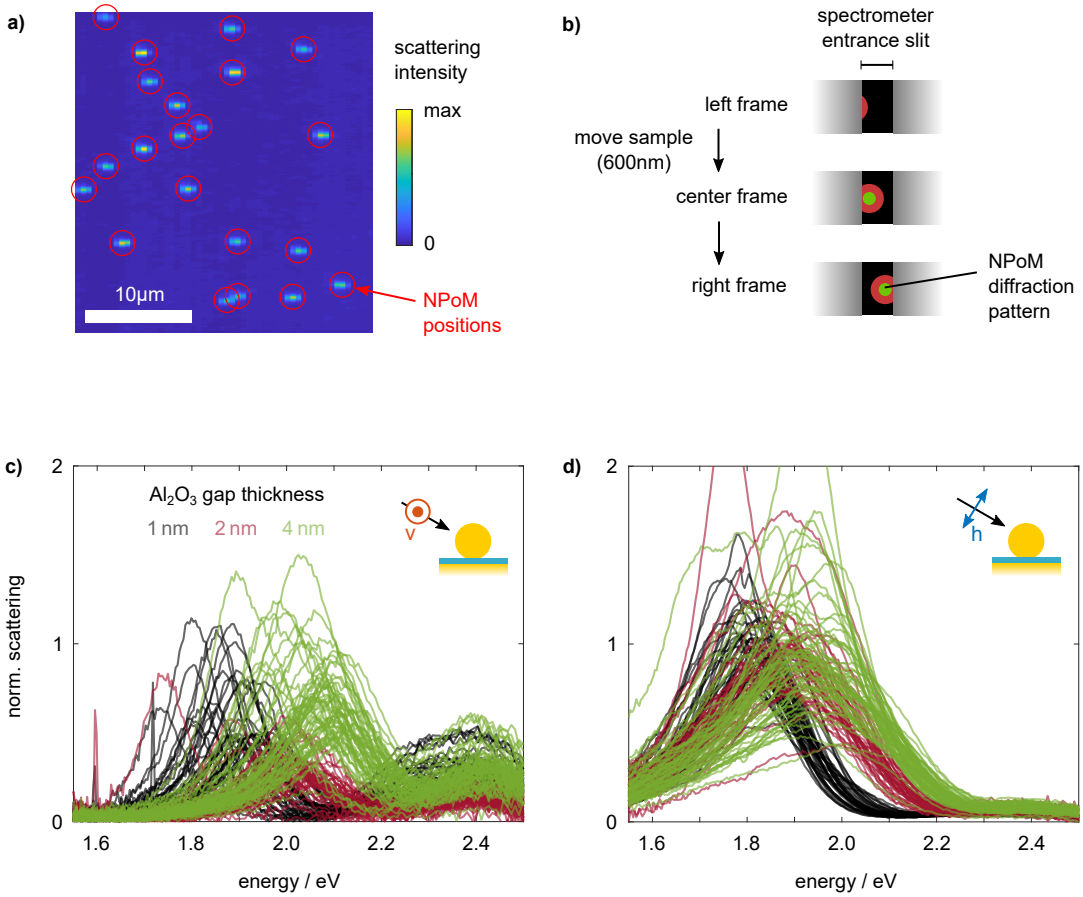

Fig. 4.21.: (a) The scattering intensity map is automatically processed to determine the positions of NPoMs (red circles). (b) Three neighboring frames are summed up to obtain the scattering spectra of the individual NPoM sketched as a red donut with a green dot. The sample is moved horizontally between each frame by the half slit width projected onto the sample. (c-d) Raw scattering spectra of all investigated NPoMs at (c) v-polarized and (d) h-polarized excitation. The gap widths are color-coded. The spectra are normalized by the average scattering maximum at each gap width.

reconstruct the two-dimensional spatial map of scattering intensities. The measured map is shown in Figure 4.21a for the h/h measurement. A peak-finding algorithm automatically detects the maxima (red circles in the Figure). Due to the automated horizontal sample scanning in discrete 600 nm steps, the nanoparticles are not necessarily positioned in the center of the spectrometer entrance slit. As visualized in Figure 4.21b, we can recover the complete information about the scattering from a single NPoM by averaging the spectra over three neighboring frames. After subtracting the scattering background signal and normalization by the lamp spectrum, we retrieve four spectra for each individual NPoM. The measurement is repeated at Al_2O_3 gap sizes of 1 nm, 2 nm, and 4 nm.

We first qualitatively analyze the spectral variations as a function of the gap thickness. To visualize the raw data, we sum up the measured spectra of both detection polarizations. Figure 4.21 shows the spectra at (c) v-polarized and (d) h-polarized detection for the color-coded gap sizes. At each gap size, we measured 40-60 individual NPoMs and manually

excluded outliers with irregular spectral shapes (between 4 and 7 measurements per gap thickness). The spectra are normalized to the average peak heights for each gap size. The resonance positions of the in-plane modes at v-polarized excitation (c) vary considerably from particle to particle, as the spectral position is very sensitive to the facet width. Qualitatively, we observe a blue-shift of the in-plane resonances for increasing gap size. The spectra measured at h-polarized excitation exhibit fewer variations within each gap thickness value. This finding is consistent with our expectations, as the out-of-plane mode is more sensitive to the gap size than the particle shape. As for the in-plane mode, the peak energy of the h-polarized scattering spectra increases with the gap size.

For quantitative analysis, we return to the measured spectra at all four excitation and detection polarization combinations. For each NPoM, the four spectra are simultaneously fitted by three Lorentzian distributions according to Equation 4.32. The free parameters are the spectral positions, widths, polarization-dependent amplitudes of the Lorentzian resonances, and global offsets. The fit results for all investigated NPoMs look similar to those in Figure 4.20b. Some spectra can be well described by only two Lorentzian contributions, corresponding to radially symmetric nanoparticles. In this case, the fit parameters of the third contribution are manually set to zero to prevent over-fitting of the spectra. Figure 4.22a summarizes the fit results of peak energy and peak widths for the three different gap sizes 1 nm (left), 2 nm (center), and 4 nm (right). Each data point originates from the fit of a single NPoM. The three modes are color-coded as blue $(1,0)$, red $(1,1)$, and orange $(1,-1)$. The average resonance positions and widths of all investigated particles at each gap thickness are shown as larger points with black error bars.

We begin the discussion with the out-of-plane mode $(1,0)$. The mean energy gradually increases with gap size from 1.78 eV (1 nm) to 1.86 eV (4 nm). Compared with the simulated QNM frequencies shown in Figure 4.15a, the experimentally obtained peak positions are significantly blue-shifted. For example, the simulation predicts an energy of about 1.6 eV at a gap size of 2 nm. However, the $(1,0)$ QNM energy is very sensitive to the nanoparticle size, as shown by the simulations in Figure 4.15a and experimentally demonstrated in Ref. [162]. Quantitatively, a reduction in nanoparticle diameter by only 25% from 80 nm to 60 nm yields a blue-shift of 150 meV. Besides that, the simulations revealed that the (10) QNM energy varies on a scale of 100 meV with the facet size. In general, the actual shape of the nanoparticle inevitably differs from the simple simulation geometry. These considerations can explain the observed spectral shift between measurement and simulation.

Increasing the gap thickness from 1 nm to 4 nm gives rise to a line broadening from 220 meV to 350 meV (FWHM). The damping parameter is larger than in the simulation, predicting an increase from only 140 meV to 240 meV. We attribute this to additional radiative and non-radiative loss channels introduced by the surface roughness of the Al_2O_3 spacer layers, the gold substrate, or the capping agents and solvent residues on the nanoparticle. Nevertheless, the general trend of the blue-shifting QNM frequencies and increased damping with the gap size agrees with the simulations.

The out-of-plane mode can only be excited at horizontal polarization. Besides the energy and damping parameters, we also analyze the amplitudes of the Lorentzian contribution. The out-of-plane orientation of the dipole moment suggests that the scattering amplitude is independent of the detection polarization. To verify this theoretic expectation with

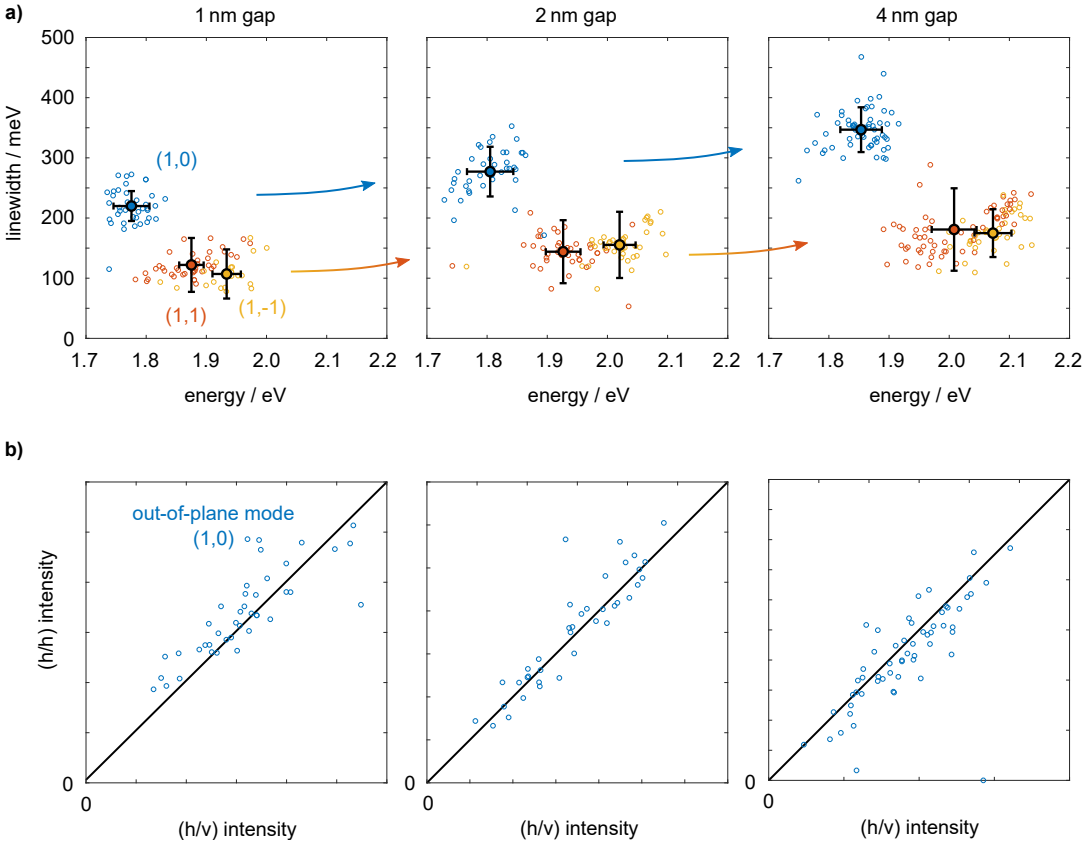

Fig. 4.22.: (a) Statistical evaluation of the out-of-plane (blue) and in-plane (red and yellow) resonance frequencies and widths obtained from the Lorentzian fits. Each marker denotes a single NPoM measurement. Peak energy and line widths increase with the thickness of the Al_2O_3 spacer. (b) The 1:1 correlation of fitted Lorentzian amplitudes at h/h and h/v polarizations demonstrates that the scattering from the out-of-plane mode is independent of the detection polarization.

the experimental data, we plot the fitted amplitude correlations between h/h and h/v measurements for the (10) mode in Figure 4.22b. The values obtained from the experiment match the theory curve (1:1 correlation, shown in black) very well at each investigated gap thickness.

As for the out-of-plane mode, Figure 4.22a shows the evolution of resonance energy and damping of the two in-plane modes $(1,1)$ and $(1,-1)$ with the gap size. We expect that the two modes are energetically degenerate if the NPoM has a perfect cylindrical symmetry. The degeneracy is lifted if the nanoparticle is elliptical. However, the direction of the semi-axes remains unknown in the first place. Therefore, we sort the two modes of each NPoM by their energy such that $(1,1)$ is the energetically lowest mode. If a single in-plane resonance frequency can describe the NPoM, the energy and damping are only assigned to the $(1,1)$ group. The energy sorting yields two point clouds in the plot with different energy but similar damping parameters. The energetic separation is a measure of the ellipticity of the nanoparticle facets. For instance, the average energies at a gap size of 2 nm are about 1.93 eV and 2.03 eV, corresponding to an energy difference of 100 meV. Comparing this result with the simulated facet-dependent QNM energies in Figure 4.14a, the difference in facet widths must be on the order of 5 nm between the semi-axes of the ellipse. This demonstrates that the facet width is a sensitive parameter for the experimentally obtained spectral positions of in-plane NPoM resonances.

The in-plane modes blue-shift with increasing gap size from approximately 1.9 eV (1 nm gap) to 2.05 eV (4 nm gap). Furthermore, the linewidth increases from about 100 meV to 180 meV, which is about half the value of the out-of-plane mode. This behavior is consistent with the simulations (compare Figure 4.15a), predicting a red-shift from 1.8 eV (2 nm gap) to 2.1 eV (5 nm gap) and a linewidth increase from about 80 meV to 150 meV. As for the out-of-plane mode, the experimentally obtained line widths are systematically larger than the simulated values.

In general, monitoring the in-plane resonance positions has applications in plasmonic sensing [194]. Extending one facet axis by only a single atom can increase the wavelength splitting of the two in-plane modes by approximately 3 nm. Furthermore, evaluating the polarization-dependent amplitudes of both in-plane modes allows the determination of the relative orientation of the ellipse semi-axes to the experimental (h,v) coordinate system. To obtain this information, Kleemann et al. [194] developed an experimental method to rotate the illumination direction 360° around the nanoparticle. Analyzing angle-dependent spectral shifts allows a very sensitive characterization of the nanoparticle facet. However, extracting quantitative information about the facet geometry requires extensive parameter sweeps in numerical simulations.

In conclusion, the asymmetric illumination in our experiment enabled us to analyze the fundamental in-plane and out-of-plane resonances of the NPoM. We modeled the measured scattering spectra as a sum of three Lorentzian resonances. By analyzing the resonance energies and widths, the fits revealed that the NPoM shape varies across the investigated particles. Despite these variations, we could demonstrate that the dependence of the NPoM scattering on the gap thickness agrees well with the numerical simulations. Decomposing the experimental spectra into the fundamental NPoM modes will be required in Chapter 5 to determine the coupling efficiency of an emitter monolayer to the NPoM modes.

5 Fluorescence enhancement of dye monolayers in plasmonic nanoresonators

Due to their strong confinement of electric fields, plasmonic nanoresonators provide a versatile framework for the local enhancement of linear and nonlinear optical processes in adjacent emitters [27, 197]. The increased local density of states inside resonators strongly impacts the spontaneous emission rate. As outlined in Chapter 2.2.4, the spontaneous emission enhancement in dielectric resonators is quantified by the Purcell enhancement

$$F_P = \frac{3}{4\pi^2}\frac{Q}{V}\left(\frac{\lambda}{n}\right)^3 \quad , \tag{5.1}$$

proportional to the ratio of the quality factor Q and mode volume V. The equation can be generalized to $F_P \sim \mathrm{Re}(Q/V)$ in dissipative resonators. Plasmonic nanoparticle-on-mirror resonators have rather moderate quality factors $Q \sim 20$ but exceptionally small mode volumes down to $V \sim 10^{-7}(\lambda/n)^3$. This corresponds to large Purcell enhancement factors of $F_P \sim 10^7$ at room temperature [63]. At the same time, the relatively broad resonances of plasmonic nanostructures allow an efficient spectral overlap with emitters, rendering the devices more tolerant to fabrication inaccuracies [10].

The nanocavity generally affects both radiative as well as non-radiative rates. Quenching is associated with increased non-radiative rates by dissipation in the metal. The decrease in fluorescence intensity lowers the internal quantum efficiency of the emitter. Therefore, an enhancement of radiative rates is desired to speed up the photon emission. The balance of non-radiative and radiative rates ultimately determines the quantum efficiency of the emitter, which is aimed to maintain or even exceed the value in free space. For instance, Russell et al. demonstrated an enhancement of the radiative rate by a factor of 1,000 for Alq_3 emitters sandwiched between a silver nanowire and a silver substrate [26]. At the same time, a high internal quantum efficiency of 0.5 could be maintained. Replacing the nanowire with a plasmonic nanoparticle like a silver nanocube further enhances the quantum efficiency by exploiting the optical nanoantenna effect. For example, Hoang et al. reported an increase in quantum efficiency of a single quantum dot from 20% (QD on glass) to 50% (QD in silver nanocube-on-mirror resonator) [28]. The radiative rate enhancement, thus, enables efficient and bright single photon sources at room temperature.

As demonstrated in Chapter 4, nanoparticle-on-mirror structures feature many fundamental modes. The spectral position of individual resonances can be controlled at least in the statistical average of many NPoMs. For instance, the out-of-plane mode is sensitive to the gap thickness, while the resonance frequency of the in-plane mode scales with the facet size. At the same time, the detected fluorescence intensity enhancement depends on both the excitation and emission enhancement. Therefore, the tunability of the NPoM modes enables the optimization of the spectral overlap of one NPoM mode with the molecule absorption

and another NPoM mode with the molecule emission. This spectral mode-matching has been demonstrated in 2D materials to maximize fluorescence enhancement [35, 198].

Plasmonic nanoresonators do not only alter the total power radiated by the emitter but also the spectral shape. This allows, for example, a selective enhancement of the emission from higher vibrational levels [31, 32]. Furthermore, it has been shown that the available modes of an NPoM shape the emission from broadband silicon quantum dots [33]. The resulting emission spectrum follows the scattering spectrum of the NPoM. Similar experiments with an asymmetric nanorod-on-mirror (NRoM) geometry showed that the emission spectrum follows the polarization dependence of the available modes [34].

Besides the spectral overlap of the NPoM modes with the emitter spectrum, the near-field distribution of the NPoM modes enormously influences the excitation and emission enhancement of emitters in the gap. Depending on its spatial position, an emitter couples to the ensemble of NPoM modes with different efficiencies. Horton et al. demonstrated that the near-field coupling translates into a distinct far-field radiation pattern of fluorescence emission [177]. Analysis of the point spread function allowed them to calculate the position of the individual emitter in the gap with sub-diffraction resolution.

However, modeling the fluorescence enhancement of emitter ensembles inside plasmonic nanoresonators remains challenging. Previous publications mainly discuss that the shape of the observed fluorescence enhancement spectra follows the scattering spectra from the nanoresonator [33, 34]. These findings prove that the emitters can radiate efficiently into the far-field via the modes provided by the nanoresonators. Quantitative comparisons have focused on the enhanced emission from individual or multiple transitions by a single plasmonic mode [27, 35, 110]. Generally, plasmonic nanoresonators feature many modes which can also spectrally overlap. Therefore, numerical simulations are required to obtain fluorescence enhancement factors for comparison with the experiment [26, 31].

In this chapter, we present a comprehensive model for the interaction between emitter ensembles and NPoMs based on a quasi-normal mode expansion in the weak coupling limit. This model extends the work of Kongsuwan et al. for a single emitter with a sharp transition [45] to an incoherent ensemble of broadband emitters. Specifically, we compute the spectral dependence of the fluorescence enhancement, giving access to the coupling coefficients of broadband emitters to particular NPoM modes. We particularly focus on the ratio of coupling coefficients between the lowest-energy out-of-plane and in-plane modes for direct comparison with experiments. In the experiment, the spectrally broad fluorescence allows us to monitor the Purcell enhancement over a wide wavelength interval. To consider variations between the nanoresonators, we analyze the polarization-dependent fluorescence enhancement of many different NPoMs. Furthermore, we study the competition of photobleaching and spontaneous emission rates, comparing the coupled and uncoupled dye monolayers. Finally, we discuss future experiments to observe strong coupling in dye monolayers. Furthermore, we present our first results on nanostructured ultrathin spacers, which are promising building blocks to enable long-range dipole-dipole interactions in the future.

5.1 Numerical model

This section presents a universal model for the fluorescence enhancement of an oriented incoherent emitter ensemble in a plasmonic nanoresonator. The procedure is divided into three steps. First, we compute the near-field coupling of a single dipole to the radiating modes of an NPoM based on Ref. [45]. Second, we calculate the excitation strength of this dipole based on the electric near-field at the excitation wavelength. In the third step, we combine the excitation and emission enhancement to derive the fluorescence enhancement of an oriented incoherent emitter ensemble.

In the experiment, we incorporate the encapsulated dye monolayers into the NPoM cavity. To directly compare experiment and simulation, we model the NPoM gap as a homogeneous dielectric layer with 4 nm thickness and a refractive index of $n = 1.5$. The gold nanoparticle is simulated as an 80 nm truncated sphere with $w = 20$ nm facet width, as sketched in Figure 5.1a.

Figure 5.1b shows the spectral positions of the computed QNMs. The resonance frequencies $\mathrm{Re}(\tilde{\omega}_i)$ and FWHM linewidths $\Gamma = 2 \cdot \mathrm{Im}(\tilde{\omega}_i)$ determine the Lorentzian resonances. The contributions are normalized by their energy content. The out-of-plane mode $(l, m) = (1, 0)$ at around 1.84 eV and the two energetically degenerate in-plane modes $(1, \pm 1)$ at around 2.1 eV are well separated in the spectrum. Higher-order modes have significant spectral overlap and accumulate at the interband transition of gold. Only QNMs with $l \leq 2$ are shown in the spectrum for better visibility. Also in the experiment, we will exclude higher-order modes from the analysis. The grey area sketches the average fluorescence emission spectrum of the dye monolayer on a gold substrate. The dye used in this work is well suited to investigate the mode-dependent coupling to the NPoM, as the broadband emission spectrally overlaps with all computed QNMs.

5.1.1 Near-field coupling of a single dipole to the NPoM modes

We model the single emitter at position $\boldsymbol{r}_{\mathrm{em}}$ as a dipole moment $\boldsymbol{\mu}(\boldsymbol{r}_{\mathrm{em}})$ with real-valued emission frequency ω_{em}. Mediated by near-field coupling with the NPoM, the dipole can radiate into the far-field via the modes of the NPoM. Specifically, we write the emitted electric field as a superposition of M quasi-normal modes $\tilde{\boldsymbol{E}}_i$ with associated complex frequencies $\tilde{\omega}_i$ [64]

$$\boldsymbol{E}(\boldsymbol{r}) = \sum_{i=1}^{M} \alpha_i(\boldsymbol{r}_{\mathrm{em}}, \omega_{\mathrm{em}})\, \tilde{\boldsymbol{E}}_i(\boldsymbol{r}) \quad , \tag{5.2}$$

where $\alpha_i(\boldsymbol{r}_{\mathrm{em}}, \omega_{\mathrm{em}})$ are the excitation coefficients of the i-th QNM. Equation 5.2 is exact if we consider all QNMs, i.e., $M \to \infty$. However, a small number of QNMs is typically sufficient for a dipole inside the cavity. For example, Kongsuwan et al. used the first $M = 20$ QNMs of the NPoM with a 1 nm dielectric gap [45]. The mode excitation coefficients α_i depend on the position and frequency of the emitter, as both the local electric field of the QNMs and the spectral overlap with the QNMs enter. Application of the unconjugated

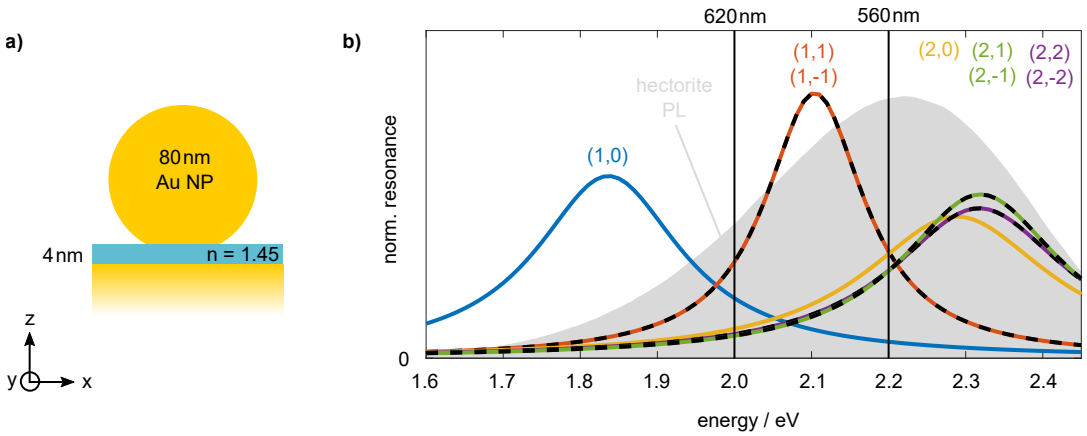

Fig. 5.1.: (a) Sketch of the simulation geometry with a 4 nm dielectric spacer between the gold nanoparticle and the gold mirror. (b) Lorentzian resonances of the computed QNMs labeled as spherical harmonics (l, m). The QNMs overlap with the broad fluorescence spectrum of the dye monolayer on a gold substrate (shaded grey). Two energies are marked in the spectrum, corresponding to the emitter wavelengths $\lambda_{\mathrm{em}} = 560\,\mathrm{nm}$ and 620 nm.

form of the Lorentz reciprocity theorem allows us to obtain a linear equation system for the mode excitation coefficients

$$\sum_{j=1}^{M} B_{i,j}(\omega_{\mathrm{em}})\,\alpha_j(\boldsymbol{r}_{\mathrm{em}}, \omega_{\mathrm{em}}) = -\omega_{\mathrm{em}}\boldsymbol{\mu}(\boldsymbol{r}_{\mathrm{em}}) \cdot \tilde{\boldsymbol{E}}_i(\boldsymbol{r}_{\mathrm{em}}) \quad , \tag{5.3}$$

using the definition of a frequency-dependent coupling matrix [45, 64]

$$B_{i,j}(\omega) = \iiint_{\Omega} \left[\tilde{\boldsymbol{E}}_j \cdot (\omega\varepsilon(\boldsymbol{r}, \omega) - \tilde{\omega}_i\varepsilon(\boldsymbol{r}, \tilde{\omega}_i))\tilde{\boldsymbol{E}}_i - \mu_0\tilde{\boldsymbol{H}}_j \cdot (\omega - \tilde{\omega}_i)\tilde{\boldsymbol{H}}_i\right] d^3\boldsymbol{r} \quad . \tag{5.4}$$

Note that this matrix is diagonal only if all materials in the simulation domain are dispersionless. In our case of dispersive gold nanostructures, the coupling matrix generally has non-zero off-diagonal values. $B_{i,j}$ depends on the frequency, as the spectral overlap between the emitter and the QNMs determines the selective coupling to particular modes. The equation system is solved by matrix inversion [45]

$$\alpha_i(\boldsymbol{r}_{\mathrm{em}}, \omega_{\mathrm{em}}) = -\omega_{\mathrm{em}} \sum_{j=1}^{M} B^{-1}_{i,j}(\omega_{\mathrm{em}})\,\boldsymbol{\mu}(\boldsymbol{r}_{\mathrm{em}}) \cdot \tilde{\boldsymbol{E}}_j(\boldsymbol{r}_{\mathrm{em}}) \quad . \tag{5.5}$$

The mode excitation coefficients are proportional to the projection of the dipole moment $\boldsymbol{\mu}$ onto the local electric field of each QNM. The internal coupling between different QNMs furthermore requires to sum over all QNMs weighted by the inverse coupling matrix $B^{-1}_{i,j}$.

In the experiment, the dye monolayer is sandwiched between two hectorite nanosheets. Hence, we assume that the dipole is located in the center of the dielectric spacer, 2 nm above the gold substrate. We use the $M = 43$ lowest energy QNMs in the mode expansion that the Comsol solver can stably compute. Figure 5.2a shows the two-dimensional map

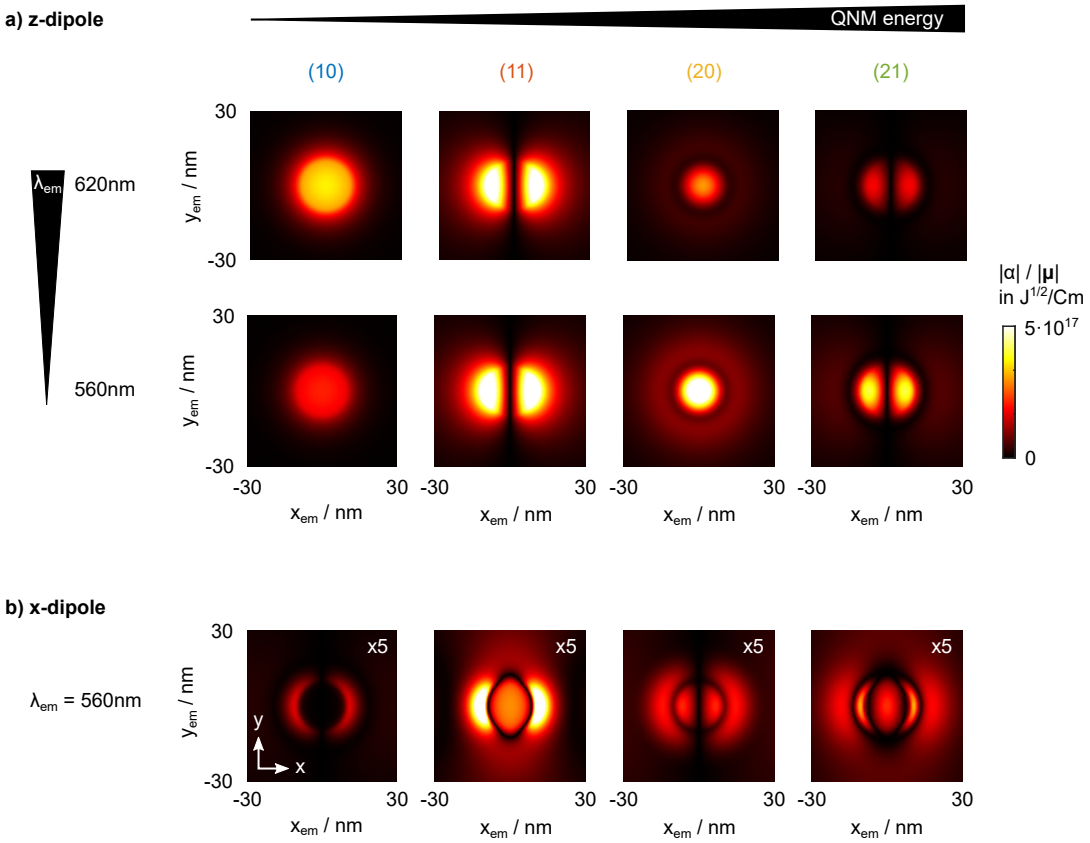

Fig. 5.2.: Near-field coupling of a single dipole to the four energetically lowest QNMs of an NPoM. (a) Spatial map of the mode excitation coefficients $|\alpha_i|$ for a z-dipole with lateral position $(x_{\mathrm{em}}, y_{\mathrm{em}})$ in the gap. Compared are the emitter wavelengths $\lambda_{\mathrm{em}} = 620\,\mathrm{nm}$ (first row) and 560 nm (second row). (b) Mode excitation coefficients as a function of the lateral position of an x-oriented dipole. Only the computation at $\lambda_{\mathrm{em}} = 560\,\mathrm{nm}$ is shown, as the results at $\lambda_{\mathrm{em}} = 620\,\mathrm{nm}$ are similar. The computed coefficients for the x-dipole are significantly smaller than for the z-dipole in (a). The values of $|\alpha_i|$ are amplified by a factor of 5 for visibility.

of the mode excitation coefficients for a dipole located at the lateral position (x_{em}, y_{em}). Compared are the coupling coefficients for the four relevant energetically lowest QNMs at two emission wavelengths of the dipole, $\lambda_{em} = 620\,\text{nm}$ and 560 nm. For the moment, we only consider dipoles oriented in z-direction. The plots show the absolute values of the mode excitation coefficients $|\alpha_i|$ normalized to the dipole moment $|\boldsymbol{\mu}|$. The spatial distribution of α matches the electric field profile of the respective QNM, as the coupling scales with the projection of the dipole moment onto the local electric field. For example, a dipole placed in the lateral center of the NPoM $(x_{em}, y_{em}) = (0, 0)$ can not couple to modes with odd values of m, such as $(l, m) = (1, \pm 1)$, since the electric field has a zero crossing in the origin. A zero-crossing of the electric field corresponds to a phase flip of α. The interference between modes gives rise to significant variations in the radiated electric field depending on the dipole position in the gap [45].

Besides variations of the α_i with the dipole position, the coupling coefficients depend on the spectral position of the emitter. At an emission wavelength of 620 nm, the mode excitation coefficients have the highest values for the $(1, 0)$ and the $(1, \pm 1)$ modes. This can be explained by the significant spectral overlap with both modes, which boosts the respective contributions in $B^{-1}_{i,j}$ (compare Figure 5.1b). In contrast, the spectral overlap with the $(1, 0)$ mode is much weaker at an emitter wavelength of $\lambda_{em} = 560\,\text{nm}$. As a consequence, α has the most dominant contributions at the $(1, \pm 1)$ and higher-order modes.

Until now, we assumed that the dipoles are oriented along the z-direction. For comparison, Figure 5.2b shows the spatial distribution of the α_i for a dipole at a lateral position (x_{em}, y_{em}) oriented along the x-direction. The mode excitation coefficients are amplified by a factor of 5 for better visibility. Obviously, the near-field coupling of an in-plane dipole is much weaker than that of an out-of-plane dipole. The Figure only shows the computation at $\lambda_{em} = 560\,\text{nm}$, as the results at 620 nm are very similar. The poor coupling of the x-oriented dipole is caused by the small in-plane electric field in the gap. Our comparison of E_x, E_y, and E_z for a 1 nm gap in Figure 4.13 also applies to the larger 4 nm gap discussed here.

5.1.2 Dye excitation enhancement by NPoMs

The theoretical framework introduced in the last section allows a quantitative description of the near-field coupling between a single dipole and the NPoM. We found that the coupling scales with the position, orientation, and emission wavelength of the dipole. Furthermore, the magnitude of the dipole moment enters into the coupling coefficient in Equation 5.5. If we consider a single dipole, the dipole strength is only a global scaling factor. However, our goal is to model the excitation and subsequent emission of an incoherent ensemble of spatially distributed emitters. This requires quantitative information about the excitation strength of a dipole as a function of its lateral position in the gap.

The excitation probability of a dipole in the gap of an NPoM at a position $\boldsymbol{r}_{em}$ is determined by the local electric field at the excitation frequency ω_{exc}. Specifically, the induced dipole

moment $\boldsymbol{\mu}$ scales with the projection of the local electric field $\boldsymbol{E}$ onto the dipole direction (unit vector $\hat{\boldsymbol{e}}_\mathrm{d}$) as

$$\boldsymbol{\mu}(\boldsymbol{r}_\mathrm{em}, \omega_\mathrm{exc}) = A(\omega_\mathrm{exc})\,[\hat{\boldsymbol{e}}_\mathrm{d} \cdot \boldsymbol{E}(\boldsymbol{r}_\mathrm{em}, \omega_\mathrm{exc})]\,\hat{\boldsymbol{e}}_\mathrm{d} \quad . \tag{5.6}$$

The absolute value of the induced dipole moment depends on the amplitude of the electric field as well as a (complex-valued) scalar absorption parameter $A(\omega_\mathrm{exc})$. The absorption probability is related to the transition dipole moment of the molecule absorption. The excitation frequency is constant in all measurements. Hence, the absorption parameter is only a global scaling factor for the overall efficiency of the excitation and emission process. In contrast, the electric field amplitude $\boldsymbol{E}(\boldsymbol{r}_\mathrm{em}, \omega_\mathrm{exc})$ is a local quantity which needs to be calculated using numerical simulations.

As sketched in Figure 5.3a, the NPoM is illuminated with a plane wave traveling perpendicular to the substrate at a wavelength $\lambda = 485\,\mathrm{nm}$. The incident electric field is polarized in x-direction. The electric field distribution is computed in Comsol using the scattered field formulation. As discussed in Chapter 4.2.6, the background field is analytically calculated to fulfill the boundary conditions. The amplitude of the electric field traveling towards the nanostructure is normalized to $|\boldsymbol{E}_\mathrm{exc}| = 1$. Figure 5.3b shows the computed electric field distribution in the xz-plane. Notably, the electric field has the largest amplitude next to the nanoparticle, with a maximum electric field enhancement of $|\boldsymbol{E}|/|\boldsymbol{E}_\mathrm{exc}| \approx 5$. In comparison, the enhancement in the gap region is about 3. The weak localization of the electric field in the gap originates from the spectral detuning of the excitation frequency from the fundamental NPoM modes. Therefore, only less confined higher-order modes are excited, which match the symmetry of the incident electric field. Note that the electric field distribution could be represented as a superposition of QNMs similar to the approach in the last section. However, the significant spectral overlap of the blue illumination laser with higher-order QNMs hinders the expansion by a small number of quasi-normal modes. In this case, the scattered field simulation is more precise in calculating the excitation field distribution.

For our application, we are interested in the electric field distribution in the center of the spacer layer where the dye molecules between the hectorite nanosheets are located. Figure 5.3c-e shows the spatial distribution of the real part of the electric field components E_x, E_y, and E_z. The electric field profile suggests that the $(l, m) = (2, 1)$ mode is efficiently excited, as E_z has one node in radial and angular directions, respectively. The x-polarized excitation generates intense vertical electric field components in the facet region with maximum $\mathrm{Re}(E_z) \approx 1$, while the in-plane contributions are considerably smaller. Outside the facet area are distinct regions with significant contributions of all electric field components.

We aim to calculate the fluorescence enhancement spectra of emitters in the NPoM gap for comparison with the experiments. Therefore, we need to consider the excitation and emission enhancement. First, the magnitude of the induced dipole moment in Equation 5.6 scales with the projection of the electric field onto the dipole direction. Knowledge of the dipole orientation, thus, allows us to determine the excitation enhancement of a particular dipole. Second, the molecule relaxes to an energetically lower level quickly after absorbing a photon. Depending on the local coupling coefficients, the molecule then

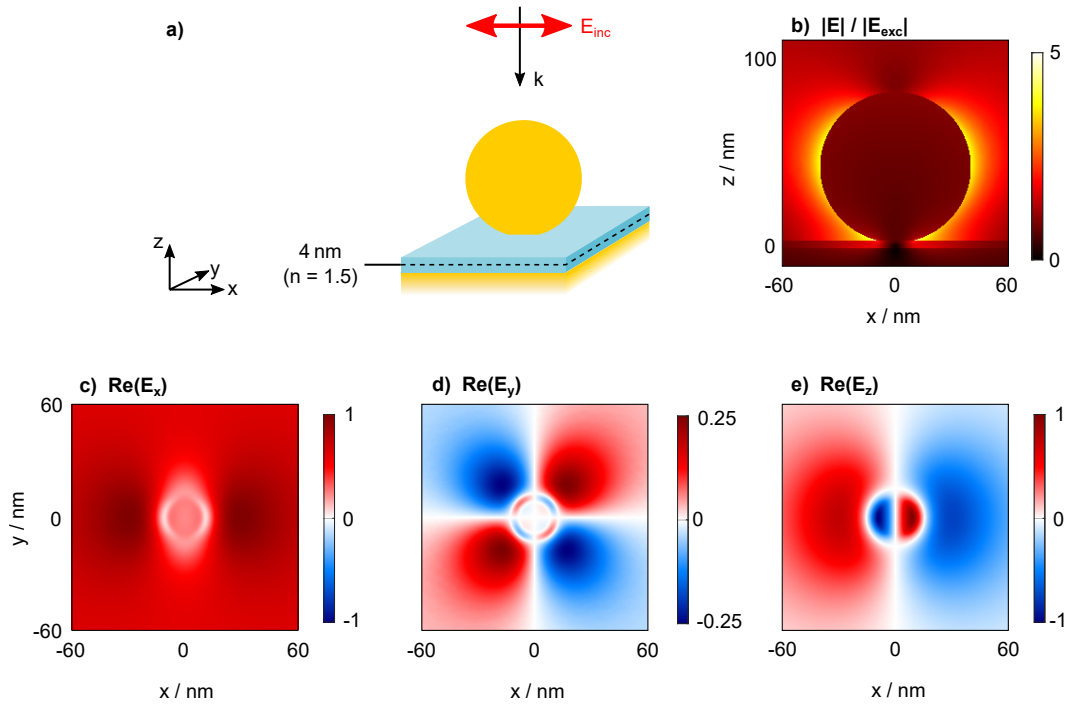

Fig. 5.3.: Simulated electric near-field distribution of the NPoM at perpendicular illumination with $\lambda = 485\,\text{nm}$ polarized in x-direction. (a) Sketch of the geometry, where the embedded dye monolayer is modeled as a dielectric with 4 nm thickness. (b) Calculated distribution of $|\boldsymbol{E}|/|\boldsymbol{E}_{\text{exc}}|$ in the xz-plane. (c-e) Spatial distribution of the real part of the electric field components E_x, E_y, and E_z in the center of the gap (xy-plane).

radiates fluorescence via the NPoM modes. The near-field coupling coefficients to the NPoM modes at a particular emission frequency ω_{em} can be calculated with Equation 5.5.

Assuming a dipole oriented in z-direction, Figure 5.4a depicts the resulting mode excitation coefficients as a function of the dipole position. The excitation field profile shown on the left is imprinted onto the spatial distribution of the mode excitation coefficient $|\alpha_i|$ in the gap shown on the right. For example, the product of the axially symmetric excitation field profile with the radially symmetric field profile of the $(1,0)$ mode yields an axially symmetric spatial pattern of the respective mode excitation coefficients. Hence, the symmetry of the excitation field distribution is passed on to the spatial distribution of the α_i. Consequently, the α_i maps of energetically degenerate modes $(l,\pm|m|)$ are not equivalent anymore upon rotation. This is demonstrated in Figure 5.4a for the modes $(1,\pm1)$ and $(2,\pm1)$. As the excitation field is x-polarized, the dipole emission prefers the $(1,1)$ over the $(1,-1)$ mode. The same holds for the $(2,\pm1)$ modes. As the dipole excitation strength is zero in the gap center, a dipole does not emit into any mode at this position.

5.1.3 Enhanced far-field emission from an incoherent dipole ensemble

Due to the near-field coupling, the emitter radiates into the far-field via the NPoM modes. Computing the far-field response is essential to compare the fluorescence enhancement with the experiment. The near-to-far-field transform provided by the software package RETOP allows us to calculate the electromagnetic far-fields $\tilde{\boldsymbol{E}}_i^{\mathrm{ff}}(\theta,\phi,\omega_{\mathrm{em}})$ and $\tilde{\boldsymbol{H}}_i^{\mathrm{ff}}(\theta,\phi,\omega_{\mathrm{em}})$ of the i-th QNM at the emission frequency ω_{em} of the emitter radiated into the direction given by the angles (θ,ϕ). For a single dipole at position $\boldsymbol{r}_{\mathrm{em}}$ in the gap, the coherent superposition of the first M quasi-normal modes weighted by the position-dependent mode excitation coefficients then yields a total electromagnetic far-field [45]

$$\tilde{\boldsymbol{E}}^{\mathrm{ff}}(\theta,\phi,\boldsymbol{r}_{\mathrm{em}},\omega_{\mathrm{em}}) = \sum_{i=1}^{M} \alpha_i(\boldsymbol{r}_{\mathrm{em}},\omega_{\mathrm{em}})\tilde{\boldsymbol{E}}_i^{\mathrm{ff}}(\theta,\phi,\omega_{\mathrm{em}}) \quad , \tag{5.7}$$

$$\tilde{\boldsymbol{H}}^{\mathrm{ff}}(\theta,\phi,\boldsymbol{r}_{\mathrm{em}},\omega_{\mathrm{em}}) = \sum_{i=1}^{M} \alpha_i(\boldsymbol{r}_{\mathrm{em}},\omega_{\mathrm{em}})\tilde{\boldsymbol{H}}_i^{\mathrm{ff}}(\theta,\phi,\omega_{\mathrm{em}}) \quad . \tag{5.8}$$

We obtain the power radiation pattern by evaluating the time-averaged Poynting flux $\langle \boldsymbol{S} \rangle = \frac{1}{2}\mathrm{Re}\left[\left(\tilde{\boldsymbol{E}}^{\mathrm{ff}}\right)^* \times \tilde{\boldsymbol{H}}^{\mathrm{ff}}\right]$. Figure 5.4b compares radiation plots of a single dipole at three exemplary positions in the gap at an emission wavelength of $\lambda_{\mathrm{em}} = 620\,\mathrm{nm}$. In agreement with the spatial distribution of the mode excitation coefficients in Figure 5.4a, the radiation of a dipole at $(x_{\mathrm{em}}, y_{\mathrm{em}}) = (5,0)\,\mathrm{nm}$ is dominated by the ring-shaped emission from the out-of-plane NPoM mode. The off-center position of the dipole breaks the cylindrical symmetry, giving rise to an asymmetric far-field radiation pattern. At $(x_{\mathrm{em}}, y_{\mathrm{em}}) = (10,0)\,\mathrm{nm}$ and $(15,0)\,\mathrm{nm}$, however, the emission from the in-plane NPoM mode takes over. It has been shown in the literature that the shape of the radiation pattern is a fingerprint of the

dipole position in the gap. An NPoM can therefore be used as plasmonic nanolens with sub-diffraction resolution [177].

In the experiment, we investigate the fluorescence enhancement of the broadband-emitting dye monolayer by the NPoM modes. Therefore, we extend the established model for a single narrowband dipole to describe an incoherent ensemble of broadband emitters in the gap [45]. To accomplish this, we calculate the far-field emission of a single dipole at every lateral position $(x_{\mathrm{em}}, y_{\mathrm{em}})$ in the gap using our polarized imaging computation method. Our theoretical predictions and experimental observations in Chapter 3.3 prove a homogeneous distribution of the dye molecules sandwiched between the hectorite nanosheets. The molecules in the gap emit incoherently into the far-field via the NPoM modes. Each dipole yields an intensity pattern $I_{x_{\mathrm{em}},y_{\mathrm{em}}}(x,y)$ at the position (x,y) on the detector. To model the homogeneous distribution of incoherent emitters, we sum up the intensities at the detector originating from all dipole positions $(x_{\mathrm{em}}, y_{\mathrm{em}})$ in the gap at a defined emission wavelength λ_{em} according to

$$I_{\mathrm{det}}(x,y,\lambda_{\mathrm{em}}) = \iint \mathrm{d}x_{\mathrm{em}}\mathrm{d}y_{\mathrm{em}}\, I_{x_{\mathrm{em}},y_{\mathrm{em}},\lambda_{\mathrm{em}}}(x,y) \quad . \tag{5.9}$$

Specifically, we integrate over a $60 \times 60\,\mathrm{nm}^2$ area in the NPoM gap. We assume that all molecules outside this area mainly emit into free space independent of the NPoM and, hence, do not contribute to the fluorescence enhancement. The calculation is repeated at different emission wavelengths between $\lambda_{\mathrm{em}} = 500\,\mathrm{nm}$ and 800 nm, covering the broadband emission from the encapsulated dye monolayer. The calculated spectra represent the fluorescence enhancement provided by the NPoM, assuming that the emission of the uncoupled dipole is spectrally flat. This calculation does not consider other photophysical processes in the molecules competing with the emission via the NPoM. In the following, we analyze the spatially integrated intensity values on the detector

$$I_{\mathrm{det}}(\lambda_{\mathrm{em}}) = \iint \mathrm{d}x\mathrm{d}y\, I_{\mathrm{det}}(x,y,\lambda_{\mathrm{em}}) \quad . \tag{5.10}$$

Figure 5.4c compares the fluorescence enhancement spectra $I_{\mathrm{det}}(\lambda_{\mathrm{em}})$ of an incoherent ensemble of dipoles oriented in x-direction (left), y-direction (center), and z-direction (right) after x-polarized excitation. The spectra are normalized to the maximum intensity of the z-dipoles, which is almost three orders of magnitude larger than that of the x-dipoles and nearly four orders of magnitude larger than that of the y-dipoles. As we know from the orientation determination in Chapter 3.3, both transition dipoles of the dye have significant out-of-plane orientations $\theta_1 = 34°$ and $\theta_2 = 54°$ on a gold substrate. Hence, we can neglect the projected in-plane dipole component of the molecules embedded in the gap, as the NPoM modes only efficiently couple to the out-of-plane components of the dipoles.

The fluorescence enhancement of the z-oriented incoherent dipole ensemble has two prominent peaks matching the spectral positions of the out-of-plane mode $(1,0)$ and the in-plane modes $(1,\pm1)$. Furthermore, higher-order modes contribute at an energy of about 2.3 eV, giving rise to the slightly asymmetric lineshape of the in-plane mode peak. We will directly compare this simulated fluorescence enhancement spectrum with the

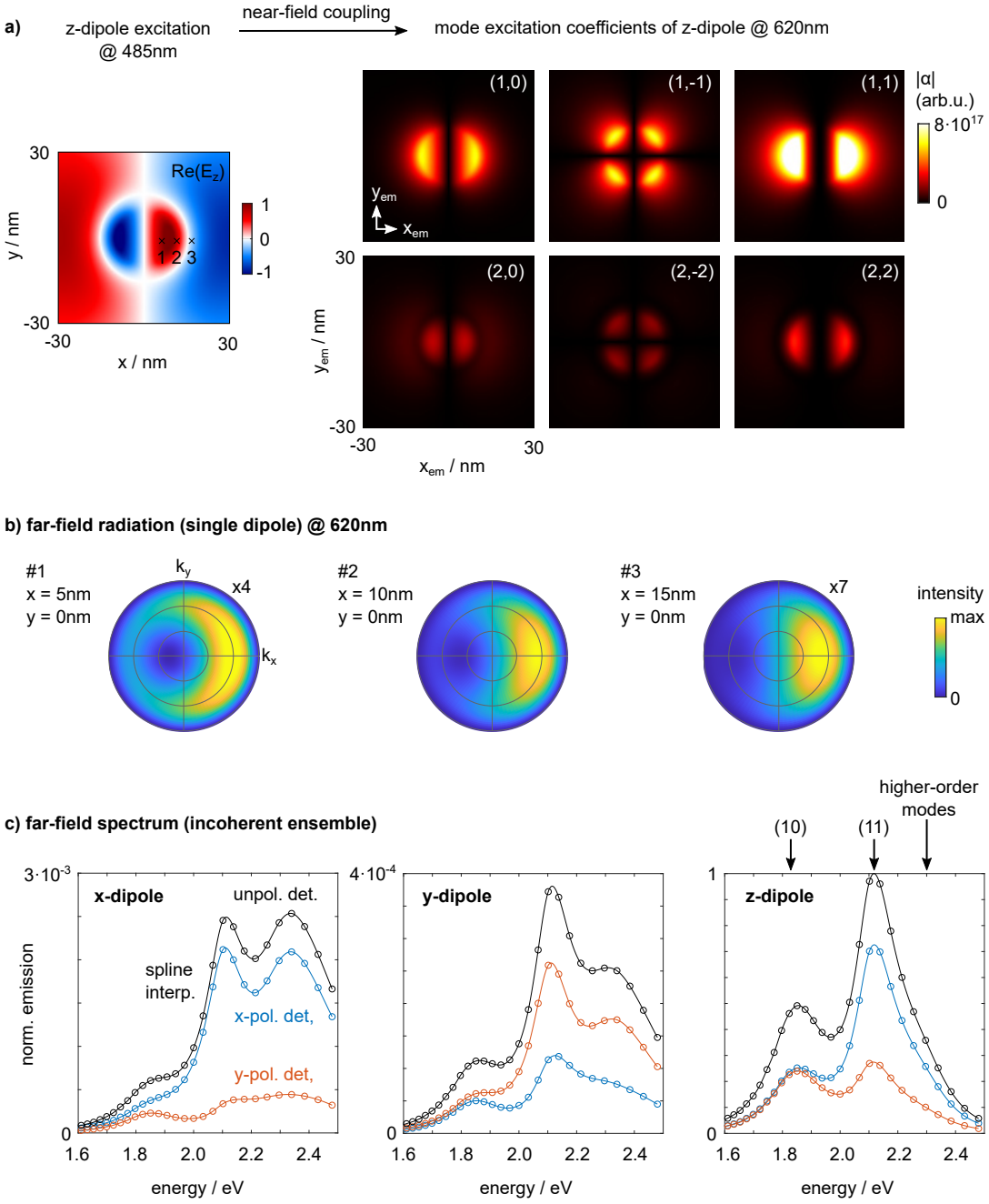

Fig. 5.4.: Fluorescence of an incoherent dye ensemble via NPoM modes. (a) The excitation field distribution at $\lambda_{\mathrm{exc}} = 485\,\mathrm{nm}$ is imprinted on the near-field mode excitation coefficients α_i of a z-dipole in the NPoM gap. $|\alpha_i|$ is shown for the six energetically lowest QNMs as a function of the dipole position $(x_{\mathrm{em}}, y_{\mathrm{em}})$. (b) At an emission wavelength of $\lambda_{\mathrm{em}} = 620\,\mathrm{nm}$, the computed radiation patterns and total intensities vary with the position of the single dipole in the gap. We compare three positions which are also marked in (a). (c) Comparison of the far-field emission spectra of an incoherent emitter ensemble in the NPoM oriented along x (left), y (center), and z (right). The spectra depend on the detection polarization. The spectral positions of the (10), (11) and higher order modes are marked above the right plot.

measurements in Chapter 5.2. Our calculations show that the peak enhancement of the in-plane mode is stronger than the out-of-plane mode at the respective resonance positions. Lorentzian fits reveal that the energy radiated via the in-plane modes is about a 75% greater than the out-of-plane mode. In the first place, this result is surprising, as the simulated scattering spectra showed that the in-plane mode radiates much less efficiently into the far-field than the out-of-plane mode (see Figure 4.19). However, the perpendicular excitation direction and the off-resonant excitation at $\lambda_{\text{exc}} = 485\,\text{nm}$ attenuate the coupling to the out-of-plane mode. This is evident from the different symmetries of the (10) mode and the excitation field distribution. We conclude that the choice of excitation parameters has a paramount influence on the coupling of dye layers to nanoresonators. Hence, the excitation process provides a variety of setscrews to optimize the dipole emission via a particular set of modes.

Figure 5.4c compares the fluorescence enhancement spectra for x- (blue) and y-polarized detection (orange). The sum of both intensities yields the unpolarized spectrum (solid black line). The emission from the (10) mode does not depend on the detection polarization, consistent with the associated out-of-plane dipole direction of the mode. The emission from the in-plane modes is sensitive to the detection-polarization, having an intensity contrast ratio of about $I_{x\text{-det.}}/I_{y\text{-det.}} = 2.6$. Hence, the emission enhancement of the dye monolayer memorizes the polarization direction of the excitation light, although the emission is incoherent. This “memory” results from imprinting the polarization-dependent excitation field profile on the dye layer, which is an important result of our theoretical modeling.

5.2 Experimental determination of the fluorescence enhancement

The broadband emission of the encapsulated dye monolayer allows us to investigate the fluorescence enhancement spectra in the experiment. For this, we prepare samples where the dye monolayer is incorporated into the NPoMs. Polarization-resolved scattering and fluorescence spectroscopy provide complementary information about the NPoM modes and their interaction with the dye monolayer. We investigate many NPoMs to provide statistical information about the coupling efficiencies for comparison with the simulation results.

5.2.1 Sample preparation

The samples are fabricated in a two-step procedure by depositing the hectorite nanosheets (compare Section 3.3.4) on a gold substrate and then dropcasting the gold nanoparticles (compare Section 4.1). Specifically, gold substrates are prepared by template-stripping from a silicon wafer using the Norland NOA63 optical adhesive. The gold substrate is made hydrophilic by air plasma treatment for 1 minute. The centrifuged and diluted aqueous hectorite nanosheet solution is dropcasted onto the substrate, dried at room temperature, and baked at 60°C for 1 hour. Then, 50 µl of the aqueous 80 nm colloidal gold nanoparticle solution is dropcasted onto the sample. The sample is covered by a

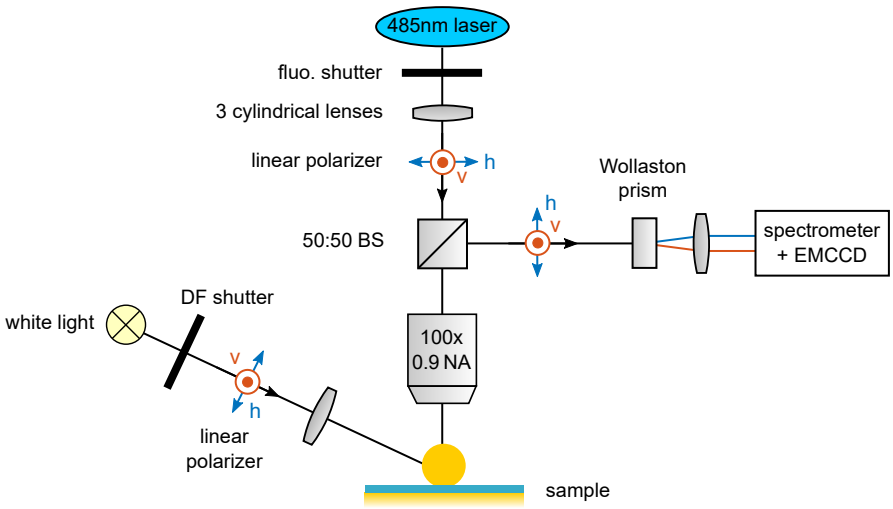

Fig. 5.5.: Experimental setup for darkfield (DF) scattering and fluorescence spectroscopy with spatial and polarization resolution. Using electronically controlled shutters, we switch between perpendicular illumination for fluorescence and side illumination for scattering measurements.

plastic hood to prevent the water droplet from evaporating. After around 20 minutes, a sufficient density of gold nanoparticles adhering to the hectorite is reached, and the residue is blown off with nitrogen.

5.2.2 Experimental setup

An independent measurement of scattering and fluorescence spectra allows us to determine the NPoM resonances and the relative coupling strengths of the dye monolayer to the NPoM modes. We combine the experimental methods for polarization-resolved fluorescence spectroscopy (see Chapter 3.3) and scattering spectroscopy (see Chapter 4.4), as shown in Figure 5.5. As in the previous experiments, we scan a large area for statistical analysis of many coupled systems. The spatial resolution lets us determine the fluorescence enhancement by comparing coupled and uncoupled dye monolayers. Furthermore, we can separate the different modes by analyzing the diffraction pattern of the NPoMs.

The fluorescence intensities are corrected by the inhomogeneous excitation intensity profile resulting from the elliptical spot profile. Furthermore, we correct the intensities by the polarization-dependent laser excitation power. Separate mechanical shutters for the fluorescence and white light excitation beam paths are electronically controlled to alternate between scattering and fluorescence measurements. The linear polarization of both excitation beams is adjusted by wire grid polarizers in electronically controlled rotation mounts. In the detection path, the horizontal and vertical polarization is spatially separated on the spectrometer camera chip by a Wollaston prism. As in the previous experiments, we choose a slit width of 1.2 µm projected onto the sample. Each frame acquired with the spectrometer camera provides spatial and spectral information. The

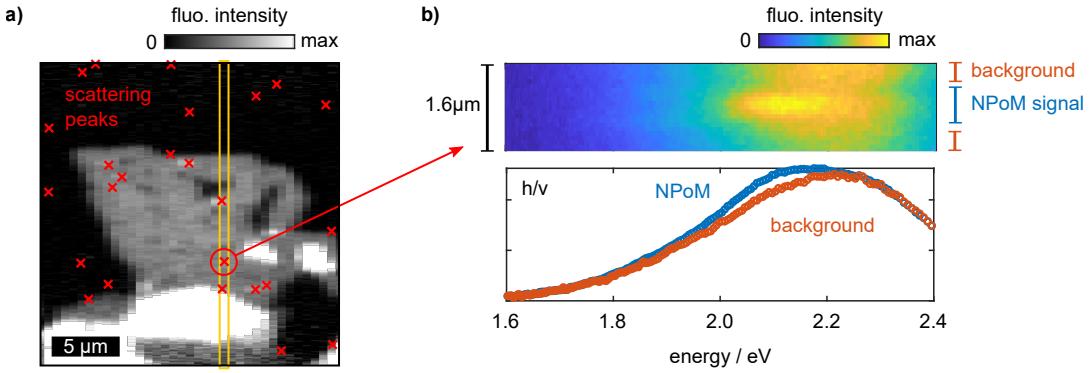

Fig. 5.6.: (a) Unpolarized fluorescence intensity map of the dye monolayer on a gold substrate. The red crosses indicate NPoM positions retrieved from scattering measurements. The yellow rectangle shows the width of the spectrometer entrance slit projected onto the sample. (b) Spatially resolved fluorescence spectrum of an NPoM on the dye monolayer at the position marked in (a) at h/v polarization. The intervals on the right denote areas of the NPoM and the uncoupled background. The plot below shows averaged fluorescence spectra of the NPoM and the background.

sample is scanned horizontally in steps of the half projected slit width to retrieve complete 2D spatial data of the sample.

The experiment aims to measure the fluorescence enhancement spectra of the dye monolayer coupled to the NPoM and to correlate it with the NPoM modes. Therefore, we first need to find relevant positions on the sample where a dye monolayer spatially overlaps with an individual NPoM. In the first step, we scan the sample over a large area to obtain fluorescence and scattering intensities at a low integration time of 1 s per frame and a laser excitation power of about 1 µW. Based on the results of the screening measurement, we choose a smaller scan area to measure a particular dye monolayer. At each scan position, fluorescence and scattering spectra are subsequently acquired. The scattering intensity map provides distinct maxima corresponding to the spatial positions of NPoMs. Figure 5.6a shows the fluorescence intensity map of a dye monolayer, integrated over all combinations of excitation and detection polarization. The red markers indicate the manually extracted positions of NPoMs retrieved from the scattering intensity map. We identify multiple spatial coincidences of dye monolayer and NPoM. Each of these relevant NPoMs is investigated in more detail, exemplarily shown for the highlighted NPoM (red circle) in the following.

The NPoM is horizontally centered in the spectrometer entrance slit, as sketched by the yellow frame in the fluorescence intensity map in Figure 5.6a. We perform a series of measurements to retrieve as much information as possible about the NPoM and the dye monolayer next to it. First, we measure the scattering spectra at both excitation polarizations. Second, we measure the fluorescence spectra in $15 + 15 = 30$ acquisitions, alternating between vertically and horizontally polarized excitation in each successive frame. We integrate 20 s per frame, corresponding to a 10 min total integration time per NPoM. The laser excitation power is 2.3 µW. This measurement scheme has distinct advantages over two acquisitions with long integration times, as we limit the impact of the inevitable photobleaching at one excitation polarization onto the second measurement with orthogonal polarization. Furthermore, we can monitor the photobleaching of the

coupled and uncoupled dye monolayer as a function of the discrete time steps provided by the successive acquisitions. Before analyzing the photobleaching (see Chapter 5.3), we add up the 15 raw spectra at each excitation polarization to determine the total fluorescence enhancement spectra. After measuring the fluorescence spectra, we repeat the scattering measurements. Sample drifts can be detected by comparing the scattering spectra before and after the fluorescence measurements. We found that sample drifts are negligible on the experiment timescale. Hence, we sum up the early and late scattering measurements at each position to increase the signal-to-noise ratio.

Figure 5.6b shows the spatially resolved fluorescence spectrum at the NPoM position marked in (a) at h/v polarization. The vertical axis represents a spatial interval of 1.6 µm on the sample. We observe an increased fluorescence intensity at the NPoM position with respect to the uncoupled dye monolayer above and below the NPoM. Furthermore, the spectral shape of the enhanced fluorescence clearly differs from the uncoupled dyes. We spatially average over the NPoM and the background fluorescence, as indicated by the intervals next to the image, to obtain the spectra of the coupled and uncoupled dye monolayer shown below the raw image. In total, the NPoM fluorescence is averaged over a sample area of $1.2\,\mu m \times 1.2\,\mu m = 1.44\,\mu m^2$, which is the product of the projected spectrometer entrance slit width and the vertical averaging interval in the image. We compare the fluorescence averaging area with the area of the field confinement area in the NPoM, approximated by the facet area $\pi(w/2)^2 \approx 300\,nm^2$. Assuming a homogeneous molecule distribution, we conclude that only about $2/10,000$ of the molecules in the averaged area are located in the NPoM gap and contribute to the observed fluorescence enhancement. This small fraction of coupled molecules explains the relatively small difference of the spectra at the NPoM position and next to it. However, the shape of the difference spectra contains all relevant information about the coupling of the dye monolayer to the different NPoM modes. For quantitative analysis, we fit the scattering and fluorescence spectra by Lorentzian resonances.

5.2.3 Fitting procedure

We first focus on the polarization-dependent scattering spectra of the NPoMs to determine the fundamental cavity resonances. The spatially resolved scattering spectra at the four combinations of excitation and detection polarization are shown in Figure 5.7a. We identify the out-of-plane mode by the dumbbell-shaped spatial profile of the h/v scattering. The spectra are processed like in Chapter 4.4, i.e., spatial integration, subtraction of the background scattering, and normalization by the lamp spectrum. To model the NPoM scattering, we fit the complete set of four measured spectra to three Lorentzian resonance functions $L^{(l,m)}(\omega)$ with polarization-dependent amplitudes according to Equation 4.32. The Lorentzian contributions are normalized by their energy content. The fit results are plotted with the measured spectra in Figure 5.7. According to the fit, the v/v and v/h spectra can be well described by two individual Lorentzian functions with similar spectral positions of 2.07 eV and 2.09 eV but different peak widths. The out-of-plane resonance peaks at around 1.86 eV. The spectral positions are consistent with the results from the last chapter, where the dependence of the resonance positions and linewidths on the gap size

was investigated. We excluded energies above 2.2 eV from the fit, which correspond to higher-order modes.

Fitting the scattering spectra with Lorentzian functions allows us to determine the spectral positions and widths of the fundamental resonances of each NPoM. We now correlate this information with the fluorescence enhancement of the dye monolayer in the NPoM resonator. The background fluorescence spectra of the uncouped dyes are obtained by linear interpolation between spectra above and below the NPoM at each wavelength (compare the raw spectra in Figure 5.6b). For better visibility of the NPoM contribution, we subtract the background fluorescence spectra from the NPoM-enhanced fluorescence. The resulting spatially resolved fluorescence enhancement spectra are shown in Figure 5.7b. The comparison with the scattering spectra demonstrates that the fluorescence enhancement peaks at the in-plane NPoM resonance energy. Furthermore, the spatial resolution of the measured spectra reveals that the dyes also couple with the out-of-plane resonance at about 1.86 eV. In the h/v measurement, the spatial profile of the fluorescence enhancement has a single-lobed pattern at the in-plane resonance, which transitions to a double-lobed pattern at the out-of-plane resonance energy. To some extent, we also observe this transition in the spatial profile of the v/v measurement, where the fluorescence pattern bends downwards with decreasing energy. We only see the lower part of the double-peak structure in this case. We conclude that the NPoM modes shape the fluorescence of the dye monolayer in the spectral and spatial dimensions, both of which are accessible with our hyperspectral imaging approach.

Visualizing the fluorescence enhancement spectra with spatial resolution is susceptible to slight variations in the fluorescence spectra above and below the NPoM (compare raw data in Figure 5.6b). The linear interpolation of the background spectra is a first-order approximation for qualitative discussions. Furthermore, the signal-to-noise ratio is relatively small at higher energies. In most investigated NPoMs, this prevents us from observing the coupling to the out-of-plane mode by the shape of the emission pattern. Therefore, we spatially integrate the measured fluorescence spectra to analyze the mode-dependent coupling coefficients quantitatively.

Based on the following considerations, we employ a comprehensive model to describe the measured fluorescence enhancement spectra. Our transition dipole orientation method in Chapter 3.3 revealed that the molecules have a defined preferential orientation within the hectorite nanosheets. We expect the molecules to form small oriented domains below the optical diffraction limit that do not average out on a macroscopic scale. Hence, each emitter and each domain experiences a different dielectric environment which can even fluctuate on ultrashort timescales due to molecule reorientations. We conclude that the spectrally broad fluorescence of the dye monolayer originates from inhomogeneous line broadening. Therefore, as in the numerical simulations, we assume that the emitted fluorescence of each dye molecule in the resonator at a particular frequency is enhanced by the available NPoM modes. We model the fluorescence enhancement as the product of uncoupled dye fluorescence $F_{\mathrm{bg}}(\omega)$ and the fitted Lorentzian far-field resonances $L^{(l,m)}(\omega)$ of the NPoM modes with indices (l, m). Other authors expect a peak shift between the near-field and the far-field response [199]. However, our fits agree very well with the measured fluorescence enhancement spectra using the far-field response, as described below. The fluorescence spectrum of the uncoupled dye monolayer is given by the background signal

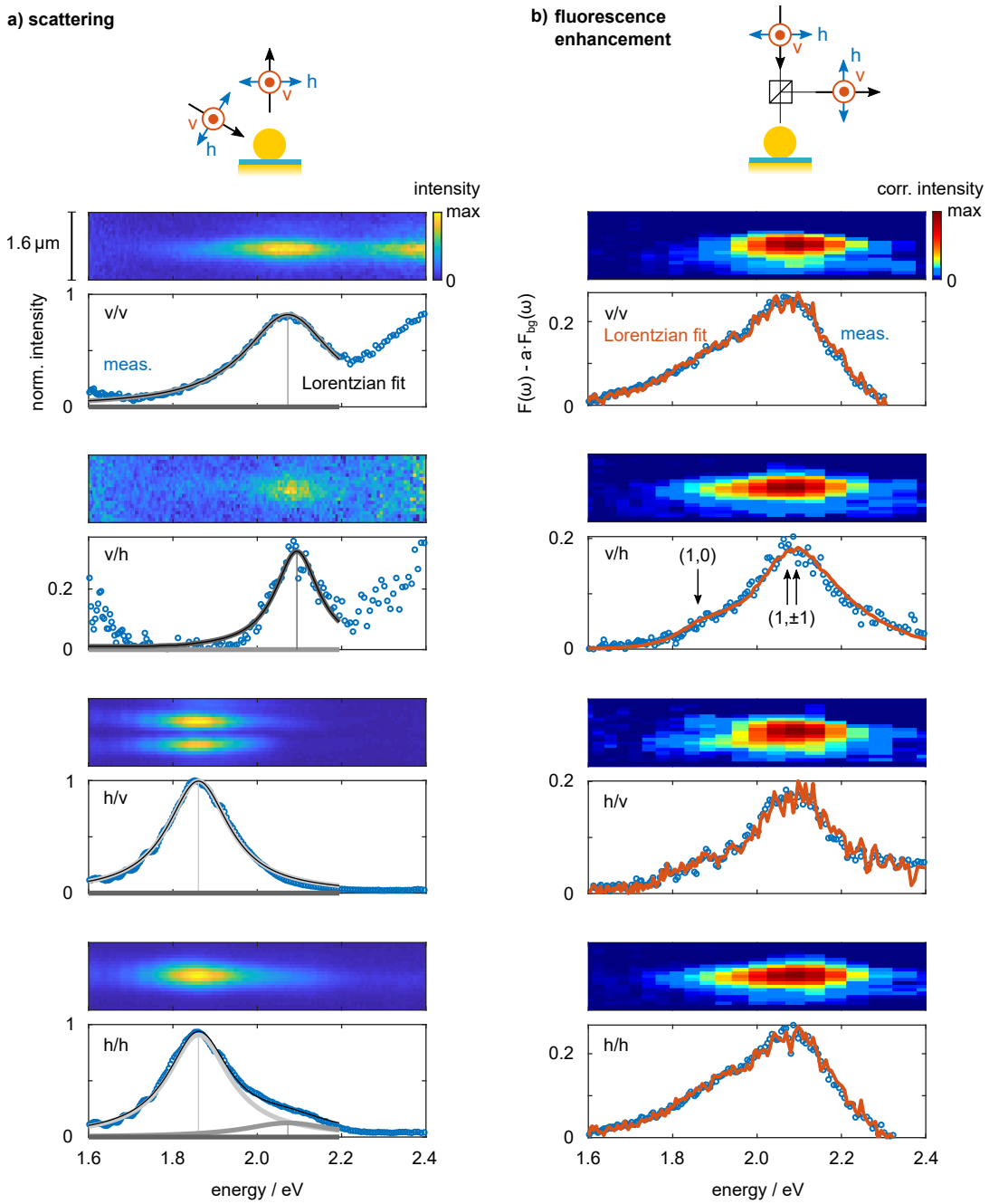

Fig. 5.7.: Scattering (left) and fluorescence enhancement spectra (right) of the NPoM on the dye monolayer (marked in Figure 5.6). For all four polarization combinations sketched in the respective pictograms, we show the spatially resolved spectra above the spatially integrated spectra (blue dots). The scattering spectra are normalized to the maximum intensity at h/v polarization. We obtain the NPoM resonances by fitting three Lorentzian functions to all scattering spectra (black line). The fitted resonances are used to model the fluorescence enhancement spectra $F(\omega) - a \cdot F_{\mathrm{bg}}(\omega)$. The fit curve is not smooth due to noise in the background spectrum F_{bg}.

$F_{\mathrm{bg}}(\omega)$ obtained from the average fluorescence spectrum above and below the NPoM. The model function for the measured fluorescence at the NPoM position for a given excitation and detection polarization reads

$$F(\omega) = a \cdot F_{\mathrm{bg}}(\omega) \cdot \left[1 + \sum_{(l,m)=\{(1,0),(1,1),(1,-1)\}} c^{(l,m)} L^{(l,m)}(\omega) \right] \quad . \tag{5.11}$$

Here, the amplitude parameter $a \approx 1$ is a scaling factor to account for spatial variations of the dye density.

The fluorescence enhancement spectra and the corresponding fits are shown in Figure 5.7. We subtract the scaled background spectra to present the signal $F(\omega) - a \cdot F_{\mathrm{bg}}(\omega)$ for better visibility. The fits agree very well with the measured spectra at all four polarization combinations. This result underlines the validity of our model to quantify the mode-specific enhancement of the fluorescence with respect to uncoupled molecules. Our model scales the noisy background spectrum $a \cdot F_{\mathrm{bg}}$ by the mode-dependent coupling coefficients $c^{(l,m)}$. Hence, the plotted fit function is not smooth. As the Lorentzian functions $L^{(l,m)}(\omega)$ are normalized by the energy content, the fitted coupling coefficients $c^{(l,m)}$ quantify the amount of energy radiated via the NPoM modes at a specific combination of excitation and detection polarization. The evaluation of the $c^{(l,m)}$, hence, allows us to investigate the relative coupling strengths to the three NPoM modes. Furthermore, we can quantify variations between different resonators by a statistical analysis of the coupling coefficients for many NPoMs. In the following, we only consider NPoMs on dye monolayers where the set of Lorentz functions can visually well describe the scattering spectra.

5.2.4 Quantitative analysis of the mode-dependent fluorescence enhancement

We present the results from 25 NPoMs on dye monolayers. Figure 5.8a shows the NPoM resonance positions and widths obtained from the Lorentzian fits to the scattering spectra. The average out-of-plane resonance energy is about 1.8 eV. Consistent with previous results from NPoMs on dielectric spacers, the in-plane resonances are mostly red-shifted to around 2 eV. Furthermore, the in-plane resonances are spectrally more narrow than the out-of-plane resonances.

As Figure 5.6b shows, the fluorescence of the uncoupled dyes increases with energy up to 2.2 eV. Consequently, the fluorescence at the out-of-plane resonance energies (1.8 eV) is about a factor of 3 weaker than at the in-plane resonance energies (2.0 eV). Therefore, the determination of coupling coefficients is less accurate for the out-of-plane mode due to its lower energy, which needs to be considered in the quantitative analysis of the coupling coefficients. Nevertheless, the fits to the fluorescence spectra generally agree very well with the measurements.

Initially, we sum up the fitted coupling coefficients at the four measured polarization combinations. This allows us to assign each evaluated NPoM three polarization-independent coupling coefficients. The histograms of the fitted coupling strengths $c^{(l,m)}$ to the three

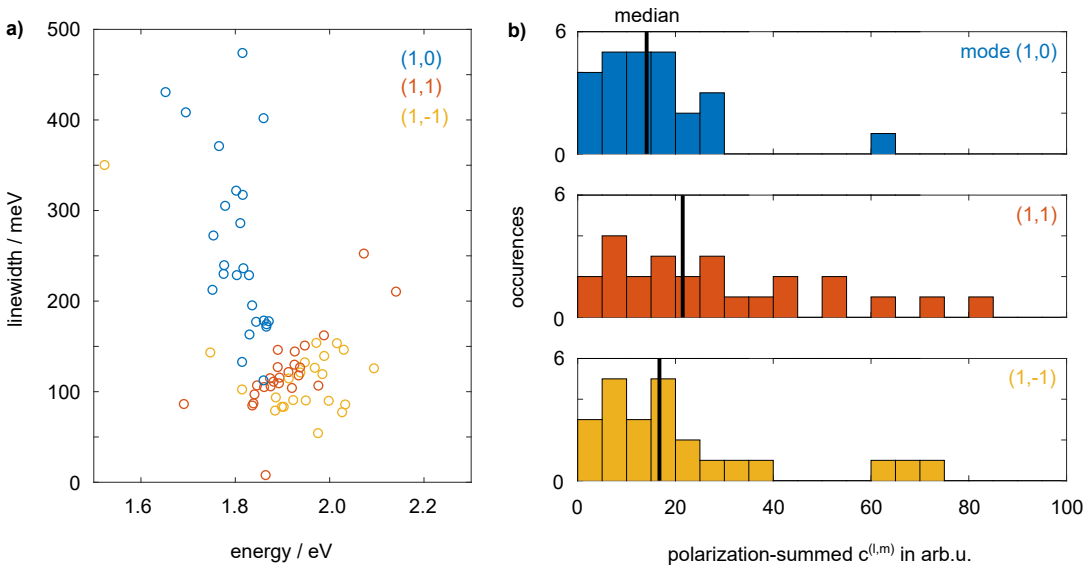

Fig. 5.8.: (a) Energy and linewidth of the Lorentzian fits to the scattering spectra of all investigated NPoMs on dye monolayers. Each dot corresponds to an individual NPoM with color-coded modes (l, m). (b) Histogram of the fluorescence coupling coefficients $\sum_{\text{pol.}} c^{(l,m)}$ obtained from all investigated NPoMs, summed over all polarizations in arbitrary units. Compared are the coupling coefficients for the out-of-plane and in-plane modes. The median values of the respective distributions are marked in black.

modes are shown in Figure 5.8b. The coupling coefficients vary significantly among the investigated NPoMs. We expect that the local field enhancement provided by the NPoM and its spatial distribution is very sensitive to the nanogap morphology. Furthermore, our analysis only considers radiative enhancements of the dye fluorescence. Dissipation in the metal, such as propagating surface plasmons launched by structural imperfections, introduces additional non-radiative decay channels, which again depend on the gap morphology. As demonstrated in the literature, the excitation of surface plasmons by nanostructures can even mediate the remote excitation and detection of dye fluorescence [200].

The black lines in Figure 5.8b denote the median values of the coupling coefficient distributions. The median values for the $(1, 1)$ and $(1, -1)$ modes are approximately 20 and 18, respectively, which is only slightly larger than the median value of 15 for the out-of-plane mode $(1, 0)$. The median values can only be seen as an estimate, as the coupling coefficients vary considerably among the NPoMs. Nevertheless, we observe that the coupling of the dye monolayer to the in-plane modes is about 27% larger than to the out-of-plane mode on average. Notably, this result qualitatively agrees with our numerical simulations presented in Figure 5.4, predicting even a 75% larger fluorescence enhancement by the in-plane modes compared to the out-of-plane mode. The dominating contribution from the in-plane modes is remarkable, as their simulated scattering intensity is much weaker than the out-of-plane mode (see Figure 4.19).

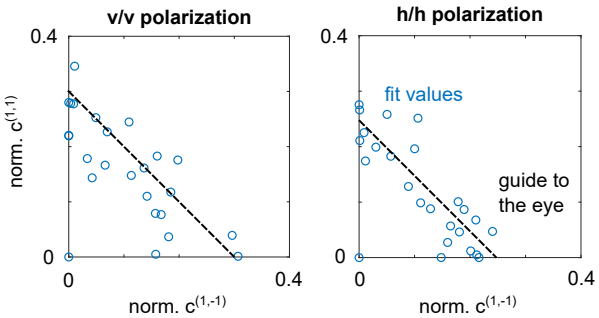

Fig. 5.9.: Influence of the NPoM ellipticity on the fluorescence enhancement. The fitted fluorescence coupling coefficients of the in-plane modes $(l, m) = (1, \pm 1)$ of v/v (left) and h/h polarization (right) are anti-correlated, as indicated by the black line (guide to the eye). The $c^{(l,m)}$ values are normalized by the total fluorescence enhancement, i.e., the sum over both in-plane modes and all four polarization combinations.

Polarization-dependent coupling by nanoparticle ellipticity

The nanoparticles are not perfectly spherical, lifting the energy degeneracy of the in-plane modes $(1, \pm 1)$. The two semi-axes of an elliptical nanoparticle are rotated by a certain angle with respect to the experimental coordinate system, causing a polarization-dependent fluorescence enhancement by the in-plane NPoM modes. We normalize the fitted coupling coefficients by the total fluorescence enhancement, i.e., the sum over the coupling coefficients of both in-plane modes and all four polarization combinations. This normalization is required to divide out the particle-dependent magnitude of the fluorescence enhancement. Figure 5.9 shows the correlation of the normalized coupling coefficients of both in-plane modes. We compare the coupling coefficients of excitation and detection polarizations pointing in the same direction, i.e., v/v and h/h measurements. The data points are anti-correlated in both polarization combinations, as the black dashed line indicates.

First, we assume an elliptical nanoparticle where the semi-axes coincide with the experimental coordinate system. If the $(1, 1)$ mode points in the v-direction, the measured coupling coefficient to this mode is most intense if excitation and detection polarization are oriented in the same direction. As the electric field profile of the polarized excitation is imprinted onto the dye layer (compare Chapter 5.1.2), the coupling to the orthogonal $(1, -1)$ mode is much weaker. If the semi-axes differ from the experimental coordinate system, the coupling to both in-plane modes can be equally efficient. Hence, we can explain the experimentally observed anti-correlation of the coupling coefficients by the statistical orientation of the nanoparticle semi-axes. This result proves that the NPoM ellipticity influences not only the scattering but also the polarization-dependent fluorescence emission of the molecules.

Our transition dipole orientation determination in Chapter 3.3 revealed that the dye monolayer has a preferential in-plane orientation. In general, the relative orientation of the molecules and the NPoM semi-axes needs to be considered in the analysis of the polarization-dependent coupling coefficients. However, the numerical simulations demonstrated that the out-of-plane component of the transition dipole dominates the coupling.

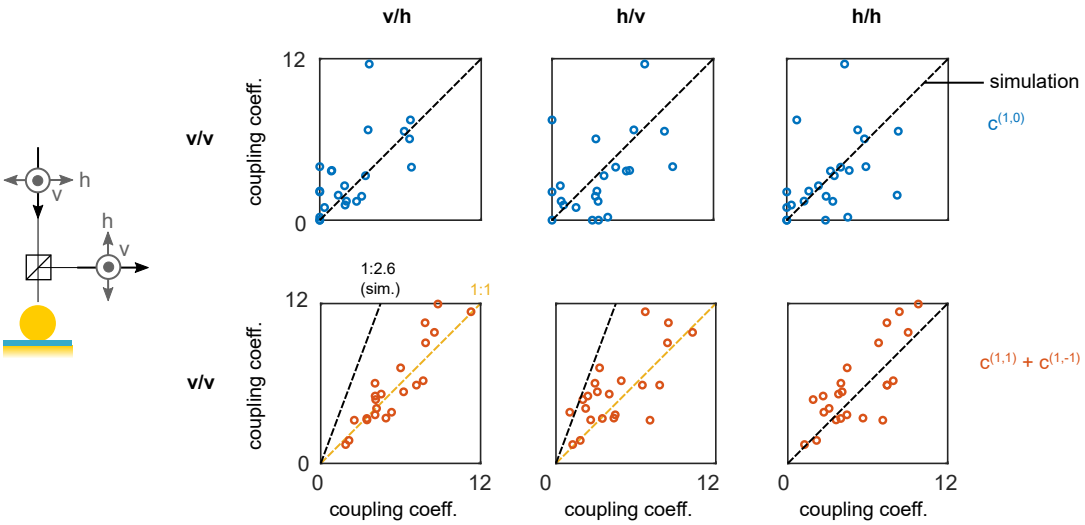

Fig. 5.10.: Polarization dependence of the fluorescence coupling coefficients for the out-of-plane mode (top) and the superposition of both in-plane modes (bottom). Shown are the correlations of the v/v measurement (vertical axis) with the other three polarization combinations v/h, h/v and h/h (horizontal axes, from left to right). The black dashed lines show the expectations based on the numerical simulations.

Furthermore, the investigated NPoMs are located on different hectorite double stacks where each in-plane preferential direction of the dye monolayer is equally probable. Hence, we do not account for the in-plane orientation of the dye monolayer in the experimental data analysis.

Polarization-dependent coupling to out-of-plane and in-plane modes

The out-of-plane NPoM mode has a vertical dipole orientation. Hence, the numerical simulations predicted that the (10) coupling coefficient is independent of excitation and detection polarization. We compare this expectation with our experimental observations by correlating the fitted coupling coefficients at different polarizations. The top row of Figure 5.10 exemplarily shows the correlation of the v/v coupling coefficient $c^{(1,0)}$ with the three other polarization combinations, corresponding to the horizontal axes of the three plots. We decide on a specific "reference" polarization v/v as the vertical axis in all plots to reduce the complexity of the data set. The ratio of the coupling coefficients varies significantly among the investigated NPoMs (blue dots). We attribute this to uncertainties in the fit and deviations from the out-of-plane orientation of the (10) mode because of nanoparticle asymmetries. On average, the experimental correlations are well described by an identity relation (black dashed line), as expected from the theoretical predictions.

We sum up the in-plane coupling coefficients $c^{(1,1)}+c^{(1,-1)}$ to average over the nanoparticle ellipticity. This allows direct comparison with our numerical simulations, where we assumed a cylindrically symmetric NPoM gap. The correlation of the "reference" v/v coupling coefficients with the other three polarization combinations is shown in the bottom row of Figure 5.10. We expect that the coupling is independent of the excitation

polarization if excitation and detection polarization are identical. This corresponds to an identity relation of the v/v and h/h coupling coefficients (black dashed line), which agrees well with our experimental findings (orange dots).

The polarization-dependent excitation field distribution is imprinted on the dipoles in the gap. Hence, the detected fluorescence is most intense if excitation and detection polarization match. The numerical simulations predict that the coupling coefficient is a factor of 2.6 larger for parallel than for perpendicular excitation and detection polarizations. This corresponds to a line with slope 2.6 in the correlation plots of v/v with v/h and h/v in Figure 5.10. However, the measured polarization dependence is much less than expected, as the deviation from the black dashed line indicates. For comparison, the yellow line with slope 1 shows the expectation without the theoretically predicted "memory" effect of the excitation polarization.

Various reasons could explain the difference between measurement and simulation. First, we used an idealized geometry in the simulation with a spherical truncated nanoparticle on a flat substrate. In the experiment, however, structural irregularities in the gap can give rise to electric field hotspots which break the symmetry of the excitation field distribution and the fields associated with the quasi-normal modes. Consequently, the excitation field distribution may not have a zero-crossing in the center of the facet, which plays a central role in our predicted "memory" effect. In the limiting case of a cylindrically symmetric excitation field distribution, we expect the fluorescence enhancement to be independent of the excitation polarization.

Second, the measured fluorescence and the computed far-field radiation resemble only the radiative decay to the ground state of the molecule. However, radiative and non-radiative decay pathways of the dye need to be considered in quantitative statements. The QNM decomposition includes radiation losses and dissipation in the imaginary part of the QNM frequencies $\tilde{\omega}_m$ [64, 170]. Hence, radiative and non-radiative rates are accessible from QNM calculations. Nevertheless, the intrinsic quantum efficiency of the dye monolayer is an unknown quantity that enters into the computation of the overall decay rate. The quantum yield of the dye monolayer could be determined from experiments similar to the Drexhage measurements [61], where the quantum efficiency is a fit parameter for the distance-dependent decay rates. Furthermore, the decay rate is correlated with the relative emission intensities from the two transitions of the dye, as we discussed in Chapter 3.5.

Third, the molecules in the dye monolayer are very densely packed, enabling a significant out-of-plane orientation of the transition dipoles. This allowed us to neglect the in-plane components of the transition dipoles in the coupling coefficient calculation. Nevertheless, the presence of the gold nanoparticle might compress the dye monolayer because of the electrostatic attraction from the gold substrate by induced image charges. To determine if the metallic nanoparticle impacts the molecule orientation, one could exchange the gold nanoparticles with off-resonant metal colloids with higher plasma frequency such as aluminum [181]. Our dipole orientation determination technique (see Chapter 3.3) could then detect spatial variations caused by the nanoparticles. Furthermore, a gold nanotip with three-dimensional position control could replace the gold nanoparticle to avoid direct contact with the dye monolayer. Gold nanotips are used for tip-enhanced photoluminescence (TEPL) [37, 83], an established technique discussed in more detail in Chapter 5.4.

5.3 Reduced photobleaching rate of dyes inside the NPoM gap

The coupling strengths are determined from the total detected number of photons emitted from dyes in the NPoM gap region in a particular time interval. However, each molecule can only emit a finite number of photons before photobleaching. The oxygen pathway is typically the essential photodegradation mechanism [201]. The dye performs an inter-system crossing from the excited singlet to the excited triplet state. The energy is transferred to ambient oxygen, inducing a transition from the oxygen triplet ground state $^3O_2$ to the singlet excited state $^1O_2^*$. The singlet oxygen is very reactive and can destroy the chromophore irreversibly. Also other photochemical reactions without oxygen are possible. For example, photoionization upon dye excitation might generate reactive radical intermediates. In our experiments, we can exclude thermal effects due to the low laser power of $< 3\,\mu W$ at widefield illumination.

The dye is susceptible to photodegradation only in the excited state. We can assign this statistical process a photobleaching rate k_{bleach} which competes with the radiative rate k_r of the dye. The average number $\langle N \rangle$ of emitted photons before photobleaching is [202, 203]

$$\langle N \rangle = \frac{k_r}{k_{\text{bleach}}} \quad . \tag{5.12}$$

The fluorescence intensity of the dye ensemble in a diffraction-limited area decreases exponentially with time. The presence of gold nanostructures can significantly enhance radiative and non-radiative rates of the molecules while the photobleaching rate remains constant. Hence, the number of emitted photons before photobleaching can increase considerably for molecules in the NPoM gap. To investigate the photobleaching in the experiment, we evaluate the time series of fluorescence spectra for coupled and uncoupled molecules.

We average over all measured polarization combinations to investigate the evolution of fluorescence spectra in 15 time steps with 40 s integration time each. Figure 5.11a compares the time series of the dye fluorescence spectra (blue to yellow color) at an exemplary NPoM position and next to it, called background. Within 10 minutes, the fluorescence intensity decreases by about 40 % on average. The background signal needs to be subtracted from the NPoM very accurately to determine the fluorescence enhancement spectra. Based on our previous findings, the enhancement is mainly provided by the NPoM modes with resonance energies well below 2.4 eV. Therefore, we use the off-resonant narrow spectral interval at 2.4 eV (shown as a grey area in the spectra) to determine the scaling factor between NPoM and background intensity. For best accuracy, the spectra are smoothed in this interval and integrated over all time steps to obtain a single scaling factor for all measured frames.

The time evolution of the fluorescence enhancement spectra after background subtraction is shown in Figure 5.11b. In the first time interval, the fluorescence difference spectrum peaks at an energy of 1.9 eV with 5,000 counts. The maximum counts decrease to around 3,500 in the last measured frame, while the spectral shape remains unchanged. For comparison, Figure 5.11c shows the photoluminescence (PL) of an exemplary NPoM without the dye

monolayer, i.e., the nanoparticle directly attached to the gold substrate without a spacer layer. The PL increases with energy, qualitatively matching the findings in the literature for bare gold PL [204]. We expect that the excitation power is too small to observe an enhancement of the gold PL by the NPoM modes. Notably, the gold PL only yields about 50 counts per frame at an energy of 1.9 eV, compared to 3,500 to 5,000 counts retrieved from the enhanced fluorescence of the dye monolayer. Hence, we can neglect the gold PL in our analysis, as it is about two orders of magnitude weaker than the fluorescence enhancement of the dye monolayer.

To investigate the photobleaching rates of the dyes inside the NPoM and next to it, we integrate the fluorescence spectra from Figure 5.11a (background) and 5.11b (fluorescence enhancement by NPoM). The temporal evolution of the fluorescence intensity is shown in Figure 5.11d on a logarithmic scale. For better visibility, the fluorescence intensity of the dyes inside the NPoM is enhanced by a factor of 8. An exponential curve is fitted to the first five measurement points in both data sets. The fitted 1/e time constant for the NPoM-enhanced fluorescence is 39 frame intervals, compared to 17 for the background fluorescence. We conclude that the NPoM increases the average time until photobleaching of dyes in the gap by more than a factor of two. This factor is an average over all molecules in the gap contributing to the fluorescence enhancement and, therefore, might be larger for molecules most efficiently coupled to the NPoM modes.

The photobleaching time constants vary significantly across all investigated NPoMs, which we attribute to variations in the gap morphology. Some of the investigated NPoMs do not enhance the photobleaching time constant. In our experiments, the actual excitation enhancement of the dye monolayer in the gap is unknown. Saturating the molecule absorption would allow us to divide out the excitation enhancement. Generally, the spatially varying excitation intensity needs to be considered to model the photobleaching dynamics [205]. Furthermore, a quantitative correlation between enhanced fluorescence and reduced photobleaching requires precise knowledge of radiative and non-radiative rates. The fluorescence lifetime could be determined from time-correlated single photon counting experiments. We demonstrated in Chapter 3.5 that the relative intensities of the two transitions of the dye monolayer act as a clock for molecule planarization. The spectral variations of the fluorescence lifetime could be determined from streak camera measurements. The proposed experiments would allow us to investigate the transition-dependent photophysics of the dye monolayer in nanoresonators. Our present measurements demonstrate that the photobleaching timescale and the total number of emitted photons before photobleaching can be significantly increased with plasmonic nanoresonators. Based on this work, future experiments will help to optimize the interaction of emitters with nanostructures for enhanced photostability and high photon emission rates.

5.4 Towards strong coupling with dye monolayers

In the previous sections, we employed a weak-coupling description for the cavity-emitter coupling. We considered a unidirectional interaction, where the emitter radiates via the NPoM modes. Our experimental data proved the applicability of this model, as the spectra could be well described by a sum over the fundamental NPoM modes. Due to the Purcell

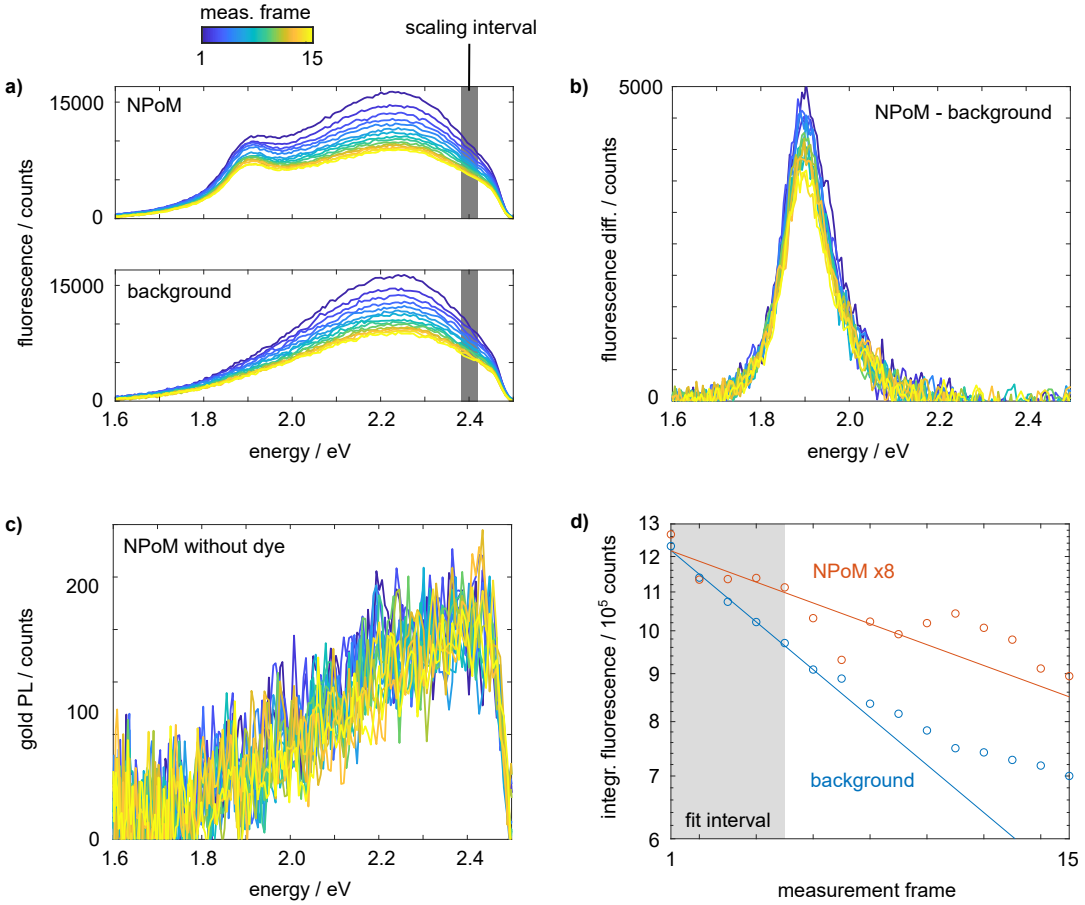

Fig. 5.11.: Increased number of emitted photons before photobleaching for the dye monolayer in the NPoM gap. (a) Color-coded time series of the fluorescence spectra at an exemplary NPoM position (top) and next to it (bottom). The intensity in the grey area is used to calculate a scaling factor between NPoM and background. (b) The difference spectra of NPoM and background yield the enhanced fluorescence of the dyes in the gap area and its temporal evolution. (c) The photoluminescence of an exemplary NPoM on the gold substrate without the dye monolayer is significantly weaker than the enhanced dye fluorescence in (b) and can therefore be neglected. (d) Decay of the spectrally integrated fluorescence of the dye monolayer in the NPoM (from (b)) and the background (from (a)), fitted by an exponential function (solid lines). The NPoM signal is enhanced by a factor of 8.

enhancement, the fluorescence spectrum of the coupled dye monolayer was shaped by the NPoM resonances.

It has been demonstrated that the small mode volume of NPoMs can allow entering the cavity-emitter strong coupling regime at room temperature [36]. In the strong coupling regime, energy can cycle back and forth between emitter and gap plasmon, generating hybrid light-matter states called polaritons. According to the literature [47, 69, 70], the atom-field coupling constant is estimated as

$$g = \frac{|\boldsymbol{\mu}_{ij}|}{\hbar}\sqrt{\frac{\hbar\omega_{ij}}{2\varepsilon_0\varepsilon V}} = 2\pi|\boldsymbol{\mu}_{ij}|\sqrt{\frac{c_0}{2\varepsilon_0\varepsilon V h\lambda_{ij}}} \tag{5.13}$$

with transition dipole moment $\boldsymbol{\mu}_{ij}$, frequency ω_{ij} of the transition $j \rightarrow i$, and mode volume V. In the following, we estimate the coupling constant of the emitters investigated in the experiment and compare it with the threshold for strong coupling.

The mode volume is estimated as the volume spanned by the area of the spherical facet $\pi(w/2)^2$ and the 4 nm gap thickness

$$V \approx \pi \cdot (10\,\mathrm{nm})^2 \cdot 4\,\mathrm{nm} = 1260\,\mathrm{nm}^3 \quad . \tag{5.14}$$

In the literature, we find typical oscillator strengths of $f \approx 1$ for structurally similar pyrene derivative molecules obtained from density functional calculations [206]. The relation between oscillator strength and transition dipole moment [207]

$$f = \frac{2m_e\Delta E}{3\hbar^2 e^2}|\boldsymbol{\mu}|^2 \tag{5.15}$$

yields the transition dipole moment $|\boldsymbol{\mu}| \approx 11.5$ Debye at an emission wavelength $\lambda_{ij} = 620$ nm. In this equation, m_e is the electron mass, e is the unit charge, and $\Delta E = hc_0/\lambda_{ij}$ is the energy difference between excited and ground states. Thus, we estimate the atom-field coupling constant for an emitter embedded in a dielectric with refractive index $n = 1.5$ as

$$g_{\mathrm{single}} = 2.9 \cdot 10^{13}\,\mathrm{rad\,s^{-1}} \approx 19\,\mathrm{meV} \quad . \tag{5.16}$$

Compared with the dye fluorescence FWHM of $\gamma_{\mathrm{em}} \approx 450$ meV, the coupling constant is about a factor of 24 smaller than the emitter losses. Furthermore, the coupling constant is significantly smaller than the NPoM resonance linewidths of $\gamma_{\mathrm{pl}} \approx 150$ meV (in-plane mode) and about 250 meV (out-of-plane mode). Hence, single molecule strong coupling with the NPoM is not feasible with this particular dye. Even with smaller NPoM gap sizes on the order of 1 nm and spectrally narrow emitters, it is experimentally very difficult to achieve strong coupling with single emitters, as discussed by Kewes et al. [208].

However, in our sample, an ensemble of $N = 315$ molecules of the dye monolayer is present in the cavity formed by the facet area, based on an area of 1 nm^2 per molecule. According to strong coupling theory [74], the coupling constant scales with the square root of the emitter number $\sqrt{N} = 17.7$. The coupling strength of the ensemble

$$g_{\mathrm{ensemble}} = \sqrt{N} \cdot g_{\mathrm{single}} \approx 335\,\mathrm{meV} \tag{5.17}$$

needs to be compared with the damping γ_{em} of the emitter and the average plasmon resonance $\gamma_{pl} = 200\,\text{meV}$

$$\frac{1}{4}(\gamma_{pl} + \gamma_{em}) \approx 163\,\text{meV} \quad . \tag{5.18}$$

As $g_{ensemble} > \frac{1}{4}(\gamma_{pl} + \gamma_{em})$, the ensemble of emitters theoretically exceeds the strong coupling threshold (see Equation 2.56) by a factor of two. This estimation assumed that all N molecules are located at the electric field hotspot in the gap and are aligned with the local electric field. Hence, our estimate is an upper limit for the coupling strength of the dye monolayer with the NPoM. In the experiment, we could not observe peak splittings in the scattering and fluorescence spectra. This allowed us to expand the dye fluorescence by a series of quasi-normal modes in the weak coupling limit. In the following, we briefly discuss the feasibility of strong coupling with the dye monolayer and outline possible future experiments.

In the literature, strong coupling with dye ensembles focuses on molecule layers forming ordered J-aggregates. Due to their large oscillator strength, methylene blue and cyanine dyes such as TDBC are used frequently [39–43]. J-aggregates exhibit very narrow linewidths on the order of 100 meV for TDBC at room temperature. Coupling strengths of up to 280 meV for TDBC aggregates with silver nano-prisms [40] and 170 meV for methylene blue molecule aggregates inside a silver nanocube-on-mirror resonator [43] have been reported. The transition dipole moment of TDBC is about 20 Debye, almost twice as large as the estimate for the pyrene derivative used in the work presented here. Despite this significant dipole moment, the reported coupling strengths are relatively moderate yet sufficient for strong coupling due to the narrow emitter linewidths. In contrast, the 450 meV linewidth of the pyrene derivative dyes significantly increases the required coupling strength to enter the strong coupling regime. Based on the broad emission spectrum of the pyrene derivatives sandwiched between the hectorite nanosheets, we conclude that the dyes do not form J-aggregates. The present work explicitly required the broadband emission spectrum to determine the coupling coefficients to the NPoM modes.

Furthermore, it has been shown in the literature that photodegradation of TDBC can diminish the observable peak splitting in the emission spectra with increasing exposure time [40]. At the same time, strong coupling has been demonstrated to suppress the photo-oxidation of molecules, as it inhibits the population of triplet states and reduces the time of the molecules in the excited state [209]. Similarly, we found in the experiments that molecules inside the NPoM gap bleach more slowly due to the Purcell enhancement in the weak coupling limit.

Finally, the strong coupling might be inhibited in the present work by spatial variations of the molecule orientations in the gap. Based on our orientation determination results, we expect the molecules in the dye monolayer to form nanoscale domains. There may be multiple domains with different in-plane orientations in the gap area. This inhomogeneous distribution might impact the emergence of coherent Rabi oscillations.

The influence of molecule domains could be investigated by tip-enhanced photoluminescence (TEPL) and tip-enhanced strong coupling (TESC) experiments [37]. Here, a gold nanotip is approached stepwise to the sample with complete three-dimensional position control using shear-force feedback. As with the nanoparticle-on-mirror system,

coupling a plasmonic gold nanotip to a gold substrate gives rise to localized gap plasmons with strong field confinement. The tip apex radius on the order of 10 nm determines the optical resolution. In addition, the optical response is again polarization dependent. Hence, the nanoscale domains in the dye monolayer could be imaged, and islands with homogeneous in-plane orientation could be selected for strong coupling experiments. In principle, the approach of the tip to the substrate allows tuning of the coupling strength between the nanocavity and the dye monolayer. Hence, the emergence of hybrid modes could be monitored at a particular position on the dye monolayer [37, 81]. Similarly, Groß et al. demonstrated that a plasmonic slit resonator as a scanning probe provides deterministic strong coupling with colloidal quantum dots [210]. In the weak coupling limit, the TEPL method has revealed extensive photophysical properties of heterostructures [83]. The distance-dependent quenching and Purcell enhancement could provide essential information about radiative and non-radiative decay rates of both transitions in the dye monolayer.

However, the continuous photobleaching of the dyes needs to be considered in the data analysis. The encapsulation of the dye monolayer might provide an oxygen barrier to decelerate the photobleaching. Our experiments revealed that the dye fluorescence intensity decreases with time, so encapsulation by hectorite nanosheets can not fully prevent photobleaching. AFM topography images (see Figure 3.14b) showed that the hectorite top layer is not entirely continuous. Hence, optimizing the sample preparation might enhance the protection of the dye monolayer from photobleaching. Comparative experiments of the dye monolayers in oxygen-free environments could eliminate oxygen-related photobleaching pathways. The idea of molecule encapsulation can possibly be transferred to quasi-zero dimensional systems where single emitters are embedded into an ultrathin protective shell. For example, Chikkaraddy et al. used host-to-guest chemistry to incorporate single methylene blue molecules into a host skeleton [38].

5.5 Towards controlled interaction of emitters with nanoresonators

Ultimate control of the cavity-emitter interaction requires the precise tunability of the emitter density and positions in the nanoresonator. The encapsulated dye monolayers investigated in this work provide a large-area coverage with known emitter density, orientation, and layer thickness. The introduction of non-fluorescent “dummy” molecules in the interlayer space of the hectorite nanosheets could allow the adjustment of the emitter density. By keeping the overall molecule density in the interlayer space constant, the out-of-plane orientation of the fluorescent molecules could be preserved. This approach, however, lacks control over the spatial position of the emitters. A precise lateral positioning can be achieved by patterning the spacer layer between the nanoparticle and mirror. In this section, we present our first steps towards controlled patterning of ultrathin dielectric layers based on nanosphere lithography (NSL) [211].

The principle is sketched in Figure 5.12. Non-functionalized polystyrene (PS) beads with a nominal diameter of 100 nm are purchased from Bangs Laboratories. The surface of a

template-stripped gold substrate is made hydrophilic by oxygen plasma treatment. The diluted aqueous PS bead suspension is spin-coated onto the gold substrate. We then deposit a nominal 2 nm Al_2O_3 layer using ALD (see Chapter 4.1). The reactants and process temperature are compatible with polystyrene. The left image in Figure 5.12 shows the topography measured with an AFM in tapping mode. The PS beads form dense monolayers with macroscopic order. The ALD process covers all exposed surfaces with the alumina layer. Consequently, the contact area of the PS beads with the gold substrate is excluded. Therefore, lifting off the PS beads yields a nanostructured ultrathin Al_2O_3 layer, as shown in the sketch. We found that the PS beads can be removed most efficiently with tape (Scotch Magic Tape, 3M). The AFM scan in the right column of Figure 5.12 demonstrates that the fabrication procedure works as expected on large areas. Below the AFM image, the line profile reveals periodic holes roughly matching the nominal thickness of the deposited alumina film. The bead size determines the periodicity of the nano-holes, which is 100 nm in our experiment. Also the shape of the hole is determined by the PS bead, as the sketch illustrates. It has been shown that plasma treatment of the PS beads decreases their size after deposition on the substrate [212]. This enables independent tuning of hole periodicity and hole diameter.

Our process exposes small areas of the gold surface in the center of the holes. Therefore, fluorescent molecules with thiol side groups can only bind to the surface in these tiny predefined regions [16]. We envision that this approach allows the deposition of small molecule ensembles in regular patterns. The average number of dyes per unit cell could be controlled by diluting the emitters with non-fluorescent molecules of the same size. The Al_2O_3 layer allows us to accurately define the gap thickness between the gold substrate and gold nanoparticles dropcasted on top of the structure. Furthermore, the alumina provides structural stability to preserve the out-of-plane orientation of the transition dipole of the fluorophores.

The controlled deposition of emitters opens up new possibilities in quantum information technology. Periodic arrays of metallic nanoparticles support collective delocalized modes called surface lattice resonances (SLRs), which arise from the hybridization of LSPRs with lattice diffraction orders [213]. It has been demonstrated that the SLRs can mediate an energy transfer between donor and acceptor molecules at a distance of 800 nm with significantly higher efficiency than in free space [214]. The collective nature of the SLR introduces spatial coherence, as shown by a double-slit experiment of molecule layers strongly coupled to the SLR [215]. Transferring nanoparticle arrays to metal substrates gives rise to hybrid modes from spatially confined gap plasmon resonances and delocalized lattice modes [216]. Therefore, nanoparticle-on-mirror arrays may pave the way toward long-range coherent energy transfer.

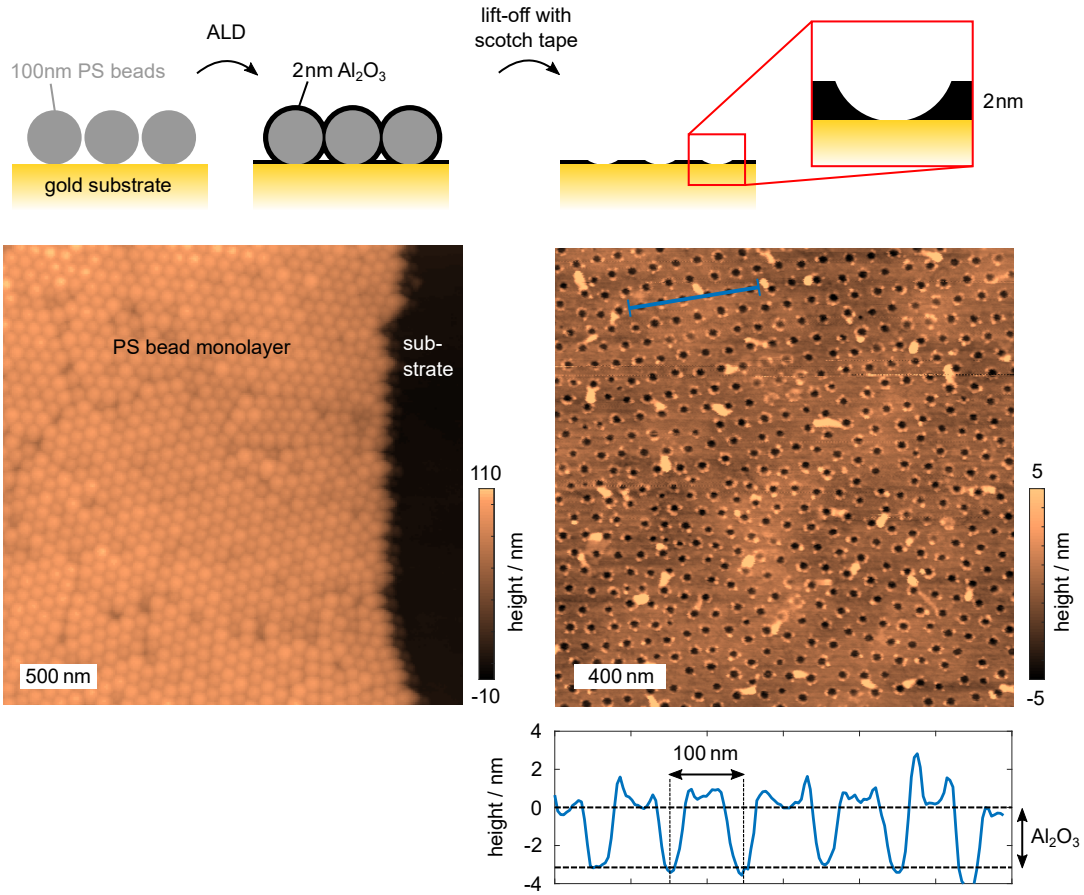

Fig. 5.12.: Nanosphere lithography for patterned ultrathin dielectric layers. The sketches in the top row illustrate the fabrication procedure of PS bead deposition, ALD, and lift-off with a scotch tape. The AFM images show the topography of the sample at exemplary positions before (left) and after (right) lift-off. The profile across the line marked in the right AFM scan reveals periodic holes. The measured hole thickness of about 3 nm roughly matches the nominal 2 nm thickness of the Al_2O_3 layer.

Conclusion

6

Metal nanoparticles feature localized surface plasmon resonances, allowing the confinement of electromagnetic fields below the optical diffraction limit [4]. In the past decades, the nanoparticle-on-mirror (NPoM) geometry attracted increasing interest in the scientific community [10–13]. The bottom-up fabrication gives precise control over each fabrication step, starting from the preparation of ultrasmooth metal substrates, the introduction of active or passive spacer layers, to the deposition of crystalline metal nanoparticles. A major advantage to horizontal structures, such as bowtie antennas, is the superior control over the gap thickness between the nanoparticle and the underlying mirror [12]. This enables the fabrication of plasmonic nanoresonators with ultrasmall mode volumes to control and manipulate the light-matter interaction on a deeply sub-wavelength scale [63]. The interaction of emitters with plasmonic nanoresonators has allowed extending our microscopic understanding of molecules by surface-enhanced Raman scattering [111]. Moreover, the radiation from quantum emitters can be tailored in the spatial, spectral, and temporal domains. Specifically, the Purcell effect can enhance the spontaneous emission rate of emitters by orders of magnitude in the weak coupling limit [28, 29]. In the strong coupling limit, the energy coherently oscillates between the emitter and cavity, modifying the energy levels [36–44].

This work investigated the interaction of oriented emitter layers with plasmonic nanoresonators. We demonstrated in experiment and simulation that multiple modes contribute to the fluorescence enhancement. The individual modes could be separated by polarization-resolved scattering and fluorescence spectroscopy and the spatial diffraction pattern on the detector. The broadband emission of the investigated dye monolayer allowed us to determine the coupling to the different NPoM modes. Moreover, applying our novel orientation determination technique to the dye monolayer, we could prove a significant and spatially uniform out-of-plane orientation of both transition dipoles. Characterizing the orientational order was essential to model the interaction with the nanoresonators, as only dipoles aligned with the local electric field can couple efficiently.

We started with a brief theoretical review of light-matter interaction and quantum emitters in Chapter 2. The dielectric function of metals could be described by two Lorentzian oscillators, representing the contributions from the free electron gas and the interband transition. We then introduced the field of plasmonics, where surface plasmon resonances supported by metal nanostructures confine electromagnetic fields below the optical diffraction limit. Our example of a dipole above an ideal conductor illustrated that the spontaneous emission significantly depends on the local environment, namely the partial local density of states (PLDOS). The Purcell enhancement of the spontaneous emission rate described the interaction with resonant cavities in the weak coupling limit. We also discussed the transition from weak to strong coupling, where the cavity-emitter interaction could be modeled as two coupled harmonic oscillators.

We aimed to investigate the interaction between broadband-emitting dye monolayers and plasmonic nanoresonators. Hence, we initially studied both systems independently. Chapter 3 characterized the optical properties of the dye monolayer sandwiched between two hectorite nanosheets. First, we presented a universal method to determine the refractive index of ultrathin planar structures based on white light reflection spectroscopy. Compared to conventional ellipsometry methods, our approach allowed a diffraction-limited spatial resolution. We pre-characterized the layer thickness by AFM measurements, which we then used as input parameters to fit the measured reflection spectra with transfer matrix calculations. Although the 4 nm thickness of the encapsulated dye monolayer is much smaller than the optical wavelength, we obtained a remarkable maximum reflection contrast of up to 15% using a Si/SiO_2 substrate. We modeled the dye monolayer as an effective medium with a single Lorentzian oscillator to account for the absorption in the blue spectral range. We found that the refractive index is very flat in the relevant spectral range, enabling us to describe the dye monolayer by a constant refractive index throughout this work.

Second, we presented a novel and intuitive method to determine the transition dipole orientations in dense dye layers from polarization-dependent fluorescence spectra. With our widefield imaging and simultaneous detection of both polarization directions, we achieved a significant speed-up for large-area screening with respect to established methods. The singular value decomposition allowed us to disentangle the contributions of the two transitions without assuming specific lineshapes. We found that only an asymmetric dipole distribution can explain our experimental data. Based on our microscopic understanding of the encapsulated dye monolayer, we developed a cone-shaped orientation distribution model of the incoherent dipole ensemble with out-of-plane angle, in-plane preferential direction, anisotropy, and a global scaling factor as only free parameters. Fits of the transfer matrix calculations to the experimental data allowed us to generate maps of the dipole orientations with diffraction-limited spatial resolution. We revealed a long-range orientational order and a strong correlation between both transitions.

Third, we demonstrated that the intensity ratio of both transitions in the dye monolayer could act as a picosecond clock for two competing processes: molecule planarization and spontaneous emission. The comparison of the dye monolayer on glass and gold substrates showed that the fluorescence emission depends substantially on the dielectric environment and the orientation of the dipoles relative to it. Furthermore, we found that the orientational order of the encapsulated dye monolayer depends on the substrate and the baking temperature. The considerable out-of-plane orientation of both transition dipoles on glass and gold substrates proved that our particular dye monolayer is well suited for efficient coupling to NPoMs.

Chapter 4 characterized gold nanoparticle-on-mirror structures in experiment and simulation. In NPoMs, an induced dipole moment in the nanoparticle couples with its image dipole in the metal substrate. To establish a low-level understanding of the fundamental modes, we computed the quasi-normal modes of the nanoresonator (QNM) and assigned indices (l, m), following a nomenclature based on spherical harmonics. The $(1, 0)$ mode corresponds to out-of-plane dipoles in the particle and substrate. The energetically degenerate $(1, \pm 1)$ modes emerge from in-plane dipole coupling. Higher-order modes with $l \geq 2$ were excluded from the further analysis due to their significant spectral overlap. To compare the

calculated modes with far-field experiments, we introduced a near-to-far-field transform with subsequent imaging into the detector plane. In the experiment, we deposited ultrathin 1 nm, 2 nm, and 4 nm alumina spacer layers between the nanoparticle and mirror. The size and shape of the colloidal nanoparticles slightly varied between the investigated nanoparticles, impacting the observed NPoM resonances. Therefore, we studied many NPoMs by polarization-resolved scattering spectroscopy. We found that the nanoparticle ellipticity lifts the energetical degeneracy of both in-plane modes. Therefore, we modeled the spectra of each NPoM by three Lorentzian contributions, corresponding to the $(1, 0)$ and $(1, \pm 1)$ modes. Notably, the spatial resolution of our experimental method allowed us to discern in-plane and out-of-plane modes by the Airy- and donut-shaped diffraction patterns. Our statistical analysis proved that the resonance energies and linewidths increase with the gap thickness, consistent with the simulations.

After characterizing the dye monolayers and NPoMs individually, Chapter 5 focused on the interaction of both systems. Both excitation and emission enhancement of each dipole in the monolayer contributed to the fluorescence enhancement by the NPoMs. The excitation enhancement was determined from the simulated near-field distribution after linearly polarized excitation at a wavelength of 485 nm. To calculate the emission enhancement, we decomposed the electric field radiated by the dipole into the quasi-normal modes supported by the NPoM. Consequently, the mode excitation coefficients varied with the dipole position and orientation, where we found that the z-component of the dipole moment dominates. Our simulations of the incoherent dye monolayer revealed that the in-plane mode generates an even more significant fluorescence enhancement than the out-of-plane mode. This result was remarkable, as the simulations of the scattering spectra in Chapter 4 showed that the in-plane mode of the NPoM only weakly radiates into the far-field. Furthermore, we theoretically predicted that the fluorescence enhancement memorizes the excitation polarization even though the emission is incoherent. Due to its broadband emission, the dye monolayer was well suited to determine the mode-dependent coupling in the experiment. As expected, we observed that the NPoM modes shape the fluorescence spectrum of the dye monolayer. For quantitative analysis, we first determined the resonance frequencies of the NPoMs by fitting the scattering spectra of each NPoM. In the second step, we fitted the fluorescence enhancement spectra by a sum of the three energetically lowest NPoM modes to obtain the coupling coefficients for each mode. In the statistical average over many NPoMs, we confirmed our theoretical expectation that the coupling to the in-plane modes is more significant than to the out-of-plane modes. Furthermore, our polarization-dependent measurements showed that the ellipticity of the nanoparticles also enters into the fluorescence enhancement spectra. However, the present experiment could not confirm the predicted “memory” effect. Generally, we employed a weak coupling description of our measurement data, where the Purcell effect enhances the spontaneous emission. We outlined how future experiments using a nanotip-on-mirror system with full three-dimensional position control could enable us to observe the transition from weak to strong coupling in dye monolayers despite the broad emission spectrum. Finally, we showed our promising first results on ultrathin nanostructured spacer layers using nanosphere lithography. Based on this, we discussed how the density and position of emitters in the nanocavity could be controlled in future experiments. Coupling emitters to plasmonic lattices might pave the way toward long-range coherent energy transfer.

In conclusion, we investigated the coupling of dye monolayers with gold nanoparticle-on-mirror systems. The efficient interaction requires a significant and uniform out-of-plane orientation of the transition dipoles, which we could reveal with our novel orientation determination method. The decomposition of the optical response of NPoMs into their fundamental modes allowed us to compare the scattering from individual NPoMs in experiment and simulation, taking into account nanoparticle size and shape variations. Considering excitation and emission enhancement, we computed the fluorescence enhancement spectra for an incoherent dipole ensemble for comparison with the experiments. Due to the broadband emission spectrum of the dye monolayer, we could characterize the spectral shaping of the fluorescence emission by the modes of the nanoparticle-on-mirror.

This thesis provided a comprehensive and intuitive insight into the interaction of oriented emitter ensembles with plasmonic nanoresonators in the weak coupling limit. We envision that our extensive numerical simulation methods will contribute to the modeling and optimization of coupled cavity-emitter systems in the future. In addition, we expect that future experiments will benefit from our spatially resolved scattering and fluorescence spectroscopy techniques and data analysis.

Bibliography

[1] D. W. Pohl, W. Denk, and M. Lanz. “Optical stethoscopy: Image recording with resolution $\lambda/20$”. In: *Applied Physics Letters* 44.7 (1984), pp. 651–653.

[2] E. Betzig, G. H. Patterson, R. Sougrat, et al. “Imaging intracellular fluorescent proteins at nanometer resolution”. In: *Science* 313.5793 (2006), pp. 1642–1645.

[3] S. W. Hell and J. Wichmann. “Breaking the diffraction resolution limit by stimulated emission: stimulated-emission-depletion fluorescence microscopy”. In: *Optics Letters* 19.11 (1994), p. 780.

[4] K. L. Kelly, E. Coronado, L. L. Zhao, and G. C. Schatz. “The Optical Properties of Metal Nanoparticles: The Influence of Size, Shape, and Dielectric Environment”. In: *The Journal of Physical Chemistry B* 107.3 (2003), pp. 668–677.

[5] D. L. Jeanmaire and R. P. Van Duyne. “Surface raman spectroelectrochemistry”. In: *Journal of Electroanalytical Chemistry and Interfacial Electrochemistry* 84.1 (1977), pp. 1–20.

[6] H. Kollmann, X. Piao, M. Esmann, et al. “Toward Plasmonics with Nanometer Precision: Nonlinear Optics of Helium-Ion Milled Gold Nanoantennas”. In: *Nano Letters* 14.8 (2014), pp. 4778–4784.

[7] S. He, R. Tian, W. Wu, W.-D. Li, and D. Wang. “Helium-ion-beam nanofabrication: extreme processes and applications”. In: *International Journal of Extreme Manufacturing* 3.1 (2021), p. 012001.

[8] M. N. O’Brien, M. R. Jones, K. A. Brown, and C. A. Mirkin. “Universal Noble Metal Nanoparticle Seeds Realized Through Iterative Reductive Growth and Oxidative Dissolution Reactions”. In: *Journal of the American Chemical Society* 136.21 (2014), pp. 7603–7606.

[9] A. Sundaramurthy, K. B. Crozier, G. S. Kino, et al. “Field enhancement and gap-dependent resonance in a system of two opposing tip-to-tip Au nanotriangles”. In: *Physical Review B* 72.16 (2005), p. 165409.

[10] G. C. Li, Q. Zhang, S. A. Maier, and D. Lei. “Plasmonic particle-on-film nanocavities: A versatile platform for plasmon-enhanced spectroscopy and photochemistry”. In: *Nanophotonics* 7.12 (2018), pp. 1865–1889.

[11] S. Lee. “Nanoparticle-on-mirror cavity: a historical view across nanophotonics and nanochemistry”. In: *Journal of the Korean Physical Society* 81.6 (2022), pp. 502–509.

[12] J. J. Mock, R. T. Hill, A. Degiron, et al. “Distance-Dependent Plasmon Resonant Coupling between a Gold Nanoparticle and Gold Film”. In: *Nano Letters* 8.8 (2008), pp. 2245–2252.

[13] D. Y. Lei, A. I. Fernández-Domínguez, Y. Sonnefraud, et al. “Revealing Plasmonic Gap Modes in Particle-on-Film Systems Using Dark-Field Spectroscopy”. In: *ACS Nano* 6.2 (2012), pp. 1380–1386.

[14] R. Chikkaraddy, X. Zheng, F. Benz, et al. “How Ultranarrow Gap Symmetries Control Plasmonic Nanocavity Modes: From Cubes to Spheres in the Nanoparticle-on-Mirror”. In: *ACS Photonics* 4.3 (2017), pp. 469–475.

[15] N. Vogel, J. Zieleniecki, and I. Köper. “As flat as it gets: ultrasmooth surfaces from template-stripping procedures”. In: *Nanoscale* 4.13 (2012), p. 3820.

[16] R. T. Hill, J. J. Mock, A. Hucknall, et al. “Plasmon Ruler with Angstrom Length Resolution”. In: *ACS Nano* 6.10 (2012), pp. 9237–9246.

[17] F. Benz, M. K. Schmidt, A. Dreismann, et al. “Single-molecule optomechanics in "picocavities"”. In: *Science* 354.6313 (2016), pp. 726–729.

[18] J. J. Baumberg, J. Aizpurua, M. H. Mikkelsen, and D. R. Smith. “Extreme nanophotonics from ultrathin metallic gaps”. In: *Nature Materials* 18.7 (2019), pp. 668–678.

[19] C. Ciracì, R. T. Hill, J. J. Mock, et al. “Probing the Ultimate Limits of Plasmonic Enhancement”. In: *Science* 337.6098 (2012), pp. 1072–1074.

[20] J. Mertens, A. L. Eiden, D. O. Sigle, et al. “Controlling Subnanometer Gaps in Plasmonic Dimers Using Graphene”. In: *Nano Letters* 13.11 (2013), pp. 5033–5038.

[21] R. Faggiani, J. Yang, and P. Lalanne. “Quenching, Plasmonic, and Radiative Decays in Nanogap Emitting Devices”. In: *ACS Photonics* 2.12 (2015), pp. 1739–1744.

[22] A. I. Chizhik, J. Rother, I. Gregor, A. Janshoff, and J. Enderlein. “Metal-induced energy transfer for live cell nanoscopy”. In: *Nature Photonics* 8.2 (2014), pp. 124–127.

[23] N. Karedla, A. I. Chizhik, I. Gregor, et al. “Single-Molecule Metal-Induced Energy Transfer (smMIET): Resolving Nanometer Distances at the Single-Molecule Level”. In: *ChemPhysChem* 15.4 (2014), pp. 705–711.

[24] N. Karedla, A. M. Chizhik, S. C. Stein, et al. “Three-dimensional single-molecule localization with nanometer accuracy using Metal-Induced Energy Transfer (MIET) imaging”. In: *The Journal of Chemical Physics* 148.20 (2018), p. 204201.

[25] C. Tserkezis, R. Esteban, D. O. Sigle, et al. “Hybridization of plasmonic antenna and cavity modes: Extreme optics of nanoparticle-on-mirror nanogaps”. In: *Physical Review A* 92.5 (2015), p. 053811.

[26] K. J. Russell, T.-L. Liu, S. Cui, and E. L. Hu. “Large spontaneous emission enhancement in plasmonic nanocavities”. In: *Nature Photonics* 6.7 (2012), pp. 459–462.

[27] T. B. Hoang, G. M. Akselrod, C. Argyropoulos, et al. “Ultrafast spontaneous emission source using plasmonic nanoantennas”. In: *Nature Communications* 6.1 (2015), p. 7788.

[28] T. B. Hoang, G. M. Akselrod, and M. H. Mikkelsen. “Ultrafast Room-Temperature Single Photon Emission from Quantum Dots Coupled to Plasmonic Nanocavities”. In: *Nano Letters* 16.1 (2016), pp. 270–275.

[29] S. I. Bogdanov, M. Y. Shalaginov, A. S. Lagutchev, et al. “Ultrabright Room-Temperature Sub-Nanosecond Emission from Single Nitrogen-Vacancy Centers Coupled to Nanopatch Antennas”. In: *Nano Letters* 18.8 (2018), pp. 4837–4844.

[30] E. Knill, R. Laflamme, and G. J. Milburn. “A scheme for efficient quantum computation with linear optics”. In: *Nature* 409.6816 (2001), pp. 46–52.

[31] M. Ringler, A. Schwemer, M. Wunderlich, et al. “Shaping Emission Spectra of Fluorescent Molecules with Single Plasmonic Nanoresonators”. In: *Physical Review Letters* 100.20 (2008), p. 203002.

[32] L. Saemisch, M. Liebel, N. F. Van Hulst, and N. F. Van Hulst. “Control of Vibronic Transition Rates by Resonant Single-Molecule-Nanoantenna Coupling”. In: *Nano Letters* 20.6 (2020), pp. 4537–4542.

[33] S. Yashima, H. Sugimoto, H. Takashina, and M. Fujii. “Fluorescence Enhancement and Spectral Shaping of Silicon Quantum Dot Monolayer by Plasmonic Gap Resonances”. In: *The Journal of Physical Chemistry C* 120.50 (2016), pp. 28795–28801.

[34] H. Sugimoto, S. Yashima, and M. Fujii. “Hybridized Plasmonic Gap Mode of Gold Nanorod on Mirror Nanoantenna for Spectrally Tailored Fluorescence Enhancement”. In: *ACS Photonics* 5.8 (2018), pp. 3421–3427.

[35] J. Huang, G. M. Akselrod, T. Ming, J. Kong, and M. H. Mikkelsen. “Tailored Emission Spectrum of 2D Semiconductors Using Plasmonic Nanocavities”. In: *ACS Photonics* 5.2 (2018), pp. 552–558.

[36] H. Leng, B. Szychowski, M.-C. Daniel, and M. Pelton. “Strong coupling and induced transparency at room temperature with single quantum dots and gap plasmons”. In: *Nature Communications* 9.1 (2018), p. 4012.

[37] K.-D. Park, M. A. May, H. Leng, et al. “Tip-enhanced strong coupling spectroscopy, imaging, and control of a single quantum emitter”. In: *Science Advances* 5.7 (2019).

[38] R. Chikkaraddy, B. De Nijs, F. Benz, et al. “Single-molecule strong coupling at room temperature in plasmonic nanocavities”. In: *Nature* 535.7610 (2016), pp. 127–130.

[39] G. Zengin, G. Johansson, P. Johansson, et al. “Approaching the strong coupling limit in single plasmonic nanorods interacting with J-aggregates”. In: *Scientific Reports* 3.1 (2013), p. 3074.

[40] G. Zengin, M. Wersäll, S. Nilsson, et al. “Realizing Strong Light-Matter Interactions between Single-Nanoparticle Plasmons and Molecular Excitons at Ambient Conditions”. In: *Physical Review Letters* 114.15 (2015), p. 157401.

[41] R. Liu, Z.-K. Zhou, Y.-C. Yu, et al. “Strong Light-Matter Interactions in Single Open Plasmonic Nanocavities at the Quantum Optics Limit”. In: *Physical Review Letters* 118.23 (2017), p. 237401.

[42] X. Chen, Y. H. Chen, J. Qin, et al. “Mode Modification of Plasmonic Gap Resonances Induced by Strong Coupling with Molecular Excitons”. In: *Nano Letters* 17.5 (2017), pp. 3246–3251.

[43] Z. He, F. Li, P. Zuo, et al. “Strong Coupling in a Hybrid System of Silver Nanoparticles and J-Aggregates at Room Temperature”. In: *Journal of Physical Chemistry C* 126.40 (2022), pp. 17141–17151.

[44] M.-E. Kleemann, R. Chikkaraddy, E. M. Alexeev, et al. “Strong-coupling of WSe2 in ultra-compact plasmonic nanocavities at room temperature”. In: *Nature Communications* 8.1 (2017), p. 1296.

[45] N. Kongsuwan, A. Demetriadou, M. Horton, et al. “Plasmonic Nanocavity Modes: From Near-Field to Far-Field Radiation”. In: *ACS Photonics* 7.2 (2020), pp. 463–471.

[46] J. D. Jackson. *Classical Electrodynamics*. 3rd ed. New York: Wiley, 1999.

[47] L. Novotny and B. Hecht. *Principles of Nano-Optics*. 2nd ed. Cambridge: Cambridge University Press, 2012.

[48] T. Gharbi, D. Barchiesi, S. Kessentini, and R. Maalej. “Fitting optical properties of metals by Drude-Lorentz and partial-fraction models in the [0.5;6] eV range”. In: *Optical Materials Express* 10.5 (2020), p. 1129.

[49] N. D. Ashcroft, Neil W., Mermin. *Solid State Physics*. New York: Saunders College Publishing, 1976.

[50] S. A. Maier. *Plasmonics: Fundamentals and Applications*. Norwell: Springer Science + Business Media LLC, 2007.

[51] P. B. Johnson and R. W. Christy. “Optical Constants of the Noble Metals”. In: *Physical Review B* 6.12 (1972), pp. 4370–4379.

[52] Y. Fu, X. Hu, C. Lu, et al. “All-Optical Logic Gates Based on Nanoscale Plasmonic Slot Waveguides”. In: *Nano Letters* 12.11 (2012), pp. 5784–5790.

[53] C. Schörner, S. Adhikari, and M. Lippitz. “A Single-Crystalline Silver Plasmonic Circuit for Visible Quantum Emitters”. In: *Nano Letters* 19.5 (2019), pp. 3238–3243.

[54] C. Schörner and M. Lippitz. “Single Molecule Nonlinearity in a Plasmonic Waveguide”. In: *Nano Letters* 20.3 (2020), pp. 2152–2156.

[55] G. Mie. “Beiträge zur Optik trüber Medien, speziell kolloidaler Metallösungen”. In: *Annalen der Physik* 330.3 (1908), pp. 377–445.

[56] A. B. Taylor and P. Zijlstra. “Single-Molecule Plasmon Sensing: Current Status and Future Prospects”. In: *ACS Sensors* 2.8 (2017), pp. 1103–1122.

[57] K. A. Willets, A. J. Wilson, V. Sundaresan, and P. B. Joshi. “Super-Resolution Imaging and Plasmonics”. In: *Chemical Reviews* 117.11 (2017), pp. 7538–7582.

[58] M. Fox. *Quantum Optics*. Oxford: Oxford University Press, 2006.

[59] W. W. Parson. *Modern Optical Spectroscopy*. 2nd ed. Springer Heidelberg New York Dordrecht London, 2015.

[60] W. L. Barnes, S. A. Horsley, and W. L. Vos. “Classical antennas, quantum emitters, and densities of optical states”. In: *Journal of Optics (United Kingdom)* 22.7 (2020), p. 73501.

[61] K. H. Drexhage. “IV Interaction of Light with Monomolecular Dye Layers”. In: *Progress in Optics* 12 (1974), pp. 163–192.

[62] T. Yoshle, A. Scherer, J. Hendrickson, et al. “Vacuum Rabi splitting with a single quantum dot in a photonic crystal nanocavity”. In: *Nature* 432.7014 (2004), pp. 200–203.

[63] S. Huang, T. Ming, Y. Lin, et al. “Ultrasmall Mode Volumes in Plasmonic Cavities of Nanoparticle-On-Mirror Structures”. In: *Small* 12.37 (2016), pp. 5190–5199.

[64] C. Sauvan, J. P. Hugonin, I. S. Maksymov, and P. Lalanne. “Theory of the Spontaneous Optical Emission of Nanosize Photonic and Plasmon Resonators”. In: *Physical Review Letters* 110.23 (2013), p. 237401.

[65] P. T. Kristensen and S. Hughes. “Modes and Mode Volumes of Leaky Optical Cavities and Plasmonic Nanoresonators”. In: *ACS Photonics* 1.1 (2014), pp. 2–10.

[66] W. Yan, R. Faggiani, and P. Lalanne. “Rigorous modal analysis of plasmonic nanoresonators”. In: *Physical Review B* 97.20 (2018), p. 205422.

[67] A. Köhler and H. Bässler. *Electronic Processes in Organic Semiconductors*. Weinheim: Wiley-VCH, 2015.

[68] W. Demtröder. *Laser Spectroscopy 1*. 5th ed. Springer Berlin Heidelberg, 2014.

[69] M. Pelton, S. D. Storm, and H. Leng. “Strong coupling of emitters to single plasmonic nanoparticles: exciton-induced transparency and Rabi splitting”. In: *Nanoscale* 11.31 (2019), pp. 14540–14552.

[70] M. Pelton, S. D. Storm, and H. Leng. “Correction: Strong coupling of emitters to single plasmonic nanoparticles: exciton-induced transparency and Rabi splitting”. In: *Nanoscale* 13.8 (2021), p. 4687.

[71] E. Waks and D. Sridharan. “Cavity QED treatment of interactions between a metal nanoparticle and a dipole emitter”. In: *Physical Review A* 82.4 (2010), p. 043845.

[72] X. Wu, S. K. Gray, and M. Pelton. “Quantum-dot-induced transparency in a nanoscale plasmonic resonator”. In: *Optics Express* 18.23 (2010), p. 23633.

[73] S. Rudin and T. L. Reinecke. “Oscillator model for vacuum Rabi splitting in microcavities”. In: *Physical Review B* 59.15 (1999), pp. 10227–10233.

[74] P Törmä and W. L. Barnes. “Strong coupling between surface plasmon polaritons and emitters: a review”. In: *Reports on Progress in Physics* 78.1 (2015), p. 013901.

[75] G. Khitrova, H. M. Gibbs, M. Kira, S. W. Koch, and A. Scherer. “Vacuum Rabi splitting in semiconductors”. In: *Nature Physics* 2.2 (2006), pp. 81–90.

[76] G. Cui and M. G. Raymer. “Emission spectra and quantum efficiency of single-photon sources in the cavity-QED strong-coupling regime”. In: *Physical Review A* 73.5 (2006), p. 053807.

[77] S. K. Kufer, E. M. Puchner, H. Gumpp, T. Liedl, and H. E. Gaub. “Single-Molecule Cut-and-Paste Surface Assembly”. In: *Science* 319.5863 (2008), pp. 594–596.

[78] O. Benson. “Assembly of hybrid photonic architectures from nanophotonic constituents”. In: *Nature* 480.7376 (2011), pp. 193–199.

[79] C. Close, K. Trofymchuk, L. Grabenhorst, et al. “Maximizing the Accessibility in DNA Origami Nanoantenna Plasmonic Hotspots”. In: *Advanced Materials Interfaces* 9.24 (2022), p. 2200255.

[80] X. Han, K. Wang, X. Xing, M. Wang, and P. Lu. “Rabi Splitting in a Plasmonic Nanocavity Coupled to a WS2 Monolayer at Room Temperature”. In: *ACS Photonics* 5.10 (2018), pp. 3970–3976.

[81] M. A. May, D. Fialkow, T. Wu, et al. “Nano-Cavity QED with Tunable Nano-Tip Interaction”. In: *Advanced Quantum Technologies* 3.2 (2020), p. 1900087.

[82] A. Elbanna, H. Jiang, Q. Fu, et al. “2D Material Infrared Photonics and Plasmonics”. In: *ACS Nano* 17.5 (2023), pp. 4134–4179.

[83] M. A. May, T. Jiang, C. Du, et al. “Nanocavity Clock Spectroscopy: Resolving Competing Exciton Dynamics in WSe2/MoSe2 Heterobilayers”. In: *Nano Letters* 21.1 (2021), pp. 522–528.

[84] K. Hasz, Z. Hu, K. D. Park, and M. B. Raschke. “Tip-Enhanced Dark Exciton Nanoimaging and Local Strain Control in Monolayer WSe2”. In: *Nano Letters* 23.1 (2023), pp. 198–204.

[85] H. Cha, J. H. Yoon, and S. Yoon. “Probing Quantum Plasmon Coupling Using Gold Nanoparticle Dimers with Tunable Interparticle Distances Down to the Subnanometer Range”. In: *ACS Nano* 8.8 (2014), pp. 8554–8563.

[86] R. T. Hill, J. J. Mock, Y. Urzhumov, et al. “Leveraging Nanoscale Plasmonic Modes to Achieve Reproducible Enhancement of Light”. In: *Nano Letters* 10.10 (2010), pp. 4150–4154.

[87] F. R. Goßler, A. M. Steiner, O. Stroyuk, A. Raevskaya, and T. A. König. “Active Plasmonic Colloid-to-Film-Coupled Cavities for Tailored Light-Matter Interactions”. In: *Journal of Physical Chemistry C* 123.11 (2019), pp. 6745–6752.

[88] C. Y. Li, S. Duan, B. Y. Wen, et al. “Observation of inhomogeneous plasmonic field distribution in a nanocavity”. In: *Nature Nanotechnology* 15.11 (2020), pp. 922–926.

[89] M. Schmelzeisen, Y. Zhao, M. Klapper, K. Müllen, and M. Kreiter. “Fluorescence Enhancement from Individual Plasmonic Gap Resonances”. In: *ACS Nano* 4.6 (2010), pp. 3309–3317.

[90] C. D. Heinrich, P. M. Reichstein, and M. Thelakkat. “Synthesis, Surface Grafting, and Fabrication of Ultrathin Polymeric SAMFETs with High Field-Effect Mobility”. In: *ACS Applied Materials and Interfaces* 10.41 (2018), pp. 35441–35448.

[91] M. Stöter, S. Rosenfeldt, and J. Breu. “Tunable Exfoliation of Synthetic Clays”. In: *Annual Review of Materials Research* 45 (2015), pp. 129–151.

[92] M. Stöter, D. A. Kunz, M. Schmidt, et al. “Nanoplatelets of sodium hectorite showing aspect ratios of 20 000 and superior purity”. In: *Langmuir* 29.4 (2013), pp. 1280–1285.

[93] M. Stöter, B. Biersack, S. Rosenfeldt, et al. “Encapsulation of Functional Organic Compounds in Nanoglass for Optically Anisotropic Coatings”. In: *Angewandte Chemie - International Edition* 54.16 (2015), pp. 4963–4967.

[94] M. Stöter, S. Gödrich, P. Feicht, et al. “Controlled Exfoliation of Layered Silicate Heterostructures into Bilayers and Their Conversion into Giant Janus Platelets”. In: *Angewandte Chemie* 128.26 (2016), pp. 7524–7528.

[95] M. Matejdes, M. Stöter, R. Czerwieniec, et al. “Sandwich-Like Encapsulation of a Highly Luminescent Copper(I) Complex”. In: *Advanced Optical Materials* 9.19 (2021), p. 2100516.

[96] D. A. Kunz, M. J. Leitl, L. Schade, et al. “Quasi-epitaxial growth of [Ru(bpy)3]2+by confinement in clay nanoplatelets yields polarized emission”. In: *Small* 11.7 (2015), pp. 792–796.

[97] C. Schnupfhagn, T. Schumacher, P. Markus, et al. “Disentangling the Orientations of Spectrally Overlapping Transition Dipoles in Dense Dye Layers”. In: *Nano Letters* 22.18 (2022), pp. 7499–7505.

[98] M. Lippitz. *Lecture Notes: Experiments in Spectroscopy*. 2022. URL: https://dx.doi.org/10.5281/zenodo.5377926.

[99] B. E. A. Saleh and M. C. Teich. *Grundlagen der Photonik*. 2nd ed. Weinheim: WILEY-VCH, 2008.

[100] G. Ford and W. Weber. “Electromagnetic interactions of molecules with metal surfaces”. In: *Physics Reports* 113.4 (1984), pp. 195–287.

[101] Y. C. Jun. “Plasmonic Control of Light Emission: Tailoring Light Emission Properties with Metal Nanostructures”. PhD thesis. Stanford University, 2010.

[102] J. W. Anthony, R. Bideaux, K. W. Bladh, and M. C. Nichols. *Handbook of Mineralogy: Silica, silicates*. Vol. 2,1. Tucson, Arizona: Mineral Data Publ., 1995, p. 322.

[103] K. Hinrichs and K. J. Eichhorn, eds. *Ellipsometry of Functional Organic Surfaces and Films*. Vol. 52. Springer Heidelberg New York Dordrecht London, 2014.

[104] Z. H. Ni, H. M. Wang, J. Kasim, et al. “Graphene Thickness Determination Using Reflection and Contrast Spectroscopy”. In: *Nano Letters* 7.9 (2007), pp. 2758–2763.

[105] G. Jin, R. Jansson, and H. Arwin. “Imaging ellipsometry revisited: Developments for visualization of thin transparent layers on silicon substrates”. In: *Review of Scientific Instruments* 67.8 (1996), pp. 2930–2936.

[106] D. E. Aspnes and A. A. Studna. “Dielectric functions and optical parameters of Si, Ge, GaP, GaAs, GaSb, InP, InAs, and InSb from 1.5 to 6.0 eV”. In: *Physical Review B* 27.2 (1983), pp. 985–1009.

[107] I. H. Malitson. “Interspecimen Comparison of the Refractive Index of Fused Silica”. In: *Journal of the Optical Society of America* 55.10 (1965), p. 1205.

[108] O. Erdem, K. Gungor, B. Guzelturk, et al. “Orientation-Controlled Nonradiative Energy Transfer to Colloidal Nanoplatelets: Engineering Dipole Orientation Factor”. In: *Nano Letters* 19.7 (2019), pp. 4297–4305.

[109] W. Lukosz and M. Meier. “Lifetimes and radiation patterns of luminescent centers close to a thin metal film”. In: *Optics Letters* 6.5 (1981), p. 251.

[110] G. M. Akselrod, C. Argyropoulos, T. B. Hoang, et al. “Probing the mechanisms of large Purcell enhancement in plasmonic nanoantennas”. In: *Nature Photonics* 8.11 (2014), pp. 835–840.

[111] H. K. Turley, Z. Hu, L. Jensen, and J. P. Camden. “Surface-Enhanced Resonance Hyper-Raman Scattering Elucidates the Molecular Orientation of Rhodamine 6G on Silver Colloids”. In: *Journal of Physical Chemistry Letters* 8.8 (2017), pp. 1819–1823.

[112] A. M. Berghuis, V. Serpenti, M. Ramezani, et al. “Light-Matter Coupling Strength Controlled by the Orientation of Organic Crystals in Plasmonic Cavities”. In: *Journal of Physical Chemistry C* 124.22 (2020), pp. 12030–12038.

[113] L. Wang, S. Guo, K. Zhou, and W. Ma. “Control of the molecular orientation in small molecule-based organic photovoltaics”. In: *Sustainable Energy and Fuels* 4.10 (2020), pp. 4934–4955.

[114] E. Toprak, J. Enderlein, S. Syed, et al. “Defocused orientation and position imaging (DOPI) of myosin V”. In: *Proceedings of the National Academy of Sciences of the United States of America* 103.17 (2006), pp. 6495–6499.

[115] X. Brokmann, M.-V. Ehrensperger, J.-P. Hermier, A. Triller, and M. Dahan. “Orientational imaging and tracking of single CdSe nanocrystals by defocused microscopy”. In: *Chemical Physics Letters* 406.1 (2005), pp. 210–214.

[116] J. Jasny and J. Sepioł. “Single molecules observed by immersion mirror objective. A novel method of finding the orientation of a radiating dipole”. In: *Chemical Physics Letters* 273.5 (1997), pp. 439–443.

[117] A. P. Bartko and R. M. Dickson. “Imaging Three-Dimensional Single Molecule Orientations”. In: *The Journal of Physical Chemistry B* 103.51 (1999), pp. 11237–11241.

[118] J. Sepioł, J. Jasny, J. Keller, and U. P. Wild. “Single molecules observed by immersion mirror objective. The orientation of terrylene molecules via the direction of its transition dipole moment”. In: *Chemical Physics Letters* 273.5-6 (1997), pp. 444–448.

[119] D. Patra, I. Gregor, and J. Enderlein. “Image Analysis of Defocused Single-Molecule Images for Three-Dimensional Molecule Orientation Studies”. In: *The Journal of Physical Chemistry A* 108.33 (2004), pp. 6836–6841.

[120] M. A. Lieb, J. M. Zavislan, and L. Novotny. “Single-molecule orientations determined by direct emission pattern imaging”. In: *Journal of the Optical Society of America B* 21.6 (2004), p. 1210.

[121] A. Hofmann, M. Schmid, and W. Brütting. “The Many Facets of Molecular Orientation in Organic Optoelectronics”. In: *Advanced Optical Materials* 9.21 (2021), p. 2101004.

[122] J. S. Kim, P. K. Ho, N. C. Greenham, and R. H. Friend. “Electroluminescence emission pattern of organic light-emitting diodes: Implications for device efficiency calculations”. In: *Journal of Applied Physics* 88.2 (2000), pp. 1073–1081.

[123] K. Hinrichs, M. Levichkova, D. Wynands, et al. “Morphology and molecular orientation of ethyl-substituted dicyanovinyl-sexithiophene films for photovoltaic applications”. In: *Thin Solid Films* 525 (2012), pp. 97–105.

[124] F. Tenopala-Carmona, O. S. Lee, E. Crovini, et al. “Identification of the Key Parameters for Horizontal Transition Dipole Orientation in Fluorescent and TADF Organic Light-Emitting Diodes”. In: *Advanced Materials* 33.37 (2021), p. 2100677.

[125] M. Gsänger, E. Kirchner, M. Stolte, et al. “High-Performance Organic Thin-Film Transistors of J-Stacked Squaraine Dyes”. In: *Journal of the American Chemical Society* 136.6 (2014), pp. 2351–2362.

[126] Y. Gao, M. C. Weidman, and W. A. Tisdale. “CdSe Nanoplatelet Films with Controlled Orientation of their Transition Dipole Moment”. In: *Nano Letters* 17.6 (2017), pp. 3837–3843.

[127] J. Kim, S. Hou, H. Zhao, and S. R. Forrest. “Nanoscale Mapping of Morphology of Organic Thin Films”. In: *Nano Letters* 20.11 (2020), pp. 8290–8297.

[128] J. Kim, H. Zhao, S. Hou, et al. “Using Fourier-Plane Imaging Microscopy for Determining Transition-Dipole-Moment Orientations in Organic Light-Emitting Devices”. In: *Physical Review Applied* 14.3 (2020), p. 034048.

[129] C. Lethiec, J. Laverdant, H. Vallon, et al. “Measurement of Three-Dimensional Dipole Orientation of a Single Fluorescent Nanoemitter by Emission Polarization Analysis”. In: *Physical Review X* 4.2 (2014), p. 021037.

[130] J. T. Fourkas. “Rapid determination of the three-dimensional orientation of single molecules”. In: *Optics Letters* 26.4 (2001), p. 211.

[131] S. A. Empedocles, R. Neuhauser, and M. G. Bawendi. “Three-dimensional orientation measurements of symmetric single chromophores using polarization microscopy”. In: *Nature* 399.6732 (1999), pp. 126–130.

[132] J. Kim, R. Chacón, Z. Wang, et al. “Measuring 3D orientation of nanocrystals via polarized luminescence of rare-earth dopants”. In: *Nature Communications* 12.1 (2021), p. 1943.

[133] D. Axelrod. “Chapter 12 Fluorescence Polarization Microscopy”. In: *Methods in Cell Biology*. Vol. 30. 1989, pp. 333–352.

[134] I.-C. Benea-Chelmus, S. Mason, M. L. Meretska, et al. “Gigahertz free-space electro-optic modulators based on Mie resonances”. In: *Nature Communications* 13.1 (2022), p. 3170.

[135] A. Safrani and I. Abdulhalim. “Liquid-crystal polarization rotator and a tunable polarizer”. In: *Optics Letters* 34.12 (2009), p. 1801.

[136] J. R. Lakowicz. *Principles of Fluorescence Spectroscopy*. Ed. by J. R. Lakowicz. 3rd ed. Boston, MA: Springer Science+Business Media, LLC, 2006.

[137] ATTO-TEC. *Absorption and emission spectrum of the ATTO 532 dye*. URL: `https://www.atto-tec.com/ATTO-532.html` (visited on 12/13/2022).

[138] M. González-Cardel, P. Arguijo, and R. Díaz-Uribe. “Gaussian beam radius measurement with a knife-edge: A polynomial approximation to the inverse error function”. In: *Applied Optics* 52.16 (2013), pp. 3849–3855.

[139] C. S. Abeywickrama, K. J. Wijesinghe, R. V. Stahelin, and Y. Pang. “Bright red-emitting pyrene derivatives with a large Stokes shift for nucleus staining”. In: *Chemical Communications* 53.43 (2017), pp. 5886–5889.

[140] Y. Guo, C. S. Abeywickrama, D. Huo, et al. “Solvation Controlled Excited-State Planarization in a Push-Pull Pyrene Dye”. In: *Journal of Physical Chemistry C* 124.16 (2020), pp. 8550–8560.

[141] I. W. Schie and T. Huser. “Methods and Applications of Raman Microspectroscopy to Single-Cell Analysis”. In: *Applied Spectroscopy* 67.8 (2013), pp. 813–828.

[142] F. Bonnier and H. J. Byrne. “Understanding the molecular information contained in principal component analysis of vibrational spectra of biological systems”. In: *The Analyst* 137.2 (2012), pp. 322–332.

[143] S. L. Brunton and J. N. Kutz. *Data-Driven Science and Engineering*. Cambridge: Cambridge University Press, 2019.

[144] T. Yoshikawa, M. Kawamoto, T. Fujihara, et al. “Long-lived cis state of azocarbazole dye with strong acceptor highly doped in a polymer matrix”. In: *Journal of the Optical Society of America B* 32.4 (2015), p. 622.

[145] H. Kalo, W. Milius, and J. Breu. “Single crystal structure refinement of one- and two-layer hydrates of sodium fluorohectorite”. In: *RSC Advances* 2.22 (2012), pp. 8452–8459.

[146] M. Daab, N. J. Eichstaedt, C. Habel, et al. “Onset of Osmotic Swelling in Highly Charged Clay Minerals”. In: *Langmuir* 34.28 (2018), pp. 8215–8222.

[147] A. Kress, X. Wang, H. Ranchon, et al. “Mapping the Local Organization of Cell Membranes Using Excitation-Polarization-Resolved Confocal Fluorescence Microscopy”. In: *Biophysical Journal* 105.1 (2013), pp. 127–136.

[148] B. Corry, D. Jayatilaka, B. Martinac, and P. Rigby. “Determination of the Orientational Distribution and Orientation Factor for Transfer between Membrane-Bound Fluorophores using a Confocal Microscope”. In: *Biophysical Journal* 91.3 (2006), pp. 1032–1045.

[149] C. K. Haluska, A. P. Schröder, P. Didier, et al. “Combining Fluorescence Lifetime and Polarization Microscopy to Discriminate Phase Separated Domains in Giant Unilamellar Vesicles”. In: *Biophysical Journal* 95.12 (2008), pp. 5737–5747.

[150] R. Camacho, D. Täuber, and I. G. Scheblykin. “Fluorescence Anisotropy Reloaded—Emerging Polarization Microscopy Methods for Assessing Chromophores’ Organization and Excitation Energy Transfer in Single Molecules, Particles, Films, and Beyond”. In: *Advanced Materials* 31.22 (2019), p. 1805671.

[151] T. Chandler, S. Mehta, H. Shroff, R. Oldenbourg, and P. J. La Rivière. “Single-fluorophore orientation determination with multiview polarized illumination: modeling and microscope design”. In: *Optics Express* 25.25 (2017), p. 31309.

[152] D. Robinson. “Comparison of the Transition Dipole Moments Calculated by TDDFT with High Level Wave Function Theory”. In: *Journal of Chemical Theory and Computation* 14.10 (2018), pp. 5303–5309.

[153] J. Hu, X. D. Xiao, D. F. Ogletree, and M. Salmeron. “Imaging the Condensation and Evaporation of Molecularly Thin Films of Water with Nanometer Resolution”. In: *Science* 268.5208 (1995), pp. 267–269.

[154] P. Matvija, F. Rozbořil, P. Sobotík, et al. “Electric-field-controlled phase transition in a 2D molecular layer”. In: *Scientific Reports* 7.1 (2017), p. 7357.

[155] H. Heinz, H. J. Castelijns, and U. W. Suter. “Structure and Phase Transitions of Alkyl Chains on Mica”. In: *Journal of the American Chemical Society* 125.31 (2003), pp. 9500–9510.

[156] D. K. Gramotnev and S. I. Bozhevolnyi. “Plasmonics beyond the diffraction limit”. In: *Nature Photonics* 4.2 (2010), pp. 83–91.

[157] E. Prodan, C. Radloff, N. J. Halas, and P. Nordlander. “A Hybridization Model for the Plasmon Response of Complex Nanostructures”. In: *Science* 302.5644 (2003), pp. 419–422.

[158] P. Nordlander, C. Oubre, E. Prodan, K. Li, and M. I. Stockman. “Plasmon hybridization in nanoparticle dimers”. In: *Nano Letters* 4.5 (2004), pp. 899–903.

[159] B. Luk’yanchuk, N. I. Zheludev, S. A. Maier, et al. “The Fano resonance in plasmonic nanostructures and metamaterials”. In: *Nature Materials* 9.9 (2010), pp. 707–715.

[160] H. A. Khan, S. W. Shah, and A. D. Khan. “Electromagnetic-Induced Transparency and Slow Light in Plasmonic Metasurfaces”. In: *Plasmonics* 17.1 (2022), pp. 51–58.

[161] S. Mubeen, S. Zhang, N. Kim, et al. “Plasmonic Properties of Gold Nanoparticles Separated from a Gold Mirror by an Ultrathin Oxide”. In: *Nano Letters* 12.4 (2012), pp. 2088–2094.

[162] F. Benz, R. Chikkaraddy, A. Salmon, et al. “SERS of Individual Nanoparticles on a Mirror: Size Does Matter, but so Does Shape”. In: *Journal of Physical Chemistry Letters* 7.12 (2016), pp. 2264–2269.

[163] E. Carbó-Argibay and B. Rodríguez-González. “Controlled Growth of Colloidal Gold Nanoparticles: Single-Crystalline versus Multiply-twinned Particles”. In: *Israel Journal of Chemistry* 56.4 (2016), pp. 214–226.

[164] B. Fleury, R. Cortes-Huerto, O. Taché, et al. “Gold Nanoparticle Internal Structure and Symmetry Probed by Unified Small-Angle X-ray Scattering and X-ray Diffraction Coupled with Molecular Dynamics Analysis”. In: *Nano Letters* 15.9 (2015), pp. 6088–6094.

[165] J.-h. Huh, J. Lee, and S. Lee. “Comparative Study of Plasmonic Resonances between the Roundest and Randomly Faceted Au Nanoparticles-on-Mirror Cavities”. In: *ACS Photonics* 5.2 (2018), pp. 413–421.

[166] J.-S. Huang, V. Callegari, P. Geisler, et al. “Atomically flat single-crystalline gold nanostructures for plasmonic nanocircuitry”. In: *Nature Communications* 1.1 (2010), p. 150.

[167] C. Lumdee, B. Yun, and P. G. Kik. “Effect of surface roughness on substrate-tuned gold nanoparticle gap plasmon resonances”. In: *Nanoscale* 7.9 (2015), pp. 4250–4255.

[168] S. M. George. “Atomic Layer Deposition: An Overview”. In: *Chemical Reviews* 110.1 (2010), pp. 111–131.

[169] J.-M. Jin. *The Finite Element Method in Electromagnetics*. New York: Wiley, 1993.

[170] P. Lalanne, W. Yan, K. Vynck, C. Sauvan, and J.-P. Hugonin. “Light Interaction with Photonic and Plasmonic Resonances”. In: *Laser & Photonics Reviews* 12.5 (2018), p. 1700113.

[171] S. G. Johnson. “Notes on Perfectly Matched Layers (PMLs)”. In: (2021). URL: https://doi.org/10.48550/arXiv.2108.05348.

[172] A. J. F. Siegert. “On the Derivation of the Dispersion Formula for Nuclear Reactions”. In: *Physical Review* 56.8 (1939), pp. 750–752.

[173] P. Lalanne. *Light-in-complex-nanostructures/MAN: V7.0.1*. 2020. URL: https://doi.org/10.5281/zenodo.3631242.

[174] P. Y. Chen, D. J. Bergman, and Y. Sivan. “Generalizing Normal Mode Expansion of Electromagnetic Green’s Tensor to Open Systems”. In: *Physical Review Applied* 11.4 (2019), p. 044018.

[175] G. Rosolen, B. Maes, P. Y. Chen, and Y. Sivan. “Overcoming the bottleneck for quantum computations of complex nanophotonic structures: Purcell and Förster resonant energy transfer calculations using a rigorous mode-hybridization method”. In: *Physical Review B* 101.15 (2020), p. 155401.

[176] J. Lin, M. Qiu, X. Zhang, et al. “Tailoring the lineshapes of coupled plasmonic systems based on a theory derived from first principles”. In: *Light: Science & Applications* 9.1 (2020), p. 158.

[177] M. J. Horton, O. S. Ojambati, R. Chikkaraddy, et al. “Nanoscopy through a plasmonic nanolens”. In: *Proceedings of the National Academy of Sciences* 117.5 (2020), pp. 2275–2281.

[178] C. F. Bohren and D. R. Huffman. *Absorption and Scattering of Light by Small Particles*. Weinheim: Wiley-VCH, 1998.

[179] D. C. Tzarouchis, P. Yla-Oijala, and A. Sihvola. “Resonant Scattering Characteristics of Homogeneous Dielectric Sphere”. In: *IEEE Transactions on Antennas and Propagation* 65.6 (2017), pp. 3184–3191.

[180] J. A. Stratton. *Electromagnetic Theory*. Piscataway: IEEE Press, 2007.

[181] U. Hohenester. *Nano and Quantum Optics*. Cham: Springer, 2020.

[182] J. Yang, J. P. Hugonin, and P. Lalanne. “Near-to-Far Field Transformations for Radiative and Guided Waves”. In: *ACS Photonics* 3.3 (2016), pp. 395–402.

[183] J. Yang, J.-P. Hugonin, and P. Lalanne. *Light-in-complex-nanostructures/RETOP: V8 (8.0)*. 2020. URL: https://doi.org/10.5281/zenodo.3609150.

[184] Q. Bai, M. Perrin, C. Sauvan, J.-P. Hugonin, and P. Lalanne. “Efficient and intuitive method for the analysis of light scattering by a resonant nanostructure”. In: *Optics Express* 21.22 (2013), p. 27371.

[185] V. Myroshnychenko, J. Rodríguez-Fernández, I. Pastoriza-Santos, et al. “Modelling the optical response of gold nanoparticles”. In: *Chemical Society Reviews* 37.9 (2008), pp. 1792–1805.

[186] W. Li. “Physics Models of Plasmonics: Single Nanoparticle, Complex Single Nanoparticle, Nanodimer, and Single Nanoparticle over Metallic Thin Film”. In: *Plasmonics* 13.3 (2018), pp. 997–1014.

[187] G. C. Li, Y. L. Zhang, and D. Y. Lei. “Hybrid plasmonic gap modes in metal film-coupled dimers and their physical origins revealed by polarization resolved dark field spectroscopy”. In: *Nanoscale* 8.13 (2016), pp. 7119–7126.

[188] R. Boidin, T. Halenkovič, V. Nazabal, L. Beneš, and P. Němec. “Pulsed laser deposited alumina thin films”. In: *Ceramics International* 42.1 (2016), pp. 1177–1182.

[189] D. O. Sigle, J. Mertens, L. O. Herrmann, et al. “Monitoring Morphological Changes in 2D Monolayer Semiconductors Using Atom-Thick Plasmonic Nanocavities”. In: *ACS Nano* 9.1 (2015), pp. 825–830.

[190] V. Devaraj, H. Jeong, C. Kim, J.-M. Lee, and J.-W. Oh. “Modifying Plasmonic-Field Enhancement and Resonance Characteristics of Spherical Nanoparticles on Metallic Film: Effects of Faceting Spherical Nanoparticle Morphology”. In: *Coatings* 9.6 (2019), p. 387.

[191] V. Devaraj, J. M. Lee, S. Adhikari, et al. “A single bottom facet outperforms random multifacets in a nanoparticle-on-metallic-mirror system”. In: *Nanoscale* 12.44 (2020), pp. 22452–22461.

[192] S. I. Bozhevolnyi and T. Søndergaard. “General properties of slow-plasmon resonant nanostructures: nano-antennas and resonators”. In: *Optics Express* 15.17 (2007), p. 10869.

[193] R. Filter, J. Qi, C. Rockstuhl, and F. Lederer. “Circular optical nanoantennas: an analytical theory”. In: *Physical Review B* 85.12 (2012), p. 125429.

[194] M.-e. Kleemann, J. Mertens, X. Zheng, et al. “Revealing Nanostructures through Plasmon Polarimetry”. In: *ACS Nano* 11.1 (2017), pp. 850–855.

[195] K. Bedingfield, E. Elliott, N. Kongsuwan, J. J. Baumberg, and A. Demetriadou. “Morphology dependence of nanoparticle-on-mirror geometries: A quasinormal mode analysis”. In: *EPJ Applied Metamaterials* 9 (2022), p. 3.

[196] J. B. Lassiter, F. McGuire, J. J. Mock, et al. “Plasmonic Waveguide Modes of Film-Coupled Metallic Nanocubes”. In: *Nano Letters* 13.12 (2013), pp. 5866–5872.

[197] J. Huang, O. S. Ojambati, R. Chikkaraddy, et al. “Plasmon-Induced Trap State Emission from Single Quantum Dots”. In: *Physical Review Letters* 126.4 (2021), p. 047402.

[198] G. M. Akselrod, T. Ming, C. Argyropoulos, et al. “Leveraging Nanocavity Harmonics for Control of Optical Processes in 2D Semiconductors”. In: *Nano Letters* 15.5 (2015), pp. 3578–3584.

[199] J. Zuloaga and P. Nordlander. “On the Energy Shift between Near-Field and Far-Field Peak Intensities in Localized Plasmon Systems”. In: *Nano Letters* 11.3 (2011), pp. 1280–1283.

[200] H. Hu, Y. Xu, Z. Hu, et al. “Nanoparticle-on-mirror pairs: building blocks for remote spectroscopies”. In: *Nanophotonics* 11.22 (2022), pp. 5153–5163.

[201] A. P. Demchenko. “Photobleaching of organic fluorophores: quantitative characterization, mechanisms, protection”. In: *Methods and Applications in Fluorescence* 8.2 (2020), p. 022001.

[202] J. Enderlein. “Single-molecule fluorescence near a metal layer”. In: *Chemical Physics* 247.1 (1999), pp. 1–9.

[203] H. Cang, Y. Liu, Y. Wang, X. Yin, and X. Zhang. “Giant Suppression of Photobleaching for Single Molecule Detection via the Purcell Effect”. In: *Nano Letters* 13.12 (2013), pp. 5949–5953.

[204] C. Lumdee, B. Yun, and P. G. Kik. “Gap-Plasmon Enhanced Gold Nanoparticle Photoluminescence”. In: *ACS Photonics* 1.11 (2014), pp. 1224–1230.

[205] D. Dregely, K. Lindfors, M. Lippitz, et al. “Imaging and steering an optical wireless nanoantenna link”. In: *Nature Communications* 5.1 (2014), p. 4354.

[206] M. Panneerselvam, A. Kathiravan, N. Johnee Britto, et al. “Delineating the effect of substituent and π-bridge flip on the photophysical properties of pyrene derivatives: answers from DFT/TD-DFT calculations”. In: *Journal of Materials Science* 57.23 (2022), pp. 10724–10735.

[207] R. C. Hilborn. “Einstein coefficients, cross sections, f values, dipole moments, and all that”. In: *American Journal of Physics* 50.11 (1982), pp. 982–986.

[208] G. Kewes, F. Binkowski, S. Burger, L. Zschiedrich, and O. Benson. “Heuristic Modeling of Strong Coupling in Plasmonic Resonators”. In: *ACS Photonics* 5.10 (2018), pp. 4089–4097.

[209] B. Munkhbat, M. Wersäll, D. G. Baranov, T. J. Antosiewicz, and T. Shegai. “Suppression of photo-oxidation of organic chromophores by strong coupling to plasmonic nanoantennas”. In: *Science Advances* 4.7 (2018).

[210] H. Groß, J. M. Hamm, T. Tufarelli, O. Hess, and B. Hecht. “Near-field strong coupling of single quantum dots”. In: *Science Advances* 4.3 (2018).

[211] J. R. Oh, J. H. Moon, H. K. Park, et al. “Wafer-scale colloidal lithography based on self-assembly of polystyrene nanospheres and atomic layer deposition”. In: *Journal of Materials Chemistry* 20.24 (2010), pp. 5025–5029.

[212] N. Vogel, S. Goerres, K. Landfester, and C. K. Weiss. “A Convenient Method to Produce Close- and Non-close-Packed Monolayers using Direct Assembly at the Air-Water Interface and Subsequent Plasma-Induced Size Reduction”. In: *Macromolecular Chemistry and Physics* 212.16 (2011), pp. 1719–1734.

[213] V. G. Kravets, A. V. Kabashin, W. L. Barnes, and A. N. Grigorenko. “Plasmonic Surface Lattice Resonances: A Review of Properties and Applications”. In: *Chemical Reviews* 118.12 (2018), pp. 5912–5951.

[214] A. K. Boddeti, J. Guan, T. Sentz, et al. “Long-Range Dipole-Dipole Interactions in a Plasmonic Lattice”. In: *Nano Letters* 22.1 (2022), pp. 22–28.

[215] L. Shi, T. K. Hakala, H. T. Rekola, et al. “Spatial Coherence Properties of Organic Molecules Coupled to Plasmonic Surface Lattice Resonances in the Weak and Strong Coupling Regimes”. In: *Physical Review Letters* 112.15 (2014), p. 153002.

[216] Q.-Y. Lin, Z. Li, K. A. Brown, et al. “Strong Coupling between Plasmonic Gap Modes and Photonic Lattice Modes in DNA-Assembled Gold Nanocube Arrays”. In: *Nano Letters* 15.7 (2015), pp. 4699–4703.

Resolving dipole distributions with linear polarizers

A

We assume an ensemble of in-plane transition dipole moments with an angle distribution $f(\phi)$. The real-valued distribution is 2π periodic, i.e., $f(\phi) = f(\phi + 2\pi)$ and is written as a Fourier series

$$f(\theta) = \sum_{k=0}^{\infty} (A_k \cos(k\,\phi) + B_k \sin(k\phi)) \tag{A.1}$$

with

$$A_0 = \frac{1}{2\pi} \int_0^{2\pi} f(\phi) \mathrm{d}\phi \quad , \tag{A.2}$$

$$A_k = \frac{1}{\pi} \int_0^{2\pi} f(\phi) \cos(k\phi) \mathrm{d}\phi, \qquad k \geq 1 \quad , \tag{A.3}$$

$$B_k = \frac{1}{\pi} \int_0^{2\pi} f(\phi) \sin(k\phi) \mathrm{d}\phi, \qquad k \geq 1 \quad . \tag{A.4}$$

In detection, the radiation of a dipole with angle β with respect to the x-axis transmitted through a linear polarizer with angle α is

$$T = \cos(\alpha - \beta)^2 \quad . \tag{A.5}$$

The ensemble of dipoles thus leads to a detected intensity of

$$I(\alpha) = \int_0^{2\pi} f(\phi) \cos(\alpha - \phi)^2 \mathrm{d}\phi = \sum_{k=0}^{\infty} \left(A_k \tilde{A}_k(\alpha) + B_k \tilde{B}_k(\alpha) \right) \tag{A.6}$$

with

$$\tilde{A}_k(\alpha) = \int_0^{2\pi} \cos(k\phi) \cos(\alpha - \phi)^2 \mathrm{d}\phi \quad , \tag{A.7}$$

$$\tilde{B}_k(\alpha) = \int_0^{2\pi} \sin(k\phi) \cos(\alpha - \phi)^2 \mathrm{d}\phi \quad . \tag{A.8}$$

Only three functions do not vanish:

$$\tilde{A}_0(\alpha) = \pi \quad , \tag{A.9}$$

$$\tilde{A}_2(\alpha) = \frac{\pi}{2} \cos(2\alpha) \quad , \tag{A.10}$$

$$\tilde{B}_2(\alpha) = \pi \sin(\alpha) \cos(\alpha) \quad . \tag{A.11}$$

Hence, the rotation of a polarizer only allows to detect the constant offset and the $k = 2$ Fourier components of the angular distribution. All other Fourier components are averaged out [150]. For a probability density we require $f(\phi) \geq 0$ for all angles ϕ and

$$\int_0^{2\pi} f(\phi)\,\mathrm{d}\phi = 1 \quad . \tag{A.12}$$

It is thus sufficient to describe the angular distribution as

$$f(\theta) = \frac{1}{2\pi}\left(1 + \tilde{a}\cos(2\phi) + \tilde{b}\sin(2\phi)\right) \tag{A.13}$$

with $|\tilde{a}|, |\tilde{b}| \leq 1$. For $\tilde{a} > 0$ we use the trigonometric identity

$$\tilde{a}\cos(2\phi) + \tilde{b}\sin(2\phi) = \sqrt{\tilde{a}^2 + \tilde{b}^2}\cos(2(\phi - \phi_0)) \tag{A.14}$$

and see that the preferred angle is the shift of the cosine

$$\phi_0 = \frac{1}{2}\arctan\frac{\tilde{b}}{\tilde{a}} \quad . \tag{A.15}$$

As the cosine is 2π periodic, we can not distinguish ϕ_0 from $\phi_0 + \pi$. We use the fit function

$$f(\phi) = \frac{1}{2\pi}\left(1 + a\cos(2(\phi - \phi_0))\right) \tag{A.16}$$

with anisotropy $a \in [0, 1]$ and in-plane preferential direction ϕ_0.

Eidesstattliche Versicherung

Hiermit versichere ich an Eides statt, dass ich die vorliegende Arbeit selbstständig verfasst und keine anderen als die von mir angegebenen Quellen und Hilfsmittel verwendet habe.

Weiterhin erkläre ich, dass ich die Hilfe von gewerblichen Promotionsberatern bzw. Promotionsvermittlern oder ähnlichen Dienstleistern weder bisher in Anspruch genommen habe, noch künftig in Anspruch nehmen werde.

Zusätzlich erkläre ich hiermit, dass ich keinerlei frühere Promotionsversuche unternommen habe.

Ort, Datum	Christoph Schnupfhagn

Colophon

This thesis was typeset with LaTeX 2_ε. It uses the *Clean Thesis* style developed by Ricardo Langner. The design of the *Clean Thesis* style is inspired by user guide documents from Apple Inc.

Download the *Clean Thesis* style at `http://cleanthesis.der-ric.de/`.